A multi-spacecraft study of interacting ICMEs and CIRs in interplanetary space

Thesis submitted for the degree of
Doctor of Philosophy
at Aberystwyth University

Duraid A. Mohammed Al-Shakarchi

Supervised by:
Dr Huw Morgan

Institute of Mathematics, Physics and Computer Sciences
Aberystwyth University

January 2018

Declaration

Word Count of thesis: ……..

This work has not previously been accepted in substance for any degree and is not being concurrently submitted in candidature for any degree.

Candidate name ……

Signed …….. (candidate)

Date ……..

Statement 1

This thesis is the result of my own investigations, except where otherwise stated. Where correction services have been used, the extent and nature of the correction is clearly marked in a footnote(s)
Other sources are acknowledged by footnotes given explicit references. A bibliography is appended.

Signed …….. (candidate)

Date ……..

Statement 2

I hereby give consent for my thesis, if accepted, to be made available for photocopying and for inter-library loan, and for the title and summary to be made available to outside organisations.

Signed …….. (candidate)

Date ……..

Acknowledgements

I wish to express my sincere gratitude to my supervisor, Dr Huw Morgan, for his support, help, and imparting his knowledge to this study; Dr Eleri Pryse, for her encouragement; and my fellow PhD students for their friendship and support throughout my time here.

I would like to express my gratitude to my beloved and supportive wife, who is always by my side when times I needed her most and helped me a lot of in making this study, my loveable children who served as my inspiration to peruse this undertaking.

My parents who prayed always for me to succeed. Thank you for all the support you have given me.

I am highly indebted to the Department of Physics- Aberystwyth University for their guidance and support in completing this endeavour.

My deep gratitude to Dr Skoug, Ruth M and Dr Lan K. Jian for helpful comments. The solar wind magnetic field and plasma data are courtesy of the ACE MAG and SWEPAM, the Wind MFI and SWE and the STEREO IMPACT and PLASTIC teams.

Many thanks and appreciations to the Iraqi Cultural Attaché and all people who have willingly helped me out with their abilities.

Abstract

This thesis is concerned with studying the interactions of interplanetary large-scale structures with the solar wind and with each other based on multi spacecraft *in-situ* observations. These structures include: interplanetary coronal mass ejections (ICMEs), stream interaction regions SIRs and heliospheric plasma sheets HPSs.

During their propagation through interplanetary space, ICMEs can interact with each other or with CIRs, making space weather forecasting more difficult. Interaction can change their configurations, dynamics, magnetic field and plasma morphologies. This includes flux rope deformation, reverse shock formation, radio emission enhancement, proton temperature increases, and ICME deflections. Caution should be exercised regarding geomagnetic storm forecasting that depends upon ICME magnetic field observations close to the sun, especially when there is an interaction with co-rotating structures, because this interaction could change the profile of the magnetic field measurements.

Chapter 3 is a case study that aims to understand more about this interaction based on multi spacecraft *in-situ* measurements. During September 09- 10, 2011 the ACE, Wind and The Solar and Heliospheric Observatory(SOHO) spacecraft measured a complex interaction between an ICME and a co-rotating interaction region CIR associated with the HPS. A forward shock, sheath, and magnetic cloud was followed by the CIR and a high-speed stream (HSS) originating from a large equatorial coronal hole. Except for a few short periods, the suprathermal electrons are unidirectional with a 180˚ pitch angle, suggesting a scenario that the magnetic field of the ICME is open through interchange reconnection. Signatures of interaction between the ICME, CIR and subsequent HSS is distributed throughout the event and not concentrated in a specific position suggesting that the structures have become entangled, or embedded. The forward shock was strong and the ICME speed is not enough to drive it. We attributed the most likely source of the shock as the ICME-CIR interaction. Distinct and Interesting features due to the ICME-CIR/HSS interaction are the heating flux discontinuity upstream of the ICME front shock, the very high proton density in the shock, the significant speed elevation within the sheath, the distortion of *Bz* in the magnetic cloud, the indistinct location of the stream interface, the unidirectional domination of the suprathermal electrons and the reverse shock at the rear boundary of the CIR. A few days earlier, The Solar Terrestrial Relation Observatory (STEREO) B recorded the passage of the CIR in absence of an ICME. Despite the disruption of the ICME, some general features of the CIR are preserved, showing compression of the CIR by the ICME by a factor of ~ 4, and enabling some qualitative comparison and further insight into the interaction.

Chapter 4 presents an *In-Situ* study of a compound stream event measured by the STEREO B on March20-25, 2011. During the period, *in situ* results were obtained by *STEREO* B measuring a compound stream containing several interacting structures. An analysis of these results suggests that the stream consists of two interplanetary coronal mass ejections (ICMEs) followed by an embedded ICME/CIR. The third ICME has merged with, and is embedded within, a CIR. A significant stream interface has appeared within the ICME3 revealing the

ability of this structure to penetrate the magnetic flux rope and change its physical properties, particularly its temperature. The sudden appearance of ICME3 within the fast wind side of the CIR causes the temperature to drop suddenly to its lowest level in about 1.2 hours, from 3.89×10^5 K to 1.07×10^4 K. Conversely, the fast wind which follows the CIR influences not only the ICME3 temperature but also its plasma β. In addition, the third ICME impacts the CIR through expansion and deceleration. Penetration of a forward pressure wave driven by this combined ICME-CIR causes an increase in the temperature and plasma beta of the second ICME and part of the first. Despite the presence of signatures from four large-scale interacting structures within the compound stream, it is difficult to reconcile the *in-situ* sequence with remote sensing observations of CMEs and ejecta close to the Sun. Compound streams therefore remain difficult to interpret, and further understanding of the subject will depend on the future study of similar events.

Chapter 5 concentrates on tracking the evolution of a CIR during its propagation through the interplanetary spiral pattern (180 degrees of longitude) and its interaction with other interplanetary structures from period 20 April 2011 to 8 May 2011 based on multi spacecraft in situ observations (STEREO B, WIND, ACE and STEREO A). The results reveal an interaction with two-magnetic cloud flux ropes embedded within the CIR at Lagrange L1 and STEREO A (STA) positions. The role of these interplanetary magnetic flux ropes was noticeable on the CIR morphology by changing its reverse shock and stream interaction (SI) behaviours, with an obvious appearance of the SI within the magnetic cloud flux rope which is embedded with the CIR. The appearance of the reverse shock at STEREO B (STB), disappearance at L1 region, and then an appearance at STEREO A, imply that the CIR reverse shock behaviour was subjected to the local interplanetary circumstance, such as transient ICME interactions. It also reveals the CIR's ability to recover its magnetic field and plasma morphology after disruption by ICMEs. The L1 ICME changes the CIR speed and dynamic pressure profiles. consequently, the acting forces at both reverse shock sides have changed, leading to the disappearance of the reverse shock at L1. At STA, the ICME deceleration has moved the position of the CIR's maximum speed (*V*max) back to the rear CIR boundary, similar to position at STB. The SIs location has approached the Vmax location. These two changes made the profile of the dynamic pressure near the rear of the CIR to return to a state similar to that seen at STB, and thus, the reverse shock reappears. The ICME-CIR interaction at L1 and STA effects the HCS by the growth of the heliospheric plasma sheet (HPS) at the front of the events which coincided with the existence of the magnetic clouds within the CIR.

Contents

Chapter 1 The Sun and Interplanetary Space 1

1.1 Introduction 1

1.2 The Solar interior and Atmosphere 1

1.3 The Solar Corona 2

1.4 Active regions and the Solar cycle 4

1.5 Filaments, Coronal Mass Ejections (CMEs) and Flares 6

1.6 Coronal Holes 8

1.7 The Geoeffectiveness of Halo CMEs: 9

1.8 The Interplanetary medium 11

1.8.1 Solar wind and Interplanetary Magnetic Field (IMF) 11

1.8.2 Magnetohydrodynamics (MHD) 16

1.8.3 Plasma and Electromagnetic Field 18

1.8.4 Heliospheric Current Sheet (HCS), Sector Boundary Crossing (SBC), and Heliospheric Plasma Sheet (HPS). 20

1.9 Interplanetary Coronal Mass Ejections (ICMEs) 24

1.9.1 ICME structure 24

1.9.2 ICME in situ signatures and parameters 25

1.9.3 ICME, Ejecta and the Magnetic cloud (MC) 30

1.9.4 Magnetic Clouds MCs and Flux Rope 32

1.9.5 Flux rope categorisation and classification 35

1.9.6 ICME Multiple-Spacecraft Observations 38

1.9.7 Total perpendicular pressure 39

1.9.8 Suprathermal electrons pitch angle distributions 43

1.9.9 Heat flux dropouts (HFDs) 45

1.9.10 Magnetic reconnection 47

1.9.11 MC and Interchange Reconnection 48

1.9.11 ICMEs and the Streamer belt 53

1.9.12 Deflections of Halo CMEs in Interplanetary Space 56

1.9.13 ICME Catalogues and Criteria 57

1.10 Corotating Interaction Regions (CIRs) 60
1.11 Magnetic storms at Earth 63
1.12 ICMEs and Space Weather 65
Chapter 2 Instrumentations 68
2.1 The Solar and Heliospheric Observatory (SOHO) 68
2.1.1 Large Angle and Spectroscopic Coronagraph (LASCO) 68
2.2 The Solar Dynamics Observatory (SDO) 68
2.2.1 The Atmospheric Imaging Assembly (AIA) 68
2.3 The WIND spacecraft 69
2.3.1 WIND Solar Wind Experiment (SWE) 69
2.3.2 WIND Magnetic Field Investigation (MFI) 70
2.4 The Advanced Composition Explorer (ACE) 70
2.4.1 ACE Magnetic Fields Experiment/Magnetometer (MAG) 71
2.4.2 ACE Solar Wind Electron Proton Alpha Monitor (SWEPAM) 71
2.5 The Solar Terrestrial Relation Observatory (STEREO) 72
2.5.1 Sun Earth Connection Coronal and Heliospheric Investigation (SECCHI) 72
2.5.2 In Situ Measurements of Particles and CME Transient (IMPACT) 73
2.5.3 Plasma and Suprathermal Ion Composition (PLASTIC) (Galvin et al., 2008) 73
Chapter 3 Properties of the HPS-ICME-CIR interaction event of 09-10/09/2011* 75
3.1 Introduction 77
3.2 Instruments 79
3.3 Results 80
3.3.1 Eruption and low-coronal propagation 80
3.3.2 ICME measurements 83
3.3.3 CIR measurements 86
3.3.4 Geomagnetic response 87
3.3.5 Heating flux distribution and interchange reconnection 87
3.3.6 HPS/HCS-ICME Interaction region 89
3.3.7 CIR compression due to the ICME 93
3.3.8 ICME-CIR/HSS interaction impacts 97
3.4 Summary and Conclusions 98
Chapter 4 The compound stream event of March 20-25, 2011 as measured by the STEREO B spacecraft 100
4.1 Introduction 102
4.2 Remote sensing observations 104
4.3 In situ observations 107

4.4 Pressure wave analysis 110
4.5 ICMEs analysis 112
4.6 CIR/ICME3 embedded 113
4.7 The impact of the ICME3/CIR merger 115
4.8 Discussion & Conclusions 115
Chapter 5 Evolution of a Co-rotating Interaction Region and its interaction with other structures over 180 degrees of longitude 117
5.1 Introduction 119
5.2 In Situ observations 121
5.3 Analyses and Discussion 125
5.4 Conclusions 130
Chapter 6 Conclusions 131
6.1 Overall conclusions 131
6.2 Future work 132

List of Figures

FIGURE 1.1 SOLAR INTERIOR AND ATMOSPHERIC LAYERS ASSOCIATED WITH SOLAR FEATURES: SUNSPOTS, PROMINENCE AND FLARE HTTPS://WWW.NASA.GOV/MISSION_PAGES/SUNEARTH/SCIENCE/SUNLAYERS.HTML 1

FIGURE 1.2 A 1D MODEL OF THE SOLAR ATMOSPHERIC LAYERS SHOWING TEMPERATURE TE[K] AND ELECTRON DENSITY NE[CM^{-1}] (GABRIEL AND MASON, 1982) 2

FIGURE 1.3 WHITE LIGHT IMAGE OF THE CORONA DURING THE JULY 11, 2010 TOTAL SOLAR ECLIPSE. THE IMAGE HAS BEEN PROCESSED WITH ADAPTIVE CIRCULAR HIGH-PASS FILTER BY HABBAL ET AL. (2013) 3

FIGURE 1.4 THE UPPER PANELS DISPLAY A CORONAL RADIAL PLOT AND SOLAR WIND SPEED AS A FUNCTION OF LATITUDES OF 3 ULYSSES POLAR ORBITS OF THE SUN DURING SOLAR MINIMUM (A), MAXIMUM (B) AND (C) MORE THAN 3 QUARTERS OF THE THIRD ORBIT OCCURRING AROUND THE SOLAR CYCLE DECLINING PHASE. THE INTERPLANETARY MAGNETIC FIELD SHOWS RED FOR INWARD POLARITY AND BLUE FOR OUTWARD. THE LOWER PANEL (D) SHOWS THE SOLAR CYCLE SUNSPOTS NUMBER (MCCOMAS ET AL., 2008). 4

FIGURE 1.5 UPPER: THE BUTTERFLY DIAGRAM OF SUNSPOTS DISTRIBUTIONS WITH LATITUDES AT BOTH HEMISPHERES. SUNSPOT POSITIONS START WITH MID-LATITUDES AND MOVE TOWARD THE EQUATOR AS THE SOLAR CYCLE PROGRESSES. BOTTOM: THE AVERAGE DAILY SUNSPOTS AREA AS A FUNCTION OF TIME. HTTPS://SOLARSCIENCE.MSFC.NASA.GOV/SUNSPOTCYCLE.SHTML... 5

FIGURE 1.6 TWO SOLAR IMAGES TAKEN BY SDO/AIA IN EUV COMPOSED OF 171, 193 AND 211 A CHANNELS, DISPLAYING THE ACTIVE REGION CHANGES DURING THE SOLAR CYCLE. THE LEFT HALF WAS TAKEN IN MAY 2010 (END OF THE LATEST SOLAR MINIMUM ACTIVITY PERIOD). THE RIGHT HALF WAS TAKEN IN DECEMBER 2014 (CURRENT SOLAR MAXIMUM PERIOD) (MORGAN AND TAROYAN, 2017). 5

FIGURE 1.7 FILAMENTS AND PROMINENCES THAT HAVE FORMED ABOVE THE CHROMOSPHERE. THEY ARE TYPICALLY OBSERVED IN H-ALPHA (656.3 NM). HTTPS://DATA.NOAA.GOV/DATASET/SOLAR-FEATURES-PROMINENCES-AND-FILAMENTS. 6

FIGURE 1.8 THE STANDARD THREE PARTS OF THE CME (CORE, CAVITY AND BRIGHT FRONT) OBSERVED BY SOHO/LASCO ON THE 27TH OF FEBRUARY 2000. ADAPTED FROM RILEY ET AL. (2008) 7

FIGURE 1.9 A SKETCH OF A CME ERUPTION MODEL. THE MAGNETIC RECONNECTION OCCURS AT THE CURRENT SHEET REGION (DARK VERTICAL LINE). THE SMALL DARK OVAL REPRESENTS THE PROMINENCE COOL MATERIAL. ADAPTED FROM MARTENS AND KUIN (1989). 7

FIGURE 1.10 THE RELATIONSHIP BETWEEN THE FLARE H-ALPHA RIBBON, PROMINENCE AND THE CME'S THREE PARTS (FORBES, 2000). 8

FIGURE 1.11 SDO/AIA 193 A CORONAL HOLE'S IMAGE. FROM HTTP://WWW.THESUNTODAY.ORG/TAG/CORONAL-HOLE/ 9

FIGURE 1.12 EXAMPLES OF (LEFT) DISK, (MIDDLE) LIMB, AND (RIGHT) BACKSIDE HALO CMES FROM LASCO/C2 WITH GOES X-RAY AND DST INDEX PLOTS (GOPALSWAMY ET AL., 2007). 10

FIGURE 1.13 ORIGINAL SOLUTION FOR THE SOLAR WIND EXPANSION OUTWARD THE SUN. ADAPTED FROM PARKER (1958) 12

FIGURE 1.14 THE PARKER SPIRAL IN THE SOLAR ECLIPTIC PLANE. THE STRAIGHT LINES ARE THE RADIAL SOLAR WIND PROPAGATION WITH A SPEED OF 400 KMS^{-1} (CONSIDERED SLOW WIND TODAY). THE SPIRAL CURVES ARE THE IMF LINES WHICH ARE EMBEDDED IN THE ROTATING SUN AND CARRIED OUT RADIALLY BY THE SOLAR WIND. ARROWS ADDED TO THE FIELD DIRECTIONS INDICATES THEIR POLARITY AT THE SUN (PARKER DID NOT SPECIFICALLY PREDICT THE INTERPLANETARY MAGNETIC POLARITY AND AVOIDED ELECTRIC FIELDS(E) AND CURRENTS(J).ADAPTED FROM (PARKER, 1963) 13

FIGURE 1.15 SOLAR WIND PARCELS LEAVE THE SUN ANALOGOUS THE FLUID SPIRALS FORMED FROM THE ROTATING SPRINKLER. ADAPTED FROM HUNDHAUSEN (1995). (RUSSELL, 2001) 13

FIGURE 1.16 THREE DIFFERENT IMF MODELS. TOP: PARKER FIELD CONFIGURATION (WITHOUT FOOT POINT MOTION). THERE IS NO TRANSPORT IN LATITUDE. THE FIELD LINES ARE HELICES LYING ON CONES WITH HALF ANGLES EQUAL TO THE SOURCE LATTITUDES. AT A GIVEN RADIAL DISTANCE, THE FIELDS ARE TIGHTLY SPIRALED IN THE EQUATOR AND RADIAL OVER THE POLE. MIDDLE: FISK IMF. DIFFERENTIAL ROTATION INTO AN ASYMMETRIC CORONA ASSUMPTION(WITH FOOT POINT MOTION). ADAPTED FROM ZURBUCHEN ET AL. (1997). LOWER: RANDOM, WITH DIFFUSIVE MOTIONS. ADAPTED FROM JOKIPII AND KOTA (1989).(ZURBUCHEN, 2007). 14

FIGURE 1.17 A COMPUTER-GENERATED VISUALISATION OF THE HCS SHOWING TWO OPPOSITELY-DIRECTED RIDGES (SECTORS) OF THE SKIRT PER SOLAR ROTATION. BOTH OF THEM ADOPT THE PARKER SPIRAL FEATURE (JOKIPII AND THOMAS, 1981). IMAGE IS COURTESY OF J. JOKIPII, UNIVERSITY OF ARIZONA. 15

FIGURE 1.18 THREE-DIMENSIONAL SCHEME OF THE INTERPLANETARY PATTERN WITH THE STREAMER IN RELATION TO THE ECLIPTIC PLANE. BECAUSE OF THE STREAMER BELT'S 7.2 DEGREE TILT, IT WILL SWEEP ACROSS THE EARTH TWICE EVERY SOLAR ROTATION. ADAPTED FROM HUNDHAUSEN (1977) 16

FIGURE 1.19 LEFT: POSITIVE AND NEGATIVE CHARGES ACCELERATE TO OPPOSITE DIRECTIONS BY THE ELECTRIC FIELD OF THE LORENTZ FORCE. RIGHT: THE MAGNETIC PART OF THE LORENTZ FORCE CHANGE THE PATH OF THE PARTICLE(RIGHT-HAND RULE). 19
FIGURE 1.20 THE HELICAL TRAJECTORY OF AN CHARGED PARTICLE IN A HOMOGENEOUS MAGNETIC FIELD. 19
FIGURE 1.21 HELIOSPHERIC CURRENT SHEET DIVIDING THE TOWARDS (RED POINTS) AND AWAY (BLUE POINTS) MAGNETIC FIELD LINES FROM THE SUN. ADAPTED FROM SMITH ET AL. (1978). 20
FIGURE 1.22 A PLASMA SHEET SCHEME VIEW OF A HELIOSPHERIC EXTENSION OF THE CORONAL STREAMER BELT SURROUNDING THE HCS WITH A HIGH-DENSITY REGION (GOSLING ET AL., 1981). 21
FIGURE 1.23 AN ECLIPTIC CROSS SECTION ILLUSTRATING THE ELECTRONS HEAT FLUX- MAGNETIC FIELD RELATION WITH THE LOCAL AND GLOBAL CURRENT SHEET (HCS). IT SHOWS THE MAGNETIC FIELD B DIRECTION (SOLID-HEADED ARROWS) AND THE ELECTRON HEAT FLUX Q DIRECTION (OPEN- HANDED ARROWS) DURING A SPACECRAFT PASSAGE THROUGH A FOLDED HCS (FROM A TO B) WHICH SEPARATE AN INWARD SECTOR ON THE LEFT FROM OUTWARD SECTOR ON THE RIGHT, INDICATED BY SHADING. THE HCS IS FOLDED BACK ON ITSELF IN A LIMITED REGION (LOCAL). ACROSS THE HCS, THE SIGN OF Q.B CHANGES BUT REMAINS THE SAME ACROSS THE LOCAL REGION WHERE BOTH Q AND B CHANGE SIGN. ADAPTED FROM CROOKER ET AL. (1996) (CROOKER, 1999) 22
FIGURE 1.24 A SCHEMATIC DIAGRAM INTENDED TO INTERPRET THE DIRECTIONS OF THE MAGNETIC FIELD LINES AND THE HEAT FLUX ALONG THE PASSAGE OF THE SPACECRAFT THROUGH THE FOLDED HELIOSPHERIC CURRENT SHEET. A POCKET OF LOCALLY FLIPPED POLARITY IS PRODUCED AS A RESULT OF THE FLUX TUBE WRAPPING AROUND ANOTHER. ADAPTED FROM CROOKER ET AL. (1996) (CROOKER, 1999) 22
FIGURE 1.25 DIAGRAM SHOWING THE TIME VARIATIONS OF 92S VALUES OF SUPRATHERMAL ELECTRONS (3DP WIND) 320 EV PITCH ANGLE DISTRIBUTION (FIRST PANEL), SWE WIND AZIMUTHAL MAGNETIC FIELD ϕ_B IN GSE COORDINATE (SECOND PANEL), ION BETA (THIRD PANEL) AND PROTON DENSITY N AND MAGNETIC FIELD MAGNITUDE B IN THE LAST PANEL. THE SECTOR BOUNDARY CROSSING CS IS IDENTIFIED BY THE RED DASHED LINES DEPENDING ON THE ELECTRONS HEAT FLUX REVEALS IN CASE: (A) THERE WAS HPS, HCS AND SECTOR BOUNDARY CROSSING MATCHING. THE HPS DEFINED BY THE COINCIDENCE OF SECTOR BOUNDARY, HIGH PLASMA BETA AND ϕ_B REVERSAL (HCS). (B) A HPS-SECTOR BOUNDARY MATCHING WITH A COMPLICATED HCS. (C) A SECTOR BOUNDARY WITHOUT HCS AND A SECTOR BOUNDARY WITHOUT HCS AND HPS. (D) A SECTOR BOUNDARY WITH A HCS BUT NO HPS. (CROOKER ET AL., 2004A) 23
FIGURE 1.26 FIVE TYPES OF CONFIGURATIONS OF HCS AND SBC. (A) THE IDEAL CONFIGURATION WITH HCS-SBC MATCHING. (B) IDEAL HCS WITH A SBC AMONGST A DOUBLE STREAMING ELECTRONS PERIOD (HCS-SBC MISMATCHING). (C) A LOCAL MAGNETIC FIELD HAS TURNED BACK ON ITSELF (MISMATCHING AND MATCHING). (D) A HCS WITHOUT SBC AND A LOCAL MAGNETIC FIELD FLIPPED BACK ON ITSELF. (E) HCS-SBC MISMATCHING BECAUSE OF THE INTERCHANGE RECONNECTION NEAR THE SUN. (OWENS ET AL., 2013) 24
FIGURE 1.27 SCHEMATIC OF AN ICME, TURBULENT SHEATH REGION AND AN ICME- DRIVEN SHOCK (AFTER LIU ET AL. (2006) 25
FIGURE 1.28 THE IDEALIZED VIEW OF THE PROPOSED MC MAGNETIC FIELD LINE GEOMETRY ON A GLOBAL SCALE BASED ON THE LUNDQUIST (1950) SOLUTION AND THE GLOBAL CONFIGURATION SKETCH OF A MC AND FOUR SPACECRAFT (HELIOS A AND B, IMP8 AND VOYAGER 2) WHERE THE IN SITU MEASUREMENTS HAVE BEEN TAKEN FROM THEM (BURLAGA ET AL., 1990). MODIFIED WITH PERMISSION FROM L. BURLAGA, GLOBAL CONFIGURATION OF A MAGNETIC CLOUD, PP. 373-377 IN PHYSICS OF MAGNETIC FLUX ROPES, GEOPHYSICAL MONOGRAPH 58, C.T. RUSSELL, E.R. PRIEST, AND L.C. LEE, EDS., AMERICAN GEOPHYSICAL UNION, WASHINGTON, D.C., 1990 BY"3 FORMATION OF STRUCTURES AND TRANSIENTS" NATIONAL RESEARCH COUNCIL. 26
FIGURE 1.29 A PLASMA BETA MODEL OF THE SOLAR ATMOSPHERE FOR THE ASSUMED FIELD MAGNITUDES OF BETWEEN 100 G AND 2500 G (GREY AREA). ADAPTED FROM (GARY, 2001), TAKEN FROM (LANG, 2013). 27
FIGURE 1.30 A STANDARD ICME-DRIVEN SHOCK RECORDED BY STEREO B. THE PANELS DISPLAY: THE MAGNETIC FIELD STRENGTH WITH RTN COMPONENTS, PROTON SPEED, PROTON DENSITY, PROTON TEMPERATURE, PLASMA BETA AND TOTAL PERPENDICULAR PRESSURE. THE ICME CONSISTS OF THE FORWARD SHOCK, SHEATH, MC FLUX ROPE AND REVERSE SHOCK (MÖSTL ET AL., 2009) 30
FIGURE 1.31 ILLUSTRATES THE SIX GENERAL TRACKS OF A SPACECRAFT THROUGH AN ICME. THE SIX TRACKS ARE DIVIDED INTO TWO POSSIBILITIES: ICME WITH A SHOCK, SHEATH, AND MC (LEFT), AND ICME WITH ONLY A MC (RIGHT).(GOPALSWAMY, 2006) 31
FIGURE 1.32 SCHEMATIC ILLUSTRATION OF A SPACECRAFT TRAVELLING THROUGH AN ICME (RILEY AND RICHARDSON, 2013). 31
FIGURE 1.33 THE FORCE-FREE STRUCTURE OF THE MC AS PROPOSED BY GOLDSTEIN (1983), DEVELOPED BY MARUBASHI (1986) AND ADAPTED BY BOTHMER AND SCHWENN (1997). THE MC SITS WITH ITS AXIS IN THE EQUATORIAL PLANE AND NORMAL TO THE RADIAL DIRECTION. 33

FIGURE 1.34 ILLUSTRATES MC GLOBAL STRUCTURE MODELS AND SKETCHES: (A) CME NEAR-SUN STRUCTURE FROM SUBRAMANIAN ET AL. (2014) (B) PARTIAL OPEN MC FLUX ROPE WITH CONSTANT A INFERRED FROM HEAT FLUX AND ENERGETIC ELECTRONS FROM LARSON ET AL. (1997) (C) IN SITU MC FITTING MODEL FROM DÉMOULIN AND DASSO (2009) (D) INTERPLANETARY FLUX ROPE NUMERICAL SIMULATION FROM VANDAS ET AL. (2002) (E) MCS GLOBAL STRUCTURE SKETCH FROM MARUBASHI AND LEPPING (2007) (F) MCS GLOBAL STRUCTURE CARTOON FROM ZURBUCHEN AND RICHARDSON (2006). (OWENS, 2016) ... 34
FIGURE 1.35 ILLUSTRATES THE OWENS (2016) VISION OF THE MAGNETIC CLOUD FLUX ROPE. IT IS NOTICEABLE THAT THE TWISTED FLUX ROPE IS CONFINED TO THE LEADING FRONT (THE GREY CLOUD) AND THE UNTWISTED MC LEGS CONNECT THE FLUX ROPE WITH THE SUN. THE BLACK ARROWS REFER TO THE HEATING FLUX ELECTRONS DIRECTIONS. THE SKETCH IS MODIFIED FROM ZURBUCHEN AND RICHARDSON (2006). 35
FIGURE 1.36 TWO TABLES SHOWING SCHEMATICS AND LABELS OF THE EIGHT MC CATEGORIES (MULLIGAN ET AL., 1998) . THE MC CONFIGURATIONS AND THEIR HELICITY LAYING IN THE ECLIPTIC PLANE ARE SHOWN IN THE UPPER PANEL AFTER BOTHMER AND RUST (1997). MC PERPENDICULAR TO THE ECLIPTIC PLANE ARE SHOWN IN THE LOWER PANEL AFTER ZHAO AND HOEKSEMA (1996). 36
FIGURE 1.37 MAGNETIC FIELD CONFIGURATION SKETCHES OF PROMINENCES AND THE EXPECTED MC FLUX ROPE TYPES (BOTHMER AND SCHWENN, 1994) 37
FIGURE 1.38 THE SOLAR CYCLE DEPENDENCE OF THE FILAMENTS AND THE MAGNETIC FIELD STRUCTURES OF MCS. FOR SIMPLICITY, MCS FLUX ROPES ORIENTATIONS ARE DRAWN WITH RESPECT TO THE ECLIPTIC PLANE. ADAPTED FROM BOTHMER AND SCHWENN (1998) BY WIMMER-SCHWEINGRUBER ET AL. (2006). 37
FIGURE 1.39 TRAJECTORIES OF FIVE SPACECRAFT FOR THE PERIOD OF NOV. 1977 TO MAR. 1978. BLACK SQUARES REPRESENT THE ICME EVENTS IN EACH SPACECRAFT (ROMERO-HERNANDEZ AND GONZALEZ-ESPARZA, 2013). 39
FIGURE 1.40 AN ILLUSTRATION OF THE THREE GROUPS OF PT PROFILES IN TERMS OF THE TRAJECTORY OF THE SPACE CRAFT ENCOUNTER THE MAGNETIC FLUX-ROPE DEPENDING ON SPREITER ET AL. (1966) GAS DYNAMIC SIMULATION RESULTS (JIAN ET AL., 2006A). 40
FIGURE 1.41 AN EXAMPLE OF GROUP 1 ICMES TOTAL PRESSURE PROFILE (LOWER PANEL) FOR THE PERIOD OF NOVEMBER 6-8, 2000, SHOWING A CENTRAL RISE IN TOTAL PRESSURE.(RUSSELL ET AL., 2005) 41
FIGURE 1.42 TOTAL PRESSURE PROFILES FOR FIVE GROUP 2 EVENTS, SHOWING A CENTRAL FLAT PLATEAU OF TOTAL PRESSURE AND AN ELEVATION TOWARD THE END OF EVENTS. (RUSSELL ET AL., 2005) 42
FIGURE 1.43 TOTAL PRESSURE MORPHOLOGY FOR FIVE GROUP 3 EVENTS. A MONOTONIC DECREASE OF PRESSURE AFTER THE INITIAL JUMP.(RUSSELL ET AL., 2005) 42
FIGURE 1.44 AN ILLUSTRATION OF THE INTERPLANETARY MAGNETIC CONFIGURATION AS INFERRED FROM HEAT FLUX ELECTRONS OBSERVATIONS. LEFT SIDE: THE BLACK ARROWS ARE THE MAGNETIC FIELD LINES AS SEEN FROM AN ECLIPTIC PLANE AND THE RED ARROWS ARE SUN OUTWARD HEAT FLUX ELECTRONS. RIGHT SIDE: THE SUPRATHERMAL ELECTRONS PITCH ANGLE DISTRIBUTIONS SEEN BY A SPACECRAFT AT L1 POSITION. AT (A), THE SUPRATHERMAL ELECTRONS STRAHL IS ANTI-PARALLEL TO THE INTERPLANETARY MAGNETIC FIELD BECAUSE THE INTERPLANETARY FIELD HAS A SUNWARD DIRECTION (PART OF AN INWARD POLARITY SECTOR). AT (C), THE STRAHL ARE PARALLEL TO THE FIELD DIRECTION BECAUSE THE FIELD IS PART OF AN OUTWARD SECTOR. AT (B), THE SUPRATHERMAL ELECTRONS ARE PARALLEL AND ANTI-PARALLEL TO THE FIELD BECAUSE THE INTERPLANETARY FIELD FORMS A CLOSED LOOP AND IS CONNECTED TO THE SUN AT BOTH ENDS. AT (D), NO STRAHL IS SEEN BECAUSE THERE IS NO CONNECTION WITH THE SUN AT ALL. (OWENS AND FORSYTH, 2013) 43
FIGURE 1.45 AN EXAMPLE OF THE DISTRIBUTION OF SUPRATHERMAL ELECTRONS WITHIN A MC. DASHED VERTICAL LINES REFER TO THE MC BOUNDARIES. IT STARTS WITH UNIDIRECTIONAL HEAT FLUX (UPPER PANEL) PARALLEL (0˚) TO THE LOCAL FIELD DIRECTION (LOWER PANEL). BIDIRECTIONAL STREAM DOMINATES IN THE MIDDLE, WITH AN ANTIPARALLEL (180˚) UNIDIRECTIONAL STREAM AT THE REAR. (CROOKER ET AL., 2008) 44
FIGURE 1.46 AN INTERPLANETARY MC FLUX ROPE IS CONNECTED THE SUN BY ITS BOTH LEGS. HEAT FLUX ELECTRONS (STRAHL) STREAMING AWAY FROM THE SUN (FOUR GREY WIDE ARROWS EMERGING FROM THE SUN) ALONG THE MAGNETIC FIELD LINES CREATES A BIDIRECTIONAL STREAMING (COUNTER STREAMING) ON THE FLUX ROPE CLOSED FIELD LINES (OPPOSITELY DIRECTED GREY ARROW WITHIN THE MC) (CROOKER AND HORBURY, 2006) 44
FIGURE 1.47 THE PITCH ANGLE DISTRIBUTIONS OBSERVED BY ACE IN JANUARY 10, 1999. THE UPPER PANEL DISPLAYS THE COLOUR-CODED 272 EV PAD FOR 12 HOURS. THE COLOUR SCALE IS FROM $1.6x10^{-31}$ TO $2x10^{-29}$ S^3 CM^{-6}. THE LOWER PANEL IS THE PAD AT 19:16:38UT AND 22:54:14UT WHICH IS INDICATED BY THE TWO BLACK AND RED ARROWS (GOSLING ET AL., 2001B). 45
FIGURE 1.48 A SKETCH OF THE TWO-POSSIBLE INTERPLANETARY FIELD LINE CONFIGURATIONS DURING HFDS. UPPER PANELS: DISCONNECTION FIELD LINE PROCESS. LOWER PANELS: INTERPLANETARY SCATTERING (CHOLLET ET AL., 2010) 46

FIGURE 1.49 THREE TYPICAL HFDS. PANEL (A): THE COLOUR-CODED SUPRATHERMAL ELECTRONS PAD WITH A LOG SCALE ELECTRON NUMBER FLUX FROM $3.2x10^3$-10^5 $cm^{-2}s^{-1}$. PANEL (B): HEAT FLUX ELECTRONS. PANEL (C): ELECTRONS TOTAL NUMBER FLUX AT E=275 EV. PANEL(D): PITCH ANGLE ANISOTROPY A. THE RED AND BLUE VERTICAL LINES MARK THE START AND END OF THE HDFS (PAGEL ET AL., 2005). 46
FIGURE 1.50 RECONNECTION BETWEEN TWO IDEAL MHD PLASMA REGIONS WITH OPPOSITELY ORIENTED MAGNETIC FIELD FLOWING TOWARDS EACH OTHERS. OPEN ARROWS INDICATES THE PLASMA FLOW DIRECTION. 48
FIGURE 1.51 UPPER SKETCH: THE DISCONNECTION IS EITHER A MERGING OF TWO OPEN MAGNETIC FIELD LINES (SOLID CURVES) AT THE FRONT EDGE OF THE HELMET STREAMER OR A MERGING OF A CLOSED MAGNETIC FIELD LINE (DASHED CURVES) IN THE CME, WHICH RELEASES A PLASMOID. LOWER SKETCH: INTERCHANGE RECONNECTION, A MERGING OF AN OPEN MAGNETIC FIELD LINE WITH ONE LEG OF THE CLOSED CME LOOP WHICH LEAVES THE SUN TOWARDS THE INTERPLANETARY MEDIUM. THE CME LOOP BECOMES OPENED AND THERE ARE NO FIELD LINES DISCONNECTED FROM THE SUN. THIS PROCESS REDUCES THE EXTENDING FIELD LINES INTO THE HELIOSPHERE FROM THREE TO ONE.(CROOKER ET AL., 2002) 49
FIGURE 1.52 LEFT PANEL: AN OPEN FLUX ROPE NESTED IN A CLOSED COIL. RIGHT PANEL: SKETCHES (A-D) ILLUSTRATE MANY EXAMPLES OF THE POSSIBILITY OF THE 3- DIMENSIONAL CME RECONNECTION (RECONNECTIONS WITH THE MAGNETIC LEGS OF A CME) (GOSLING ET AL., 1995). 49
FIGURE 1.53 ILLUSTRATES INTERCHANGE RECONNECTION BETWEEN A COILED FIELD LOOP AND AN OPEN FIELD LINE EMERGING FROM A CORONAL HOLE. THE PROCESS CREATES AN OPEN HELICAL LOOP AND A SMALL CLOSED LOOP (DOTTED LINES). MODIFIED FROM HARRA ET AL. (2007). 50
FIGURE 1.54 TWO SUCCESSIVE MAGNETIC CLOUDS WITH DIFFERENT SUPRATHERMAL ELECTRONS DISTRIBUTION PROFILES. DASHED VERTICAL LINES REPRESENT THEIR BOUNDARIES. THE FIRST ONE (CLOUD 59) IS UNIDIRECTIONAL (UPPER PANEL) AND ANTIPARALLEL (180˚) TO THE LOCAL FIELD DIRECTION (LOWER PANEL). THE SECOND CLOUD (CLOUD 60) STARTS AS UNIDIRECTIONAL, AND IS THEN BIDIRECTIONAL ALONG THE MIDDLE , THEN ENDS WITH AN OPEN UNIDIRECTIONAL HEAT FLUX (CROOKER ET AL., 2008) 51
FIGURE 1.55 THE DASHED LINE IS THE OPEN MAGNETIC FIELD LINE WHICH APPROACHES THE HELMET STREAMER (CLOSED SOLID LINE). X IS THE RECONNECTION POINT OF THE TWO MAGNETIC FIELD LINES. THE LOWER PANEL SHOWS THE NEW CONFIGURATION WHERE THE PLASMA PARCEL (BLOB) IS RELEASED AND RESIDES ON THE OPEN MAGNETIC FIELD LINE WHERE PREVIOUSLY IT WAS AT THE LOOP'S CUSP. THE MAGNETIC FIELD LINE TURNS BACK ON ITSELF BETWEEN LOCALIZED CURRENT SHEETS MARKED BY THE TWO TINY DOTTED LINES. THE WHOLE FRAME MOVES AWAY ''AS A TRANSIENT PLASMA SHEET'' (CROOKER ET AL., 2004A). .. 51
FIGURE 1.56 MISMATCHING BETWEEN TRUE SECTOR BOUNDARIES AND LOCAL POLARITY REVERSALS IN Bϕ DURING DECEMBER 1994 TO AUGUST 1995. THE RED LINES REFER TO TRUE SECTOR BOUNDARIES IDENTIFIED BY THE WIND SUPRATHERMAL ELECTRONS 3DP SPECTROGRAMS. THE YELLOW SHADE HIGHLIGHTS MISMATCHES BETWEEN TRUE SECTOR BOUNDARIES AND LOCAL Bϕ REVERSALS. ADAPTED FROM (CROOKER ET AL., 2004B). 52
FIGURE 1.57 A TOWARD SECTOR FOLLOWS AN AWAY SECTOR, AND A LOOP INTERVENES. AT THE LEADING LEG OF THE LOOP, THE FIELD POINTS OUTWARD THE SUN, WHEREAS POINT INWARDS IN THE TRAILING LEG, THUS MATCHING THE FIELDS IN THE ADJACENT SECTORS. THE LEADING LEG OF THE LOOP HAS CONNECTED WITH AN OPEN FIELD LINE THERE. THE DOTTED FIELD LINE EXTENDS FROM THE LOOP REPRESENT THE OUTER PART OF THE NEW OPEN FIELD LINE AND IS SUPPOSED TO LIE UP OR BELOW THE PLANE OF THE FIGURE. THIS PROCESS OPENED THE CLOSED LOOP AND PRODUCED AN INVERTED FIELD LINE IN THE LOOPS' LEADING LEG. FINALLY, THE TRUE SECTOR BOUNDARY IS LOCATED BETWEEN THE LEADING LEG AND THE AHEAD AWAY FIELD LINE WHEREAS THE FIELD REVERSAL MARKING THE HCS LIES BETWEEN THE TWO LEGS. (CROOKER ET AL., 2004B) 52
FIGURE 1.58 A SET OF RISING CORONAL LOOPS DRAWN ROUGHLY PERPENDICULAR TO THE ECLIPTIC, WHICH HAVING RECONNECTION ASSUMPTION (LOWER PANEL) AND HAVE NOT UNDERGONE RECONNECTION (UPPER PANEL).(GOSLING, 1990) 53
FIGURE 1.59 MULTIPLE CURRENT SHEETS (HEAVY LINES) AND SMALL HELMETS BORDERED BY LARGE HELMETS OVER HIGH LATITUDE FILAMENTS.(CROOKER ET AL., 1993) 54
FIGURE 1.60 ILLUSTRATES THE THREE FEATURES OF CORONAL STREAMER BELT AS AN OUTFLOW CHANNEL. ADAPTED FROM CROOKER ET AL. (1993) 54
FIGURE 1.61 THE RELATIONSHIP BETWEEN SECTOR BOUNDARY CROSSINGS, STREAMER BELTS, AND CME FLUX ROPES. A) THE CME FLUX ROPE FORMATION FROM THE HELMET ARCADE AT THE BASE OF THE HCS. AA' SHOWS HOW THE RECONNECTING FIELDS RE-ESTABLISH THE HELMET ARCADE BELOW THE COIL (CROOKER ET AL., 1998). B) THE FIELDLINES OF THE FLUX ROPE'S LEGS MATCH THE TOWARD AND AWAY DIRECTION OF ADJACENT SECTORS. C) MAGNETIC LONGITUDAL Bϕ PROFILE MEASURED BY ULYSSES SPACECRAFT. IT ROTATES FROM OUTWARD TO INWARD POLARITY ACROSS THE MAGNETIC CLOUD FLUX ROPE AT THE SECTOR BOUNDARY (FORSYTH ET AL., 1997). (CROOKER AND HORBURY, 2006) 55
FIGURE 1.62 SCHEMATIC ILLUSTRATION OF A SLOW(LEFT) AND FAST(RIGHT) CME PROPAGATION THROUGH INTERPLANETARY SPACE. ADAPTED FROM WANG ET AL. (2004). 56

FIGURE 1.63 A CO-ROTATING STREAM STRUCTURE SKETCH OF THE INNER HELIOSPHERE. LEFT PANEL: MAGNETIC FIELD LINES WITHIN FAST (RED) AND SLOW (BLUE) SOLAR WINDS. A STREAM INTERFACE (BLACK LINE) LIES WITHIN THE COMPRESSION REGION BETWEEN FORWARD AND REVERSE WAVES. RIGHT PANEL: M IS THE SOLAR MAGNETIC AXIS. THE SOLAR WIND BELT IS INCLINED TO THE SOLAR ROTATION AXIS(R). THE SI IS THE RIDGE IN INTERPLANETARY SPACE WHERE THE FAST STREAM CATCHES UP TO THE SLOW STREAM AHEAD OF IT (BLACK). THE FAST STREAM IS SLOWED WHERE THE SLOW IS ACCELERATED. ALSO, BOTH ARE DEFLECTED ALONG THE SI. RIGHT PANEL ADAPTED FROM PIZZO (1991). (OWENS AND FORSYTH, 2013) 60
FIGURE 1.64 A SCHEME ILLUSTRATING THE GEOMETRY (UPPER PANEL) AND PROFILES OF SIR WITH FORWARD SHOCKS (S) , REVERSE SHOCKS (F), COMPRESSION REGIONS (S',F') , STREAM INTERFACE SI (CURVED LINE BETWEEN S' AND F') AND RAREFACTION REGION R (RICHARDSON ET AL., 1996), AFTER BELCHER AND DAVIS (1971)..... 62
FIGURE 1.65 A SCHEMATIC ILLUSTRATION OF THE SIR FIELD LINE GEOMETRY. THE COMPRESSION AREA IS SHADED IN GREY. THE SOLID LINE REFERS TO THE SIR AREA WHICH IS BOUNDED BY THE SHOCK, WHEREAS THE DOTTED LINE REFERS TO THE SIR AREA (NEAR IN SITU) BOUNDED BY A PRESSURE WAVE. (STEINBERG ET AL., 2005) 63
FIGURE 1.66 THE TYPICAL DST RESPONSE DURING MAGNETIC STORMS DUE TO AN ICME (TOP), AN A CIR (BOTTOM) (TSURUTANI ET AL., 2006) . THE DST DERIVED FROM A NETWORK OF NEAR-EQUATORIAL GEOMAGNETIC OBSERVATORIES THAT MEASURES THE INTENSITY OF THE EQUATORIAL ELECTROJET (THE RING CURRENT) 64
FIGURE 1.67 A SCHEMATIC ILLUSTRATION OF TWO TYPICAL CME AND CIR PARAMETERS ACCOMPANIED MAGNETIC STORMS. B: THE MAGNETIC FIELD STRENGTH, BI: ONE OF THE CARTESIAN COMPONENT, V: SOLAR WIND SPEED, N: DENSITY, T: TEMPERATURE, DST: EXPECTED RESPONSE OF THE GEOMAGNETIC INDEX AND e^-: > 2.0 MEV ELECTRON FLUX AT GEOSYNCHRONOUS ORBIT. (KATAOKA AND MIYOSHI, 2006)..... 65
FIGURE 1.68 A DISPLAY OF THE CORRELATION BETWEEN THE ANNUAL SUNSPOTS NUMBERS (YELLOW AREA) AND THE GEOMAGNETIC DISTURBED DAYS WITH THE GEOMAGNETIC AP INDEX $\geq$ 40 (RED AREA). COURTESY NOAA GEOPHYSICAL DATA CENTRE BOULDER, CO, USA..... 66
FIGURE 1.69 SEPS AND GEOMAGNETIC STORMS, THE TWO INTERPLANETARY CONSEQUENCES OF CMES. CMES SPEED V_{CME} MORE THAN THE SOLAR WIND SPEED V_{SW} SHOULD EXCEED THE MAGNETO SONIC SPEED V_{MS} TO DRIVE A SHOCK. CMES CAUSE GEOMAGNETIC STORMS WHEN THEY HAVE SOUTHWARD MAGNETIC FIELD DIRECTION (BZ<0) (GOPALSWAMY, 2009B). 67
FIGURE 2.1 ILLUSTRATES A SIMPLE SCHEME OF A FARADAY CUP MEASUREMENT OF CHARGED PARTICLE FLUX. (KASPER, 2002)..... 70
FIGURE 2.2 ACE TRAJECTORY AND MISSION ORBIT FROM THE EARTH TO L1 POSITION (AUGUST 25, 1997 TO DECEMBER 17, 1997) HTTP://WWW.SSG.SR.UNH.EDU/MAG/ACE.HTML..... 71
FIGURE 2.3 LEFT PANEL: THE LEADING (RED) AND TRAILING (BLUE) TRAJECTORY OF STA & STB TO THE EARTH. RIGHT PANEL: STA & STB OPPOSITE ORBITAL PATHS AROUND THE SUN.(KAISER AND ADAMS, 2007) 72
FIGURE 2.4 AN ARTIST'S SCHEME OF STB AND ITS INSTRUMENTS. SECCHI AND PLASTIC INSTRUMENTS ARE POINTED SUNWARD, WHEREAS SWAVES ANTENNAS AND IMPACT BOOM ARE PLACED ON THE OPPOSITE END (KAISER AND ADAMS, 2007). 74
FIGURE 3.1 THE L1 SPACECRAFT POSITIONS ACE, WIND AND SOHO ON SEPTEMBER 09, 2011 (1RE= 6371.2 KM) 80
FIGURE 3.2 COMPOSITE EUV IMAGE OF THE SOLAR DISK AND LOW CORONA MADE USING AIA/SDO OBSERVATIONS DURING 2011/09/06 12:00. THE THREE-COLOR RED-GREEN-BLUE IMAGE CHANNELS ARE COMPOSED OF OBSERVATIONS MADE IN THREE AIA CHANNELS: 171Å, 193Å AND 211Å RESPECTIVELY, CORRESPONDING TO THEIR MOST DOMINANT EMISSION LINES OF FE IX, FE XII AND FE XIV WITH FORMATION TEMPERATURES~ 0.7, 1.2 AND 2.0 MK. THE IMAGES HAVE BEEN PROCESSED USING MULTISCALE GAUSSIAN NORMALIZATION (MGN, (MORGAN AND DRUCKMÜLLER, 2014))..... 81
FIGURE 3.3 THE SEPTEMBER 6,2011 AR11283 FLUX ROPE. THE UPPER LEFT PANEL DISPLAYS THE S SIGMOID AT 22:03 UT WHEREAS THE OTHER PANELS SHOW THE MAGNETIC FLUX ROPE SEQUENCE FOR A FEW MINUITES. THESE IMAGES HAVE BEEN PROCESSED USING MGN. THE TWO ARROWS ON THE UPPER LEFT PANEL DETERMINE THE TWO ENDS OF THE S SIGMOID AND THE THE BLACK CIRCULES ON ALL PANELS DISPLAY THE FLUX ROPE PROGRESS POSITION DURING THE PANELS TIMES. 82
FIGURE 3.4 TOP ROW SHOWS A LASCO C2 IMAGE OF 2011/09/06, 23:36 UT, SHOWING A HALO CME SKEWED TOWARDS THE NORTH-WEST AND A PREVIOUS 3-PART CME IN THE NORTH-WEST. BOTTOM ROW SHOWS A STEREO COR2 A IMAGE OF 2011/09/06, 23:39 UT. THE CME OF INTEREST IS DISTRIBUTED FROM AROUND -30 TO +60 FROM THE EQUATOR. THE PREVIOUS 3-PART CME IS AT HIGH LATITUDE, ALTHOUGH THERE IS SOME OVERLAP BETWEEN THE TWO CMES. THE LEFT IMAGES HAVE BEEN PROCESSED USING A DYNAMIC SEPARATION TECHNIQUE TO REMOVE QUIESCENT RADIAL STRUCTURE (MORGAN AND HABBAL, 2010), AND THE RIGHT IMAGES HAVE BEEN PROCESSED USING THE NORMALIZING RADIAL GRADED FILTER OF MORGAN ET AL. (2006)..... 83
FIGURE 3.5 DISPLAYS THE EVENT MAGNETIC FIELD AND PLASMA PARAMETERS. FROM THE UPPER PANEL: THE ACE COLOR-CODED ELECTRONS PITCH ANGLE DISTRIBUTIONS F(V) ($CM^{-6}\ S^3$) AT 272 EV ENERGY (COLOR-CODING FOR F(V) IS LOGARITHMIC AND RANGES FROM $5\times10^{-31}S^3CM^{-6}$(DARK BLUE) TO $2\times10^{-29}S^3CM^{-6}$(DARK RED)), MAGNETIC FIELD STRENGTH B(NT), BΦ(DEG), BΘ(DEG), PROTON TEMPERATURE TP(K), SOHO PROTON TEMPERATURE TP(K), ACE(BLACK) AND SOHO(RED) PROTON SPEED

VP(KM S^{-1}), DST INDEX(NT), ACE/SOHO COMBINE TOTAL PRESSURE PT(PPA) AND PROTON DENSITY NP(CM^{-3}) FROM SOHO. 84
FIGURE 3.6 THE INTERPLANETARY MAGNETIC FIELD VECTORS (BX,BY AND BZ) AND THEIR DIRECTIONS THROUGH THE MC. BLUE VERTICAL LINES ARE THE MC BOUNDARIES. THE SYMBOLS W, S AND N REFER TO THE FLUX ROPE DIRECTIONS: WEST, SOUTH AND NORTH RESPECTIVELY. 85
FIGURE 3.7 DISPLAYS THE PHOTOSPHERIC MAGNETIC FIELD MAP OF SEPTEMBER 6, 2011 AND A SCHEMATIC OF THE MAGNETIC FLUX ROPE STRUCTURE. THE EUV IMAGE IS BY AIA/SDO, AND THE PHOTOSPHERIC FIELD MEASUREMENT IS GAINED THROUGH GAUSSIAN SMOOTHING OF HMI/SDO. IT ALSO ILLUSTRATES INTERCHANGE RECONNECTION (IR) BETWEEN THE SEPTEMBER 6 CME FROM AR11283 AND CORONAL HOLE CH475. CORONAL HOLE INWARD FIELD LINES DIVERGE TOWARDS THE FLUX ROPE LEG OUTWARD FIELD LINE AND AN IR HAS OCCURRED. RED ARROWS REFER TO THE INWARD FIELD LINE, BLUE ARROWS REFER TO THE OUTWARD FIELD LINES AND GREY ARROW REFER TO THE SITE OF IR (MODIFIED FROM HARRA ET AL. (2007)). 88
FIGURE 3.8 DISPLAYS THE PITCH ANGLE DISTRIBUTIONS OF THE SUPRATHERMAL ELECTRONS BEFORE/DURING (SOLID LINE) AND AFTER (DASHED LINE) THE CIR REVERSE SHOCK. THE DEPLETION AROUND 90˚ IS CLEAR AFTER THE SHOCK ARRIVAL. EACH PROFILE IS THE MEDIAN OF DISTRIBUTIONS MEASURED OVER A PERIOD OF AROUND 9 HOURS BEFORE AND AFTER THE SHOCK. THE ERROR BARS SHOW THE STANDARD DEVIATION OF VALUES DURING THIS 9-HOUR PERIOD. 89
FIGURE 3.9 THIS FIGURE HIGHLIGHTS THE ACE AND SOHO REGION A WHERE THE HPS, HCS, SBC AND THE ICME FORWARD SHOCK OCCURS (THE SOHO PROTON DENSITY PROFILE IS TO COVER THE ACE MISSING DATA). FROM TOP TO BOTTOM, THE PANELS SHOW HEAT FLUX DISTRIBUTION, BΦ, NP, B, ACE(BLACK) AND SOHO(RED) PROTON SPEED VP(KM S^{-1}), AND ACE(BLACK) AND SOHO(RED) PROTON TEMPERATURE TP(K). THE TWO BLUE VERTICAL LINES REFER TO THE HPS BOUNDARIES, THE DOTTED RED VERTICAL LINE REFERS TO THE SBC-HCS REGION AND THE BROWN DASHED VERTICAL LINE REFERS TO THE ICME FORWARD SHOCK. NOTE THAT THE HEAT FLUX DISTRIBUTION (TOP PANEL) SHOWS THE ELECTRON FLUX ON A LOG SCALE TO VISUALISE VARIATIONS OF LOW SIGNALS. 90
FIGURE 3.10 PROPERTIES OF REGION A AS MEASURED BY WIND. FROM TOP TO BOTTOM: HEAT FLUX DISTRIBUTION (MEASURED BY ACE), BΦ, NP, B, VP, PLASMA BETA, VTH, TP(K), ENTROPY, DYNAMC PRESSURE (NPA) AND PT (NPA). THE ACE SUPRATHERMAL ELECTRON DISTRIBUTION IS INCLUDED (1ST PANEL) FOR COMPARISON. THE GREEN SHADED REGION(REGION A) IS THE HPS.THE DOTTED RED LINE REFERS TO THE SBC-HCS REGION AND THEDOTTED BROWN VERTICAL LINE REFERS TO THE ICME FORWARD SHOCK. 91
FIGURE 3.11 HIGHLIGHTS THE ICME-CIR INTERACTION REGION (YELLOW AREA). FROM THE UPPER PANEL: ACE SUPRATHERMAL ELECTRONS PITCH ANGLE DISTRIBUTIONS(DEG), MAGNETIC FIELD MAGNITUE B(NT), PROTON DENSITY NP(CM^{-3}) FROM SOHO, PRORON TEMPERATURE TP(K), TOTAL PRESSURE PT(PPA) FROM WIND, MAGNETIC PRESSURE PG(PPA), ACE/SOHO COMBINE DATA OF TOTAL PRESSURE PT(PPA) , SOLAR WIND VELOCITY THREE COMPONENTS IN GSE COORDINATION (KM/S): VX, VY, VZ, AND PROTON SPEED VP(KM/S). PURPLE VERTICAL LINE REFER TO THE MC ONSET, THE GREEN VERTICAL LINE IS THE CIR REVERSE SHOCK AND THE THREE DOTTED RED VERTICAL LINE ARE THE NOMINATED SIS. P1 & P2 IN PANEL SIX ARE THE TWO MAGNETIC PRESSURE PEAKS AT THE FRONT AND REAR BOUNDARY OF THE ICME. 94
FIGURE 3.12 LEFT PANELS: CIR L1 SPACECRAFT DATA OF NP(CM^{-3}) FROM SOHO, PLASMA BETA FROM WIND, PLASMA BETA FROM ACE/SOHO COMBINE,TP(K) FROM ACE, B(NT) FROM ACE, TOTAL PRESSURE PT(NPA) FROM WIND, TOTAL PRESSURE PT(PPA) FROM ACE/SOHO COMBINE, MAGNETIC PRESSURE P_G (PPA), ANE PROTON SPEED(KMS^{-1}) FROM ACE FOR THE PERIOD (10/09 09:00 UT- 11/09 06:00 UT). RIGHT PANELS: CIR STB DATA WITH THE SAME MAGNETIC FIELD AND SOLAR WIND PARAMETERS FOR THE PERIOD (04/09 06:00 UT- 07/09 00:00 UT). 95
FIGURE 4.1 STEREO B EUVI 195 A IMAGES, WITH AN ACTIVE REGION CIRCLED IN RED. THE TIME OF THE IMAGES IS 12:15 UT (LEFT) AND 14:15 UT (RIGHT), COINCIDING WITH THE OCCURRENCE OF TWO FLARES IN THE ACTIVE REGION. THESE IMAGES HAVE BEEN PROCESSED USING MULTISCALE GAUSSIAN NORMALIZATION MORGAN AND DRUCKMÜLLER (2014). 104
FIGURE 4.2 SOHO/LASCO C2 IMAGES FOR 17-03-2011 (11:48 UT- 21:36 UT) DISPLAY MULTIPLE DYNAMIC FEATURES. DIFFERENT COLOURED ELLIPTIC OUTLINES INDICATE DIFFERENT EVENTS AS DESCRIBED IN THE MAIN TEXT. THESE IMAGES HAVE BEEN PROCESSED TO REMOVE LARGE-SCALE QUIESCENT STRUCTURES (I.E. STREAMERS) USING THE DYNAMIC SEPARATION TECHNIQUE (MORGAN ET AL. (2012);MORGAN, 2015). 105
FIGURE 4.3 FURTHER DETAIL OF THE ACTIVE REGION CIRCLED IN RED IN FIGURE 4.1 AS OBSERVED BY EUVI/STB IN THE 195 A CHANNEL. TWO SEPARATED SYSTEMS OF CORONAL LOOPS ARE LABELLED 1 AND 2 AND DETAILED IN THE MAIN TEXT. 106
FIGURE 4.4 SOHO/LASCO C2 IMAGE OF THE MARCH 21, 2011, 15:36 UT LARGE CME.THE LEFT IMAGE HAS BEEN PROCESSED USING A DYNAMIC SEPARATION TECHNIQUE(MORGAN AND HABBAL, 2010) , AND THE RIGHT IMAGE HAS BEEN PROCESSED USING NORMALIZING RADIAL GRADED FILTER OF MORGAN ET AL. (2006). 107
FIGURE 4.5 THE MAGNETIC FIELD AND PLASMA PARAMETERS OF THE EVENT. FROM THE TOP THE PANELS DISPLAY THE SUPRATHERMAL ELECTRON PITCH ANGLE DISTRIBUTION (194–314 EV), THE MAGNETIC FIELD STRENGTH B(NT), BR, BT, BN(NT), CONE ANGLE

(DEG), CLOCK ANGLE (DEG), PROTON DENSITY NP(CM^{-3}), PROTON SPEED VP(KMS^{-1}), PROTON TEMPERATURE TP(K)(BLACK) AND EXPERIMENTAL TEMPERATURE TEX (K)(RED), SOLAR WIND PLASMA BETA , DYNAMIC PRESSURE (NPA), AND TOTAL PERPENDICULAR PRESSURE (PPA). 109
FIGURE 4.6 THE MAGNETIC FIELD AND PLASMA PARAMETERS FOR THE DURATION OF MARCH 20, 12:00 UT – MARCH 24, 00:00 UT. FROM THE UPPER PANEL: MAGNETIC FIELD STRENGTH B(NT), PROTON DENSITY NP(CM^{-3}), PROTON SPEED VP(KMS^{-1}), PROTON TEMPERATURE TP(K)(BLACK) AND EXPERIMENTAL TEMPERATURE TEX(K)(RED), SOLAR WIND PLASMA B, ENTROPY, ALFVEN SPEED AV, MACH NUMBER M_A, DYNAMIC PRESSURE PDY(NPA), AND TOTAL PERENDICULAR PRESSURE PT(PPA).... 111
FIGURE 4.7 THE MAGNETIC FIELD AND PLASMA PARAMETERS FOR THE DURATION MARCH 23, 00:00 UT – MARCH 25, 12:00 UT. FROM THE UPPER PANEL: THE SUPRATHERMAL ELECTRON PITCH ANGLE DISTRIBUTION (194–314 EV), MAGNETIC FIELD STRENGTH B(NT), BR, BT, BN(NT), CONE ANGLE (DEG), CLOCK ANGLE(DEG), PROTON DENSITY NP(CM^{-3}), PROTON SPEED VP(KMS^{-1}), PROTON TEMPERATURE TP(K) AND EXPERIMENTAL TEMPERATURE TEX (K)(RED LINE), SOLAR WIND PLASMA B, ENTROPY, DYNAMIC PRESSURE (NPA), AND TOTAL PERPENDICULAR PRESSURE (PPA). 114
FIGURE 5.1 A SCHEMATIC OF THE 2D SOLAR EQUATORIAL PLANE OF A SIR STRUCTURE IN THE INNER HELIOSPHERE. THE GREY SHADED AREA IS THE COMPRESSION REGION INCLUDE THE STREAM INTERFACE. SOLID LINES SHOW THE MAGNETIC FIELD LINES AND THE LENGTH OF THE ARROWS IS A MEASURE OF THE FLOW SPEED (PIZZO, 1978). 119
FIGURE 5.2 IN SITU MEASUREMENTS OF STB, WIND AND STA. FOR BOTH STA AND STB (A AND C PANELS): SUPRATHERMAL ELECTRONS PITCH ANGLE DISTRIBUTIONS (194-314 EV), MAGNETIC FIELD MAGNITUDE B(NT), CONE ANGLE(DEG), CLOCK ANGLE(DEG), PROTON SPEED VP($KMSEC^{-1}$), PROTON DENSITY NP(CM^{-3}), PROTON TEMPERATURE TP(˚K) AND AND EXPERIMENTAL TEMPERATURE TEX (K)(RED LINE), PLASMA BETA AND TOTAL PERPENDICULAR PRESSURE PT(PPA). FOR WIND (B PANEL): ACE SUPRATHERMAL ELECTRONS PITCH ANGLE DISTRIBUTIONS (272 EV), MAGNETIC FIELD MAGNITUDE B(NT), CONE ANGLE(DEG), CLOCK ANGLE(DEG), PROTON SPEED VP(KM SEC^{-1}), PROTON DENSITY NP(CM^{-3}), THERMAL VELOCITY, PLASMA BETA AND TOTAL PERPENDICULAR PRESSURE PT(PPA). 123
FIGURE 5.3 ACE MEASUREMENTS: SUPRATHERMAL ELECTRONS PITCH ANGLE DISTRIBUTIONS (272 EV), MAGNETIC FIELD MAGNITUDE B(NT), BΘ(DEG), BΦ(DEG), PROTON DENSITY NP(CM^{-3}), PROTON SPEED VP($KMSEC^{-1}$), PROTON TEMPERATURE TP(˚K) AND EXPERIMENTAL TEMPERATURE TEX (K)(RED LINE), AND PLASMA BETA. THE FIRST BLUE SHADED IS THE HPS REGION, WHEREAS THE SECOND IS THE MAGNETIC FLUX ROPE. 124
FIGURE 5.4 IMAGES OF THE CORONAL HOLE (CIRCLED RED) BY STB EUVI 195A (APRIL 19, 2011, LEFT), SDO/AIA 193A (APRIL 25, 2011, MIDDLE) AND STA EUVI 195A (MAY 03, 2011, RIGHT) (AVAILABLE AT HTTP://EAGLE.IMAPS.ABER.AC.UK/) . 124
FIGURE 5.5 IN SITU MEASUREMENTS OF STB(A), WIND(B) AND STA(C). FOR BOTH STA AND STB, THE PANELS DISPLAY: MAGNETIC FIELD MAGNITUDE B(NT), CONE ANGLE(DEG), PROTON SPEED VP(KM SEC^{-1}), AZIMUTHAL VELOCITY VN, PROTON DENSITY NP(CM-3), PROTON TEMPERATURE TP(˚K), PLASMA BETA, ENTROPY, DYNAMIC PRESSURE(NPA) AND TOTAL PERPENDICULAR PRESSURE PT(PPA). FOR WIND PANELS: MAGNETIC FIELD MAGNITUDE B(NT), CONE ANGLE(DEG), PROTON SPEED VP(KMS^{-1}), AZIMUTHAL VELOCITY VY, PROTON DENSITY NP(CM-3), THERMAL VELOCITY VTH, PLASMA BETA, ENTROPY, DYNAMIC PRESSURE(NPA), TOTAL PERPENDICULAR PRESSURE PT(PPA). THE BLUE SHADED ARE THE FLUX ROPES REGIONS AT WIND AND STA. 126
FIGURE 5.6 THE FAINT SIGNATURE OF A CME OBSERVED ON APRIL 24 07:54 UT FROM THE STA COR2 CORONAGRAPH. THE IMAGE HAS BEEN PROCESSED TO REMOVE STATIC RADIAL STRUCTURES (I.E. STREAMERS). 127
FIGURE 5.7 MAY 03, 17:43 UT CME. THE LEFT PANEL DISPLAYS THE ACTIVE REGION WITH A FILAMENT ERUPTION CIRCLED IN RED (OBSERVED BY STA EUVI 195). THE RIGHT PANEL SHOWS THE CME WHICH OBSERVED BY SOHO LASCO C2 (AVAILABLE AT HTTP://EAGLE.IMAPS.ABER.AC.UK/). 129

List of Tables

TABLE 1.1 SOLAR WIND PARAMETERS AT 1AU (AROUND SOLAR MINIMUM), COMPILED BY SCHWENN (1990), (SCHWENN, 2006). 12
TABLE 1.2 SUMMARY OF ICME PROPERTIES AT 1 AU. ADAPTED FROM (ZURBUCHEN AND RICHARDSON, 2006) 29
TABLE 1.3 NUMBER OF ICME EVENTS IDENTIFIED BY EACH AUTHORS (RUSSELL AND SHINDE, 2005) 58
TABLE 1.4 NUMBER OF ICME EVENTS IDENTIFIED BY ONLY ONE AUTHOR (RUSSELL AND SHINDE, 2005) 58
TABLE 1.5 A COMPARISON OF STATISTICAL PROPERTIES OF ICMES AT 1 AU FROM MANY AUTHORS (MITSAKOU AND MOUSSAS, 2014) 59
TABLE 2.1 THE AIA 10 CHANNELS, THE DOMINANT IONS OBSERVED IN EACH CHANNEL, AND THE CORRESPONDING TEMPERATURE REGIME FOR THAT ION. (LEMEN ET AL., 2012). 69
TABLE 3.1 THE IN SITU MAGNETIC FIELD AND SOLAR WIND PLASMA INSTRUMENTS OF ACE, WIND, STB AND SOHO 79

List of Abbreviations

Abbreviation	Details
3DP	Three- dimensional Plasma and Energetic Particle Investigation
ACE	Advanced Composition Explorer
AIA	Atmospheric Imaging Assembly
AR	Active Region
AU	Astronomical Unit (1.5×10^{11} m)
BDEs	Bidirectional Electrons
CDAWeb	Coordinated Data Analysis Web
CIR	Corotating Interaction Region
CME	Coronal Mass Ejection
Dst	Index of geomagnetic activity
EIT	Extreme Ultra Violet Imaging Telescope
EUV	Extreme Ultra Violet
EUVI	Extreme Ultraviolet Imager
GOES	Geostationary Operational Environment Satellite
GSE	Geocentric Solar Ecliptic coordinates
GSM	Geocentric Solar Magnetospheric coordinates
HCS	Heliospheric Current Sheet
HET	High Energy Telescope
HFD	Heat Flux Dropout
HPS	Heliospheric Plasma Sheet
HSS	High Speed Stream
ICME	Interplanetary Coronal Mass Ejection
IMF	Interplanetary Magnetic Field
IMP	Interplanetary Monitoring Platform
IMPACT	*In Situ* Measurements of Particles and CME Transient

ISEE-3	International Sun-Earth Explorer 3 spacecraft
ISPM	International Solar Polar Mission
L1	Lagrangian point
LASCO	Large Angle and Spectroscopic Coronagraph
LET	Low Energy Telescope
MAG	Magnetometer
MC	Magnetic Cloud
NEAR	Near Earth Asteroid Rendezvous – Shoemaker spacecraft
NOAA	National Oceanic and Atmospheric Administration
PAD	Pitch Angle Distribution
PLASTIC	Plasma and Suprathermal Ion Composition
PVO	Pioneer Venus Orbiter spacecraft
R_E	Earth Radius (6.38×10^6 m)
RTN	Radial- Tangential- Normal system
SBC	Sector Boundary Crossing
SDO	Solar Dynamics Observatory
SECCHI	Sun Earth Connection Coronal and Heliospheric Investigation
SEPs	Solar Energetic Particles
SEPT	Solar Electron Proton Telescope
SI	Stream Interface
SIR	Stream Interaction Region
SIT	Suprathermal Ion Telescope
SOHO	Solar and Heliospheric Observatory
SSC	Storm Sudden Commencement
STEREO	Solar Terrestrial Relation Observatory
SWEA	Solar Wind Electron Analyzer
SWEPAM	Solar Wind Electron Proton Alpha Monitor
SXR	Soft X-Ray
UV	Ultra Violet

Chapter 1

The Sun and Interplanetary Space

1.1 Introduction

The Sun is the source of the life on our planet, and the light and warmth that radiates from this dynamic star influences not only the Earth but the entire solar system. The characteristics of the so-called solar wind, although it was discovered 60 years ago, are still being investigated by spacecraft today. Within interplanetary space, the interaction between the solar wind and the interplanetary magnetic field which is bound to the Sun and expands along the heliosphere has allowed solar charged particles to propagate through it in spiral patterns due to the solar rotation. The most important interplanetary large-scale features in this medium are interplanetary coronal mass ejections (ICMEs) and stream interaction regions (SIRs). The following chapter is an overview of the dynamic Sun, the interplanetary medium and the large-scale features of the interplanetary medium.

1.2 The Solar interior and Atmosphere

The Sun is an ordinary star comprised of a mass of about 73.5% Hydrogen, 25% Helium and 1.5% other elements. Figure 1.1 illustrates the solar interior and atmospheric layers. The boundaries of these layers are identified in terms of their radial distance from the Sun.

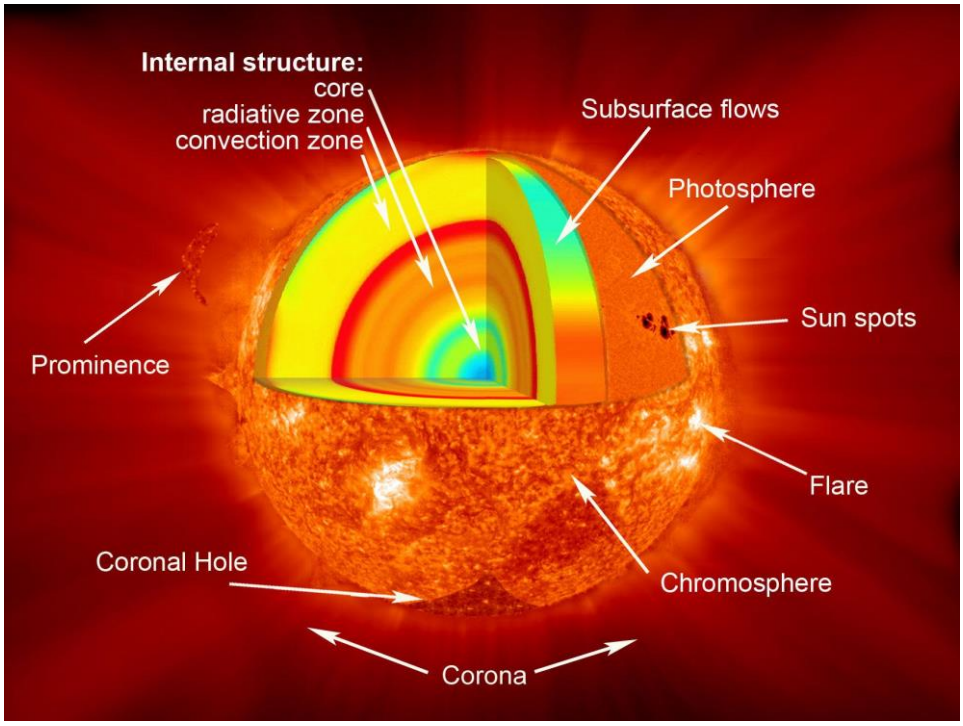

Figure 1.1 Solar interior and atmospheric layers associated with solar features: Sunspots, Prominence and Flare https://www.nasa.gov/mission_pages/sunearth/science/Sunlayers.html

The solar energy is generated by the fusion of hydrogen to helium in the Sun's core. The energy is transported from the core to the surface through both the radiative and convective zones. The first layer of the atmosphere is a visible one, the photosphere, which has a thickness of about 500 km and temperature of about 5800 k. The most noticeable features of this layer are sunspots. They are the coolest part of the surface, with a temperature of about 4200 k. Sunspots occur over intense magnetic field regions and look dark only in comparison with the surrounding hotter and brighter photospheric regions. Above the photosphere, the temperature increases gradually to 8500 k with 2000 km thickness. This is the chromosphere. Here the gas density is a million times lower than in the photosphere. Noticeable solar features of this layer are spicules- fountains which rise and fall up to about a few million metres with a speed of about 2000 m/s. The H- alpha images of this layer display massive loops of dense and cool gas (with temperatures of around 10^4 k) and look dark against the background disk where they called filaments. When the filament is seen at the limb of the solar disk with a bright loop, it is called a prominence. At a height of about 2000 km above the photosphere, the temperature rises rapidly over the space of a few hundreds of kilometres, up to 500000 k. This is the transition zone. Within this thin region, hydrogen is stripped of its electrons due to ionization. This region is often observed through the emission lines of ions such as C IV or O IV. The outermost part of the solar atmosphere is the Corona. In this region, the temperature continues to rise and reaches 10^6 k at about 8000 km. Figure 1.2 displays the temperature and density of the solar atmospheric layers.

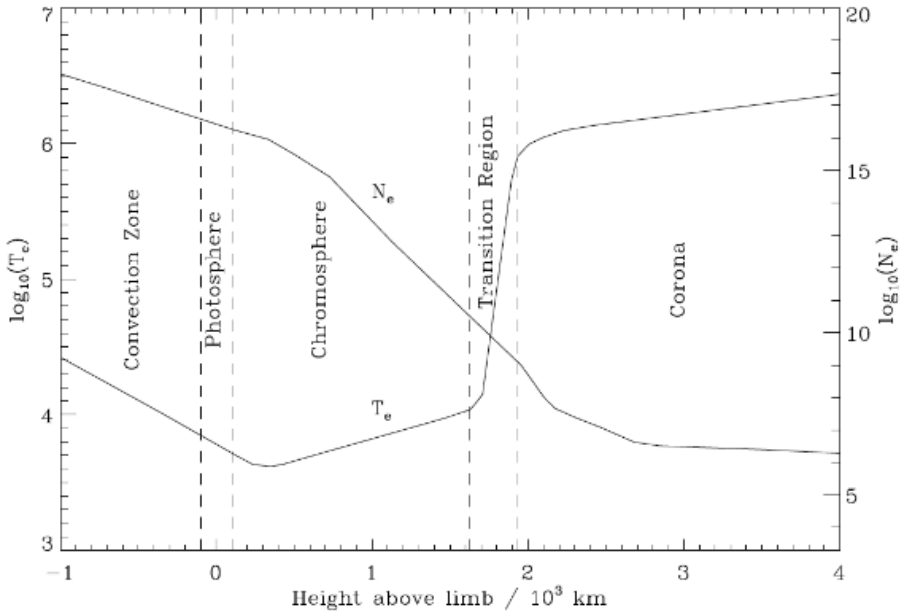

Figure 1.2 A 1D model of the Solar atmospheric layers showing temperature Te[k] and electron density Ne[cm^{-1}] (Gabriel and Mason, 1982)

1.3 The Solar Corona

The corona, from the Latin word meaning 'Crown' is the outermost solar atmosphere layer, which continuously expands out into the heliosphere. During a total solar eclipse, it is the only visible solar atmospheric region, as depicted in Figure 1.3. Coronagraphs are special telescopes containing an occulting element used to observe the extended corona outside of

a total solar eclipse. The corona can also be observed in the radio (Kruger and Schmahl, 1981), UV (Gabriel, 1971), and Soft X Ray SXR (Vaiana *et al.*, 1973). The transition to higher temperatures ends in the corona with a temperature of about 10^6 k and starts to elevate gradually, as illustrated in Figure 1.2. Within the corona itself, the density, magnetic field magnitude and electron temperature vary considerably depending on the type of region (e.g. open or closed magnetic field). Large-scale closed-field regions are associated with active regions and sunspots in the low corona and photosphere. Open-field regions are called coronal holes, and extend outwards into the heliosphere. Temperatures range from less than 1 MK in the solar quiet regions to more than 3 MK in active regions. The distribution of open and closed regions changes with the 11-year solar activity cycle. The magnetic field flux is also variable, ranging from about 10^{-3} T in quiet regions to about 0.4 T in active regions (Feldman and Landi, 2008;Wiegelmann et al., 2014).

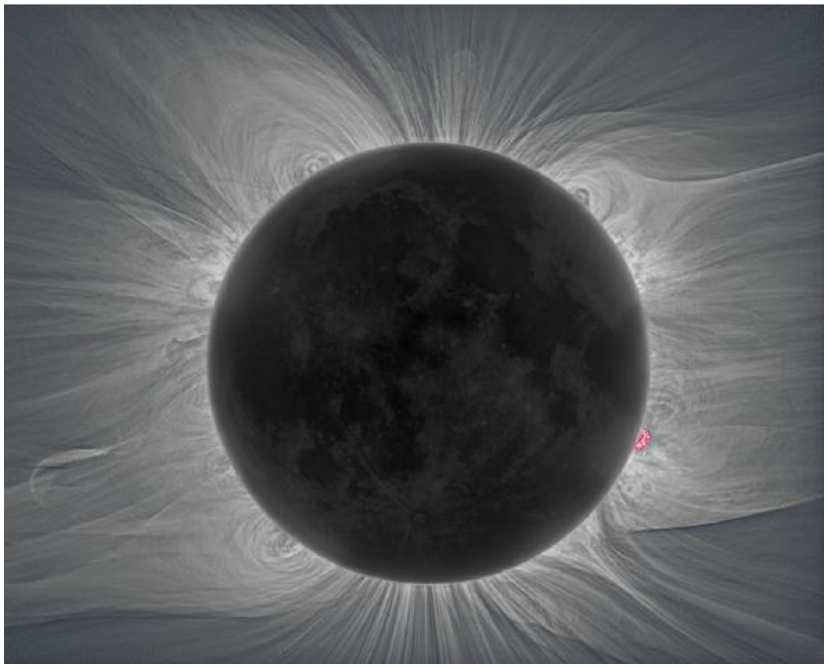

Figure 1.3 White light image of the corona during the July 11, 2010 total solar eclipse. The image has been processed with Adaptive Circular High-Pass Filter by Habbal et al. (2013)

The light emanating from the corona contains two components: The K- and F-coronae. The low corona shines by visible photospheric lights scattered by coronal electrons, which are superposed with bright emission lines. This electron scattered component is called the K-corona (from the German Kontinuum) and emits as a continuous spectrum without Fraunhofer lines (absorption lines). The K-corona is dominant until about $2R_\odot$ Solar radii ($R_\odot$ = 6.96 x 10^5 km) and its observations are used to infer the electrons density and other diagnostics. The second coronal component is the F- corona, which is the sunlight scattered from interplanetary space dust particles. This coronal component becomes dominant beyond 2.5 $R_\odot$.

The coronal shape changes during the 11 years of the solar cycle. At solar minimum, the densest or brighter corona is seen confined within the helmet streamers and is long and

symmetrical at the equator, with faint plumes at the dim poles. The helmet streamers are sandwiched between opposite magnetic polarities and are associated with the extended equatorial neutral current sheet. At solar maximum, the shape is more complex, less symmetrical and can contain streamers close to the poles**.** Figure 1.4 shows the coronal open and closed field lines configuration over a period of about 16 years. Panel (a) displays the bimodal field lines distribution during solar minimum. Here it can be seen that the streamer belt lies clearly at the equator. Coronal holes occupy mid and high latitudes. Panel (b) shows the closed field loops dominating most of the Sun's surface, with a streamer belt tilted around the equator. Coronal holes are much smaller and may appear at any latitude. Panel (c) shows the field lines returning to the solar minimum configuration as in panel (a) but with a solar magnetic polarity flip.

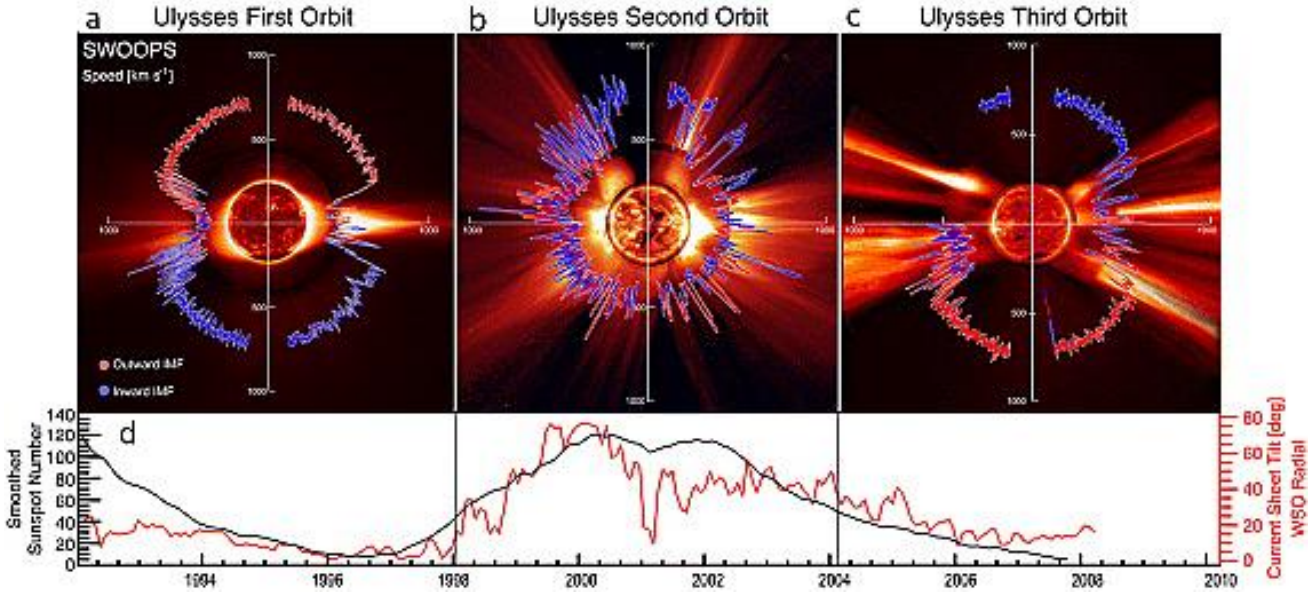

Figure 1.4 The upper panels display a coronal radial plot and solar wind speed as a function of latitudes of 3 Ulysses polar orbits of the Sun during solar minimum (a), maximum (b) and (c) more than 3 quarters of the third orbit occurring around the solar cycle declining phase. The interplanetary magnetic field shows red for inward polarity and blue for outward. The lower panel (d) shows the solar cycle sunspots number (McComas et al., 2008).

1.4 Active regions and the Solar cycle

Active regions are areas of strong magnetic field that appear in EUV and X-ray images as nests of bright and closed magnetic flux tubes rooted in the photosphere. These regions are caused by magnetic flux rising from the subsurface into the corona and are associated with sunspots. Magnetic field instabilities lead to reconnection, which can trigger the eruption of a bright solar flare. Active regions are dense features in the low corona with a typical electron density about 10^9 cm^{-3} (Del Zanna and Mason, 2003). They contain temperatures ranging between about 1-4 million K (Brooks et al., 2011;Aschwanden et al., 2013;Leonard and Morgan, 2014). In addition, active region numbers and distributions reveal a strong association with sunspots. Sunspot locations, sizes and numbers change at all Sun disk's latitudes on both hemispheres during the nearly periodic 11-years solar cycle. At the beginning of the cycle, sunspots appear at ± 30 degrees latitudes and drift down towards the equator, where they end up at the end of the cycle. Figure 1.5 displays sunspot latitudes and areas from 1870-present in a butterfly diagram.

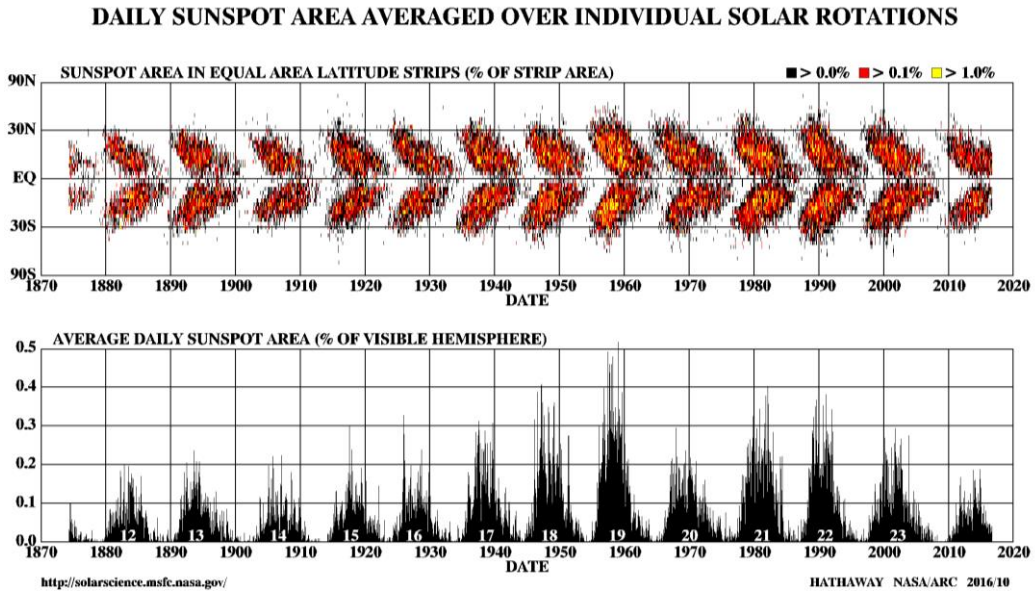

Figure 1.5 Upper: the butterfly diagram of sunspots distributions with latitudes at both hemispheres. Sunspot positions start with mid-latitudes and move toward the equator as the solar cycle progresses. Bottom: the average daily sunspots area as a function of time. https://solarscience.msfc.nasa.gov/SunspotCycle.shtml.

During the solar maximum period, flares, filament eruptions and coronal mass ejections happen more often, which is associated with significant changes in solar UV and EUV radiation and material ejections. More sunspots lead to an increase in manifestations of solar activity. Figure 1.6 shows the progress of active regions during solar cycle 23.

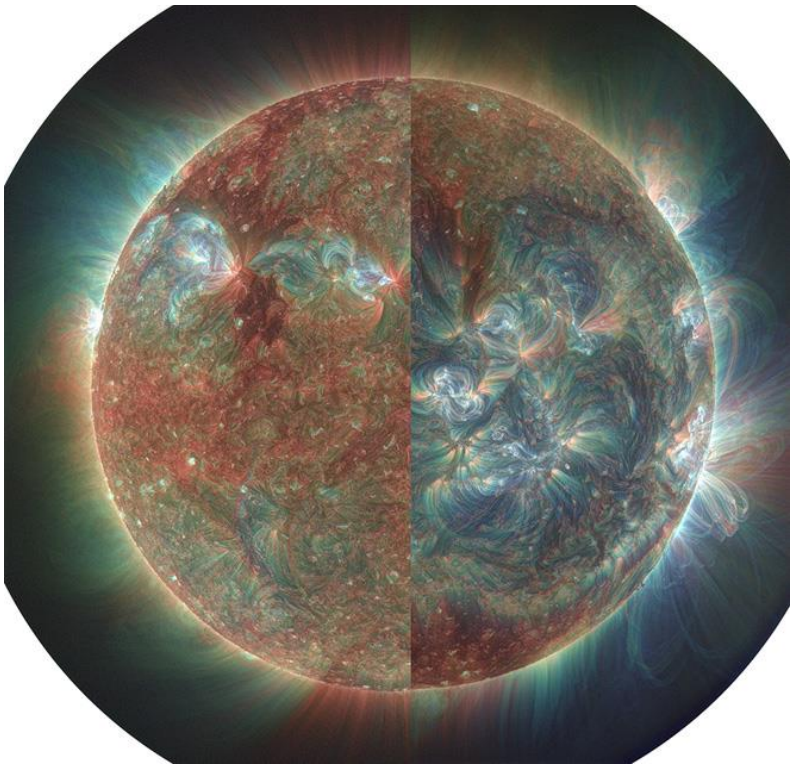

Figure 1.6 Two Solar images taken by SDO/AIA in EUV composed of 171, 193 and 211 A channels, displaying the active region changes during the solar cycle. The left half was taken in May 2010 (end of the latest solar minimum activity period). The right half was taken in December 2014 (current solar maximum period) (Morgan and Taroyan, 2017).

1.5 Filaments, Coronal Mass Ejections (CMEs) and Flares

Filaments are massive loops of dense and cool material arching up from the photosphere and suspended along magnetic field lines. By using EUV observations, filaments appear dark in absorption on the solar disk, in contrast to the bright corona. When seen above the Sun's limb, they appear brighter than the surrounding corona and are called Prominences (Figure 1.7). They have a temperature of about 10^4 k, with electron densities ranging between 10^9-10^{11} cm^{-3} (Labrosse *et al*., 2010). Filaments are often associated with Coronal mass ejections and their cool material make up the CME core part (Vourlidas *et al.*, 2013). Dark filaments in H-alpha erupt and disappear on the disk when an eruption happens.

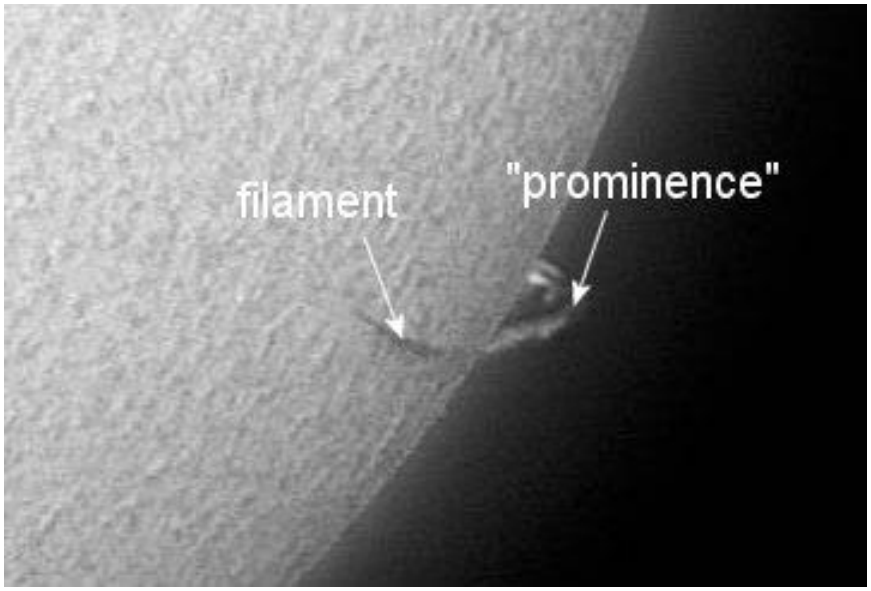

Figure 1.7 Filaments and Prominences that have formed above the chromosphere. They are typically observed in H-alpha (656.3 nm). https://data.noaa.gov/dataset/solar-features-prominences-and-filaments.

Coronal mass ejections (CMEs) are spectacular large-scale eruptions of matter (electrons, protons, and quantities of heaver ions such as helium, iron and oxygen) and have magnetic fields that travel with broad distributions of velocities reaching 2000 km/s, even occasionally exceeding 3000 km/s, with a typical mass between 1×10^{11} – 4×10^{13} g (e.g. (Hudson et al., 1996;Yashiro et al., 2004)). The CME energy ranges from 10^{-2} – 10 J/m^3 (Forbes, 2000) with total kinetic and potential energies of 10^{22}-10^{25} J, similar to solar flares (Emslie *et al.*, 2004). CMEs which originate from closed fields that erupt from the solar corona into the heliosphere (Chen, 2011) are associated with flares, erupting filaments or both (Gopalswamy *et al*., 2003b)

CMEs can be observed in many wavelengths, including with the white light in which they were detected for the first time by the coronagraph NASA's seventh orbiting solar observatory OSO-7 (Tousey, 1973), with soft x-rays (Gopalswamy *et al.*, 1997), extreme ultra violet (Chen, 2009) and radio waves (Maia *et al*., 1999). According to their morphology, CMEs are classified as belonging to one of two main shapes: 1) Narrow CMEs which display jet- like motions with an angular width of less than 10° (Wang *et al*., 1998a) and 2) Normal CMEs, which consist of a standard three-part structure: the bright front, the dark cavity, and the embedded bright core representing the filament plasma (Illing and Hundhausen, 1985). Webb and Hundhausen

(1987) found that about 30% of CME events have a 3-part structure**.** Figure 1.8 shows a typical three-part structure CME as observed by SOHO/LASCO.

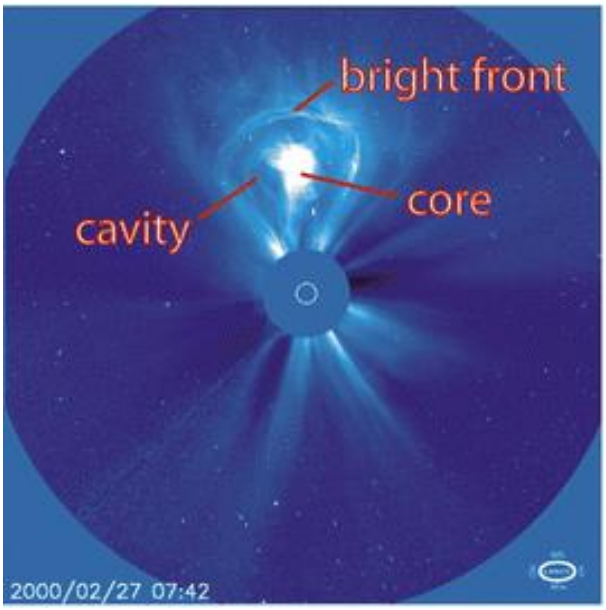

Figure 1.8 The standard three parts of the CME (core, cavity and bright front) observed by SOHO/LASCO on the 27th of February 2000. Adapted from Riley et al. (2008)

CMEs can be described as eruptions which contain a twisted flux rope originating from an erupted filament. This filament is kept in equilibrium through closed magnetic field lines until a magnetic instability leads to the equilibrium being lost and a flux rope rising upward. Down the prominence and above closed magnetic field lines (see Figure 1.9), a magnetic reconnection takes place at a current sheet (dark vertical line). The CME traps hot plasma below it. The closed magnetic field region upper the prominence is supposed to erupted as a magnetic flux rope in the interplanetary medium. So it contain cool and dense prominence material (Lin et al., 2004;Chen, 2011). Figure 1.9 illustrates a CME eruption model.

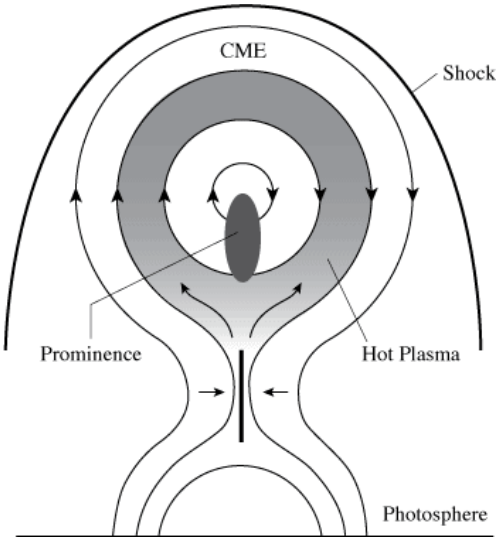

Figure 1.9 A sketch of a CME eruption model. The magnetic reconnection occurs at the current sheet region (dark vertical line). The small dark oval represents the prominence cool material. Adapted from Martens and Kuin (1989).

Flares are sudden rapid and intense eruptions associated with reconnection, which rapidly convert stored magnetic energy into thermal energy (heating) and the acceleration of bursts of highly energetic particles. The energy from flares can reach about 10^{25} J (Koskinen, 2011). Their emissions can be observed by a wide spectrum ranging from radio to X ray (Howard, 2011). Solar energetic particles often originate in a flare. The relationship between them was observed early by Forbush (1946). Flares are classified by their X-ray flux output into B, C, M and X classes. This classification system was designed by the National Oceanic and Atmospheric Administration (NOAA). Solar flares form over sunspots or active regions, and tend to coincide with the 11-years solar cycle. There is no fixed relationship between flares and CMEs, but flares are thought to be an aspect of the underlying CME process and are associated with their eruption reconnection (Chen, 2011). Wang and Zhang (2007) found that about 10% of X class flares were not associated with CMEs. Many models show the relationship between H-alpha ribbons, CMEs and disappearing filaments. Figure 1.10 is an example of such a model.

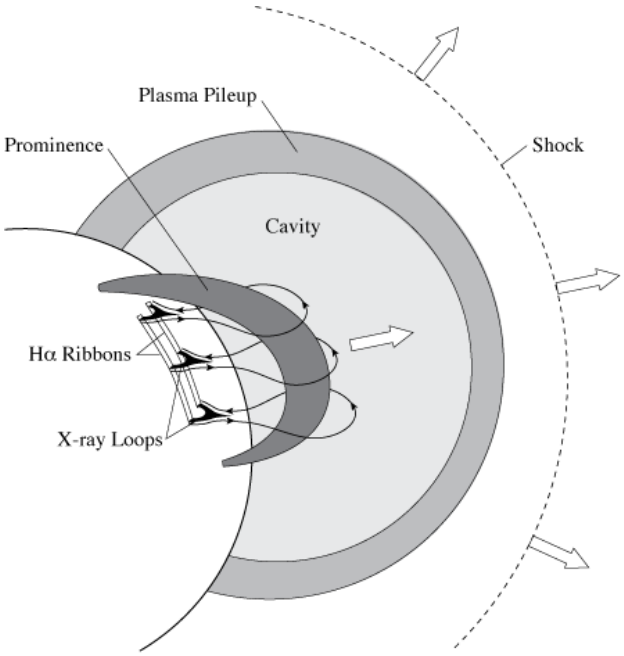

Figure 1.10 The relationship between the flare H-alpha ribbon, prominence and the CME's three parts (Forbes, 2000).

1.6 Coronal Holes

Coronal holes are regions of open magnetic field lines located within the corona. They appear as dark areas when observed in X-ray and EUV images (Figure 1.11). This darkness is due to their low temperature and densities. Solar material evacuated along the unipolar field lines of coronal holes generates high speed solar wind streams (HSSs). At solar minimum, large coronal holes dominate the North and South Pole regions whereas small equatorial coronal holes are seen at low- and mid-latitudes at solar maximum. They are either isolated or possess a polar extension. Coronal holes' HSSs are less tightly wound in the Parker spiral patterns. A compressed boundary between a high speed solar wind and slow solar wind in front of it

causes stream interaction regions (SIRs). When these regions pass by the Earth, disturbances occur within the geomagnetic field, and auroras occur more frequently.

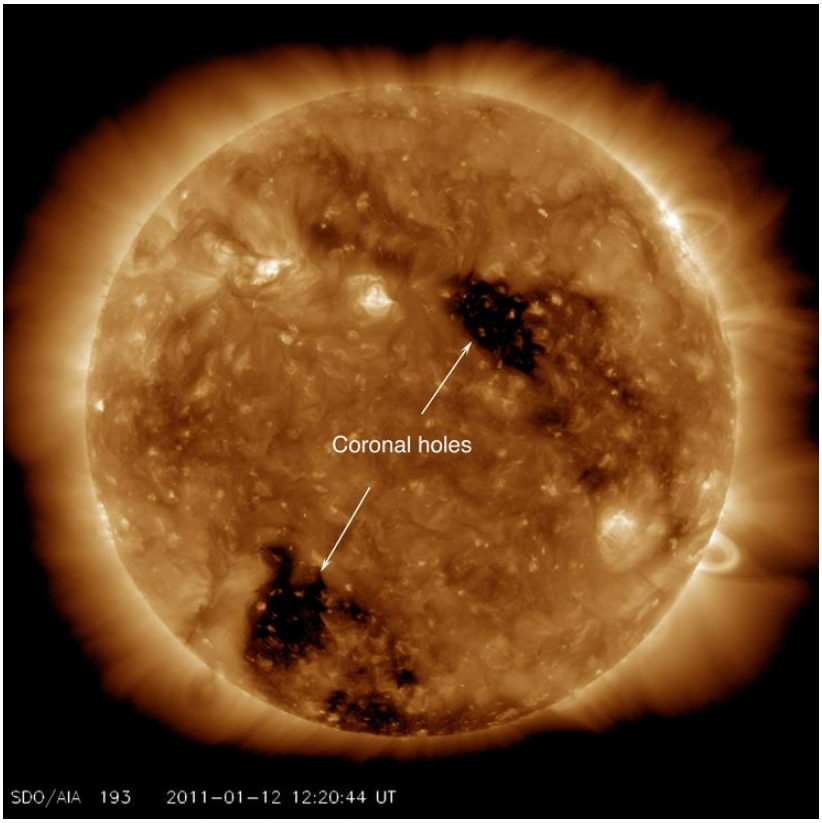

Figure 1.11 SDO/AIA 193 A Coronal hole's image. From http://www.thesuntoday.org/tag/coronal-hole/

1.7 The Geoeffectiveness of Halo CMEs:

A Halo CME is a subset of CMEs (Howard *et al.*, 1985). Large CMEs will appear as halo CMEs when they are propagating towards or away from the observer. Therefore, CMEs that appear as halos from Earth are more likely to be geoeffective. Through the use of a coronagraph instrument, a halo CME can be seen surrounding the occulting disk. The major period of halo CME observations begun in 1995 with LASCO, the space coronagraph on board SOHO which regularly observed CMEs (Brueckner *et al.*, 1995). Halo CMEs have been classified by Gopalswamy et al. (2003a) as either :

- Type F (full halo), with a 360° angular width; appears surrounding the occulting disk of the coronagraph. These are classic halo CMEs and originate from the active regions near the centre of the visible solar front disk or the solar backside disk.

-Type A (asymmetric halo), with a 360°angular width; originates from the active region near the visible solar limb. We can see type A CMEs through LASCO/C2 as a wide halo CME, but they do not encircle the coronagraph occulting disk. They give a full halo appearance because their extension on the opposite side can be seen. With time, they expand by to a C3 field of view.

-Type P (partial halo), with a ≥ 120° angular width. They appear as incomplete halos surrounding the occulting disk.

The ability of CMEs to cause geomagnetic storms is known as geoeffectiveness. This is measured in terms of geomagnetic index such as the *Dst* index (Gopalswamy et al., 2007;Gopalswamy et al., 2008). CMEs have a high geoeffectiveness when they impact the Earth with propagation angles exceeding 90° from the Earth's line of sight, and their dominant axial magnetic field faces southward (therefore more likely to reconnect with Earth's magnetic field). Front side halo CMEs are potential sources of geomagnetic storms (Zhao and Webb, 2003). This type of CME increases in geoeffectiveness when they originate from near the central meridian (Cid *et al.*, 2012). From 1996 to 2005, about 75% of disk halos were geoeffective (*Dst*≤-50), whereas 60% of limb halos were geoeffective (Gopalswamy *et al.*, 2007). Likewise, ''the difference in flare sizes among geoeffective halos is not significant''(Gopalswamy et al., 2007). The geoeffectiveness of halo CMEs is reduced with increasing distance of their solar source locations from the central meridian. The overall geoeffectiveness is smaller for limb halos and most of the huge magnetic disturbances are caused by front side disk halos (Gopalswamy, 2009b). The probability of geoeffectiveness for halo CMEs originating from the limb was investigated with 25 limb halo CMEs during solar cycle 23, and only 4 of them were found to be geoeffective- all of these originating in the west limb (Cid et al., 2012). The earth encountering front side halo CMEs are believed to be one of the main drivers of hazardous space weather (Wang et al., 2014) . Figure 1.12 shows an example of the geoeffectiveness of three types of halos.

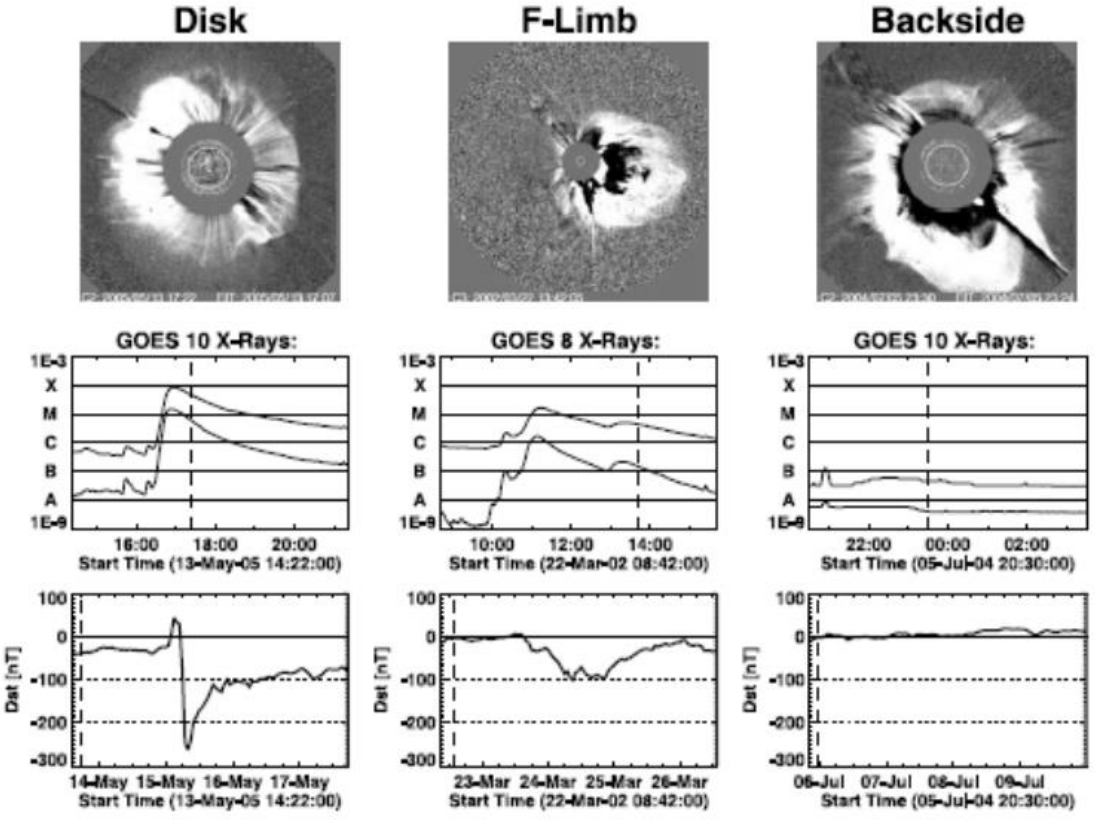

Figure 1.12 Examples of (left) disk, (middle) limb, and (right) backside halo CMEs from LASCO/C2 with GOES X-Ray and Dst index plots (Gopalswamy et al., 2007).

1.8 The Interplanetary medium

1.8.1 Solar wind and Interplanetary Magnetic Field (IMF)

The high temperature rising from the photosphere to the corona and then into interplanetary space requires a high amount of energy input to the corona in order to maintain this large temperature difference and the bulk outflow of the corona into interplanetary space. The full details of this process are not yet known. To have a pressure decrease eventually with values close to the interstellar medium pressure values, the continues rising in temperature make the corona be not as a hydrostatic equilibrium medium, but a region of continuously expanding of plasma. From 1951 to 1957, Biermann published a series of reports based on the observations of comets tails, which led him to assume continuous solar radiations and particles in all the time. The comet tail images revealed clouds moving along the rear, which were used to measure speeds and accelerations of these particle emissions (Brandt, 1970). Sydney Chapman (1957) formulated the first theory about coronal expansion by testing the coronal expansion distance assuming a statistical formula and using the hydrostatic equilibrium and thermal conduction:

$$\frac{dP}{dr} = -\rho g \tag{1.1}$$

$$F=-4\pi r^2 k\frac{dT}{dr} \tag{1.2}$$

Where P is the coronal gas pressure at distance of r from the Sun's centre. ρ *is the coronal gas density at distance of* r *from the Sun's centre. G* is gravitational acceleration. F is the heat flux, K is the thermal conductivity and T is the temperature in degree Kelvin (k).

Chapman considered the thermal conductivity important in sustaining the corona and its expansion, and posited that the gaseous medium close to Earth is part of the coronal extension. The different pressures between the corona and the interstellar medium hot gas can produce enough pressure to contract the gravity, to ensure a constant material outflow from the Sun. With this idea, Parker (1958) began to calculate the coronal expansion speed as a function of height for various temperatures with the consideration of mass, momentum and energy conservation. This study suggests that the corona base requires being heated with a more active mechanism than the simple thermal conductivity, which is the thermal convection (Akasofu and Chapman, 1972). Parker (1958) derived an equation of motion which no longer relied on the idea of a hydrostatic corona: a supersonic spherical and isothermal flow radially away into the interplanetary space like that of Biermann's corpuscular radiation.

The outflow plasma kinetic pressure is much greater than the magnetic and thermal pressure. This outflow was termed the Solar Wind. The driven equation of motion is:

$$Vr\frac{dVr}{dr} = -\frac{1}{nm_H}\frac{d}{dr}(2nRT) - \frac{GM_{Sun}}{r^2} \tag{1.3}$$

Where *n* is total particle density, m_H is hydrogen mass ($1.6\text{x}10^{-24}$ gm), Vr is the radial velocity of the coronal gas expansion, r is distance from the Sun's centre, R is the Boltzmann constant ($1.4\text{x}10^{-16}$ erg/k), T is the temperature(k), G is the gravitational constant ($6.67\text{x}10^{-8}$ $\text{cm}^3/\text{gm. s}^2$) and M_{Sun} is the Sun's mass ($1.99\text{x}10^{33}$ gm). This new view took into account the solar wind outflow speed as a function of heliocentric distance for different coronal temperatures (Figure 1.13).

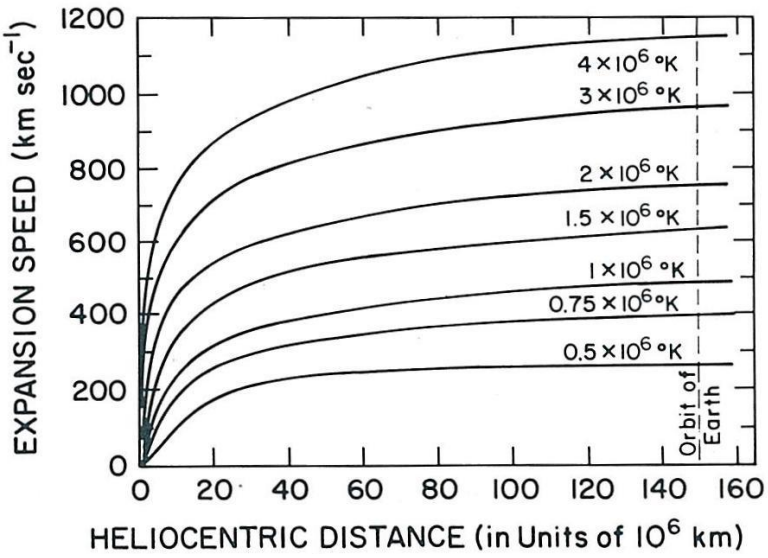

Figure 1.13 Original solution for the solar wind expansion outward the Sun. Adapted from Parker (1958)

In addition, Parker suggested a magnetic field shape which was frozen-in to the radial outflow of the solar wind, with the condition that the solar kinetic energy should be greater than the magnetic field energy density. Since the magnetic field is about 10^{-9} tesla, this means that the magnetic energy density should be about $4\text{x}10^{-13}$ J/m^3, which is far smaller than the solar wind kinetic energy density ($4\text{x}10^{-10}$ J/m^3). Consequently, the solar wind carries the magnetic field outwards (Ratcliffe, 1972). The dominant orientation angle of the magnetic field relative to the radial depends on the local solar wind velocity, distance and latitude.

The solar wind consist of electrons, protons, alpha particles and a low amount of other elements. *In situ* measurements have discovered typical solar wind proton temperatures, densities and speeds of about $1.2 \text{ x } 10^5$ k, 468 kms^{-1} and 8.7 cm^{-3}. Table 1.1 shows the solar wind statistical properties at 1 AU.

	Low speed wind (LSM)	Fast wind (HSS)
Flow speed v_p	$250-400\ \text{km s}^{-1}$	$400-800\ \text{km s}^{-1}$
Proton density n_p	$10.7\ \text{cm}^{-3}$	$3.0\ \text{cm}^{-3}$
Proton flux density $n_p\ v_p$	$3.7 \times 10^8\ \text{cm}^{-2}\ \text{s}^{-1}$	$2.0 \times 10^8\ \text{cm}^{-2}\ \text{s}^{-1}$
Proton temperature T_p	3.4×10^4 K	2.3×10^5 K
Electron temperature T_e	1.3×10^5 K	1×10^5 K
Momentum flux density	$2.12 \times 10^8\ \text{dyne cm}^{-2}$	$2.26 \times 10^8\ \text{dyne cm}^{-2}$
Total energy flux density	$1.55\ \text{erg cm}^{-2}\ \text{s}^{-1}$	$1.43\ \text{erg cm}^{-2}\ \text{s}^{-1}$
Helium content n_p/n_{He}	2.5%, variable	3.6%, stationary

Table 1.1 Solar wind parameters at 1AU (around solar minimum), compiled by Schwenn (1990), (Schwenn, 2006).

The Sun's magnetic field is usually approximated to a dipole. It is generally tilted relative to the Sun's rotation axis and changes as the 11- year solar cycle progresses. Due to this rotation, the interplanetary magnetic geometry, as proposed by Parker (1958), to be an Archimedian spiral, which was later termed the Parker Spiral (Figure 1.14).

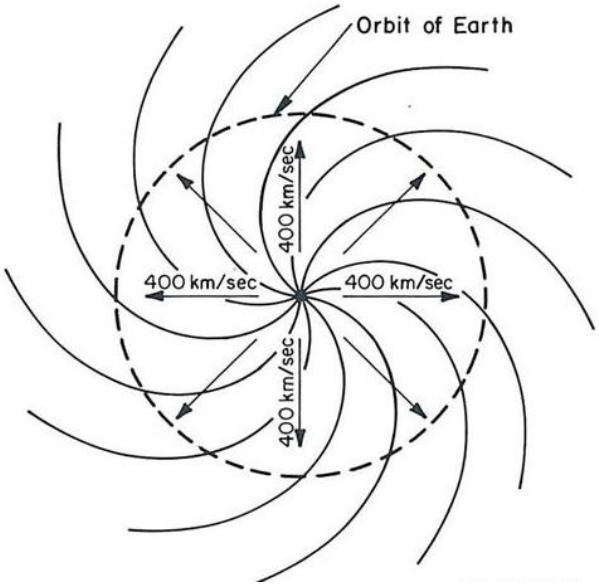

Figure 1.14 The Parker spiral in the solar ecliptic plane. The straight lines are the radial solar wind propagation with a speed of 400 kms^{-1} (considered slow wind today). The spiral curves are the IMF lines which are embedded in the rotating Sun and carried out radially by the solar wind. Arrows added to the field directions indicates their polarity at the Sun (Parker did not specifically predict the interplanetary magnetic polarity and avoided electric fields(E) and currents(j).adapted from (Parker, 1963)

With the solar rotation, the solar wind particles which are emitted from the same source lines up to form the Archimedean spiral and Since the magnetic field lines extending through these particles originate from the same source origin, the interplanetary field lines also form these same spiral patterns, at an angle about 45° to the solar radial direction, and they rotate with the constant angular solar wind velocity (Figure 1.15). The final configuration is a magnetic axis aligned with the rotation axis (Russell, 2001).

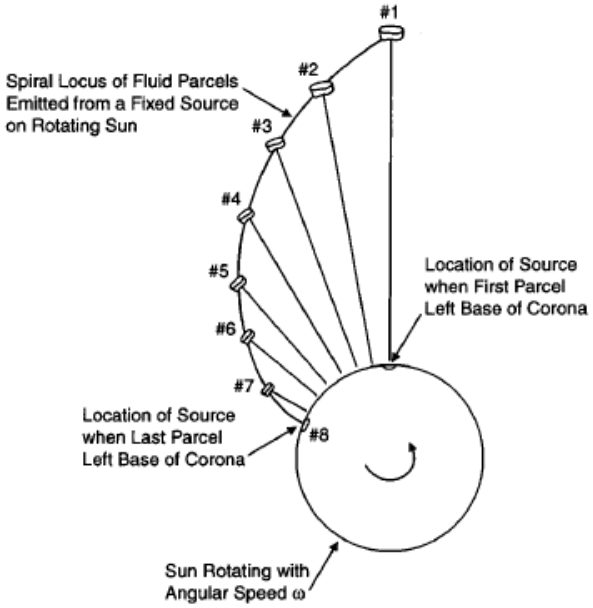

Figure 1.15 Solar wind parcels leave the sun analogous the fluid spirals formed from the rotating sprinkler. Adapted from Hundhausen (1995). (Russell, 2001)

A more complex IMF configuration has been proposed by Fisk (1996) in an attempt to interpret Ulysses high energetic particles at heliospheric high latitudes. This model showed that the magnetic field foot points on the solar wind source rotate differentially around their axis. In the process of moving away from the solar equator, the magnetic field line becomes gradually less tightly wound with latitude, until a magnetic field line originating exactly from the point of the pole remains purely radial. This means that the Sun's magnetic field is not only constantly expanding, but it is offset slightly from the Sun's axis of rotation. The field lines in this model connect directly from low to high heliospheric latitudes. Figure 1.16 shows three different IMF models.

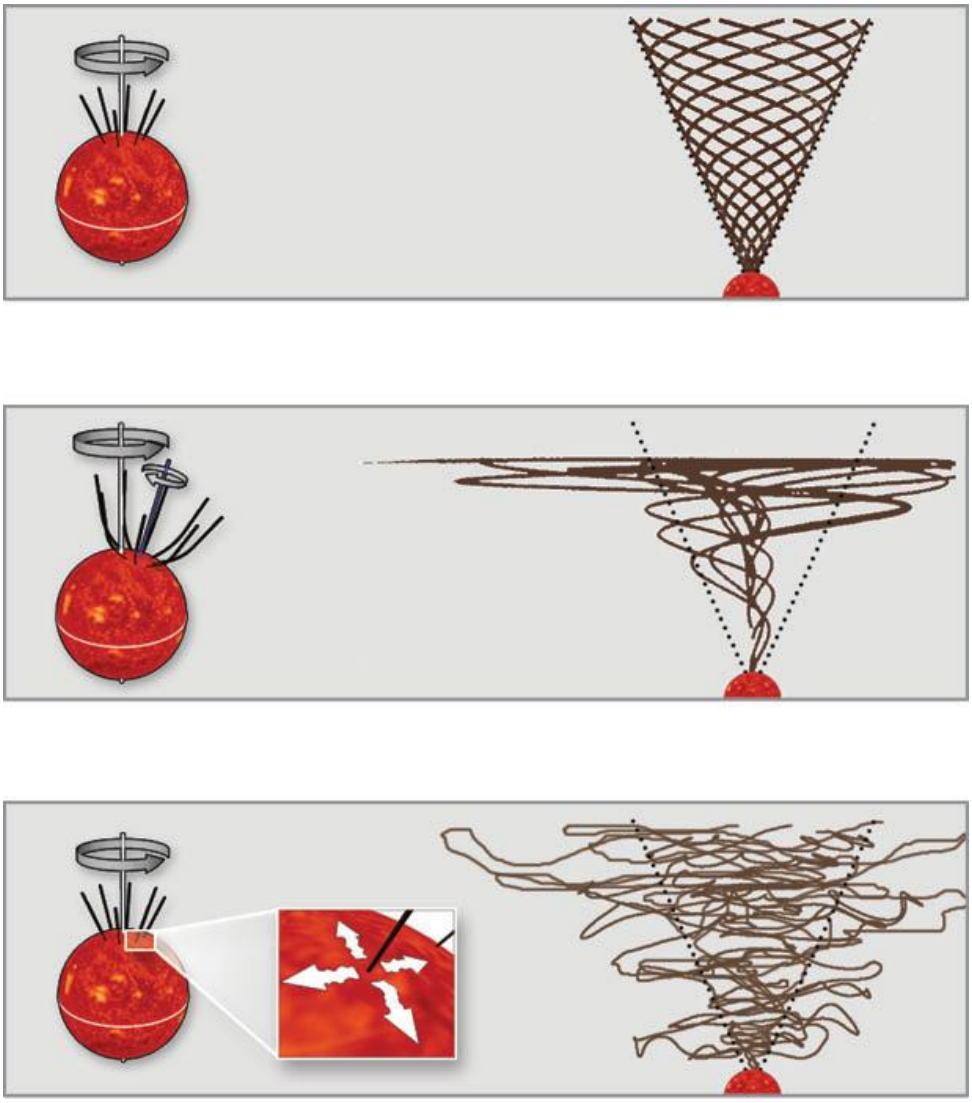

Figure 1.16 Three different IMF models. Top: Parker field configuration (without foot point motion). There is no transport in latitude. The field lines are helices lying on cones with half angles equal to the source lattitudes. At a given radial distance, the fields are tightly spiraled in the equator and radial over the pole. Middle: Fisk IMF. Differential rotation into an asymmetric corona assumption(with foot point motion). Adapted from Zurbuchen et al. (1997). Lower: random, with diffusive motions. Adapted from Jokipii and Kota (1989).(Zurbuchen, 2007).

Between the opposite polarities of the northern and southern solar hemispheres, a neutral boundary sheet arises, termed the heliospheric current sheet (HCS), expected to have a flat, inclined shape near the sun.The HCS wraps around the Sun in the shape of a ballerina's twirling skirt (Figure 1.17).

IMF is a vector quantity B and has three directional axis components in the cartisian coordinate system (B_x, B_y, and B_z). B is often weak and expressed in units of nano Tesla (nT) with an average value of about 6 nT. B_x and B_y are oriented parrallel to the elliptic, whereas Bz is perpendicular to the elliptic. When the IMF and the Earth magnetospheic field lines are oriented antiparallel to each other, reconnection is more likely to occur, resulting in an energy transfer from the solar wind to the magnetosphere. The strongest coupling between them occurs when B_z oriented is southward.

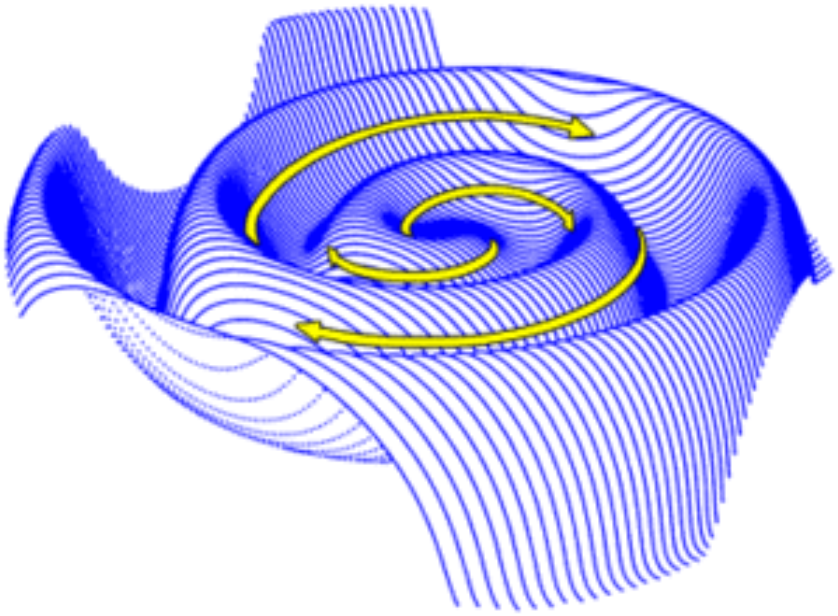

Figure 1.17 A computer-generated visualisation of the HCS showing two oppositely-directed ridges (sectors) of the skirt per solar rotation. Both of them adopt the parker spiral feature (Jokipii and Thomas, 1981). Image is courtesy of J. Jokipii, University of Arizona.

The Sun's rotational axis is tilted at 7 degrees to the Sun-Earth equatorial plane which explains the 14-day polarity inversion. The changes over the Earth year is because the 7 degree angle varies relative to Earth's orbit. With the Sun's rotation, the polarity pattern sweeps over the Earth, causing a magnetic sector configuration in which the IMFs are inward for about 7 to 14 days and then outward as the Earth travels from the southern to the northern hemisphere. During this interval, the streamer belt sweeps across the Earth twice with every solar rotation (Figure 1.18).

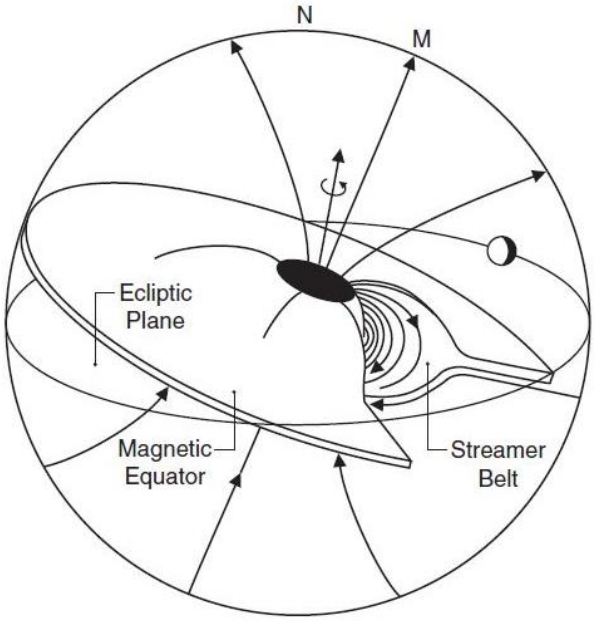

Figure 1.18 Three-dimensional scheme of the interplanetary pattern with the streamer in relation to the ecliptic plane. Because of the streamer belt's 7.2 degree tilt, it will sweep across the Earth twice every solar rotation. Adapted from Hundhausen (1977)

1.8.2 Magnetohydrodynamics (MHD)

Magnetohydrodynamic describes electrically conducting fluids (hydro), such as plasma, in the presence of the magnetic field (magneto). The MHD equations combine the reduction of the non-relativistic approximation of Maxwell's equations and the dynamics of the neutral plasma equation of Navier-stokes extended by the Lorentz force term, the equation of mass continuity of the plasma Ohm's law and the adiabatic gas law.
The fundamental equations of the MHD use the assumption:

$$\frac{\partial \rho}{\partial t} + \nabla.(\rho V) = 0 \tag{1.4}$$

This is the continuity equation which describes the relationship between the plasma density (ρ) and the fluid velocity (V) in time(t).
Another equation that describes the conservation of momentum is the equation of motion:

$$\rho \frac{\partial V}{\partial t} + \rho(V.\nabla)V = -\nabla P + j \times B + qE + \rho g + F \tag{1.5}$$

Where ∇P is the plasma pressure gradient, j is the current density (given by the Maxwell equation: $j = \frac{1}{\mu} \nabla \times B$), B is the magnetic induction, $j \times B$ is Lorentz force per unit volume, q is the charge density, E is the electric field strength, ρg is the gravitational force and F indicates the effect of viscosity.

Equation (1.5) relates the fluid velocity (V) to density (ρ) and to the electromagnetic Lorentz force acting on the fluid element.
The heat elevations or reductions can express by the energy equation as the net effect of energy production and loss, as the plasma propagate in the space:

$$\frac{\partial \rho}{\partial t} + V.\nabla P + \gamma P \nabla . V = E_l \tag{1.6}$$

Where E_l is the total energy loss function and γ is the ratio of specific heat at constant pressure to specific heat at constant volume. The temperature T of the plasma can be determined from the ideal gas pressure P and the density ρ using the equation of state:

$$P = R\rho T = nK_B\, T \tag{1.7}$$

Where R is the universal gas constant (8.3×10^3 m^2 s^{-2} deg^{-1}), n is the total number of particles per unit volume and K_B is Boltzmann constant (1.381×10^{-23} J deg^{-1}).
These fundamental equations follow the assumption that the concept of charge conservations is irrelevant, which means:

$qE \to 0$ under MHD approximation, and Poisson's equation ($\nabla E = \frac{\rho_e}{\epsilon}$) becomes:

$$\nabla E = 0 \tag{1.8}$$

Where ρ_e is the charge density and ϵ is the permittivity of free space.
Calculating the curl of the electric field E and using one of Maxwell's equations:

$$\nabla \times E = -\frac{\partial B}{\partial t} \tag{1.9}$$

The magnetic field B must satisfy the condition of Gauss' law for B:

$$\nabla . B = 0 \tag{1.10}$$

This equation means that there are no magnetic sources or monopoles.
By merging of Ampere's law ($\nabla \times B = \mu_0\, j$) and Ohm's law ($j = \sigma(E + V \times B)$) leads to the induction equation, which eliminates the electric field and relates V to B and finally leads to the derivation of Alfven's frozen flux theorem.

$$\nabla \times B = \mu_0 \sigma (E + V \times B) \tag{1.11}$$

Using Faraday's law and assuming that σ is constant:

$$\nabla \times(\nabla \times B)= \mu_{\circ}\sigma \left(-\frac{\partial B}{\partial t} +\nabla \times(V\times B)\right) \quad (1.12)$$

$$\nabla \times(\nabla \times B)= \nabla(\nabla . B) - \nabla^2 B = -\nabla^2 B \quad (1.13)$$

$$\frac{\partial B}{\partial t} = \nabla \times (V \times B) + \eta \nabla^2 B \quad (1.14)$$

Where η (Ohmic magnetic diffusivity) $= \frac{1}{\mu_0 \sigma}$

The MHD induction equation expresses that a magnetic field can change due to plasma motion or diffusion.

1.8.3 Plasma and Electromagnetic Field

Plasma react strongly to electromagnetic fields and therefore, the field of electric and magnetic forces is important to understanding the behaviour of solar and interplanetary plasma. Charged particle (q) in the plasma moves under the influence of Lorentz force. Subsequently, its equation of motion is:

$$m\frac{dV}{dt} = F = q(E + V \times B) \quad (1.15)$$

Where V is the velocity of the charged particle, E is the electric field and B is the magnetic field.

In the Lorentz force, the electric field accelerates negative and positive charges in opposite directions, whereas the magnetic part is always perpendicular to the velocity of the particle. Therefore the magnetic field can only change the particle's path(it cannot work on the charge). Figure 1.19 displays the charged particles movements in a circular motion about the magnetic field lines within a static and homogeneous magnetic field, with an angular frequency, also called gyro frequency, for species α :

$$\omega_\alpha = \frac{q_\alpha B}{m_\alpha} \quad (1.16)$$

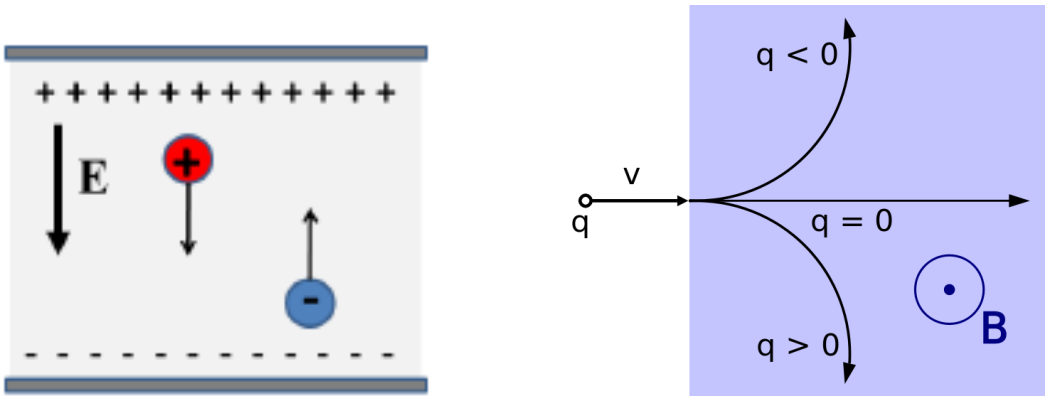

Figure 1.19 Left: positive and negative charges accelerate to opposite directions by the electric field of the Lorentz force. Right: the magnetic part of the Lorentz force change the path of the particle(right-hand rule).

The Lorentz force per unit volume acting on electric current density ($J = \rho_q V$) and charge density is given by :

$$f = \rho_q E + J \times B \tag{1.17}$$

Equation (1.17) describes a simple harmonic oscillator at the gyro frequency. For an electron ω_α= 1.76 X 10^{11} B, while for proton ω_α= 9.58 X 10^7 B. The unit of gyro frequency is rad s^{-1} and B is given in Tesla. The radius of this gyro motion is gyroradius:

$$r = \frac{mv}{qB} \tag{1.18}$$

Where v is the particle velocity perpendicular to the magnetic field.
The particle motion is divided into two components: 1- linear motion along the magnetic field at a constant velocity. 2- circular motion in the plane perpendicular to the magnetic field. The trajectory of a charged particle can illustrated in Figure 1.20.

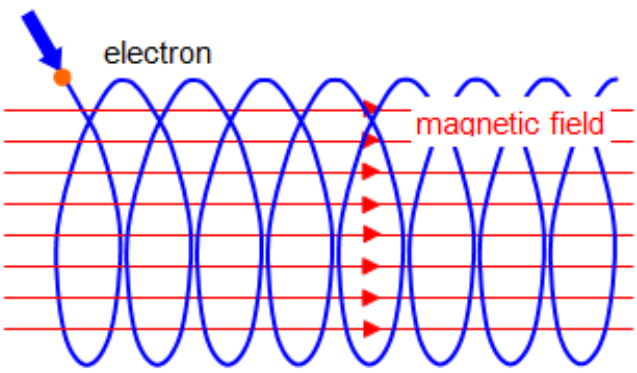

Figure 1.20 The helical trajectory of an charged particle in a homogeneous magnetic field.

1.8.4 Heliospheric Current Sheet (HCS), Sector Boundary Crossing (SBC), and Heliospheric Plasma Sheet (HPS).

The HCS was discovered by Wilcox and Ness (1965) and defined as the boundary which divides interplanetary space into two hemispheres with oppositely directed magnetic fields polarities (outward and inward) originating from the Sun (

Figure 1.21) (Svalgaard *et al.*, 1975). During the Earths passage through the sheet, its magnetic field orientation changes, which is referred to a sector boundary crossing (SBC). This orientation is displayed by the interplanetary magnetic field azimuthal angle (ϕ_B), and changes based on changes to the *Bx* and *By* magnetic field components. It is oriented outward when its values are between 90 and 270 degrees. Sector boundary crossing areas are associated with a rising in plasma density and a reduction of solar wind speed (Smith, 2001).

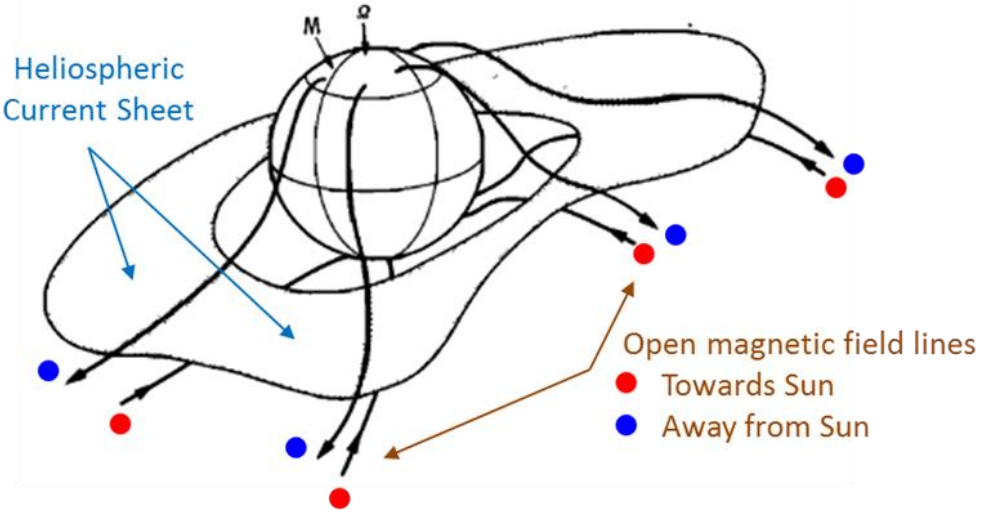

Figure 1.21 Heliospheric current sheet dividing the towards (red points) and away (blue points) magnetic field lines from the Sun. Adapted from Smith et al. (1978).

The Heliospheric Plasma Sheet (HPS) is defined as a sheath which encases (Crooker *et al.*, 2004a) straddles (Winterhalter *et al.*, 1994) or borders (Suess *et al.*, 2009) the HCS. It can be identified by the presence of an enhancement in the solar wind plasma density, plasma beta, a decrease of the *He*/*H* in the vicinity of the HCS as well as the inversion of the interplanetary magnetic field sector (Winterhalter et al., 1994;Borrini et al., 1981;Simunac et al., 2012). Figure 1.22 displays a HPS scheme which extends the helmet streamer and surrounds the HCS.

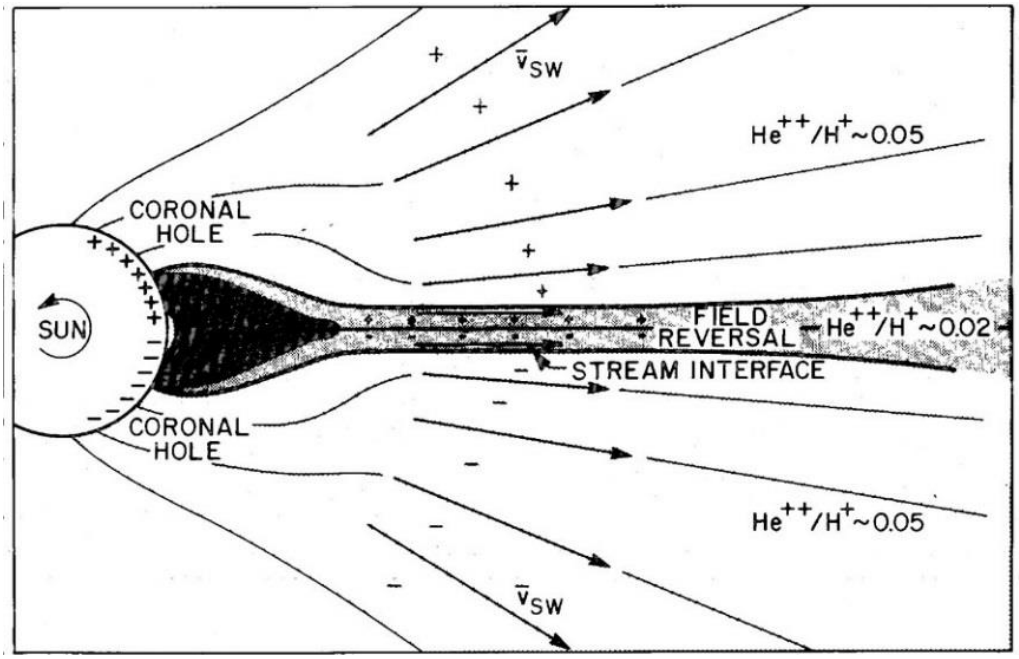

Figure 1.22 A plasma sheet scheme view of a heliospheric extension of the coronal streamer belt surrounding the HCS with a high-density region (Gosling et al., 1981).

The sector boundary is assumed to be the equivalent of the current sheet, which allows for the possibility of its identification from the magnetic field invasion from inward to outward the Sun (or vice versa) along the interplanetary Parker spiral. This assumption is not always correct, as the advent of the suprathermal electron pitch angle distribution has shown. Using energies > 2kev, Kahler and Lin (1994) and Kahler and Lin (1995) found a high degree of mismatch between the sector boundaries which were identified by the magnetic field reversals and those which were identified by electrons streams polarity reversals. Crooker *et al.* (1996) and Kahler *et al.* (1998) used an adaptive technique assuming that the heat flux would flow outwards from the Sun strahl through the magnetic field lines either parallel or antiparallel to the interplanetary magnetic field direction. The electron direction relative to the magnetic field displays a real polarity even as the local field lines folded back on themselves. The new technique allowed scientists to identify true and false sector boundaries. By using low energy solar wind electrons heat flux, Crooker et al. (1996) tested 2 days of October 1978 of ISEE data, encountering 14 reversals of the magnetic field lines, and proposed predictions for the directions of heat flux and the magnetic field scheme (Figure 1.23).

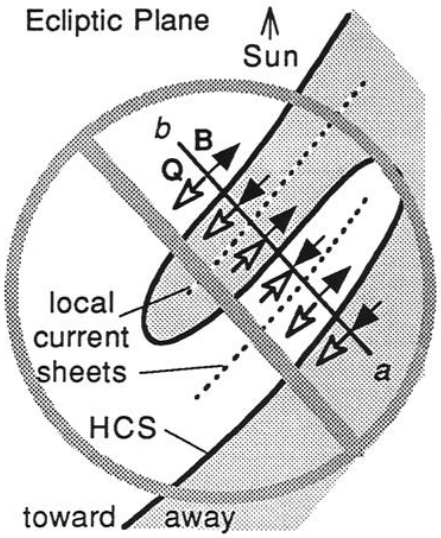

Figure 1.23 An ecliptic cross section illustrating the electrons heat flux- magnetic field relation with the local and global current sheet (HCS). It shows the magnetic field B direction (solid-headed arrows) and the electron heat flux Q direction (open- handed arrows) during a spacecraft passage through a folded HCS (from a to b) which separate an inward sector on the left from outward sector on the right, indicated by shading. The HCS is folded back on itself in a limited region (local). Across the HCS, the sign of Q.B changes but remains the same across the local region where both Q and B change sign. Adapted from Crooker et al. (1996) (Crooker, 1999)

Crooker et al. (1996) proposed a flux tube structure wrapped around another such structure. Due to these structures, a pocket of local reversed polarities occurs. The false polarity pockets can be created through this occurrence (Figure 1.24).

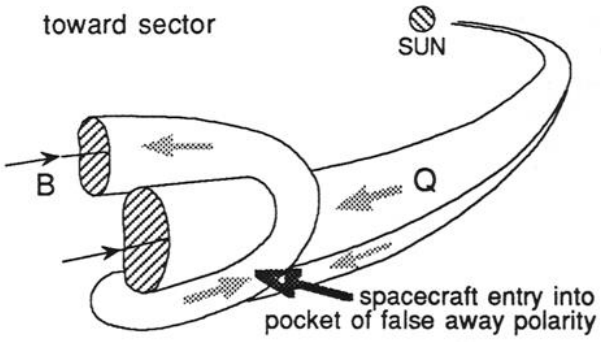

Figure 1.24 A schematic diagram intended to interpret the directions of the magnetic field lines and the heat flux along the passage of the spacecraft through the folded heliospheric current sheet. A pocket of locally flipped polarity is produced as a result of the flux tube wrapping around another. Adapted from Crooker et al. (1996) (Crooker, 1999)

The solar wind heat flux electrons pitch angle distributions have been used to identify the magnetic polarities of IMF around the HCS (Kahler *et al*., 2003). By using suprathermal electron pitch angles (3DP wind) with energies of > ~ 80 eV, solar wind ion and magnetic field data, and analysing eight cases of inversions during nine successive solar rotation for the period of Dec 1994-Aug 1995, Crooker *et al.* (2004b) discovered mismatches between sector boundaries identified by both sets of data. Many sector boundaries without magnetic field azimuth angle (ϕ_B) reversals have been found. The mismatched intervals are attributed to the local magnetic fields inversions during their travel through the sector boundary location. This signature is consistent with the passage of coronal stream belt loops which are magnetically

opened by the interchange reconnection released by one of the two loop legs from the Sun, and the polarity of each of the two legs matches the SB structure. The details of the interchange reconnection process are discussing in the section 1.9.10. Figure 1.25 displays an example of the sector boundary not always fitting with the Winterhalter *et al.* (1994) HPS definition and coinciding with the HCS.

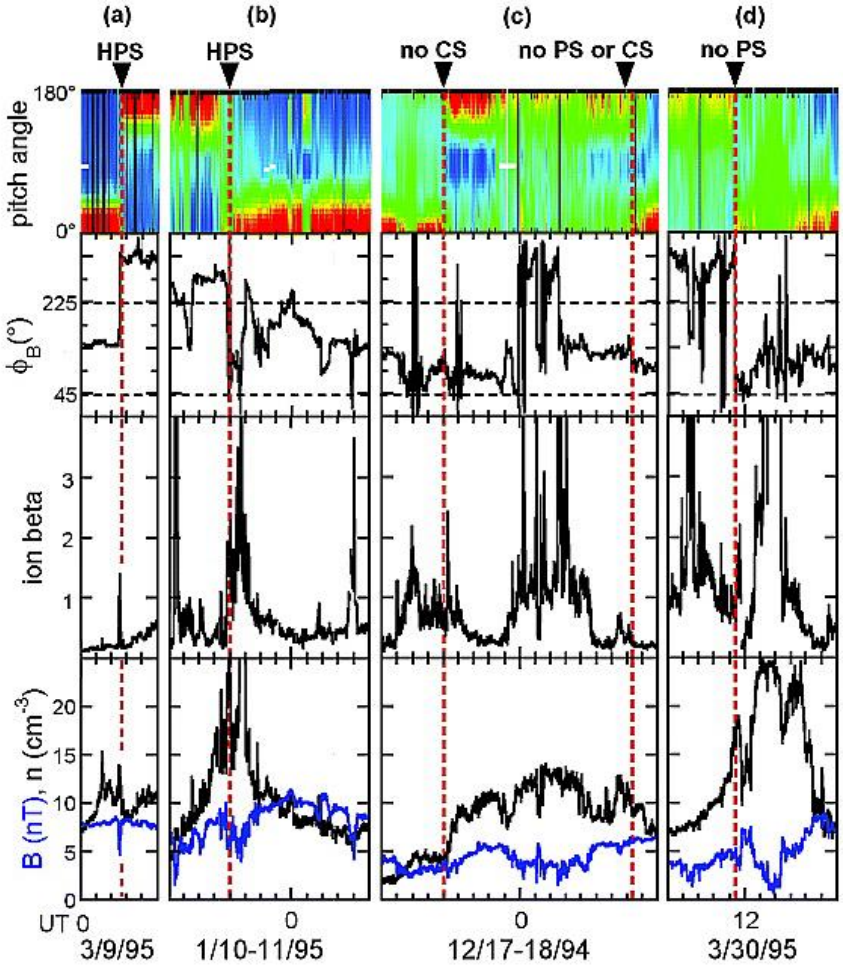

Figure 1.25 Diagram showing the time variations of 92s values of suprathermal electrons (3DP Wind) 320 eV pitch angle distribution (first panel), SWE Wind azimuthal magnetic field ϕ_B in GSE coordinate (second panel), ion beta (third panel) and proton density n and magnetic field magnitude B in the last panel. The sector boundary crossing CS is identified by the red dashed lines depending on the electrons heat flux reveals in case: (a) there was HPS, HCS and Sector boundary crossing matching. The HPS defined by the coincidence of sector boundary, high plasma beta and ϕ_B reversal (HCS). (b) a HPS-sector boundary matching with a complicated HCS. (c) a sector boundary without HCS and a sector boundary without HCS and HPS. (d) a sector boundary with a HCS but no HPS. (Crooker et al., 2004a)

Owens *et al.* (2013) have proposed five possible heliospheric magnetic field configurations and corresponding sector boundary crossings and heliospheric current sheet relative positions (Figure 1.26). These new categories clarify the relationship between the suprathermal electron pitch angle distributions and the interplanetary azimuthal magnetic field B_ϕ and explain how the SB-HCS mismatch is caused as a result of the local magnetic fields, which turn back over themselves during their way to the sector boundary.

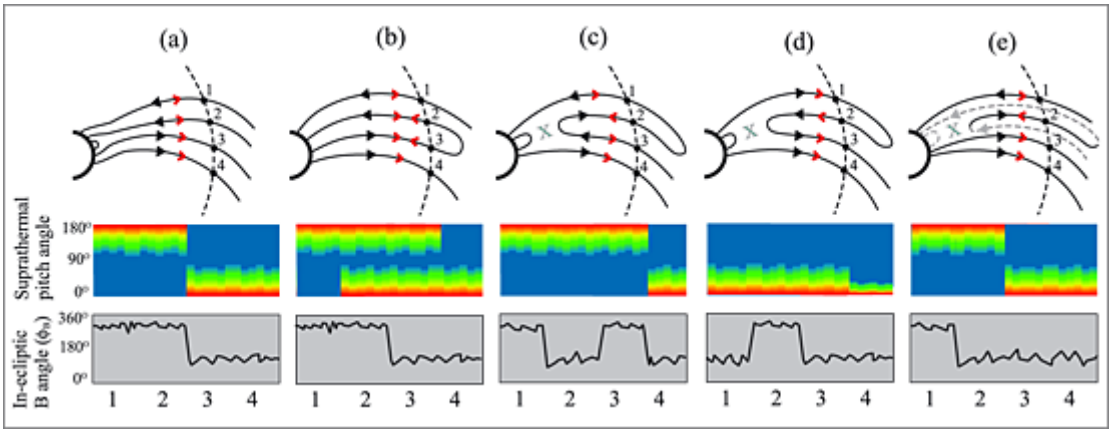

Figure 1.26 Five types of configurations of HCS and SBC. (a) the ideal configuration with HCS-SBC matching. (b) ideal HCS with a SBC amongst a double streaming electrons period (HCS-SBC mismatching). (c) a local magnetic field has turned back on itself (mismatching and matching). (d) a HCS without SBC and a local magnetic field flipped back on itself. (e) HCS-SBC mismatching because of the interchange reconnection near the sun. (Owens et al., 2013)

1.9 Interplanetary Coronal Mass Ejections (ICMEs)

1.9.1 ICME structure

Interplanetary coronal mass ejections (ICMEs) are interplanetary manifestations of coronal mass ejections (Zurbuchen and Richardson, 2006). They are large-scale interplanetary magnetic structures which propagate through interplanetary space and sometimes impact on Earth (Richardson and Cane, 2010). The main substructure of the ICME is the magnetic cloud (MC). So, Some ICMEs are called magnetic clouds (details in section 1.9.3). During their movement from the Sun, MCs move through the interplanetary medium, and when they are fast enough (being faster than the surrounding solar wind), plasma and magnetic field accumulates at their front boundary, forming high magnetic strength, speed and temperature fronts called shocks, which are identified by *in situ* observations as a sudden increase in magnetic field, proton temperature, density and speed. The separated turbulent region between the front shock and the MC is called the Sheath (Gosling, 1990). It is a compressed, dense and heated solar wind region compared with the MC and the ambient solar wind (Mitsakou and Moussas, 2014), and contains large amplitude fluctuations of the magnetic field, which often contains a high southward *Bz* magnetic field component that can affect the Earth's magnetosphere (Tsurutani and Gonzalez, 1997;Gonzalez et al., 2002). When the ICME has a shock it is called an ICME-driven shock (Wimmer-Schweingruber et al., 2006) (Figure 1.27).

Propagating fast shocks in the interplanetary space are divided with respect to the ambient solar wind frame of reference to forward shock that propagate toward the encountered slower solar wind, and reverse shock propagate back into the following solar wind. During the ICME propagation, deformations in the shock surface can arise both from asymmetries in the ICME's internal structure and in the ambient solar wind into which the ICME propagates. Many studies suggest that shocks can be observed over about 90 degrees in longitude from the position of solar energetic events compared with up to about 50 degrees for related ICMEs(Richardson and Cane, 1993).

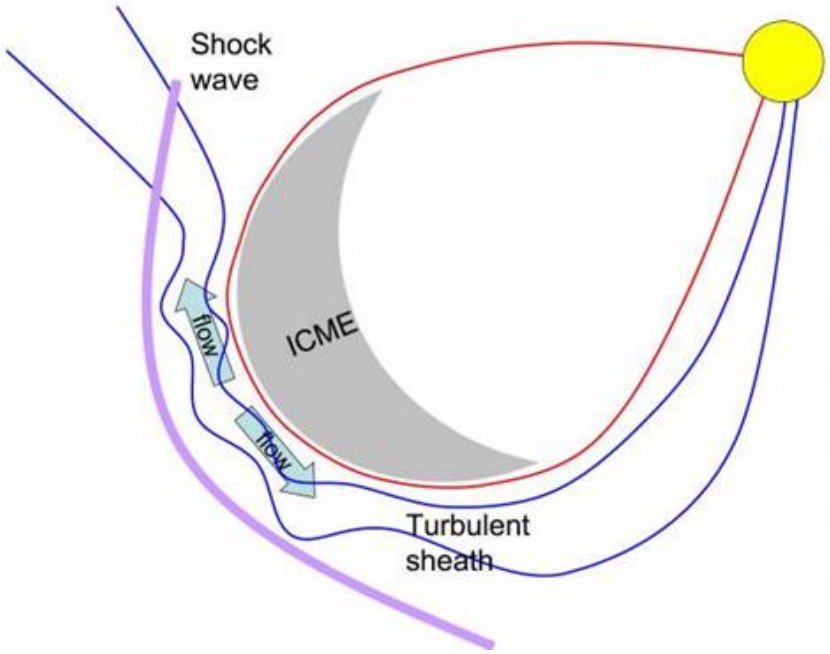

Figure 1.27 Schematic of an ICME, turbulent sheath region and an ICME- driven shock (after Liu et al. (2006)

In situ instruments on spacecraft that measure the solar wind identify ICME shocks by recording a sudden rise in plasma magnetic field, speed, temperature and density. The earliest remote measurement of a shock in the corona is a metric type II radio burst (Nelson and Melrose, 1985), which is thought to occur due to the acceleration of the non-thermal electrons by the plasma emission mechanism at the front of the shock (Gopalswamy, 2009a). Energetic particles are another feature of interplanetary shocks (Wild and Smerd, 1972). Ion and electron acceleration at the ICME-driven shock leads to the emission of energetic particles (Kahler et al., 1978). ICMEs also interact with the ambient solar wind, therefore the identification of ICME boundaries 'has been highly subjective and controversial' (Gopalswamy, 2006). It is difficult for the spacecraft to detect the sheath region (Zhang and Burlaga, 1988), but there is a higher chance of detecting the shock wave because it occupies a larger spatial region than the magnetic cloud (MC) (Schwenn, 2006).

As the ICME propagates itself through interplanetary space, many of its internal characteristics and configurations change and extend. This means that is signatures are not always noticeable in all events (Gopalswamy, 2006). One of the parameters which remains the same is the charge state or ionization level, which stays high inside the MC (Rodriguez et al., 2004). It can be used to identify the ICME in the Heliosphere by using a sum of properties related to its temperature, velocity, magnetic field and density.

1.9.2 ICME *in situ* signatures and parameters

The term Magnetic cloud was first suggested by Morrison (1954), and is used to refer to the magnetic field and plasma ejections from the Sun (Klein and Burlaga, 1982). It is a substructure of the ICME (Richardson and Cane, 2010). Using multi-spacecraft observations, Burlaga *et al.* (1981) confirmed the distinct substructure of a MC, which follows a turbulent region behind a front shock wave. They defined the MC as a solar wind structure with a coherent smooth magnetic field direction rotation and a high magnetic field magnitude in

comparison with the ambient background (Figure 1.28). This signature is associated with a low proton temperature and is displayed over a time interval of about 24 hours. At the orbit of the Earth, the MC characteristically displays a magnetic field magnitude enhancement (>10 nT) and a radial size of about (0.25) AU, while the direction rotates smoothly during a large angle (Klein and Burlaga, 1982). However, these measurements are not detected in all ICMEs (Richardson and Cane, 2010). One of the most important changes in the MC is the rapid decrease in plasma pressure with solar distance. This process means that the flux rope will be driven into radial expansion (Démoulin and Dasso, 2009).

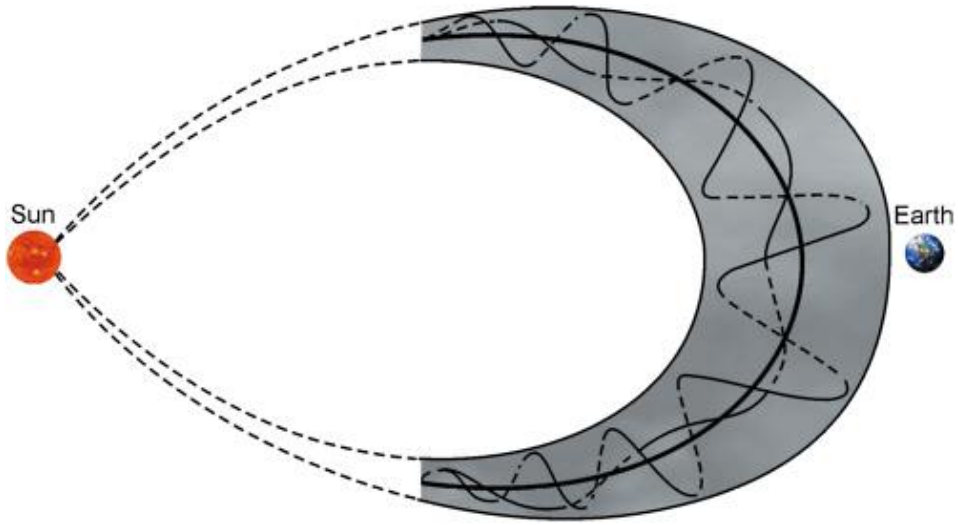

Figure 1.28 The idealized view of the proposed MC magnetic field line geometry on a global scale based on the Lundquist (1950) solution and the global configuration sketch of a MC and four spacecraft (Helios A and B, IMP8 and Voyager 2) where the in situ measurements have been taken from them (Burlaga et al., 1990). Modified with permission from L. Burlaga, Global configuration of a magnetic cloud, pp. 373-377 in Physics of Magnetic Flux Ropes, *Geophysical Monograph 58, C.T. Russell, E.R. Priest, and L.C. Lee, eds., American Geophysical Union, Washington, D.C., 1990 by"3 Formation of Structures and Transients" National Research Council.*

On average, MCs account for about 30% of ICMEs (Wu and Lepping, 2011). Du et al. (2010), however, found that about 43% of ICMEs were MCs. This percentage is not constant, but changes with the sunspot cycles, from about 15% at solar maximum to about 100% at solar minimum (Kilpua *et al.*, 2012).

The solar wind possesses complex structures of plasma and magnetic field. In order to detect ICMEs, scientists use many practical criteria, such as plasma beta, which displays the ratio of the solar wind thermal pressure to its magnetic pressure, forming a scale of domination in the solar atmosphere and heliosphere.

The magnetic pressure P_B is calculated using the magnetic field transverse to its direction:

$$P_B = \frac{B^2(Tesla)}{2\mu o} \tag{1.19}$$

Where B is the magnetic field magnitude, and μ_o is the permeability of free space (4π x 10^{-7} NA^{-2}).
Thermal pressure P_{th} is generated by the hot coronal plasma owing to thermal motion of its particles:

$$P_{th} = NkT \tag{1.20}$$

Where N is the particle number density, k is Boltzmann constant (1.38065 x 10^{-23} JK^{-1}), and T is the temperature.
P_{th} and P_B become equal for B:

$$B = [(2\mu_o k)\ NT]^{1/2} \tag{1.21}$$

The value of Plasma β in the solar atmosphere varies from greater than 1(β>1) in the lower region (photosphere), to less than 1(β<<1) in the mid Corona, and β>1 in the upper region of Corona. Within MCs, the magnetic pressure is typically high which dominates this region and that leads them to have a low plasma (>1) compared with the ambient solar wind where β is relatively high. Figure 1.29 shows a plasma beta model over an active region and illustrates β as a function of height. The gas pressure here dominates the magnetic pressure in the photosphere and upper corona.

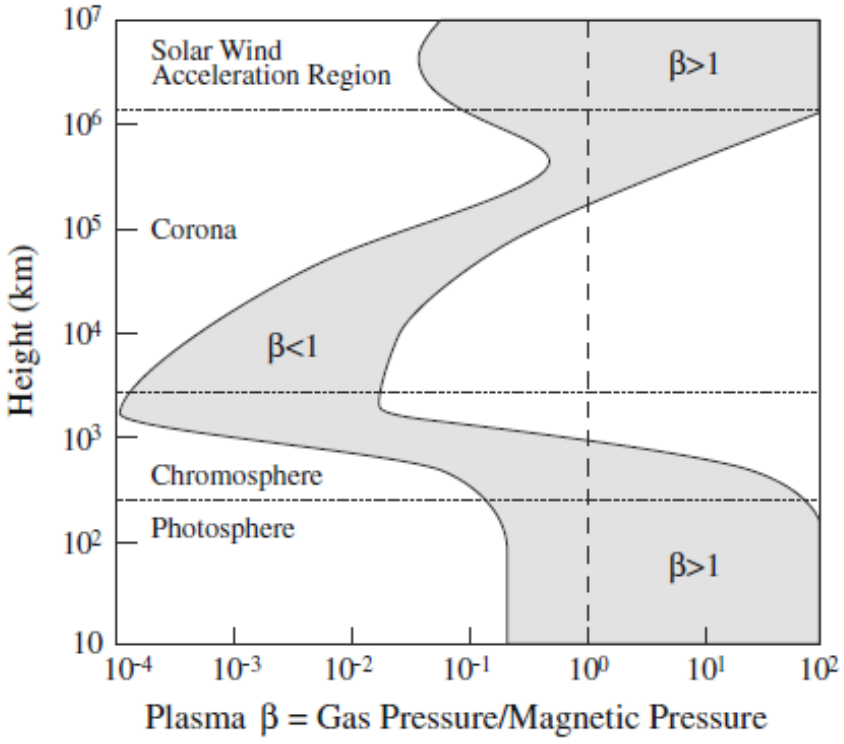

Figure 1.29 A plasma beta model of the solar atmosphere for the assumed field magnitudes of between 100 G and 2500 G (grey area). Adapted from (Gary, 2001), taken from (Lang, 2013).

Similarly, lower temperatures are recorded in MCs than in the ambient solar wind, due to their expansion through the interplanetary medium (Richardson and Cane, 1995;Cane and

Richardson, 2003). An unusually low proton temperature during anomalous solar wind intervals has been recorded by Gosling *et al.* (1973). This phenomenon has been linked to interplanetary MCs by Richardson and Cane (1995) based on an empirical correlation that was computed between the solar wind speed and its proton temperature (Lopez, 1987). They concluded that $T_p < 0.5\,T_{\rm ex}$ can be considered as a criterion to identify these interplanetary ejecta, where T_{ex} is the expected proton temperature obtained from Lopez (1987), with the empirical correlation computed based on two solar wind velocities:

$$T_{ex}\,(\mathrm{K}) = \begin{cases} (0.031\,V_{\rm SW} - 5.1)^2 \times 10^3, & V_{\rm SW} < 500\ \mathrm{Km/s} \\ (0.51\,V_{\rm SW} - 142) \times 10^3, & V_{\rm SW} \geq 500\ \mathrm{Km/s} \end{cases}$$

Although the ICME temperature reduction and $T_p < 0.5\,T_{ex}$ ration are different in MC and non-MC ejecta, and during ICME-ICME interaction, the authors still use it as one of the main reliable *in situ* signatures for ICMEs (Zurbuchen and Richardson, 2006). The ICME propagation and evolution through interplanetary space are significantly dependent on its ejecta velocity. The individual MC speed plasma morphology often displays steady decelerations in accordance with its expansion ranges, taking into consideration that not all MCs appear to have an expansion signature. This behavior is changeable when MCs are associated with corotating interaction regions and a coronal high-speed stream.

In spite of the radial reduction in the density of the solar wind ions, the relative abundance of helium remains constant throughout a large distance of the heliosphere (Von Steiger and Richardson, 2006). It has been put forth that helium abundance is the best signature with which to track an ICME in interplanetary space. The He^{+2}/H^{+} ratio is one of the most utilized and reliable ICME composition signatures which reflects the enhanced alpha particles to proton ratio. The typical ICME N_α/N_p is about > 8% (Borrini *et al.*, 1982).

Table 1.2 provides a summary of *in situ* ICME signatures at 1 AU. ICMEs have many distinct characteristics, but they have no one unique set of properties. Just a few ICMEs have all the listed characteristics (Richardson and Cane, 2010). Figure 1.30 shows a sample event of ICME magnetic and solar wind morphologies:

Signature	Description	Selected reference
B1: B Rotation	$>>30^{\circ}$, smooth	Klein and Burlaga (1982)
B2: B Enhancement	> 10 nT	Hirshberg and Colburn (1969); Klein and Burlaga (1982)
B3: B Variance decease		Pudovkin et al. (1979); Klein and Burlaga (1982)
B4: Discontinuity at ICME boundaries		Janoo et al. (1998)
B5: Field line draping around ICME		(Gosling and McComas, 1987); (McComas et al., 1989)
B6: Magnetic clouds	(B1, B2 and $\beta=\frac{\sum nkT}{B^2/(2\mu_0)} <1$)	(Klein and Burlaga, 1982); (Lepping et al., 1990)
P1: Declining velocity profile/expansion	Monotonic decrease	(Klein and Burlaga, 1982); (Russell and Shinde, 2003)
P2: Extreme density decrease	≤ 1 cm^{-3}	(Richardson et al., 2000)
P3: Proton temperature decrease	$T_p < 0.5\, T_{\exp}$	(Gosling et al., 1973);(Richardson and Cane, 1995)
P4: Electron temperature decrease	$T_e < 6$ x 10^4 K	(Montgomery et al., 1974)
P5: Electron temperature increase	$T_e >> T_p$	(Sittler and Burlaga, 1998); (Richardson et al., 1997)
P6: Upstream forward shock/" Bow Wave"	Rankine-Hugoniot relations	(Parker, 1961)
C1: Enhanced α/proton ratio	$He^{2+}/H^{+} > 8\%$	(Hirshberg et al., 1972); (Borrini et al., 1982)
C2: Elevated oxygen charge states	$O^{7+}/O^{6+} > 1$	(Henke et al., 2001); (Zurbuchen et al., 2003)
C3: Unusually high Fe charge	$\langle Q \rangle_{Fe} > 12$; $Q_{Fe^{>15+}} > 0.01$	(Bame et al., 1979); (Lepri et al., 2001); (Lepri and Zurbuchen, 2004)
C4: Occurrence of He^{+}	$He^{+}/\ He^{2+} > 0.01$	(Schwenn et al., 1980); (Gasling et al., 1980); (Gloeckler et al., 1999)
C5: Enhancements of Fe/O	$\frac{(Fe/O)_{CME}}{(Fe/O)_{photosphere}} > 5$	(Ipavich et al., 1986)
C6: Unusually high $^3He/^4$ He	$\frac{(^3He/^4He)_{CME}}{(^3He/^4He)_{photosphere}} > 2$	(Ho et al., 2000)
W1: Ion acoustic waves		(Fainberg et al., 1996); (Lin et al., 1999)
S1: Bidirectional strahl electrons		(Gosling et al., 1987)
S2: Bidirectional ~ MeV ions	2nd harmonic > 1st harmonic	(Palmer et al., 1978); (Marsden et al., 1987)
S3: Cosmic ray depletion	Few % at ~ 1GeV	(Forbush, 1937); (Cane, 2000)
S4: Bidirectional cosmic rays	2nd harmonic > 1st harmonic	(Richardson et al., 2000)

Table 1.2 Summary of ICME properties at 1 AU. Adapted from (Zurbuchen and Richardson, 2006)

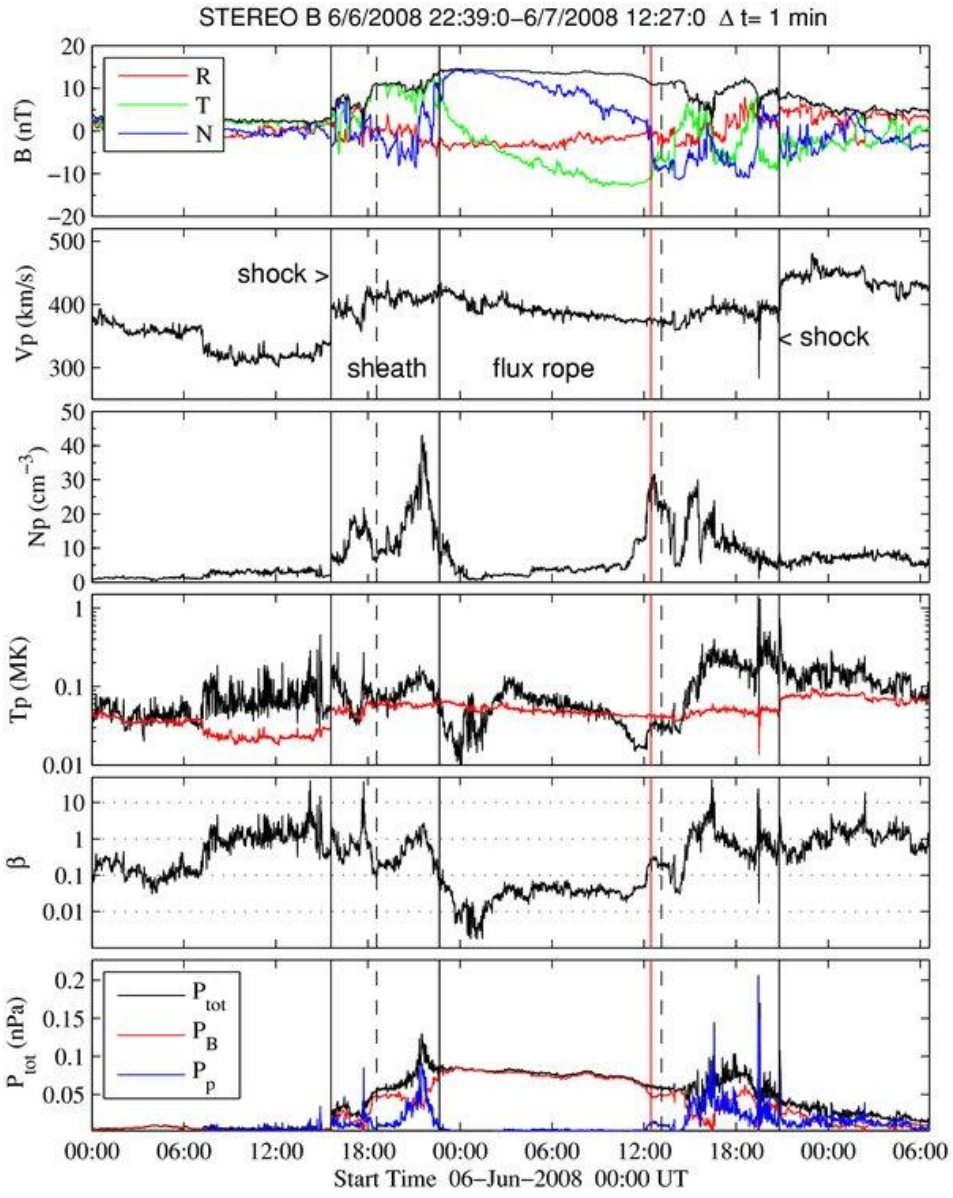

Figure 1.30 A standard ICME-driven shock recorded by STEREO B. The panels display: the magnetic field strength with RTN components, proton speed, proton density, proton temperature, plasma beta and total perpendicular pressure. The ICME consists of the forward shock, sheath, MC flux rope and reverse shock (Möstl et al., 2009).

1.9.3 ICME, Ejecta and the Magnetic cloud (MC)

During the last 40 years, ICME had various names such as, ejecta, piston, and driver gas (Richardson and Cane, 2010). Burlaga *et al.* (1981) defined an ICME possessing a flux rope as a magnetic cloud (MC). During the passage of a spacecraft into the inner regions of the ICME, all plasma and magnetic field parameters experience significant changes, including plasma temperature, velocity and density. Also, the characteristic magnetic field magnitude and direction will manifest differently depending on the spacecraft's trajectory within the ICME. This trajectory has six general scenarios (Gopalswamy, 2006) as is shown in Figure 1.31:

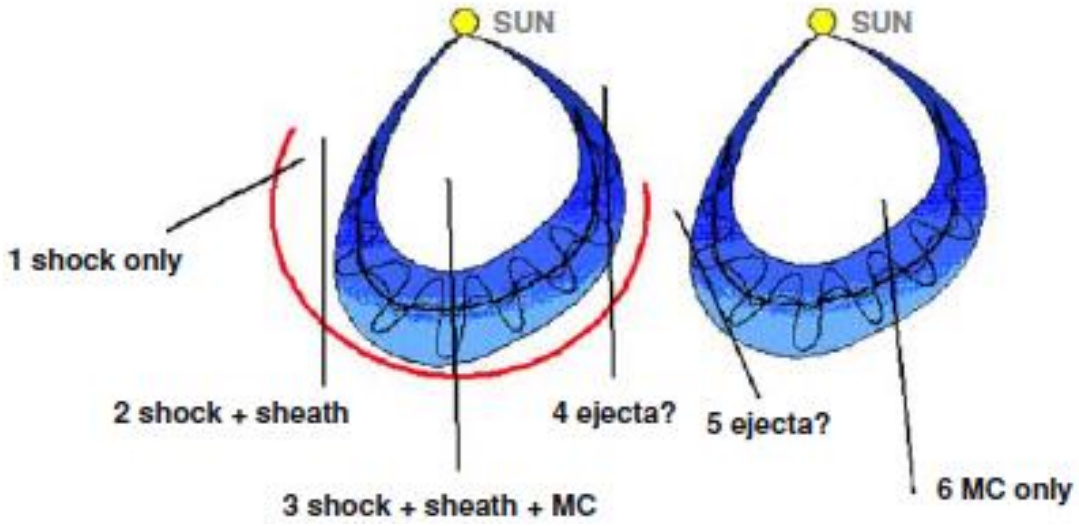

Figure 1.31 Illustrates the six general tracks of a spacecraft through an ICME. The six tracks are divided into two possibilities: ICME with a shock, sheath, and MC (left), and ICME with only a MC (right).(Gopalswamy, 2006)

Track 1: the spacecraft traverses the ICME only through the shock.
Track 2: the spacecraft pass through the shock and the sheath of the ICME (track 1 and 2 never encounter the nose of the ICME).
Track 3: the spacecraft passes through the shock, the sheath and the MC.
Track 4: the spacecraft trajectory travels the path of shock+ sheath+ ejecta (the flank of the MC where there is no flux rope).
Track 5 and 6: the trajectories are similar to 4 and 3 respectively, but without shock and sheath.
According to the above scenarios, the passage trajectory of the spacecraft decides the appearance of the flux rope. One of the most significant questions is how to explain the relationship between MC and ejecta. The answer can be determined by the spacecraft's trajectory scenario in Figure 1.32 .

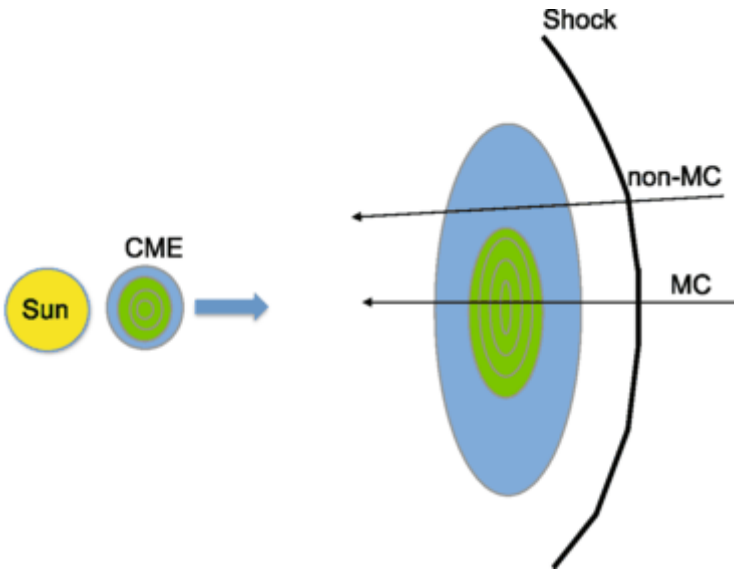

Figure 1.32 Schematic illustration of a spacecraft travelling through an ICME (Riley and Richardson, 2013).

The Riley and Richardson (2013) scenario depicted in Figure 1.32 suggests that all ICMEs have a magnetic cloud (the flux rope region), which is embedded inside the huge ejecta. When the spacecraft passes sufficiently close to the flux rope region, the MC can be observed. By assuming a flux rope launched in a heliographic equator with a cross section as illustrated in Figure 1.32, it can be expected that the spacecraft will intercept the MC over a wide range of longitudes (magnetic field rotation) but confined to near-equatorial latitudes. On the other hand, when the spacecraft trajectory occurs at higher latitude, it will pass through the shock, the sheath and finally the ejecta, and there is no magnetic field rotation because of the absence of the flux rope in this area. ICMEs can be classified into three classes according to their plasma properties and magnetic field signatures (Al-Haddad et al., 2013):

1- Magnetic cloud (MC): has a high magnetic field magnitude with a smooth rotation, low proton temperature (Burlaga *et al.*, 1981) and low plasma beta.
2- Ejecta or Magnetic Cloud-like: its typical magnetic field is less than that of the MC, and sometimes it is weak and has little smooth rotation. This type has been noticed during spacecraft passage through the legs of the ICME, where the magnetic field configuration is different than that of the MC (weak strength and little rotation) (Zhang et al., 2007;Marubashi and Lepping, 2007). Möstl *et al.* (2010) confirmed this fact with STEREO observations. The proton thermal velocity of the ejecta is higher than of the MC and lower than that of the shock (Lepping et al., 2006).
3- Complex ejecta: this type of ejecta results from the interaction of successive coronal mass ejections (Burlaga *et al.,* 2002). 'The relationship of MCs to ICMEs (ICMEs-drive shocks) is still an open issue in space research' (Kilpua *et al*., 2013). In their *in-situ* regions, only about one-third of MC signatures can be detected during ICME events.

1.9.4 Magnetic Clouds MCs and Flux Rope

The absence of a MC signature due to spacecraft trajectory has been studied by using multiple spacecraft observations (Kilpua *et al.*, 2011). Most of the previous remote and *in situ* analysis of CME has sparked debate on whether all CMEs have a flux rope or not. Gosling (1990) concludes that in an *in situ* region about 30% of interplanetary coronal mass ejections have flux ropes. Marubashi (2000) estimates that about 80% of ICMEs have MCs, however this percentage decreases in the work of Li *et al.* (2011) to approximately 48%, about 33% with Richardson and Cane (2010) and about 40% with Vourlidas et al. (2013) .

In order to better understand the MC, Goldstein (1983) described the magnetic field in an MC by using a cylindric force free structure ($\nabla \times B = \alpha B$), where α is a function of position. In the case of the flux rope, Burlaga (1988) assumed that α is a constant depending on the Lundquist (1951) solution, meaning that the variable α indicates that there is an infinite number of possible configurations. This is currently the most respected model describing the cloud's magnetic field. Figure 1.33 illustrates the cylindrical MC force-free structure. The magnetic field has rolled up around itself in the magnetic cloud.

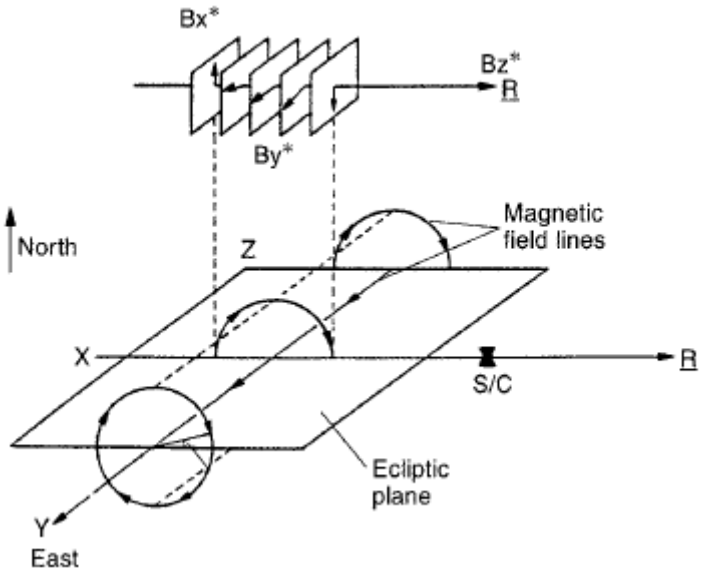

Figure 1.33 The force-free structure of the MC as proposed by Goldstein (1983), developed by Marubashi (1986) and adapted by Bothmer and Schwenn (1997). The MC sits with its axis in the equatorial plane and normal to the radial direction.

Due to counter streaming heating flux within the MCs, it has suggested that they have closed magnetic loops with two legs connected to the Sun. Because of solar rotation, the MC legs track the Parker spiral rotation. These basic facts led to the production of several MC models as an axial magnetic field extending from the Sun surface, propagated through interplanetary space and passing the Earth with a twisted toroidal magnetic field flux rope along its length. Several studies considered the MC to be the main part of the ICME. MC models were also developed based on force-free models and Burlaga's modification, such as is the case with Marubashi (1986) whose model depends on the previous model while neglecting α. Other researchers made different assumptions, including assuming a cylindrical symmetry to the MC (Burlaga *et al.,* 1990), self-similarly expanding cylindrical fitting (Marubashi and Lepping, 2007) and the elliptical model (Hidalgo *et al.*, 2002). Figure 1.34 shows different MC models. According to Démoulin (2013): 'So far, no model has been proven to best represent a large set of MCs'.

To understand the contrast between the different ICME types , the six tracks of Gopalswamy (2006) could be the key to understanding (Kim *et al*., 2013). However, the most important questions are whether all CMEs have a flux rope structure, and whether MC and ejecta have the same origin. It has been suggested that according to the post eruption arcades, they should have the same origin (Gopalswamy *et al.*, 2008). Ejecta observations of solar cycle 23 show a significant deflection, especially in the case of ejecta and MC which do not have a shock. In this case the ejecta and MC sources are close to the disk centre.

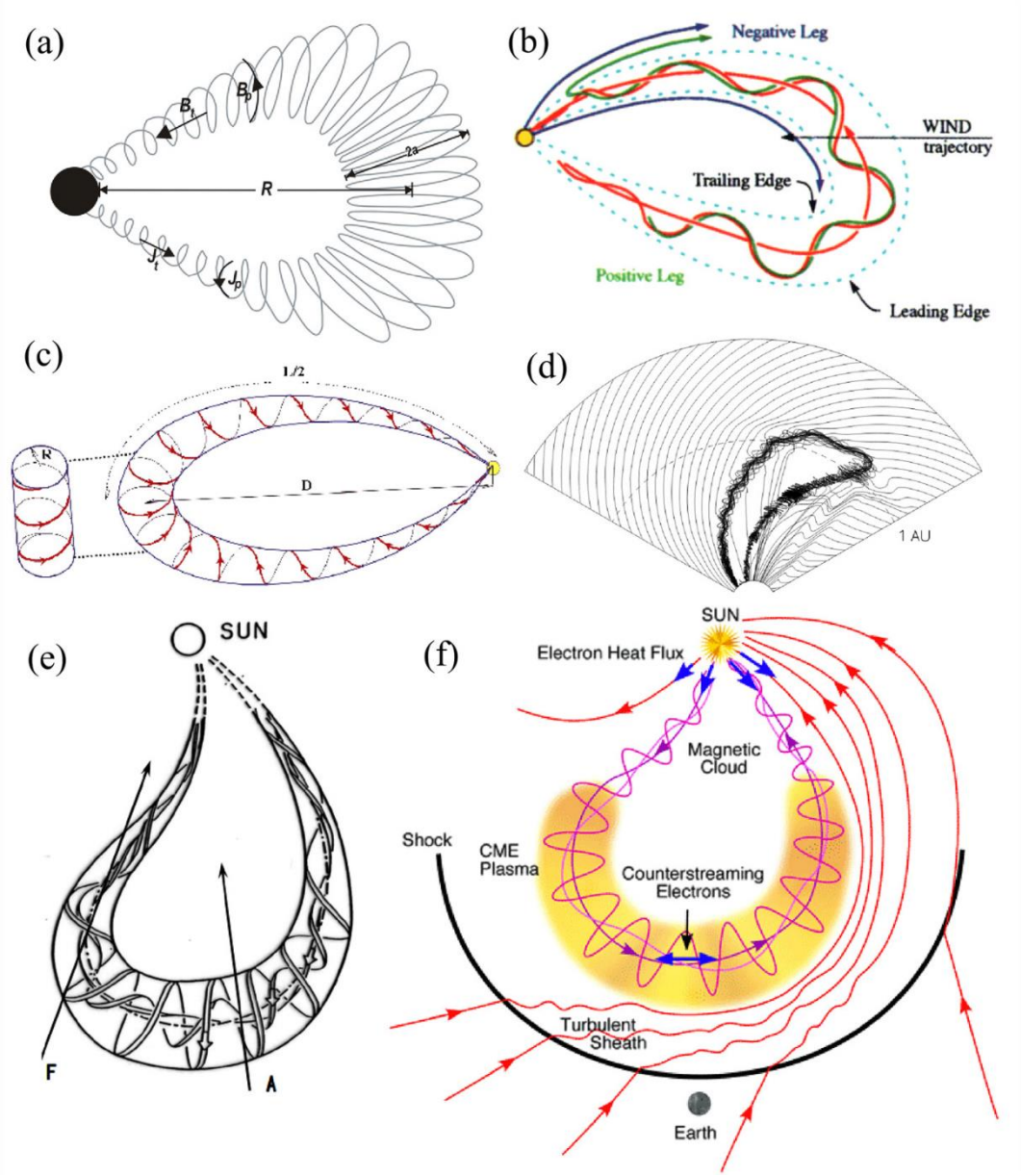

Figure 1.34 illustrates MC global structure models and sketches: (a) CME near-Sun structure from Subramanian et al. (2014) (b) partial open MC flux rope with constant α inferred from heat flux and energetic electrons from Larson et al. (1997) (c) in situ MC fitting model from Démoulin and Dasso (2009) (d) interplanetary flux rope numerical simulation from Vandas et al. (2002) (e) MCs global structure sketch from Marubashi and Lepping (2007) (f) MCs global structure cartoon from Zurbuchen and Richardson (2006). (Owens, 2016)

Another question is whether ejecta have the standard flux rope configuration initially near the Sun, and whether there is another solar large scale structural effect on them, which makes them drift from the Sun-Earth line. It has been proposed that this large structure could be coronal holes which are positioned between the centre of the CME and the Sun-Earth line (Gopalswamy *et al*., 2008). Mäkelä *et al*. (2013) found a coronal hole influence on 54 MC and non-MC associated with CMEs originating from locations between 15E- 15W on the solar disk. By using a coronal hole influence parameter which depended on the coronal hole average magnetic magnitude, area, and distance from the CME source position, they concluded that ejecta-associated CME tend to be deflected by nearby coronal holes. The deviation of the CME away from the disk centre and the small CME's angular width are the main reasons why

the spacecraft trajectory passes only through the ICME flank and misses the flux rope. This suggests that all CMEs have flux rope eruptions (Xie *et al.*, 2013). The Direction parameter (D) displays how much the CME propagation is directed towards Earth and computes the degree of the CME asymmetry (Moon et al., 2005;Kim et al., 2008). The deflection of the ejecta which accompany CMEs tends to be away from the disk centre whereas the deflection of MC tends towards the disk centre. Kim *et al.* (2013) proposed that 'all CMEs have a flux rope structure and the trajectory of the CME essentially decides the observed ICME structure'.

In a recent study, Owens (2016) found that the interplanetary twisted magnetic flux rope structure is restricted or trapped within the MC's leading edge, and its two legs which magnetically connect the flux rope with the solar surface are non-twisted rope legs. This may explain the lack of the flux rope structure in the MC legs when they pass through the spacecraft. The new feature of the MC and its two non-twisted rope legs is illustrated in Figure 1.35 .

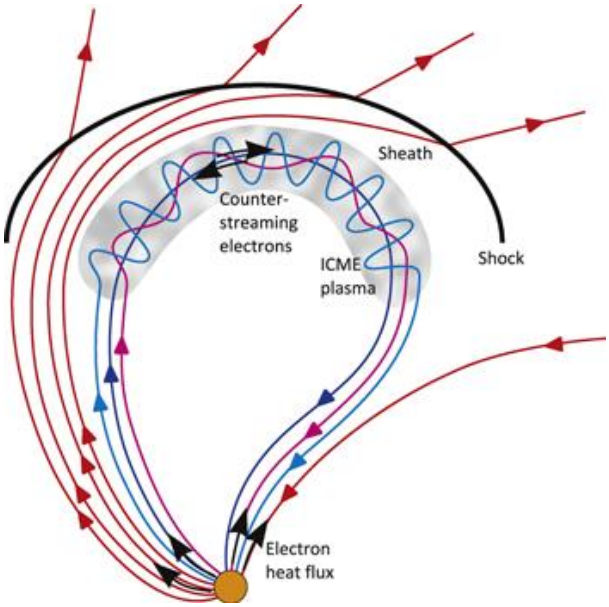

Figure 1.35 illustrates the Owens (2016) vision of the magnetic cloud flux rope. It is noticeable that the twisted flux rope is confined to the leading front (the grey cloud) and the untwisted MC legs connect the flux rope with the Sun. The black arrows refer to the heating flux electrons directions. The sketch is modified from Zurbuchen and Richardson (2006).

1.9.5 Flux rope categorisation and classification

In a study based on Helios 1,2 measurements of MCs in the inner heliosphere, Bothmer and Rust (1997) came up with a model of the magnetic configuration which classified MC structures and their magnetic helicity into four different categories based on the conception of the flux tube and the field lines orientations within the MCs. According to the leading and trailing north-south field polarities and east-west field polarities in the flux rope centre, the four flux ropes categories divided into SEN(SWN) types MC, where the magnetic field vector turns firstly from south(S) to east(E) (west(W)) in the MC axis, and finally to north(N) at the MC rear boundary, and vice-versa in the case of NES(NWS). The four MC configurations are shown in Figure 1.36 (upper panel). Two of these structures display right hand flux ropes and two left hand.

Mulligan *et al.* (1998) found that all MCs cannot be forced into these four classifications, so they proposed another four categories of MC with the same conventions and depending on the main axes as perpendicular to the ecliptic plane. These new structures are: WNE, ESW, ENW and WSE (Figure 1.36, lower panel). All these new configurations start with the orientations E or W, since the rope turns from west to east or vice versa, with two right hand helicities and two left hand helicities also. In contrast to the previous four categories, the B_Z component does not change its signal. Based on the north-south component, the MCs have been divided into bipolar, which means that B_Z changes its sign within the MC rotation, and unipolar, which means that B_Z maintains its sign (Mulligan *et al.*, 1998). Both reflect the flux rope axis tilt with respect to the ecliptic plane.

Magnetic Cloud Type	 SEN	 SWN	 NES	 NWS
Leading Field	South (-Bz)	South (-Bz)	North (+Bz)	North (+Bz)
Axial Field	East (+By)	West (-By)	East (+By)	West (-By)
Trailing Field	North (+Bz)	North (+Bz)	South (-Bz)	South (-Bz)
Helicity	LH	RH	RH	LH

Magnetic Cloud Type	 WNE	 ESW	 ENW	 WSE
Leading Field	West (-By)	East (+By)	East (+By)	West (-By)
Axial Field	North (+Bz)	South (-Bz)	North (+Bz)	South (-Bz)
Trailing Field	East (+By)	West (-By)	West (-By)	East (+By)
Helicity	RH	RH	LH	LH

Figure 1.36 Two tables showing schematics and labels of the eight MC categories (Mulligan et al., 1998) . The MC configurations and their helicity laying in the ecliptic plane are shown in the upper panel after Bothmer and Rust (1997). MC perpendicular to the ecliptic plane are shown in the lower panel after Zhao and Hoeksema (1996).

Bothmer and Schwenn (1994) determined that the sites of the solar prominences magnetic field structures are related to their associated magnetic flux ropes. From filaments polarities and orientations, it may be assumed that prominences have the four different types of flux ropes (SEN, SWN, NES and NWS) (Figure 1.37). For the three different MCs types that they observed (SEN, NES and SWN), four out of five prominences were associated with the MCs of the same flux rope type.

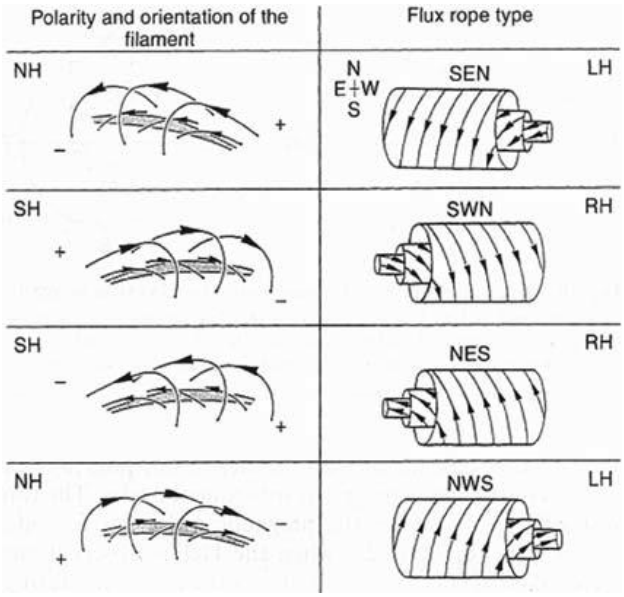

Figure 1.37 Magnetic field configuration sketches of prominences and the expected MC flux rope types (Bothmer and Schwenn, 1994)

Within MCs, the magnetic field rotation direction is found to be correlated with the solar cycle. Based on the Helios 1 and Helios 2 measurements for the period of 1974 to 1980 at distances between 0.3 to 1 AU, a study by Bothmer and Schwenn (1998) on MC flux ropes found that 74% of MCs display south to north rotations of the magnetic field vector. Their additional measurements for of prominence and sunspots bipolar regions revealed that MCs dominate with SN type rotation in odd cycles and NS type rotation in even cycles (Figure 1.38). These behaviours are due to their source regions which have a solar hemispheric dependence.

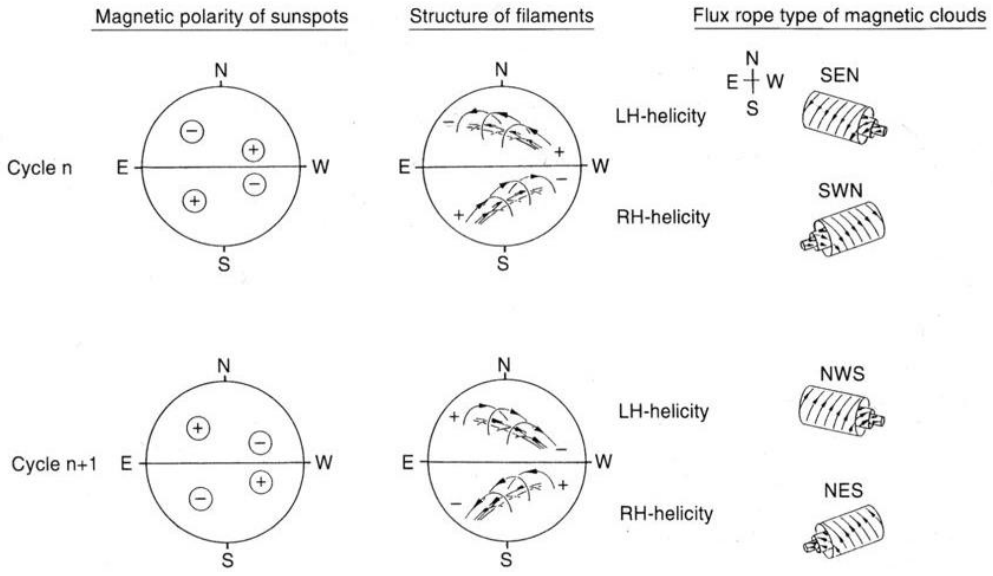

Figure 1.38 The solar cycle dependence of the filaments and the magnetic field structures of MCs. For simplicity, MCs flux ropes orientations are drawn with respect to the ecliptic plane. Adapted from Bothmer and Schwenn (1998) by Wimmer-Schweingruber et al. (2006).

1.9.6 ICME Multiple-Spacecraft Observations

Multi-point measurements of ICMEs show that each event has its own individual complicated evolution and configuration. Thus, there is no single simple model that can cover all ICME behaviours. This variety can be seen in the morphology of the ICMEs which have been observed (Kilpua *et al*., 2011). On the Sun, and also during the ICME propagation through interplanetary space, the erupting flux rope can develop an axial twist and interact with the ambient solar wind (Lynch *et al.*, 2009). The signature of this rope is difficult to detect, or becomes absent, as the spacecraft distance from the ICME centre increases. Multipoint ICME observations support this assertion. Multi-spacecraft observations aid in the interpretation of flux-rope structure and help scientists make progress in their research on the evolution of CME in the inner heliosphere (Kilpua *et al.*, 2011) .

The observations of the STEREO and L1 spacecraft allow for more accurate comprehension of ICME behaviours, and for more accurate identification of their boundaries, especially when STEREO is at a normal angle with the Earth. Over the last three decades, there have been many studies which depend on multi-spacecraft measurements.

In this section, a few of these multi-spacecraft studies in different decades are described in order to show their importance with regards to researching ICME properties and characteristics. Mulligan *et al.* (1999) present many ICME events, using WIND and Near-Earth Asteroid Rendezvous – Shoemaker (NEAR) spacecraft data for each event, with angular separations from 1.2° to 33.4° in longitudes and ∼ 1AU to 5.4 AU. They found that the ICME which were seen by WIND and NEAR have similar signatures when the separation angle of the spacecraft is about 1° in azimuth relative to the Sun. However, the vector signatures (at NEAR) begins to differ from those observed at WIND when NEAR is separated by about 5.4˚ in azimuth from the Earth even though the strength of the field and the background solar wind in the events display similarities at both spacecraft. By increasing the separation angle between them to 11.3°, the magnetic field signatures became more different, but the most significant thing was the magnetic helicity of the MC, which was the same at both spacecraft. Basing their research on other spacecraft measurements, Crooker and Intriligator (1996) examined a MC observed by the Interplanetary Monitoring Platform spacecraft IMP 6-8 near 1 AU and by Pioneer 11 which was located 4.8 AU away from the IMP spacecraft in Oct. 1974. They found that the MC had similar magnetic field signatures even though there was a huge separation between the two observations. On the other hand, they concluded that the cross-sectional length of the MC exceeded the radial width by about a factor of 8. This could be estimated because the longitudinal separation between the two spacecraft gave an approximation for the cross-sectional length of the MC. Mulligan and Russell (2001) used the observational data of the International Sun-Earth Explorer 3 spacecraft (ISEE3) and Pioneer Venus Orbiter (PVO) to study an ICME event in August 27, 1978. The angular separation between the two spacecraft was found to be 0.02 AU radially and 0.21 AU in longitude.

After 2006, the advent of STEREO resulted in many multi-spacecraft studies. Kilpua *et al.* (2009) studied many ICME events with the help of two L1 spacecraft (WIND and ACE), and STEREO during 19-23 May 2007. The separation between STEREO A and B at that time was 9˚. Romero-Hernandez and Gonzalez-Esparza (2013) studied the physical properties of five ICMEs

events as detected by five spacecrafts: Helios 1, Helios 2, IMP-8, Voyager 1 and Voyager 2 during the ascending phase of solar cycle 21 (November 1977- March 1978) (See Figure 1.39). Although the shock and the MC parameters show a significant dispersion around 1 AU, they found radial widths of MCs and their sheaths continued in their expansion at greater heliocentric distance, making the forward shock separate from its driver with a small Mach numbers (<2). Due to the ejecta expansion beyond 1 AU, the total pressure classification might not be useful at these distances.

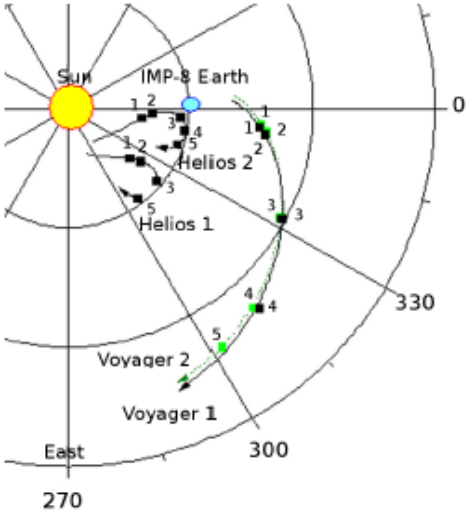

Figure 1.39 Trajectories of five spacecraft for the period of Nov. 1977 to Mar. 1978. Black squares represent the ICME events in each spacecraft (Romero-Hernandez and Gonzalez-Esparza, 2013).

Because of the huge dimensions of ICMEs and the lack of multipoint observations, the real three-dimensional configurations of ICMEs is still poorly understood (Kilpua *et al*., 2011). The successful identification of the *in-situ* ICME signature depends on the available data, in addition to the ICME occurrence and varying timespans of different events.

1.9.7 Total perpendicular pressure

Most ICME parameters (velocity, density, temperature, and magnetic field) cannot be used to uniquely identify the ICME occurrence, because any of these signatures could be missing. The total plasma pressure perpendicular to the magnetic field (Russell *et al.*, 2005) is a physical parameter which represents information from multiple components of the plasma, and can help identify the start and end of the ICME constituent parts. Both the plasma and the magnetic field of the solar wind bestow a pressure force perpendicular to the magnetic field direction, which cannot happen with the magnetic field alone because it exerts no pressure along its length (Jian *et al.*, 2005b).

Russell *et al.* (2005) define total perpendicular pressure (P_t) as the sum of the magnetic pressure and thermal pressure ($B^2/2\mu_\circ + nkT$). As stated in Figure 1.40, they have drawn a flux rope sketch as the magnetic obstacle to the flow in Spreiter *et al.* (1966) gas dynamic model of solar wind interaction with the Earth's magnetosphere.

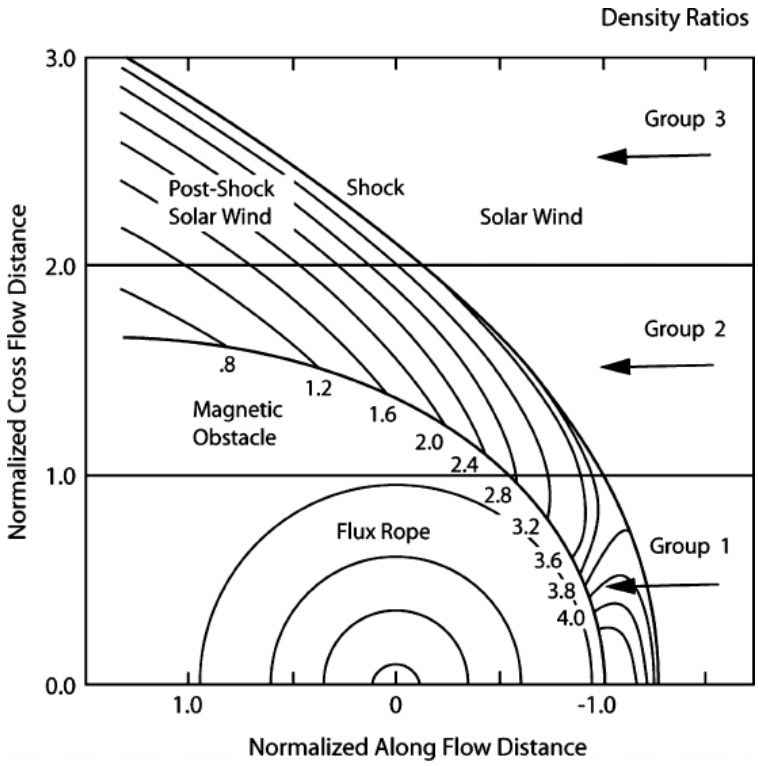

Figure 1.40 An illustration of the three groups of Pt profiles in terms of the trajectory of the space craft encounter the magnetic flux-rope depending on Spreiter et al. (1966) *gas dynamic simulation* results (Jian et al., 2006a).

Within the ICME, each solar wind parameter changes at a different way and at a different time. Regarding to the P_t behavior inside the ICME, the first measurements taken by the spacecraft show a sharp increase in the P_t during its traverse through the shock, followed by a slight gradient through the sheath. The most significant signature appears when the spacecraft enters the flux rope and crosses the centre of the ICME, where the P_t becomes high, and subsequently, decline corresponding with the flux-rope expansion. So, a sharp drop in P_t at the rear of the magnetic cloud and at the front expected to occur. The P_t profiles of ICMEs have been classified into three groups depending on the location of the spacecraft (obstacle) passage (Jian et al., 2005a;Russell et al., 2005;Jian et al., 2006b):

Group 1: agree with ICME events and the enhancement of P_t is in the middle of ejecta. That means the spacecraft penetrates the ICME from the nose (the centre of the flux-rope). Group 3: Corresponds to ICME events where the P_t rises rapidly and then decays gradually. This means that the spacecraft traverses the ICME from the flank or far away from the flux rope centre. Group 2: The spacecraft encounters the ICME near the magnetic obstacle. In this case, the ICME has a rapid increasing of P_t if it is preceded by a shock, with a pressure plateau and then returns to its low-pressure state.The following figures and text look in more detail at examples of each group.

Figure 1.41 shows an example of a group 1 standard ICME event (shock, sheath and flux-rope obstacle). It illustrates an ICME event observed by Wind on November 6-8, 2000. It shows a sharp P_t rise through the shock, followed by a roughly constant Pt (plateau) during the sheath.

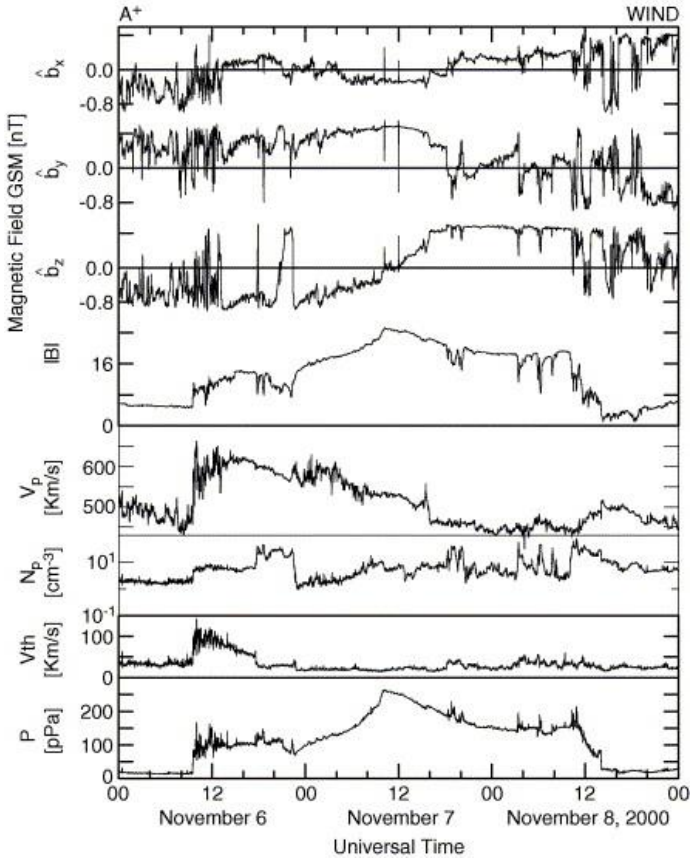

Figure 1.41 An example of group 1 ICMEs total pressure profile (lower panel) for the period of November 6-8, 2000, showing a central rise in total pressure.(Russell et al., 2005)

Next to the magneto- sheath P_t plateau, the spacecraft samples the slow smooth rotation region of the MC with an obvious P_t elevation because of the magnetic flux-rope. This increase continues until the spacecraft reaches the centre of the rope, after which the pressure begins to decline, and a second P_t plateau appears. Eventually, the total perpendicular pressure returns to its original state.

The total perpendicular pressure is not an indicator of where the spacecraft leaves the sheath and accesses and leaves the MC flux-rope. It simply identifies the place that is influenced by the ICME (Russell *et al.,* 2005). Group 1 is a standard ICME/magnetic flux-rope, consisting of a leading P_t jump at the shock, followed by a first pressure plateau in the sheath, and then an arise in the first half of the MC flux-rope, a central maximum peak due to part or full magnetic pressure being balanced by the curvature force. It is the same as in the Magnetosphere of the Earth, pursues by a reduction (second plateau) and ultimately a sharp drop at the rear. The P_t profile does not often display a central maximum, which means that the central region sometimes has a reasonably constant pressure or there is a maximum pressure at the end of the ICME, perhaps because of a compression of a stream overtake to the ICME rear region, making the flux rope continue to compress and expand after its central P_t maximum (Gosling *et al.*, 1994). It could also be due to the spacecraft passage through the ICME flank where the magnetic pressure is weak (maybe there are little twisted field lines in the rope), leading the plasma pressure to dominate the magnetic (dynamic) pressure. This type of event is categorised as Group 2. Figure 1.42 shows five examples of Group 2 events (Russell *et al*., 2005).

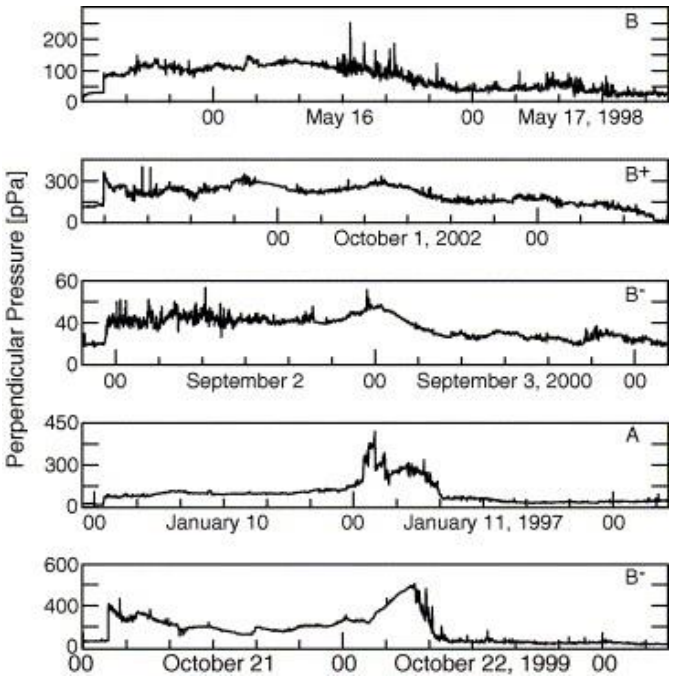

Figure 1.42 Total pressure profiles for five group 2 events, showing a central flat plateau of total pressure and an elevation toward the end of events. (Russell et al., 2005)

The last group (Group 3) is illustrated in Figure 1.43**.** This figure shows five events which show a rapid rise of pressure at the beginning, followed by a monotonic decay. The spacecraft crosses through just the shock front, leading the temperature and density to be elevated. The spacecraft is far away from the flux-rope and there is no magnetic obstacle behind this region. It is rarefied and cool, so P_t will decrease monotonically.

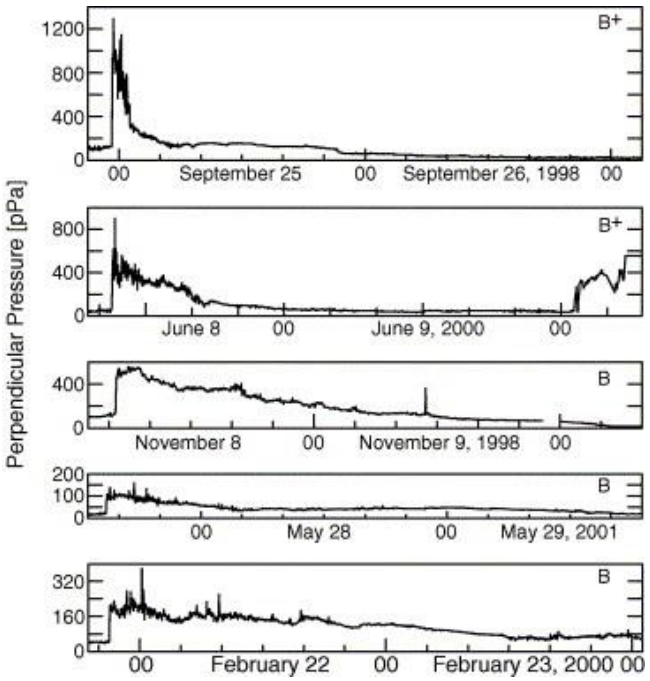

Figure 1.43 Total pressure morphology for five group 3 events. A monotonic decrease of pressure after the initial jump.(Russell et al., 2005)

1.9.8 Suprathermal electrons pitch angle distributions

Suprathermal electrons (>80 eV) are one of the most important indicators used to study ICME properties (Gosling *et al.*, 1987). They exist in a continual stream emitted from the Sun along the magnetic field lines which connect to the Sun by one or both ends. Their distribution indicates whether these magnetic field lines are open or closed (Crooker and Webb, 2006). The strahl, which are the anti-sunward heat flux electrons that typically travel away from the Sun either parallel or antiparallel to the interplanetary magnetic field direction (centred on 0˚ or 180˚ pitch angle) (Gosling, 1990) reveal the polarity of the interplanetary magnetic foot point connected to the Sun, regardless of the occurrence of any local magnetic field flipping or folding (Burlaga *et al.*, 1998) between the observation position and the Sun. Figure 1.44 illustrates the relationship between the interplanetary magnetic field and the strahl.

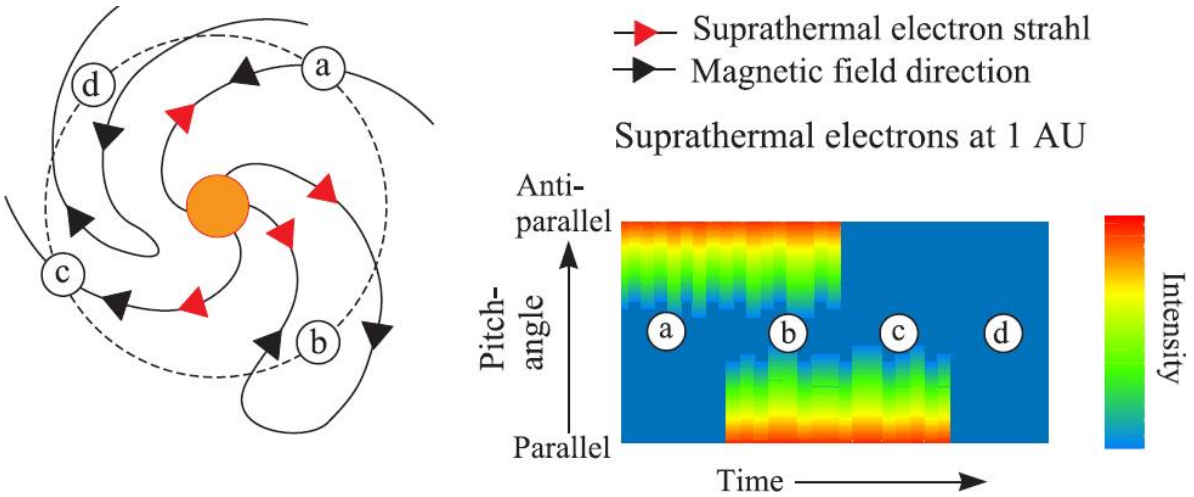

Figure 1.44 An illustration of the interplanetary magnetic configuration as inferred from heat flux electrons observations. Left side: the black arrows are the magnetic field lines as seen from an ecliptic plane and the red arrows are Sun outward heat flux electrons. Right side: the suprathermal electrons pitch angle distributions seen by a spacecraft at L1 position. At (a), the suprathermal electrons strahl is anti-parallel to the interplanetary magnetic field because the interplanetary field has a Sunward direction (part of an inward polarity sector). At (c), the strahl are parallel to the field direction because the field is part of an outward sector. At (b), the suprathermal electrons are parallel and anti-parallel to the field because the interplanetary field forms a closed loop and is connected to the sun at both ends. At (d), no strahl is seen because there is no connection with the sun at all. (Owens and Forsyth, 2013)

The suprathermal electrons stream is either unidirectional and distributed along open field lines or is a bidirectional electron (BDEs) stream (counter-streaming) which typically represents the signature of an ICME magnetic cloud having closed flux rope fields connected to the Sun at both ends (Gosling, 1990), (see Figure 1.45). While they are in interplanetary space, the solar wind electrons have two populations: a low energy, dense and thermal core (about 95% of the total electrons), as well as a hot and more tenuous suprathermal tail (Anderson et al., 2012;Kajdißc et al., 2013).

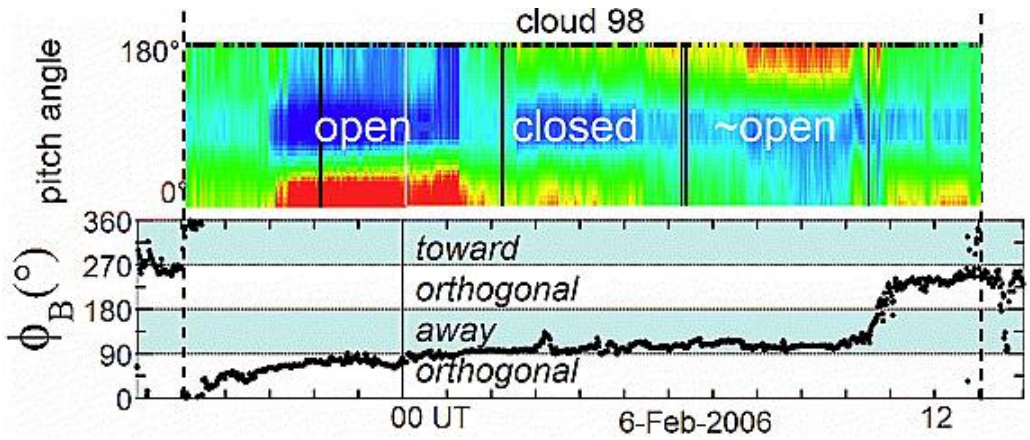

Figure 1.45 An example of the distribution of suprathermal electrons within a MC. Dashed vertical lines refer to the MC boundaries. It starts with unidirectional heat flux (upper panel) parallel (0˚) to the local field direction (lower panel). Bidirectional stream dominates in the middle, with an antiparallel (180˚) unidirectional stream at the rear. (Crooker et al., 2008)

The presence of counter-streaming electron distributions is the best indicator of closed interplanetary magnetic field lines (Figure 1.46), but they are not unique to ICMEs, nor are they a necessary signature for them (Anderson *et al.*, 2012). Sometimes the ICME have intermittent intervals of counter-streaming electrons, which means they have a mixture of open and closed magnetic field lines (e.g. (Shodhan et al., 2000;Crooker and Horbury, 2006)) or just open field (Rouillard et al., 2009). In addition, there are many other mechanisms that can be considered as sources of the bidirectional electron distributions, such as the Earth's bow shock connections (Feldman et al., 1982;Haggerty et al., 2000) and the connection with interplanetary shocks, whether ICME or SIR shocks (Steinberg et al., 2005). On the other hand, Gosling *et al.* (2001b); Gosling *et al.* (2002); Skoug *et al.* (2006) have referred to another bidirectional electron distribution which is caused by the depletion of the halo particles at around a 90˚ pitch angle.

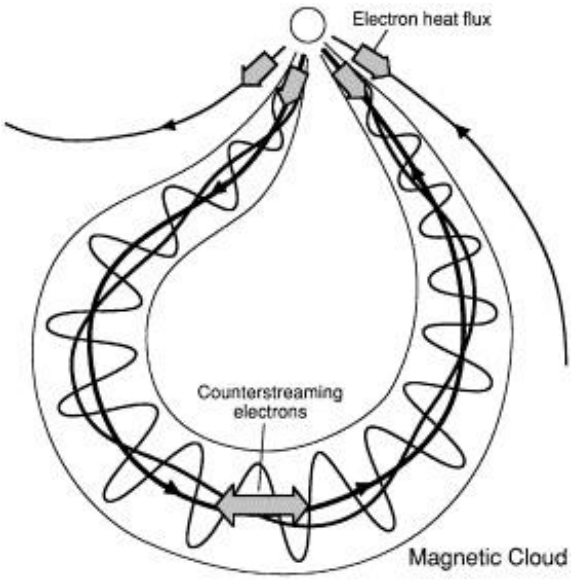

Figure 1.46 An interplanetary MC flux rope is connected the Sun by its both legs. Heat flux electrons (strahl) streaming away from the Sun (four grey wide arrows emerging from the Sun) along the magnetic field lines creates a bidirectional streaming (counter streaming) on the flux rope closed field lines (oppositely directed grey arrow within the MC) (Crooker and Horbury, 2006)

Because of the difference in initial conditions at the coronal source, the widths and amplitudes of the two streams are different (Anderson *et al.*, 2012). The multiple current sheets at the sector boundaries are 'waves superposed on the HCS by turbulent eddies in the solar wind' (Suess *et al*., 1995). These waves should possess an amplitude high enough to generate enough energy for the HCS to fold back on itself with false and true sequences of magnetic polarities (Crooker *et al*., 1996) . The suprathermal electron pitch angle distributions on PAD diagrams of ACE often show clear depletions which are symmetric to about 90˚ pitch angle at the upstream of the reverse shocks. According to Skoug *et al.* (2006), 'depletions are produced by a combination of adiabatic mirroring and focusing of electrons due to magnetic moment conservation associated with a magnetic field enhancement beyond the spacecraft' (see Figure 1.47)**.**

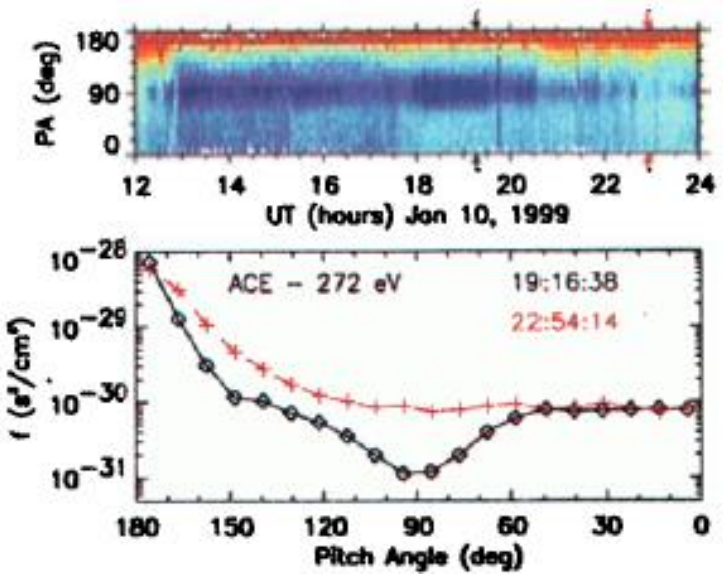

Figure 1.47 The pitch angle distributions observed by ACE in January 10, 1999. The upper panel displays the colour- coded 272 eV PAD for 12 hours. The colour scale is from 1.6x10^{-31} to 2x10^{-29} s^3 cm^{-6}. The lower panel is the PAD at 19:16:38UT and 22:54:14UT which is indicated by the two black and red arrows (Gosling et al., 2001b).

1.9.9 Heat flux dropouts (HFDs)

Heat flux dropouts (HFDs) can also be used to detect magnetic flux that is disconnected from the Sun. Since the suprathermal electrons strahl always flows outward from the Sun, the HFD can detect either the interplanetary field lines that have been completely disconnected from the Sun, or the strahl being dispersed into other pitch angle distributions (Chollet *et al*., 2010). This second occurrence indicates the disconnection is not the only cause of the phenomenon (Figure 1.48). HFD is a 'necessary but insufficient condition' (Pagel *et al*., 2005).

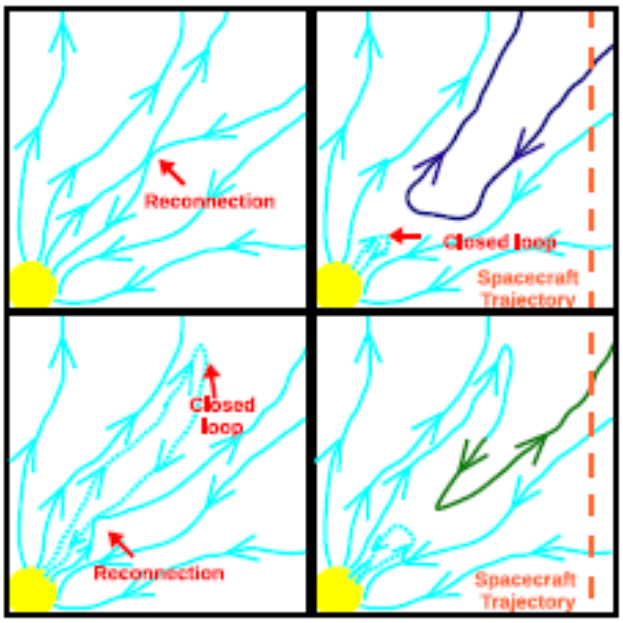

Figure 1.48 A sketch of the two-possible interplanetary field line configurations during HFDs. Upper panels: disconnection field line process. Lower panels: interplanetary scattering (Chollet et al., 2010).

The sectors near the boundary crossing regions often witness a heat flux dropout (Fitzenreiter and Ogilvie, 1992;Crooker, 2003). HFDs can last between 1.6 to 18 hours, with a mean duration of about 4.4 hours (McComas *et al.*, 1989). Most HFD events are consistent with rising plasma beta (Crooker, 2003). Figure 1.49 displays examples of HFDs.

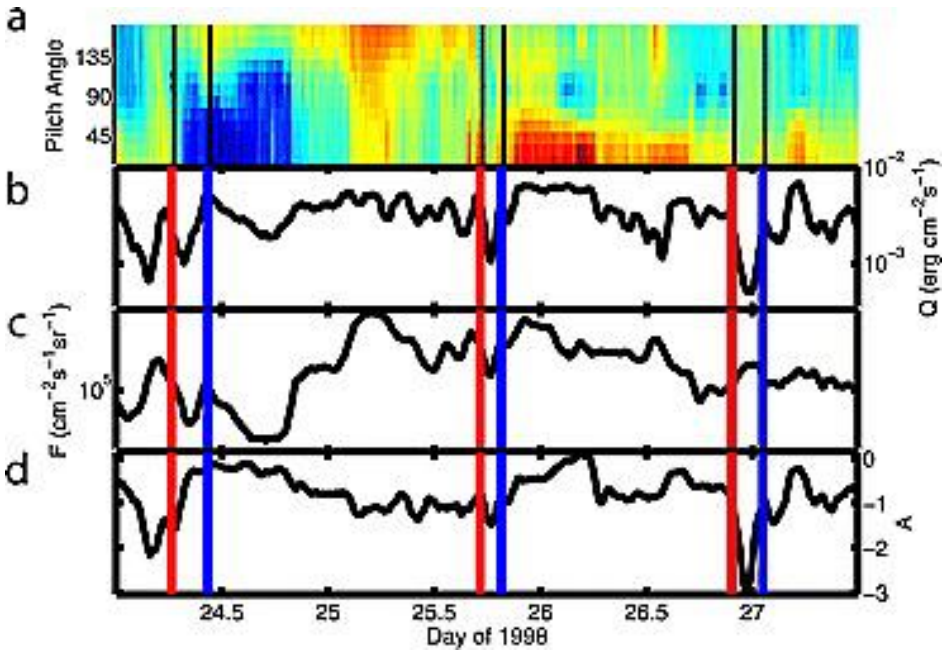

Figure 1.49 Three typical HFDs. Panel (a): the colour-coded suprathermal electrons PAD with a log scale electron number flux from 3.2x10^3-10^5 cm^{-2}s^{-1}. Panel (b): heat flux electrons. Panel (c): electrons total number flux at E=275 eV. Panel(d): pitch angle anisotropy A. The red and blue vertical lines mark the start and end of the HDFs (Pagel et al., 2005).

Based on the findings from 25 HFD events containing ISEE3 electron data, magnetic field disconnection from the Sun has been proposed as one of the two reasons which can explain HFD events (the other being pitch angle scattering) (McComas *et al*., 1989). At high electron energies (between 2-8 *KeV*), at least 8 of the 25 HFD events maintained their connection with the Sun (Lin and Kahler, 1992).
HFDs outside of ICMEs are 'relatively common' (Pagel *et. al*, 2005). Approximately 10% of HFDs were found to coincide with disconnected flux, while 15% were due to the pitch angle scattering and 82% were associated with a rise in proton plasma beta (Pagel *et al.*, 2005).

1.9.10 Magnetic reconnection

Magnetic reconnection is a fundamental dynamical process which explain many physical processes in solar corona, interplanetary space and magnetosphere. It occurs when opposite directed magnetic field lines approach each other and interact, resulting in a change in the conductivity of plasma elements in a magnetic field. In region where there is a central current sheet with opposing directed field lines at its both sides, the opposite magnetic field lines are pulled inwards because the opposition between the plasma's electrical resistivity between the opposing magnetic field lines and the currents which are necessary to sustain the shear in the magnetic field lines. This can be displayed by the Maxwell equation:

$$\vec{V} \times \vec{B} = \mu_0 \vec{J} + \mu_0 \epsilon_0 \frac{\delta \vec{E}}{\delta t} \tag{1.22}$$

Where μ_0 is the permeability of free space and ϵ_0 is the permittivity of free space.

Magnetic reconnection occurs when the conditions for frozen-in flux break down and the diffusion term in the induction equation becomes more important than plasma motion. Consequently, a conversion of magnetic energy into kinetic energy and heat, and an alternation in the magnetic field topology. Figure 1.50 shows reconnection between two plasma regions with oppositely oriented fields flow towards each other. Such situation arises for example at the interface between the southward interplanetary magnetic field and Earth's magnetosphere. A thin current sheet forms between the regions introducing a large magnetic field gradient.
The current sheet's resistivity leads to an approaching of the magnetic flux from each sides of the current sheet, meet at the current sheet and hence to cancel the magnetic flux arriving from the opposite side. The total pressure becomes balanced between the current sheet and its surrounding on both side.

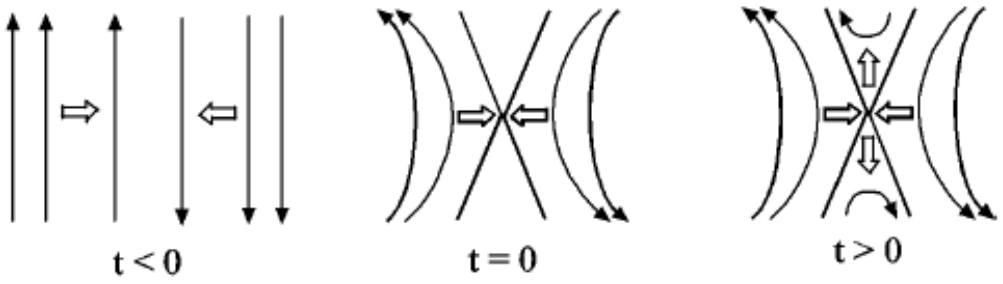

Figure 1.50 Reconnection between two ideal MHD plasma regions with oppositely oriented magnetic field flowing towards each others. Open arrows indicates the plasma flow direction.

1.9.11 MC and Interchange Reconnection

In Solar-terrestrial physics applications, the magnetic field can be considered to have two significant configurations: the open magnetic field line which has one end rooted in the Sun and the other end drawn outward into the heliosphere, and the closed magnetic field line which forms a flux loop which is connected and rooted at both ends with the active regions on the solar surface. During their propagation through interplanetary space, ICMEs interact with the ambient solar wind, and sometimes this interaction leads to a process called interchange reconnection, which is a change in magnetic topology. It can be recognised in suprathermal electron pitch angle distributions (Crooker *et al*., 2008).

The disconnection process is thought to be the only interpretation of the problem of balancing CME magnetic flux added to the heliosphere. This mechanism leads to the formation of a completely disconnected U-shaped structure of plasmoids (in two dimensions), due either to the open field lines merging or to several closed field lines merging. In order to avoid or reduce the high interplanetary 'magnetic field magnitude catastrophe' (Gosling, 1975;McComas, 1995) brought on by the continuous increase of magnetic flux in the heliosphere, 'interchange reconnection' has been suggested as an alternative to the disconnection process. The term 'interchange reconnection' was coined by Crooker *et al.* (2002) to describe the reconnection between a closed magnetic loop of a CME and an open field line, and to describe how this closed loop become open during this reconnection (Owens *et al.*, 2011). This process suggested to occurs with a CME leg until it becomes completely open and its leading edge has leaved the vicinity of the sun, meaning that it is not a complete disconnection which is taking place, but rather a merging between the open and closed magnetic field lines. The term 'interchange reconnection' helps to distinguish this process from disconnection. Figure 1.51 shows the difference between disconnection and interchange reconnection (in two dimensions).

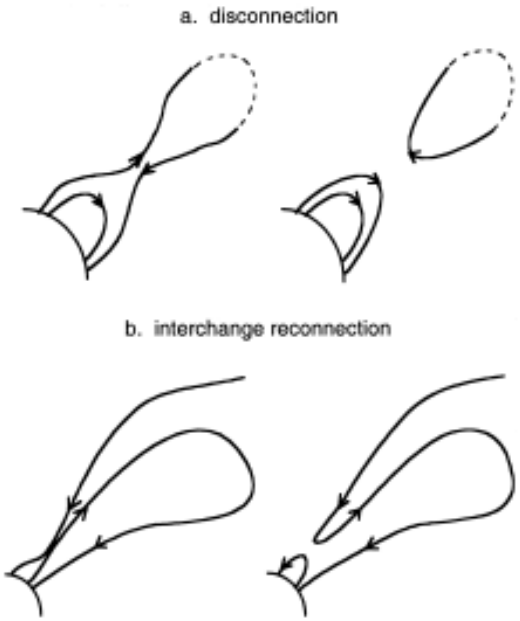

Figure 1.51 Upper sketch: The disconnection is either a merging of two open magnetic field lines (solid curves) at the front edge of the helmet streamer or a merging of a closed magnetic field line (dashed curves) in the CME, which releases a plasmoid. Lower sketch: interchange reconnection, a merging of an open magnetic field line with one leg of the closed CME loop which leaves the sun towards the interplanetary medium. The CME loop becomes opened and there are no field lines disconnected from the Sun. This process reduces the extending field lines into the heliosphere from three to one.(Crooker et al., 2002)

Interchange reconnection was used for the first time by Gosling *et al.* (1995) in order to explain the unidirectional heating flux (strahl) beams associated with open ICME field lines. They posited a partial disconnection process which was the three-dimensional version of the Figure 1.51a disconnection. In this version of the process, closed magnetic field lines reconnect with neighbouring field lines instead of with themselves. There are two ways in which this can occur: an interchange reconnection can happen if the neighbouring field lines are open, or a partial disconnection will occur if they are closed. Figure 1.52 illustrates the partial disconnection of a CME flux. This process reduces the contribution of CME closed flux ropes to the heliosphere.

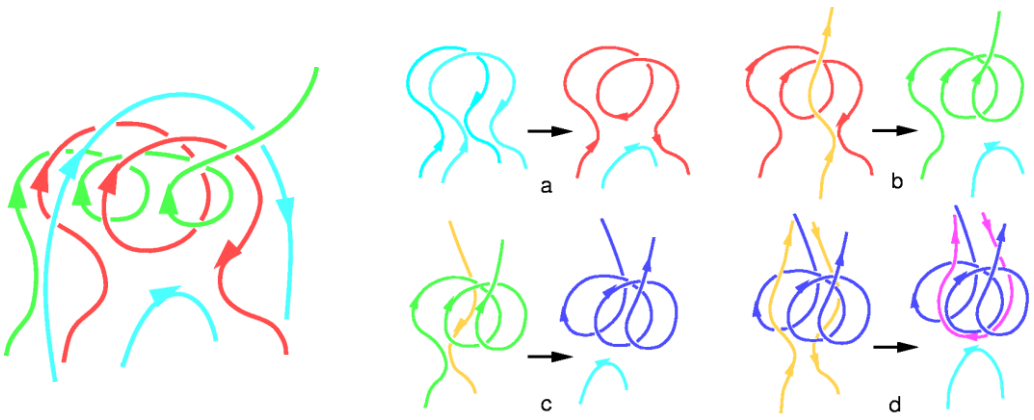

Figure 1.52 Left panel: an open flux rope nested in a closed coil. Right panel: Sketches (a-d) illustrate many examples of the possibility of the 3- dimensional CME reconnection (reconnections with the magnetic legs of a CME) (Gosling et al., 1995).

Due to their belief that most of ICMEs observed out to 5 AU are closed, the researchers came to the inaccurate conclusion that this process occurs on a small fraction of magnetic field lines. Subsequent studies demonstrate that the opposite is true. By analysing 48 MCs, Shodhan *et al.* (2000) found that the presence of open magnetic field lines ranged from 0-100% with an average of about 41% at 1AU. This result supports the suggestion that interchange reconnection continues until ICMEs are completely open. It was also discovered that larger MCs have more closed field lines, especially at solar maximum.

Interchange reconnection can occur at various locations. Figure 1.53 shows a three-dimensional view of interchange reconnection between a negative leg of a CME and a positive open field line, but the process can also occur in the foot of a simple arcade loop along the flank or at the end of the MC flux rope.

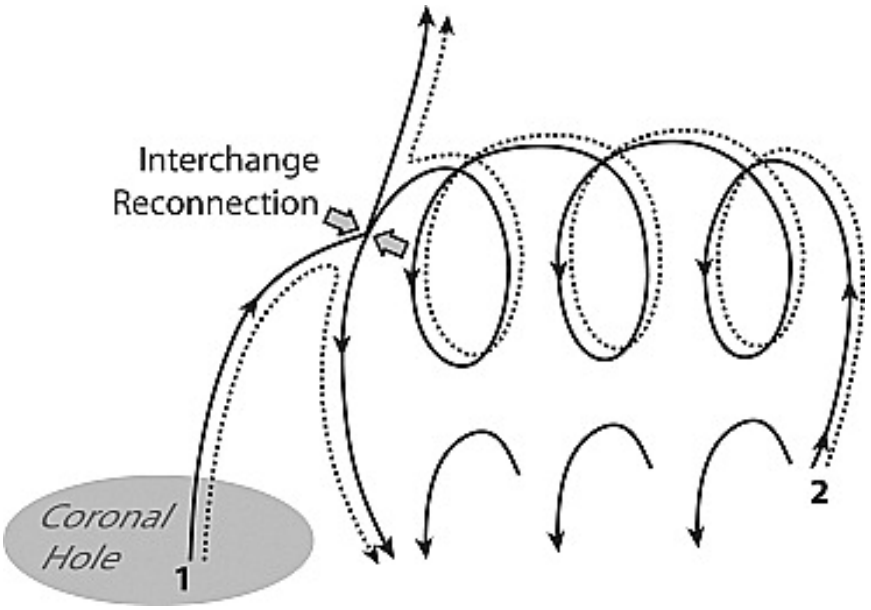

Figure 1.53 Illustrates interchange reconnection between a coiled field loop and an open field line emerging from a coronal hole. The process creates an open helical loop and a small closed loop (dotted lines). Modified from Harra et al. (2007).

The open and closed fields within the interplanetary magnetic cloud can be identified in measurements by 0 or 180 degrees unidirectional suprathermal electrons pitch angle distributions (Figure 1.54).

Interchange reconnection has been described and proposed by many researchers, without use of the actual term 'interchange reconnection', including Wang and Sheeley Jr (1993) and Fisk et al. (1999), and many modified schemes and scenarios have been suggested to describe this process. Many studies also note indications of the process based on remote sensing observations.

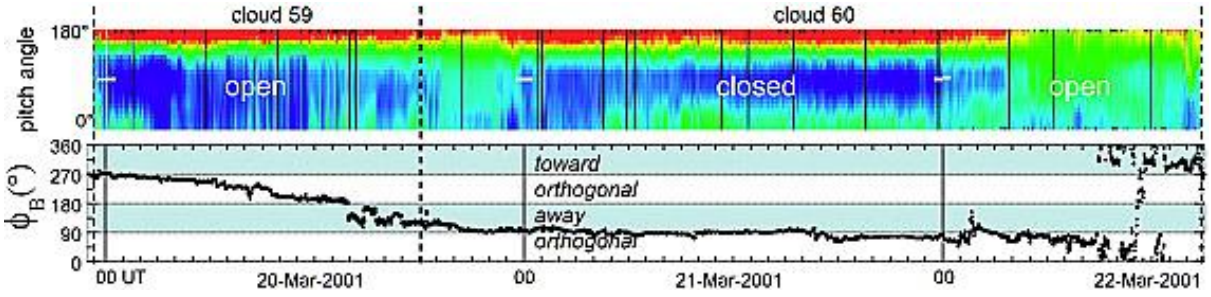

Figure 1.54 Two successive magnetic clouds with different suprathermal electrons distribution profiles. Dashed vertical lines represent their boundaries. The first one (cloud 59) is unidirectional (upper panel) and antiparallel (180˚) to the local field direction (lower panel). The second cloud (cloud 60) starts as unidirectional, and is then bidirectional along the middle , then ends with an open unidirectional heat flux (Crooker et al., 2008)

Interchange reconnection is thought to be responsible for high proton density of transient plasma sheets as well as the mismatch at sector boundaries between true interplanetary magnetic polarity reversals and local magnetic field reversals in the heliosphere (Crooker *et al.*, 2004ab). The high overall HPS proton density has been attributed to the discontinuous plasma parcels released in the HPS as a result of the reconnection between open and adjacent closed field lines (Wang et al., 1998b;Wang et al., 2000). The blobs which originate and are released from the belt streamer's core sometimes take the shape of puffs or moving features and depart as bundles or packages of magnetic flux. Wang *et al.* (1998b); Wang *et al.* (2000) and Zurbuchen *et al.* (2001) use interchange reconnection to interpret the transient plasma sheet's high proton density as well as the magnetic field reversals through this region (Figure 1.55).

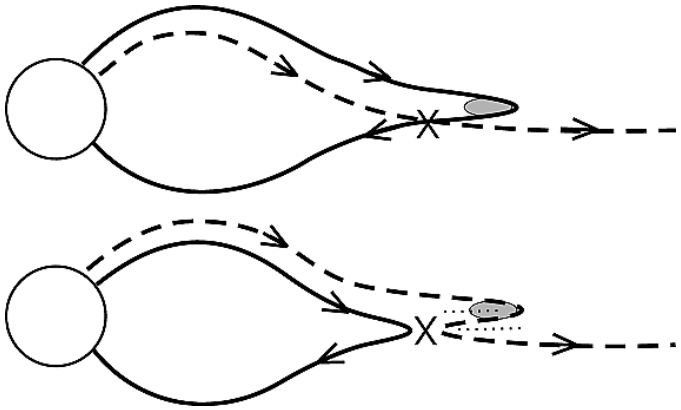

Figure 1.55 The dashed line is the open magnetic field line which approaches the helmet streamer (closed solid line). X is the reconnection point of the two magnetic field lines. The lower panel shows the new configuration where the plasma parcel (blob) is released and resides on the open magnetic field line where previously it was at the loop's cusp. The magnetic field line turns back on itself between localized current sheets marked by the two tiny dotted lines. The whole frame moves away ''as a transient plasma sheet'' (Crooker et al., 2004a).

Mismatches have been found between true sector boundaries and local polarity reversals in $B\phi$ (Figure 1.56). In most cases, the field does not tend to continue to point along the Parker spiral in a sense opposite to its true polarity. Here $B\phi$ looks to be hovering approximately orthogonal to the interplanetary Parker spiral. The figure displays many interplanetary longitudal field inversions without sector boundary crossing, but most of these SBC align with field flips.

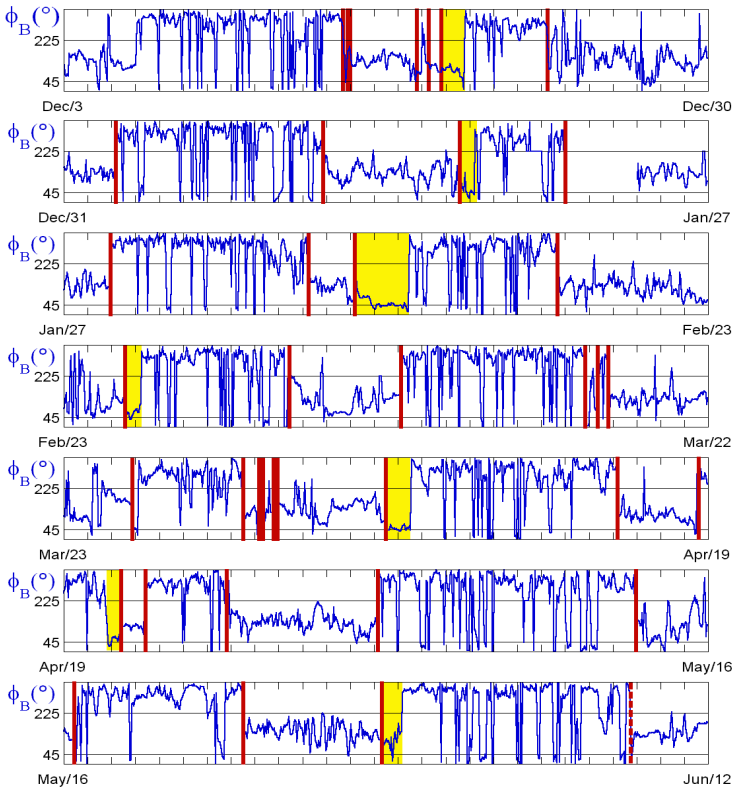

Figure 1.56 Mismatching between true sector boundaries and local polarity reversals in Bϕ during December 1994 to August 1995. The red lines refer to true sector boundaries identified by the Wind suprathermal electrons 3DP spectrograms. The yellow shade highlights mismatches between true sector boundaries and local Bϕ reversals. Adapted from (Crooker et al., 2004b).

The schematic in Figure 1.57 offered an opportunity to understand these mismatching. The pattern of outflowing loops- sector boundary embedded and magnetically opened by the interchange reconnection can interpret how the true sector boundary which is independent of any local current sheet reversals, can be separated from the HCS temporarily.

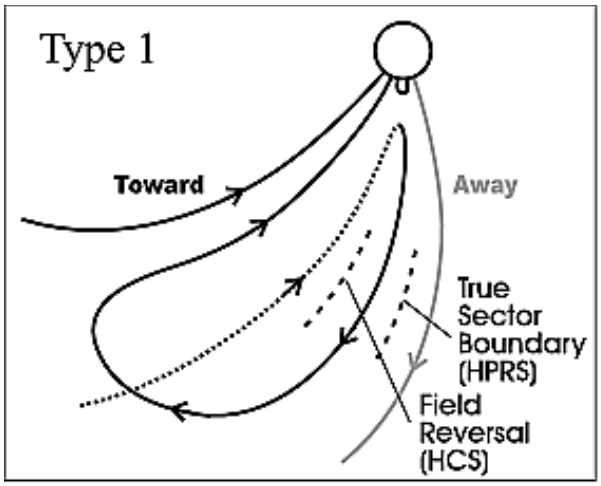

Figure 1.57 A toward sector follows an away sector, and a loop intervenes. at the leading leg of the loop, the field points outward the sun, whereas point inwards in the trailing leg, thus matching the fields in the adjacent sectors. The leading leg of the loop has connected with an open field line there. The dotted field line extends from the loop represent the outer part of the new open field line and is supposed to lie up or below the plane of the figure. This process opened the closed loop and produced an inverted field line in the loops' leading leg. Finally, the true sector boundary is located between the leading leg and the ahead away field line whereas the field reversal marking the HCS lies between the two legs. (Crooker et al., 2004b)

1.9.11 ICMEs and the Streamer belt

The streamer belt is the extension of the helmet arcade apex into interplanetary space, and is the boundary between the two opposite magnetic field hemispheres which encloses the HCS. CMEs occur primarily under the helmet stream belt umbrella and close to active regions (Hundhausen, 1993), and are considered to be bulging bubbles or huge occlusions in the HCS (Crooker and Intriligator, 1996). The streamer belt extends above regions of closed field lines near the Sun. It is often a conduit for CME activity and is also the location of the slowest and highest-density solar wind (Schwenn, 1990) and CMEs. Streamer belts are heliospheric pathways for CMEs (Crooker *et al.*, 1993). Two models have been proposed by Gosling (1990) (Figure 1.58) to illustrate the interplanetary extension of the rising coronal closed loops. The upper sketch has not undergone the reconnection process wheras, the lower having done so. The reconnected coronal loops form a closed flux rope rising into the interplanetary space with both ends rooted in the Sun. Due to solar rotation, the coronal loops will bend, and a coherent magnetic field rotation of the flux rope may be recorded during its passage past a spacecraft.

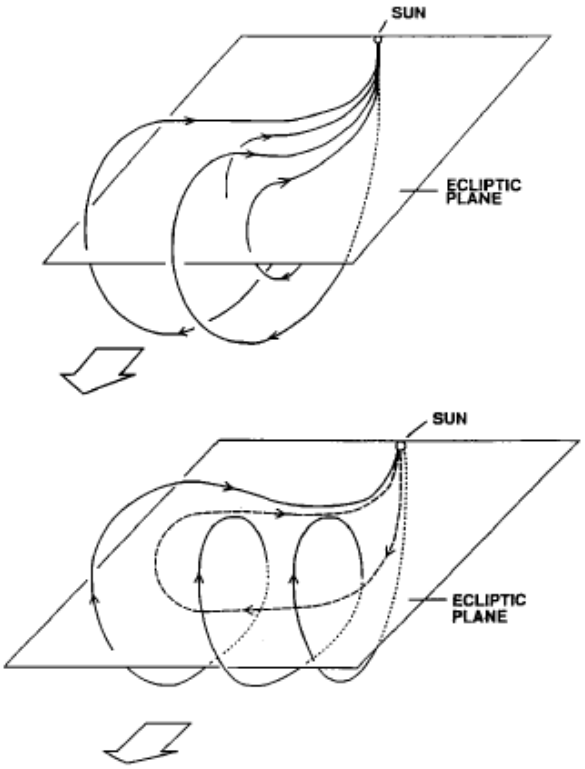

Figure 1.58 A set of rising coronal loops drawn roughly perpendicular to the ecliptic, which having reconnection assumption (lower panel) and have not undergone reconnection (upper panel).(Gosling, 1990)

Crooker *et al.* (1993) considered the appearance of the streamer belt to be that of a disk of variable thickness depending on the number and size of its base helmet configurations, meaning that the HCS consists of more than a single surface, but is instead an extension changing layer with variable number of current sheets streaming from multiple helmet arcades of finite length. It is therefore a compound heliospheric current disk of variable

thickness. The discontinuities in streamer belt measurements obtained from spacecraft can be attributed to the highly variable number of current sheets surrounding the flux tubes (see Figure 1.59).

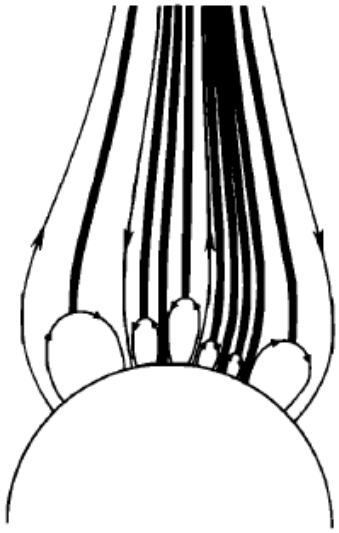

Figure 1.59 Multiple current sheets (heavy lines) and small helmets bordered by large helmets over high latitude filaments.(Crooker et al., 1993)

The coronal streamer belt outflows can either be (a) quiet, (b) small-scale ejections that expand slowly from multiple helmets, or (c) large scale CME eruptions with or without flux rope signatures (Figure 1.60). Consequently, interplanetary space is filled with plaited magnetic flux tubes and multiple current sheets with cross-sections spread out parallel to the plane of the streamer belt.

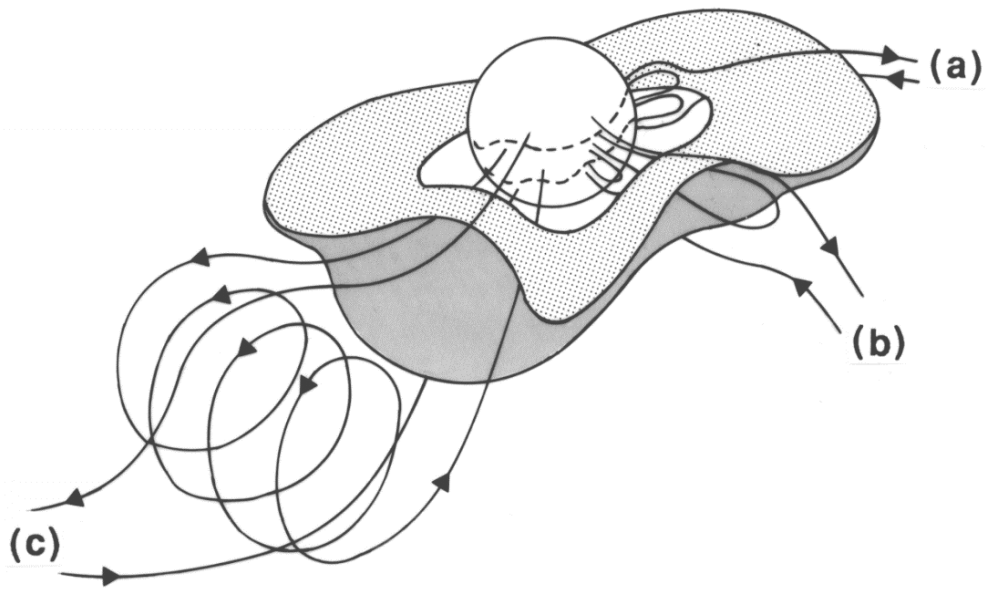

Figure 1.60 Illustrates the three features of coronal streamer belt as an outflow channel. Adapted from Crooker et al. (1993)

From the heliospheric topology depicted above, there should be increased expectation of observing MCs at sector boundaries. In Figure 1.61, showing the middle of the solar disk, the coil over the equator represents a CME flux rope (panel a) which was produced by the reconnection between the magnetic field arcade and the foot point shear (Gosling, 1990). The lower right a-a' cross section shows the reconnecting fields role to re-establish the helmet arcade below the coil. The local polarity of the flux rope's two legs will be the same as that of their sides' open field lines (panel b) (which are the true polarities). Panel (c) shows the Ulysses measurements of an azimuthal magnetic field of a MC at a sector boundary location of 4.4 AU (Forsyth *et al*., 1997). During the MC passage, there was a magnetic reversal from 270 to 90 degrees. Unexpectedly, the magnetic polarity change occurred during the long interval of the MC. The HCS has been locally replaced by the CME. The reversals of $B\phi$ within the MC confirms that the polarities of the legs cannot identified based on the local magnetic field where they have the opportunity to turn back on themselves, but rather based on the suprathermal electrons pitch angle distributions relative to their magnetic field polarity(Kahler et al., 1999).

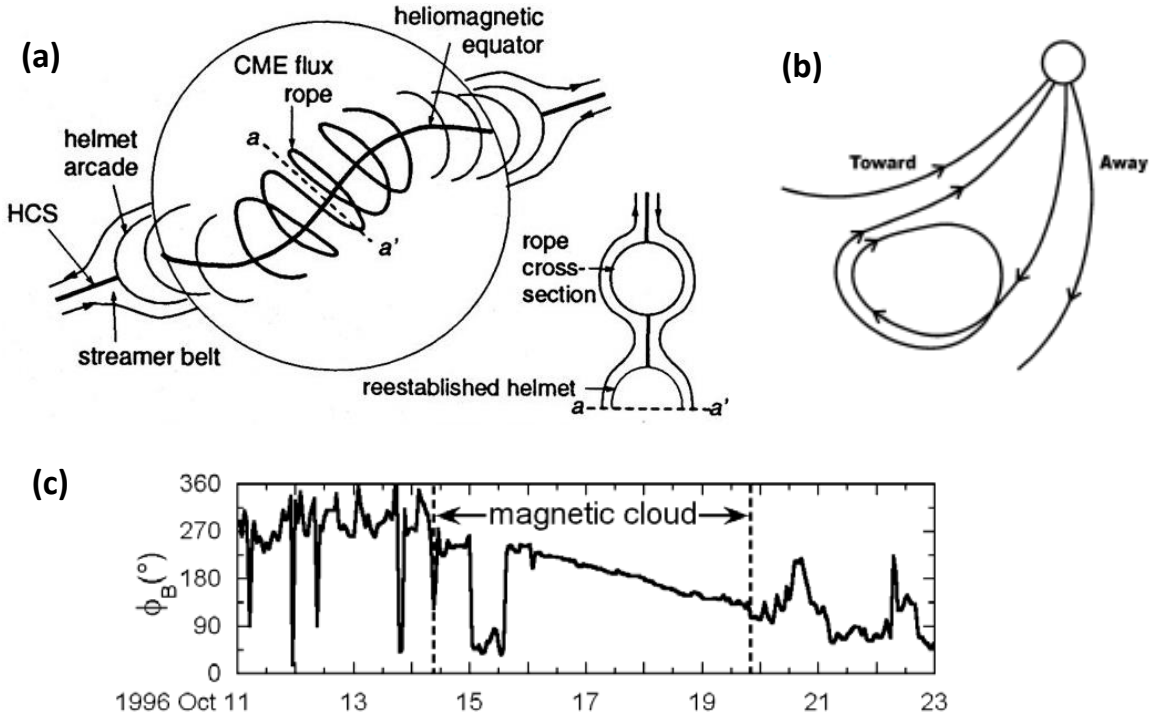

Figure 1.61 The relationship between sector boundary crossings, streamer belts, and CME flux ropes. a) The CME flux rope formation from the helmet arcade at the base of the HCS. aa' shows how the reconnecting fields re-establish the helmet arcade below the coil (Crooker et al., 1998). b) The fieldlines of the flux rope's legs match the toward and away direction of adjacent sectors. c) Magnetic longitudal Bϕ profile measured by Ulysses spacecraft. It rotates from outward to inward polarity across the magnetic cloud flux rope at the sector boundary (Forsyth et al., 1997). (Crooker and Horbury, 2006)

1.9.12 Deflections of Halo CMEs in Interplanetary Space

Assuming the interplanetary magnetic field is frozen in the interplanetary solar wind plasma and that the CMEs travel in a radial direction, the background solar wind ahead of fast CMEs cause a pile up of the magnetic field and an enhancement in the total ahead pressure, which deflects the CME from the radial direction to the east (when the CME is faster than the ambient solar wind). This means that CMEs are deflected not only in the corona, but also in the interplanetary medium(Wang *et al.*, 2014). CME-CME interaction is another cause of CME deflections. The deflection angle can be 10° or more (Shen et al., 2012;Lugaz et al., 2012) and in many cases may be more than 20° eastward or westward (Lugaz *et al*., 2010).

CME deflection was proposed for the first time by Wang et al. (2002) (Wang et al., 2014). Because of the Parker spiral, CMEs undergo east-west deflections during their propagation through the interplanetary medium (Wang et al., 2002;Zhang et al., 2003). By analysing 124 structured CMEs with their locations listed by Cremades and Bothmer (2004), and using the Extreme ultraviolet imaging telescope and the Michelson Doppler imager on board SOHO, along with Hα measurements, Cremades *et al.* (2006) found that CME deflections exist in the lower corona. After the STEREO era, many studies showed that CME deflections in the corona could be more than 20˚ (Gui et al., 2011;Shen et al., 2011). Kilpua *et al.* (2009) studied the ICME rate during the period of Jan 2007-Jan 2009 using data from STEREO and WIND spacecraft, and found that CME deflections tend towards lower latitudes than their source locations during solar minimum, whereas the deflections have no overall trends during solar maximum. In the case of a CME traveling more slowly than the ambient solar wind, the background solar wind following the slow CME will push it and cause an accumulation in the magnetic field and an enhancement in the total pressure behind it, which provides the force to deflect it to the west. According to Wang *et al.* (2004) 'slow CMEs can be deflected more easily than fast ones' (Wang *et al.*, 2004). Figure 1.62 shows schematic illustrations of both slow and fast CME propagation through interplanetary space.

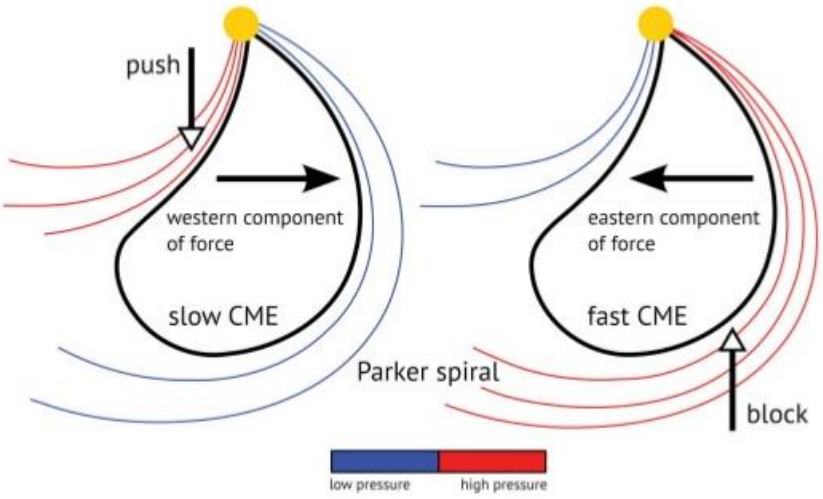

Figure 1.62 Schematic illustration of a slow(left) and fast(right) CME propagation through interplanetary space. Adapted from Wang et al. (2004).

Based on a statistical examination of halo CMEs from March 1997 to 2000, Wang *et al.* (2002) suggested that the distribution of geoeffective halo CMEs possess an east-west asymmetry. They found that the number of west hemisphere geoeffective halo CMEs is larger than that of east hemisphere ones by a magnitude of 57%. This result has also been confirmed by Cane and Richardson (2003) and Zhang *et al.* (2003). Indeed, this east-west asymmetrical distribution also occurs with sunspots and other solar magnetic structures, such as solar flares (Meunier, 2003).

Recently, STEREO unveiled a new approach to study CME propagation in interplanetary space by using large field of view observations and tracking CMEs continuously from the Sun to *in situ* locations via elongation-time maps called J-maps (Davies *et al.*, 2009). By comparing CME features in the outer coronagraph (COR2) and the heliospheric imager (HI) images, scientists can use the J- maps to locate the front edge of the CME and then track its path with the J-map HI2 image. Many studies use indirect links between remote sensing images and *in situ* data to identify the probability of CME deflection in interplanetary space (Rodriguez et al., 2011;Isavnin et al., 2013).

1.9.13 ICME Catalogues and Criteria

When a spacecraft passes through an ICME at its outer boundary, the observation data changes. As soon as it travels into the inner regions of the CME, all plasma and magnetic field parameters experience significant changes including magnetic strength, plasma temperature, velocity and density. Despite several catalogues containing lists of ICMEs events, the ICME criteria are still in dispute (Russell and Shinde, 2005). These catalogues are based on different criteria taken from spacecraft databases (ACE, Wind, STEREO A&B and other interplanetary observations), and follow the general structural identification of ICMEs. ICMEs can be identified by many criteria, even if an universal ICME is not determined yet (Richardson and Cane, 2010). When the standard ICME signatures are compared with the ambient solar wind, they may consist of one or more of the following: High magnetic field magnitude with smooth rotation through the magnetic cloud, low plasma beta, low proton temperature and plasma speed decline in the flux rope region, and He/H ratio and ion charge states enhancement. Zurbuchen and Richardson (2006) have concluded that there is ‘no crisp answer on how to identify an ICME’.

In order to highlight this further, this section discusses two studies: Russell and Shinde (2005) and Mitsakou and Moussas (2014), and describes their approach to different criteria of ICME identification. Russell and Shinde (2005) compare the ICME lists of different authors in separate studies: Larson (2002), Cane and Richardson (2003), Leppings’ list of Lepping (2004) and Russell and Shinde (2005), with events lists being based on WIND spacecraft data for the period 1995-2002. First, they examined rates of occurrence and the coincidence of events. The analysis aimed to highlight the range of their results rather than determining which one was the correct one. The first difference between them was in the ICME selection criteria. Table 1.3 shows a number of Magnetic Clouds (MCs) events identified by each group. There is a contrast between the numbers for different authors. The right column displays the number of events which were identified by at least one group.

Year	Cane and Richardson	Larson	Lepping	Russell and Shine	Events in one or more lists
1995	-	8	8	3	10
1996	4	4	4	3	5
1997	22	21	17	6	26
1998	38	13	11	12	40
1999	28	3	4	3	28
2000	53	12	14	11	58
2001	47	15	10	5	47
2002	22	-	10	3	26
Total	214	76	78	46	240

Table 1.3 Number of ICME events identified by each authors (Russell and Shinde, 2005)

Table 1.4 shows events which were identified by only one group. It reveals a significant difference for Cane and Richardson. Their criteria are more flexible, or liberal, and this is perhaps due to their reliance on multiple solar wind measurement sources. Also, Larson (2002) and Lepping (2004) lists are focused on the ICMEs which possess MCs whereas Cane and Richardson's (2003) list was more comprehensive (focused on both MC and Ejecta). The diversity of ICME criteria prove that there is no consensus on how to identify them (Russell and Shinde, 2005).

Year	Cane and Richardson	Larson	Lepping	Russell and Shine	All agreed
1995	-	1	1	1	-
1996	0	0	0	1	2
1997	2	2	1	0	5
1998	20	0	1	1	5
1999	22	0	1	1	1
2000	30	1	1	1	7
2001	15	0	0	0	3
2002	22	-	1	0	-
Total	124	4	6	5	23

Table 1.4 Number of ICME events identified by only one author (Russell and Shinde, 2005)

A statistical study performed by Mitsakou and Moussas (2014) compared the ICME properties they obtained (1996-2008) with other published ICMEs characteristics. They also identified the boundaries of ICMEs and their sheaths during solar cycle 23. Table 1.5 shows a comparison of the statistical properties of ICMEs at *in situ* position from many researchers. They determined that 'It is obvious that every ICME case is different from any other' (Mitsakou and Moussas, 2014). They used the following criteria based on typical ICMEs signatures to determine their boundaries. These were: 1- High magnetic field magnitude, 2- Low proton temperature, 3- low proton density, 4- low plasma beta, 5- Large and smooth

magnetic field rotation, 6- Decreasing proton speed and 7- a driven shock. It is not necessary for all these signatures to be measured in every ICME, but traits 1 or 5 should be present with at least two of traits 2,3,4,6 or 7.

The same comparison period was performed with the Richardson and Cane (2010) and Jian *et al.* (2006a) lists, which have been updated online. Richardson and Cane (2010) identified 310 ICMEs, whereas Jian *et al.* (2006a) identified 274, compared with 325 ICMEs by Mitsakou and Moussas (2014). All of them agreed with 210 events, and 81% of Mitsakou and Moussas (2014) cases were mentioned in Richardson and Cane's (2010) catalogue versus 77% that were mentioned in Jian *et al.* (2006a). However, 85% of Richardson and Cane (2010) cases were mentioned in Mitsakou and Moussas (2014) versus 91% of Jian *et al*. (2006a).

It was concluded that the authors agreed on the average values of the properties in some cases, whereas they disagreed in others. The most important reasons for these differences were that it was 'difficult to objectively identify ICMEs, as there are many different signatures that are taken into consideration in each study' meaning that the ICMEs boundaries or the time periods for the same cases were often not the same in different catalogues. The different origins of the databases may also lead to different mean values in ICME properties.

	Temporal window	B [nT]	V [km s^{-1}]	D [cm^{-3}]	T [K]	W [AU
Bothmer and Schwenn (1998) (magnetic clouds)	1974 – 1981	17.7	478	6.47		0.24
Liu, Richardson, and Belcher (2005)	1975 – 2002	7.35	458	6.16	0.354×10^5	0.25
Wang, Du, and Richardson (2005)	1975 – 2003	8.3	456	6.7	0.292×10^5	0.19
Forsyth *et al.* (2006)	1975 – 1980	10.3	483	7.03	0.443×10^5	0.31
Gopalswamy (2008) (magnetic clouds)	1996 – 2005	18	487	8.5	0.9×10^5	
Mitsakou, Babasidis, and Moussas (2009)	2003 – 2006	9.2	525	6.5	1.28×10^5	0.29
Richardson and Cane (2010)	1996 – 2009	10.1	476	6.9	0.487×10^5	0.33
this work	1996 – 2008	10.1	467	6.8	0.76×10^5	0.27

Table 1.5 A comparison of statistical properties of ICMEs at 1 AU from many authors (Mitsakou and Moussas, 2014)

1.10 Corotating Interaction Regions (CIRs)

Slow dense plasma flows originate in the closed solar magnetic field lines (Gosling *et al*., 1981), while the fast plasma streams arise in open field lines, such as coronal holes (Krieger *et al.,* 1973). During its propagation away from the Sun, a fast stream collides with the slower streams ahead. This interaction between them forms a compression ridge and a rarefaction on the trailing edge of the fast stream (Parker, 1963;Hundhausen, 1972).

When the fast solar wind stream overtakes the slower one, this results in a formation called the Stream Interaction Region (SIR) (Pizzo, 1978). During the solar rotation (27 days), the SIR pattern co-rotates with the Sun and forms a spiral flow called the Corotating Interaction Regions (Gosling and Pizzo, 1999). This is a recurrent stream structure in the solar equatorial plane (Balogh et al., 1999;Crooker et al., 1999). The fast-slow interaction begins in the inner part of the heliosphere and expands with increasing distance (Richter and Luttrell, 1986). The leading boundary of the CIR propagates toward the slower stream, forming a forward wave (shock), while the trailing boundary propagates back into the trailing high stream, forming a reverse wave (shock) (Hundhausen and Gosling, 1976). The compression region between them is called the Stream Interface(SI) (Burlaga, 1974). Shocks at 1 AU are not 'completely developed' (Gonzalez *et al.*, 1999). Figure 1.63 shows a co-rotating stream structure in the inner heliosphere.

As with the ICME, the morphology of an SIR varies on a case by case basis. During the period of 1995-2004, Jian et al. (2006b) found that the occurrence rate of SIR shocks at *in situ* regions is about 24% and only 70% of this rate are forward.

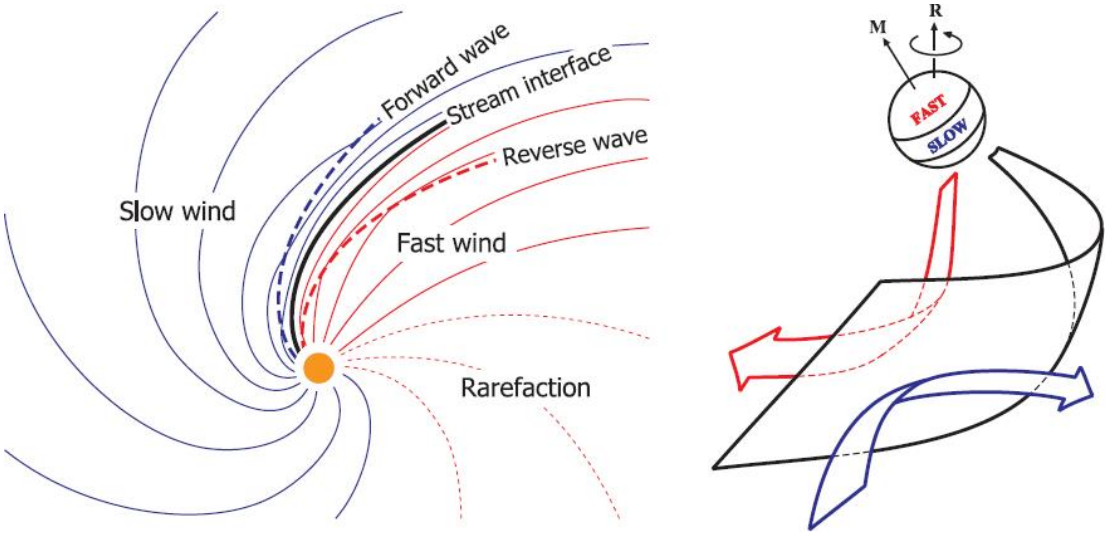

Figure 1.63 A Co-rotating stream structure sketch of the inner heliosphere. Left panel: magnetic field lines within fast (red) and slow (blue) solar winds. A stream interface (black line) lies within the compression region between forward and reverse waves. Right panel: M is the solar magnetic axis. The solar wind belt is inclined to the solar rotation axis(R). The SI is the ridge in interplanetary space where the fast stream catches up to the slow stream ahead of it (black). The fast stream is slowed where the slow is accelerated. Also, both are deflected along the SI. Right panel adapted from Pizzo (1991). (Owens and Forsyth, 2013) .

Stream interfaces were first observed by (Siscoe *et al.*, 1969) as a flow shear. Belcher and Davis (1971) were the first to study the boundary separation between the slow, cold, dense stream and the hot, fast, tenuous stream of the solar wind. Burlaga (1974) called this boundary the 'Stream Interface'. The two plasma streams of the SI originate in different regions of the corona (Wimmer-Schweingruber *et al*., 1999). Later, the SI was described as a sudden drop in the plasma density associated with a rise in the proton temperature and occurring at speeds less than 459 km/s with discontinuous changes in alpha particles. Within the solar wind flow, SIs are sites of discontinuous shears (Gosling *et al*., 1978). The high proton elevation of SIs has been attributed to an increase in entropy (Intriligator and Siscoe, 1994;Lazarus et al., 2003) and plasma velocity across the SI (Jian *et al*., 2006b).

The highest total perpendicular pressure of the CIR plasma appears in the vicinity of the SI (Gosling and Pizzo, 1999). The P_t parameter is a good indicator with which to study the morphology of ICMEs and CIRs (e.g. Russell *et al.*, 2005) because it presents the sum of the magnetic and plasma thermal pressure perpendicular to the magnetic field, meaning there is a contribution of magnetic field and plasma to the pressure. The peak pressure and the dynamic pressure of the stream on the opposite sides of the SI are equal. Therefore the maximum pressure is a good indicator to use when identifying the passage of the SI (Jian *et al.*, 2006b). Sometimes many discontinuities in the pressure morphology are apparent, which is due to shocks arising to a supersonic across the SI and exceeds the compressional wave speed. The characteristics of SIRs can be summarized as: 1. An overall increase in the solar wind velocity. 2. The P_t reaches a maximum at the SI. 3. The increase in the gradient of the P_t causes the plasma streams to drift towards the SI from each side (maximum P_t at the SI with gradual decrease to both sides). 4. A sudden reduction and a compression in the proton density and magnetic field strength at the location of the SI. 5. An increase in temperature and flow deflection at an SI. 6. An increase in the entropy per proton (Ln ($T_P^{3/2}/N_P$)). These signatures are not necessarily present in all events (Jian et al., 2008c). Figure 1.64 illustrates the morphology of SIRs, including forward and reverse shocks.

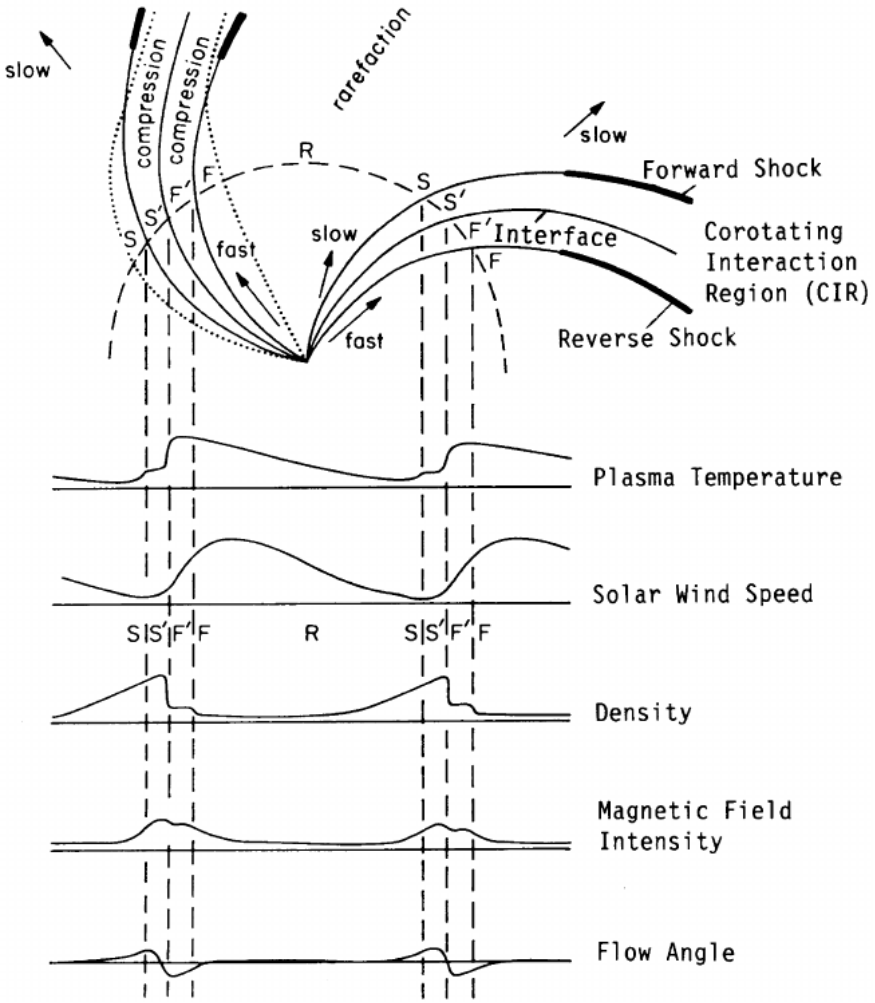

Figure 1.64 A scheme illustrating the geometry (upper panel) and profiles of SIR with forward shocks (S) , reverse shocks (F), compression regions (S',F') , stream interface SI (curved line between S' and F') and rarefaction region R (Richardson et al., 1996), after Belcher and Davis (1971).

The variations in SIR characteristics may display the effect of other structures on them, for example the meeting of a transient slow solar wind of the SIR with a slow coronal mass ejection (Jian *et al.*, 2006b). Suprathermal electrons also appear within high-speed solar winds, which are emitted from the solar coronal holes and associated with CIRs. BDE streams are sometimes associated with these CIRs at the head and follow the passage of their reverse shocks or waves at 1 AU, but occur most frequently at the reverse shock and can last a period of about 2 days after the spacecraft connection to the stream interaction region at 3 to 5 AU (Steinberg *et al*., 2005). The electron heat flux enhancement appears at both the forward and reverse shocks of the CIR at distances of between 2-5 AU, based on Ulysses data (Gosling *et al.*, 2001a). This enhancement flux is a consequence of the energizing electrons at the shocks leaking out of the CIR upstream towards the solar wind, producing beams of field aligned electrons which are directed away from the CIR on both sides. At 1 AU, the CIR is more likely to have forward and reverse waves than shocks at its boundaries According to Gosling and Pizzo (1999): 'whereas shocks are known to be sources of suprathermal electrons, forward and reverse waves are not generally recognized to be significant producers of suprathermal

electron enhancements' (Steinberg *et al*., 2005). On the other hand, the counter streaming electrons at forward and reverse CIR shocks can be produced through other mechanisms, such as the connection with the Earth's bow shock (Feldman *et al*., 1982) and the depletions occur around the 90˚ pitch angle because of the magnetic focusing and mirroring (Gosling *et al*., 2001b). Figure 1.65 illustrates the geometry of the magnetic field lines during the SIR.

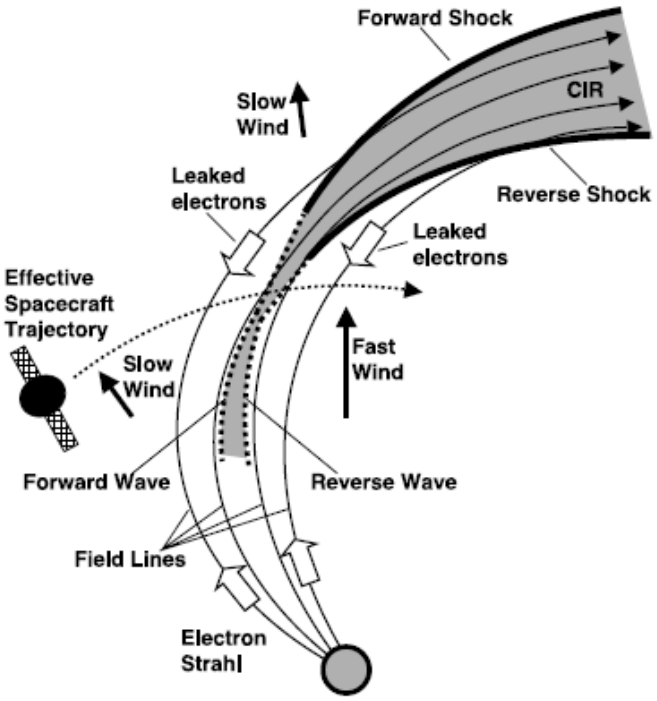

Figure 1.65 A schematic illustration of the SIR field line geometry. The compression area is shaded in grey. The solid line refers to the SIR area which is bounded by the shock, whereas the dotted line refers to the SIR area (near in situ) bounded by a pressure wave. (Steinberg et al., 2005)

1.11 Magnetic storms at Earth

Magnetic storms that are caused by ICMEs occur in three main phases: Storm Sudden Commencement (SSC) (the initial phase), the main phase, and the recovery phase (Guarnieri et al., 2006). Storms which are caused by CIRs have the same phases, with the differences between them being: 1) In the initial phase of the ICME storm, there is a SSC, whereas in the CIR storm there is a gradual initial phase without an SSC (Tsurutani et al., 1995), 2) During the main phase, the reduction of *Dst* (the index of storm strength) of the ICME storm is higher (hundreds of nT) than in the deceasing of SIR storm (which makes the ICME storms more intense) (Gonzalez *et al.*, 1999), 3) ICME storms have a recovery phase that is shorter than that of the CIR. 4) ICME storms mainly occur during the ascent phase of the solar cycle (solar maximum) due to an increase of CME events. Figure 1.66 compares the response of the Dst index for both ICME and CIR.

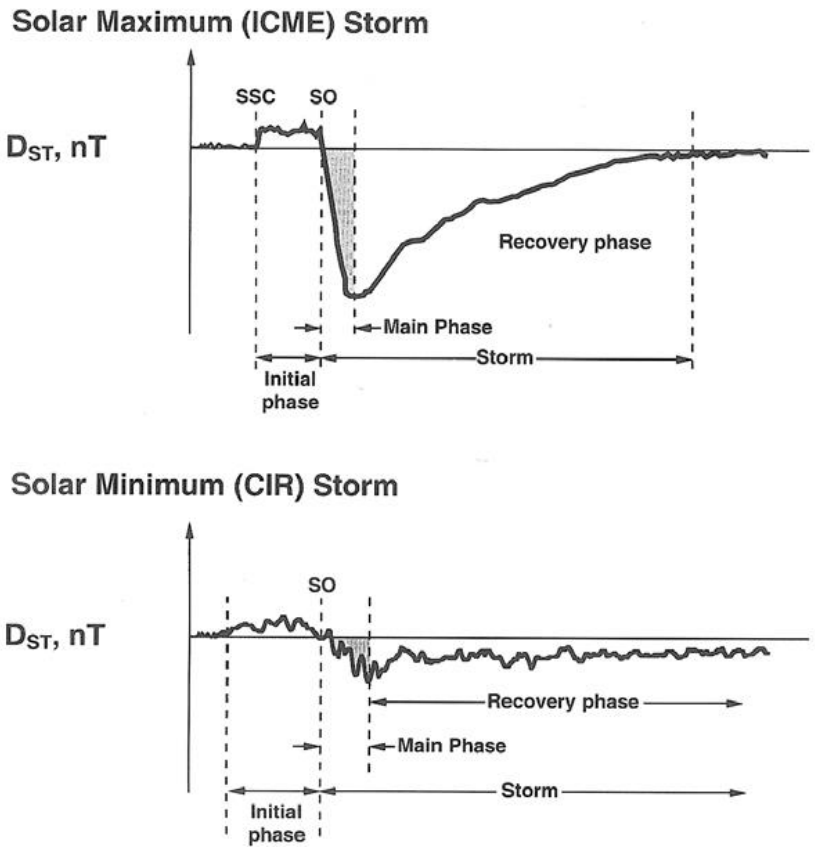

Figure 1.66 The typical Dst response during magnetic storms due to an ICME (top), an a CIR (bottom) (Tsurutani et al., 2006) . The Dst derived from a network of near-equatorial geomagnetic observatories that measures the intensity of the equatorial electrojet (the ring current)

Kataoka and Miyoshi (2006) present a schematic illustration of two typical CME and CIR plasma structures (Figure 1.67) after studying the interfaces between interplanetary shocks and SI during CME- and CIR-associated magnetic storms. The flux enhancement was more effective with CIR-associated storms than with CME-associated ones. The existence of all three ICME parts (MC, sheath and shock) in the same event changed the general configuration of the geomagnetic disturbance morphology due to compression of the magnetosphere by the shocks. The geomagnetic storms were classified into five groups according to the reduction values of *Dst*: Weak: (-30 to -50) nT, Moderate: (-50 to -100) nT, Strong: (-100 to -200) nT, Severe: (-200 to -350) nT, and Great: (<-350) nT (Loewe and Prölss, 1997). Both CME and CIR can be responsible for the weak and moderate storms, whereas only CMEs can be responsible for the other types (Gopalswamy et al., 2007).

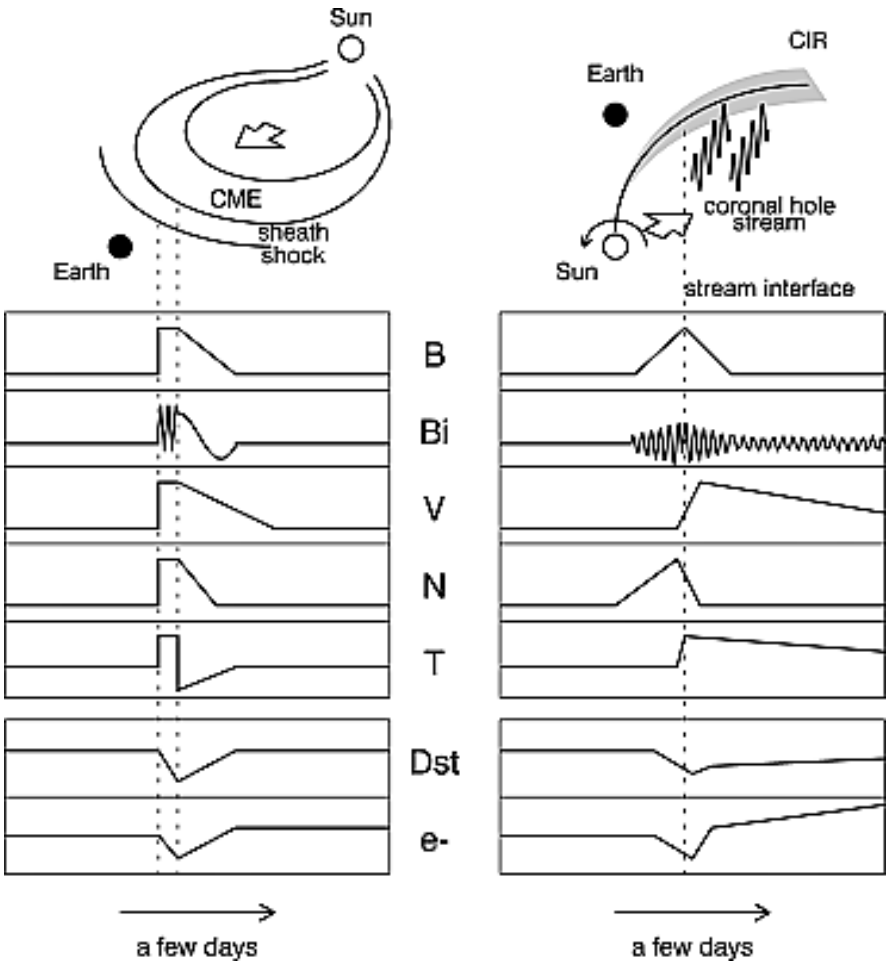

Figure 1.67 A schematic illustration of two typical CME and CIR parameters accompanied magnetic storms. B: the magnetic field strength, Bi: one of the Cartesian component, V: solar wind speed, N: density, T: temperature, Dst: expected response of the geomagnetic index and e^-: > 2.0 MeV electron flux at geosynchronous orbit. (Kataoka and Miyoshi, 2006).

1.12 ICMEs and Space Weather

Solar activity plays an important role in most of the variations which take place in the solar-terrestrial environment. This is due to changes in the amount and the energy of electromagnetic radiation and high energy particle emissions resulting from solar events.

Solar activity can be divided in to two categories: 1) long-term activity as represented by the 11 years' sunspot cycle, where the number of sunspots changes from a minimum to a maximum and again to minimum values. During the ascent phase, the solar atmosphere witnesses an increase solar flares, filament eruptions and CMEs, which leads to a solar wind energy enhancement and a rise in the number of geomagnetic storm events. In the descent phase, however, these events decline in frequency (Figure 1.68). 2) Short-term activity, as represented by short (lasting from a few to several minutes) and temporary rises in solar electromagnetic radiations and energetic particles associated with the above events. This can

cause many short-lived impacts on our space environment, such as magnetic storms, ionospheric storms, auroras, and high frequency fadeout.

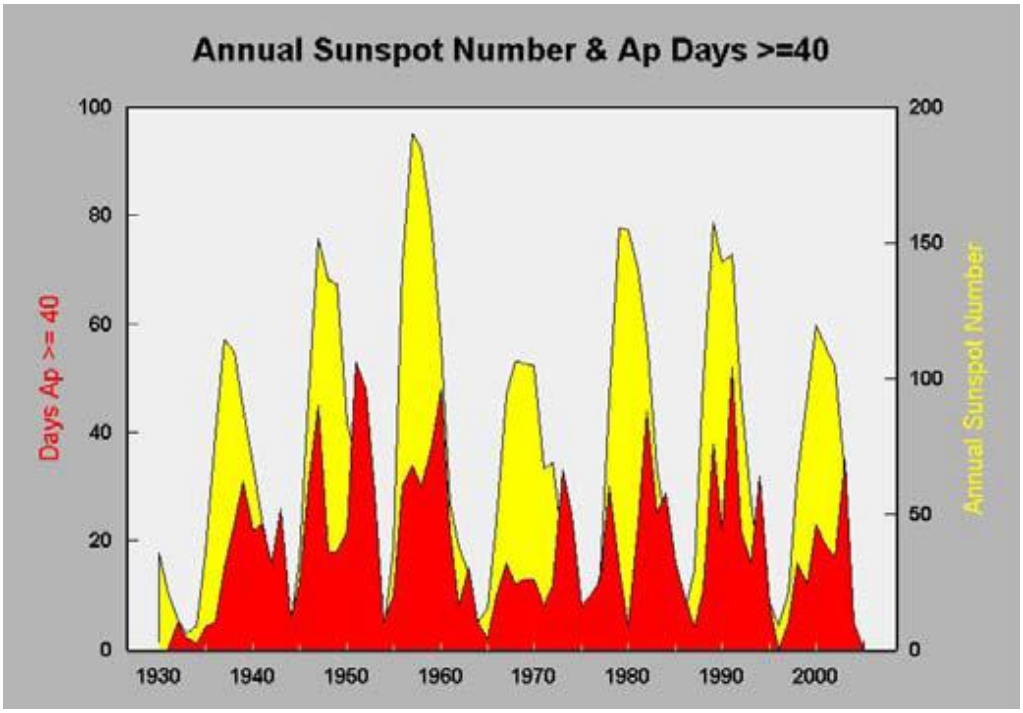

Figure 1.68 A display of the correlation between the annual sunspots numbers (yellow area) and the geomagnetic disturbed days with the geomagnetic Ap index ≥ 40 (red area). Courtesy NOAA Geophysical Data Centre Boulder, CO, USA.

Space weather is the term used to describe the physical variations and disturbances which begin in either the solar atmosphere, interplanetary space, magnetosphere, or the Earth's upper atmosphere and occur over the above-described solar activity time scales. Space weather can impact the safety of humans and technology both in space and on the ground. Electromagnetic radiation and energetic particles can harm astronauts' safety, damage spacecraft equipment and degrade satellite sensors, while magnetic disturbances can lead to damage to power pipelines, ionospheric increased ionization, interruption of high frequency radio waves and GPS fadeout and power systems outages (Cannon *et al.*, 2013).

Coronal mass ejections events are deeply influenced by the solar activity cycle, with values ranging from < 0.5 per day at solar minimum to > 6 per day at solar maximum (Gopalswamy *et al*., 2003a). They are often associated with phenomena such as flares, radio bursts and solar energetic particle events, as observed by Radio waves, EUV, X rays, and H-alpha, in either spectra or images. The interplanetary B_z magnetic field under quiescent conditions is very weak, except for some small-amplitude Alfvenic fluctuations. The relationship between ICMEs (encompassing MCs, sheaths and shocks), and geomagnetic storms stems from the fact that ICMEs are the source of the interplanetary southward magnetic field enhancement. Every part of the ICME contributes to changes in geomagnetic indices, such as *Dst*, but in different ways.

The ICME shock is the first remarkable signature of an ICME arrival due to the associated solar energetic particles (SEPs). Through the interplanetary medium, shocks continue to produce SEPs as long they are strong. The Geostationary Operational Environment Satellite System (GOES) was the first to record the impact of ICME particles on space weather by observing an energetic storm particle with the ICME forward shock passage. Solar energetic particles can pose a risk to high-flying aircrafts, damage spacecraft and satellite electronic devices, and harm astronauts (Turner, 2006). As the CME departs the Sun, many factors will determine the geoeffective level of the ICME and therefore its ability to change the Earth's space weather. These factors include its magnetic field strength, its shocks energetic particles, deflection, deceleration, speed, and the Earth arrival time. Gopalswamy (2009b) has summarized two key space weather aspects of CMEs and their geospacer consequences. The two interplanetary consequences of CMEs are SEPs and Geomagnetic storms (Figure 1.69).

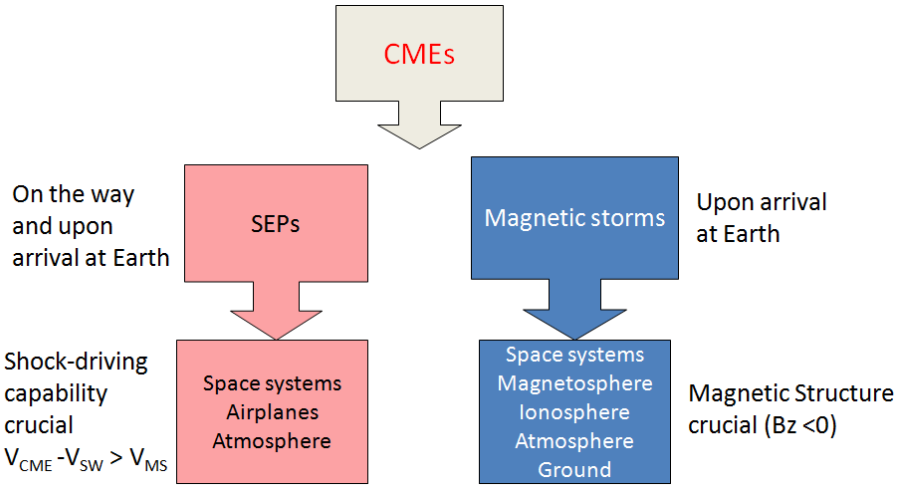

Figure 1.69 SEPs and Geomagnetic storms, the two interplanetary consequences of CMEs. CMEs speed V_{CME} more than the solar wind speed V_{SW} should exceed the magneto sonic speed V_{MS} to drive a shock. CMEs cause geomagnetic storms when they have southward magnetic field direction (Bz<0) (Gopalswamy, 2009b).

Chapter 2

Instrumentations

The remote sensing and *in situ* observations presented in this work comes from multiple instruments onboard several spacecraft. This chapter presents and describes these spacecraft and their instruments. The wide range of measurements available from these instruments helps us to understand the connection between solar events and their interplanetary signatures.

2.1 The Solar and Heliospheric Observatory (SOHO)

The Solar and Heliospheric Observatory (SOHO) is a joint NASA-ESA spacecraft (Domingo *et al.*, 1995) which was launched in December 1995. Its objective was to study the Sun, from the deep core to the outer corona, and to understand more about the solar wind from its orbit around the L1 Lagrange point, the location of Sun-Earth gravitational equilibrium with a distance of about 1.5x 10^6 km upstream of the Earth with a spin axis directed toward the Sun. SOHO had 12 instruments on board, consisting of telemetry instruments that worked in ultraviolet and visible light, and *in situ* measuring instruments.

2.1.1 Large Angle and Spectroscopic Coronagraph (LASCO)

This consists of a set of three optical telescopes with different fields of view (Brueckner *et al*., 1995), which are designed to block the white light coming from the solar disk and obtain the faint emissions of the corona. The three optical systems used are C1, C2, and C3, which capture images the solar corona from 1.1 to 30 solar radii. C2 and C3 are externally occulted coronagraphs observing the regions between 1.5 to 6 and 3.7 to 30 solar radii respectively, and they are still working well.

2.2 The Solar Dynamics Observatory (SDO)

SDO is a NASA mission, the flagship of the living with a star (LWS) programme (Pesnell, 2015), which was designed to provide images of the Sun with a level of detail impossible previously. Its goal is to study the solar atmosphere in many wavelengths and understand more its impact on the Earth and on near-Earth interplanetary space. SDO was launched in February 11, 2010 with a circular geosynchronous orbit, and including three instruments: the Helioseismic and Magnetic Imager (HMI), The Extreme Ultraviolet Variability Experiment (EVE), and The Atmospheric Imaging Assembly (AIA). The HMI (Schou *et al*., 2011) was designed to study oscillations and the magnetic field of the solar photosphere. Full-disk observations of the magnetic field are provided at the wavelength 6173 A with 1 arc second resolution.

2.2.1 The Atmospheric Imaging Assembly (AIA)

AIA (Lemen *et al*., 2012) consists of four telescopes that provide full solar disk images with high spatial and temporal resolutions in seven EUV channels: Fe XVIII (94 A), Fe VIII, XXI (131 A), Fe IX (171 A), Fe XII, XXIV (193 A), Fe XIV (211 A), He II (304 A), and Fe XVI (335 A), and

three UV to Visible channels, covering the solar atmosphere in temperatures ranging between 6000 to 2x10^7 ˚k. Table 2.1 display the ten AIA wavelength channels and their uses.

Channel	Primary ion(s)	Region of atmosphere	Char. log(T)
4500 Å	continuum	photosphere	3.7
1700 Å	continuum	temperature minimum, photosphere	3.7
304 Å	He II	chromosphere, transition region	4.7
1600 Å	C IV + cont.	transition region, upper photosphere	5.0
171 Å	Fe IX	quiet corona, upper transition region	5.8
193 Å	Fe XII, XXIV	corona and hot flare plasma	6.2, 7.3
211 Å	Fe XIV	active-region corona	6.3
335 Å	Fe XVI	active-region corona	6.4
94 Å	Fe XVIII	flaring corona	6.8
131 Å	Fe VIII, XXI	transition region, flaring corona	5.6, 7.0

Table 2.1 The AIA 10 channels, the dominant ions observed in each channel, and the corresponding temperature regime for that ion. (Lemen et al., 2012).

2.3 The WIND spacecraft

The WIND spacecraft (Harten and Clark, 1995) was launched in November 1, 1995. Its main object was to study the interplanetary medium by measuring the magnetic field, charged particles and continuously monitoring the solar wind conditions near Earth. WIND's orbit was a very complicated petal orbit ranging between $10R_E$ and $80R_E$ away from the Earth, and taking the spacecraft up to angle of 60° from the ecliptic plane with respect to the Earth. It spent a long time in the magnetotail before beginning to orbit the Sun at the L1 Lagrange point.

2.3.1 WIND Solar Wind Experiment (SWE)

A two solar wind data analyser instruments undertaken by the Faraday Cup(FC) sub-systems which designed to measure the thermal protons and positive ions (Ogilvie *et al.*, 1995). To analyse the solar wind, it considered to be as a fluid with velocity $\overrightarrow{\mathcal{V}p}$, thermal speed ω_p, and density n_p as a function of position and time (Steinberg *et al.*, 1996). The instrument deal with particles as accounts to generate accurate values of these plasma parameters. The FC instrument investigate the 3D distribution of protons and alpha particles with velocity space $f_p(\vec{\mathcal{V}})$ and $f\alpha$ $(\vec{\mathcal{V}})$ through measurements of the reduced distribution function. The FC principle of the ion instrument is: the particles' flux passage through the FC instrument produces a current which clash with one or more electrically-insulated collector plates (Figure 2.1) (Kasper, 2002). In the left panel (a), positive particles q_+ (red arrows) and negative particles q_- (blue arrows) pass through the instrument entrance area A with various parallel speeds $\mathcal{V}_{II}$ to the symmetric axis instrument, and hit the insulted collector plate. Because of the collector location which grounded the green wire, surplus charge does not accumulate on the collector. The current flows through the wire measure by an ammeter.

The properties of positive and negative particles are interwined because they have different average speed. The left design was improved as can be seen in the right panel (b) by inserting

two wire grids. The outer grid grounded the green wire and a high positive charge voltage $V_{H.V}$ was supplied to the inner grid in order to fend off particles of the desired charge. This operation is like shielding the collector plate from positively charged particles with insufficient energy to penetrate the region between the two grids. The particle with charge q and mass m are reflected unless

$$\frac{\frac{1}{2}mv_{II}^2}{q} \geq V_{H.V} \tag{2.1}$$

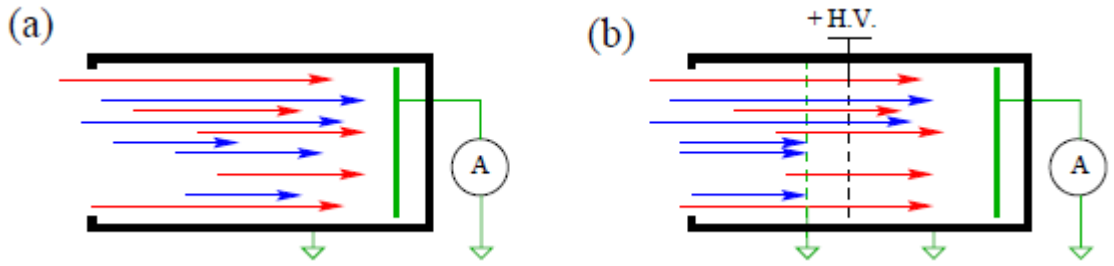

Figure 2.1 Illustrates a simple scheme of a Faraday Cup measurement of charged particle flux. (Kasper, 2002)

2.3.2 WIND Magnetic Field Investigation (MFI)

This is comprised of a dual triaxial fluxgate magnetometer that measures the DC vector magnetic fields up to a time resolution of 22 or 11 vectors/sec. The MFI is an instrument developed from the legacy of magnetometers carried by Voyager, ISPM, GIOTTO and the Mars observer mission. The advantage of using the dual magnetometer can be seen especially in weak interplanetary magnetic field measurements. It provides high temporal resolution of the interplanetary magnetic field 3-D measurements. For 24 hours, the 92 sec Kp data is publicly available at the Coordinated Data Analysis Web (CDAWeb). After about 1 week, the MFI team produces data calibrated to 3 sec, 1 min, and 1 hr averages in both GSE and GSM coordinates.

2.4 The Advanced Composition Explorer (ACE)

The ACE spacecraft was launched in August 25, 1997, and carries a set of instruments to measure the elemental, isotopic, and ionic charge-state composition of the corona, solar wind, the local interstellar medium and galactic matter. ACE orbits the L1 Lagrangian point (Figure 2.2) and provides continuous measurements of the interplanetary magnetic field, the solar wind parameters, solar energetic particles and heliospheric and galactic accelerated particles.

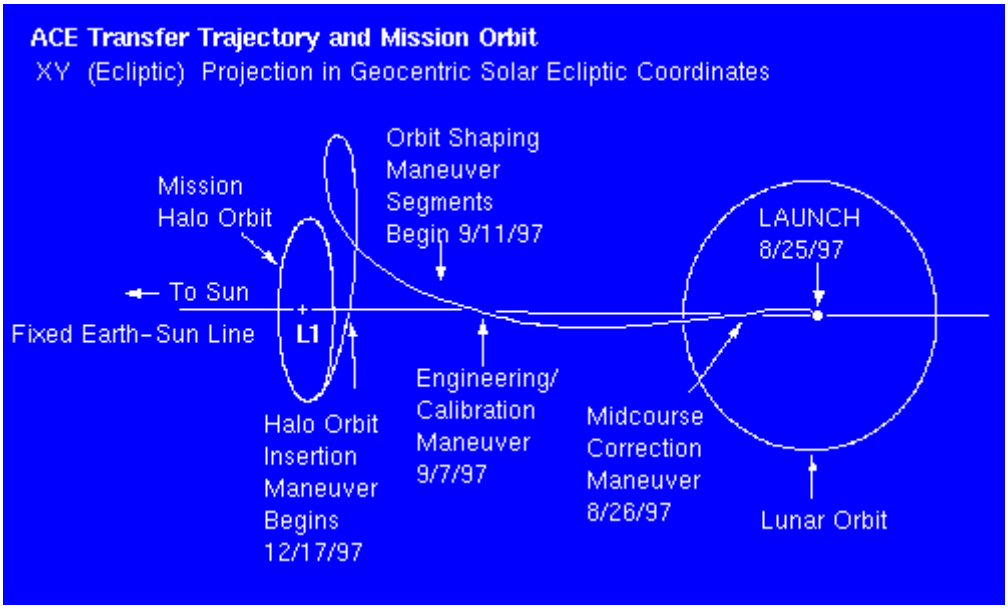

Figure 2.2 ACE trajectory and mission orbit from the Earth to L1 position (August 25, 1997 to December 17, 1997) http://www.ssg.sr.unh.edu/mag/ACE.html.

2.4.1 ACE Magnetic Fields Experiment/Magnetometer (MAG)

The Magnetic Fields Experiment MAG (Smith et al., 1998a) consists of twin vector triaxial fluxgate magnetometers which measure IMF characteristics in three dimensions over a wide range of frequencies using the flight spare of WIND MFI. It provides high-resolution measurements of the magnetic field ranging between 3 and 6 vectors S^{-1} resolution. It is normal to use MAG data averaged over 16 secs, 5 min, 1 hr or even 1 day depending on the requirement.

Various coordinate systems are used to study the solar terrestrial environment. The Geocenteric Solar Magnetospheric (GSM) coordinate system has been used commonly to measure Real Time ACE. GSM is centered along the Earth's magnetic dipole axis and is useful for identifying the Earth's magnetosphere variations. *B*x is perpendicular to the *B*y-*B*z plane, extending between the Earth and the Sun's centre and points towards the Sun, whereas By is perpendicular to the *B*x-*B*z plane, containing the Earth's dipole axis and completing the orthogonal coordinate system. *B*z represents the Earth's north magnetic dipole. For STEREO spacecraft, the Radial-Tangential-Normal (RTN) system has been used. This system can be aligned with the spacecraft, the Earth or with any other planet. R points radially away from the Sun's centre towards the observer, T is perpendicular both to R and to the solar rotational axis, and N represents the product of R and T.

2.4.2 ACE Solar Wind Electron Proton Alpha Monitor (SWEPAM)

The SWEPAM instruments (McComas *et al.*, 1998) measure the three-dimensional characteristics of solar and suprathermal electrons. They provide detailed knowledge of the solar wind conditions and ideal data set for both heliosphere and magnetospher, which can be used in conjunction with concurrent data from spacecraft such as Ulysses. SWEPAM-I collects full 3-D plasma measurements of protons and alpha particles

every 64 s with an energy resolution ΔE/E ≈ 5 %, an angular resolution of 5˚ in the polar heading, and 3˚ to 4.5˚ in the azimuthal orientation. SWEPAM-E collects full 3-D plasma electron measurements within the same timeframe as SWEPAM-I, with an energy resolution of ≈ 12% wide.

The SWEPAM-E plots of suprathermal electrons pitch angle distribution display functions at 10 energies, ranging from 73 eV to 1137 eV. Each pitch angle bin is 9° degrees, spanning from 0° to 180°. 272 eV energy is typically representative of the suprathermal population, however lower energies can still be part of the thermal core distribution, depending on the conditions. Higher energies can more easily be contaminated by energetic particles, light or other substances, since they are typically lower in numbers.

2.5 The Solar Terrestrial Relation Observatory (STEREO)

STEREIO (Kaiser et al., 2008) is NASA's third solar-terrestrial programme mission. Twin spacecraft were successfully launched in October 26, 2006 to their orbits around the Sun. During their orbital journey, one of them travelled further ahead (STEREO A), whereas the other (STEREO B) fell behind the Earth (Figure 2.3). These two positions allow for unique and 3-D views of the Sun and the interplanetary medium, including CME evolution and propagation. Each year the separation angle between the two spacecraft increases by about 44 to 45 degrees. Each spacecraft has on board four instruments packages, two instruments and two instruments suites, with a total of 13 instrument each.

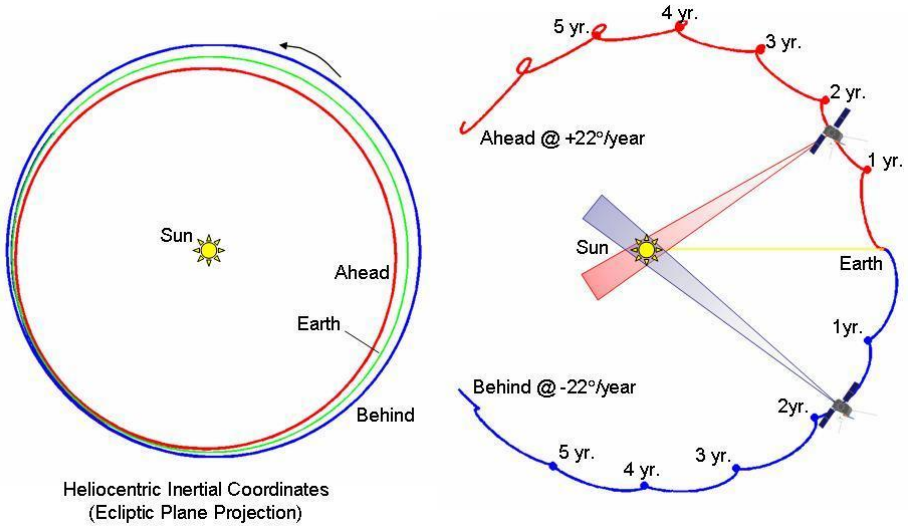

Figure 2.3 Left panel: the leading (red) and trailing (blue) trajectory of STA & STB to the Earth. Right panel: STA & STB opposite orbital paths around the Sun.(Kaiser and Adams, 2007)

2.5.1 Sun Earth Connection Coronal and Heliospheric Investigation (SECCHI)

SECCHI (Howard *et al*., 2008) consists of a suite of remote sensing instruments that study the 3-D evolution of CMEs originating from the Sun, travelling to the interplanetary space and eventually to Earth. These instruments are:

- Two White Light Inner and Outer Coronagraphs (COR1, COR2) which capture images of the solar corona in a field of view ranging from 1.4 to 4 solar radii for COR1 with a pixel size start from 512x512 with 15 arcsec pixel^{-1} resolution to 2048x2048 with 3.75 arcsec pixel^{-1} resolution (Thompson *et al*., 2010) and a field of view ranging from 2.5 to 15 solar radii for COR2. It provides a full-resolution images of 1024x1024 with 14.7 arcsec pixel^{-1} resolution (Howard *et al.*, 2008).
- Extreme Ultraviolet Imager (EUVI): used to observe the upper chromosphere in the ionized helium emission at 304 A wavelength, and the inner corona in the ionized iron emissions at 171A, 195A, and 284A (Howard *et al.*, 2008).
- Heliospheric Imager (HI1, HI2): observes CMEs with field of view of 15 to 215 solar radii on the respective Earthward side of the Sun (Howard *et al.*, 2008).

2.5.2 *In Situ* Measurements of Particles and CME Transient (IMPACT)

IMPACT (Luhmann *et al*., 2008) consists of seven instruments distributed over two suites:

- The boom suite, which includes: Solar Wind Electron Analyzer SWEA, Suprathermal Electron Telescope SET, and Magnetometer MAG, located on the IMPACT boom mast. MAG (Acuña *et al.*, 2008) measures the three components of the vector magnetic field in a range of +/- 512 nT.
- The SEP suite, which includes: the Solar Electron Proton Telescope (SEPT), the Suprathermal Ion Telescope (SIT), the Low Energy Telescope (LET), and the High Energy Telescope (HET). This suite of instruments samples the 3-D distribution and provide the plasma characteristics for solar energetic ions and electrons and the local vector magnetic field.

2.5.3 Plasma and Suprathermal Ion Composition (PLASTIC) (Galvin et al., 2008)

This measures the *in situ* solar wind characteristics of protons and alpha particles, as well as the mass and charge state composition of heavy ions in order to distinguish CMEs plasma from the ambient solar wind. It consists of a package of three sensors:

- Solar Wind Sector (SWS) proton channel: measures the solar wind proton density, velocity, temperature and alpha to proton ratio with a time resolution of up to 1 min.
- Solar Wind Sector (SWS) composition channel: measures the charge state distribution, elemental composition and heavy ion temperature and speed.
- Wide Angle Partition (WAP): measures the suprathermal ion distribution functions.

Figure 2.4 displays an artist's rendition of STB instruments.

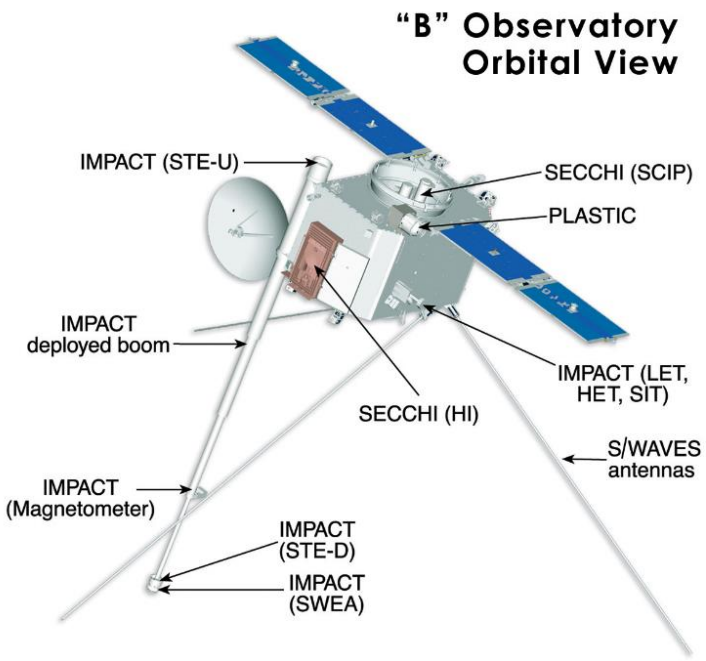

Figure 2.4 An artist's scheme of STB and its instruments. SECCHI and PLASTIC instruments are pointed sunward, whereas SWAVES antennas and IMPACT boom are placed on the opposite end (Kaiser and Adams, 2007).

Chapter 3

Properties of the HPS-ICME-CIR interaction event of 09-10/09/2011*

* This chapter has been accepted for publication in the Journal of Geophysical Research-Space Physics (**DOI:**10.1002/2017JA024849).

Abstract

During September 09-10, 2011 the ACE, Wind and SOHO spacecraft measured the complex interaction between an interplanetary coronal mass ejection (ICME) and a co-rotating interaction region (CIR) associated with the heliospheric sector boundary. Except for a few short periods, the suprathermal electrons are unidirectional, suggesting the ICME magnetic field has opened through interchange reconnection. Signatures of interaction are distributed throughout the event suggesting that the structures have become entangled, or embedded. Since the ICME speed is relatively low, the strong forward shock must be caused by the ICME-CIR interaction. Other interesting features are the upstream heating flux discontinuity, the very high proton density in the frontal boundary of the heliospheric plasma sheet and the forward shock, the significant speed elevation within the sheath, the distortion of *Bz* in the magnetic cloud, the indistinct location of the stream interface, the unidirectional domination of the suprathermal electrons and the reverse shock at the CIR rear boundary. There is an unusual delay between the proton density and temperature profiles. Furthermore, large differences in proton speed and forward shock density measured between L1 spacecraft indicates high variation at small spatial scales. A few days earlier, STEREO B recorded the undisturbed CIR, which shows that (i) some general features of the CIR are preserved (ii) the CIR is compressed by a factor of ∼4 by the ICME and (iii) a magnetic exhausted region at the front of the CIR is a continuous feature and is not formed due to the ICME interaction.

A survival of a magnetic exhausted region at the front of the CIR before and with the interaction, suggests that care must be taken in the interpretation of many other similar cases. Accurate interpretation of many complex *in situ* interaction events is difficult without a comparison of events in the absence of interaction.

3.1 Introduction

Coronal mass ejections (CME) are eruptions of magnetised plasma from the solar atmosphere, with a broad range of propagation speeds and mass (Gopalswamy and Kundu, 1992;Hudson et al., 1996). Interplanetary coronal mass ejections (ICME) are the interplanetary manifestation of CMEs, identified by *in situ* measurements of the solar wind (Burlaga et al., 1981;Zurbuchen and Richardson, 2006;Richardson and Cane, 2010). Slow, dense solar wind, which manifests itself as streamers or pseudostreamers in the corona, are associated with closed field regions of the Sun (Gosling et al., 1981;Morgan et al., 2013), whilst the fast, low-density streams arise from open field regions (Krieger et al., 1973). The distribution of slow and fast winds can be complex, and changes rapidly during the solar cycle in relation to the magnetic configuration of the photosphere (Morgan and Habbal, 2010;Morgan, 2011). The interaction between streams form compression or rarefaction termed Stream Interaction Regions SIR(Parker, 1963;Hundhausen and Gosling, 1976;Pizzo, 1978) or Co-rotating Interaction Regions (CIR) when an SIR recurs with solar rotation (Gosling and Pizzo, 1999;Jian et al., 2006b).

ICMEs may interact strongly with the ambient solar wind, making precise identification of their boundaries difficult (Gopalswamy, 2006). Two common complex interaction cases are ICME-ICME interaction and ICME-SIR interaction. For example, Burlaga et al. (1987) studied the interaction between a magnetic cloud (MC) and a CIR using 3 spacecrafts at different longitudes. Lepping et al. (1997) described an event measured approximately 175 R_E upstream of the Earth, consisting of a shock wave observed ahead of an MC whose speed exceeded the ambient solar wind speed. Furthermore, the MC was followed and overtaken by a CIR that compressed the rear of the MC, and a two-stream interface (SI) observed an hour later. Significant to this case was the sudden rise in the magnetic field magnitude from 21 nT to 30 nT within the MC and an abnormal twin-peaked density in the solar wind following the MC. The sudden increase of the MC magnetic field could have been the result of CIR-induced compression at the rear boundary of the MC. The CIR interaction with the MC may have produced an instability which formed a complex boundary. Alternatively, it might have been part of another solar event, or the high stream interaction with the current sheet. This ambiguity highlights the difficulty of interpreting complex interacting streams and ICMEs.

Wei et al. (2003) studied many cases of interaction between MCs and the ambient solar wind, concluding that these interactions complicate the identification of the MC boundaries. Another well-studied case of ICME-CIR interaction occurred during the passage of an MC following a CIR during January 1997 (Burlaga et al., 1998). Its most remarkable feature was a very high density and $^4He^{++}/H^+$ ratio in the rear of the MC originating from the prominence material core of the CME. The further development of ICME-HSS interaction studies was made possible by the Sun Earth Connection Coronal and Heliospheric Investigation (SECCHI,(Howard et al., 2002)) instruments on board the Solar Terrestrial Relations Observatory (STEREO(Kaiser, 2005)), in particular the Heliospheric Imagers (HI). Rouillard et al. (2009) used HI to identify the geometry of CIRs and their interaction with ICMEs at 1 AU based on HI-1B and HI-2B time-differenced images of the July 19, 2007 event. Farrugia et al. (2011) studied a complex MC-CIR interaction near the heliospheric current sheet on

November 19-20, 2007. Multiple spacecrafts measurements enabled a reconstruction of the flux rope structure, and clear signatures of forward and reverse shocks near Earth.

Often associated with CIRs are sector boundaries (SBs), or the heliospheric current sheet (HCS), between large-scale regions of inward and outward directed magnetic fields (Wilcox and Ness, 1965;Svalgaard and Wilcox, 1975). SBs are associated with increased ion flux, plasma density and a decreased solar wind speed(Crooker et al., 2004a;Blanco et al., 2006;Khabarova and Zastenker, 2011). In the context of ICME-SIR interaction regions, the identification of a single sector boundary becomes more difficult or impossible. Furthermore, there is often considerable mismatch between sector boundaries identified by magnetic field reversals and those identified by electron polarity reversals (Kahler and Lin, 1994;Kahler and Lin, 1995;Crooker et al., 2002). For example, Crooker et al. (1996) found 14 reversals of the magnetic field during 2 days of measurements, and proposed a multiple flux tube structure resulting in pockets of 'false' polarities and a folded heliospheric current sheet.

CME-coronal hole interaction can result in interchange reconnection between the closed magnetic loops of CMEs and a neighbouring open field (see, for example Crooker et al., 2002;Crooker et al., 2004b;Wang and Sheeley Jr, 2003;Harra et al., 2007;Fisk, 2005). Interchange reconnection leads to localized magnetic field reversals near sector boundaries, particularly in the presence of ICMEs. In the case of closed neighbouring field lines, a partial disconnection will be the dominant mechanism. Gosling et al. (1995) used interchange reconnection to explain the unidirectional heating flux (strahl) beams associated with opened field lines in ICMEs resulting from partial disconnection. By analysing 48 MCs, Shodhan et al. (2000) found sizeable signatures of open magnetic field at 1AU, and suggested a process of continual interchange reconnection which continued until the ICMEs became completely open.

Winslow et al. (2016) conclude that caution should be exercised regarding geomagnetic storm forecasting that depends upon ICME magnetic field observations close to the sun, especially when there is an interaction with co-rotating structures, because this interaction could change the morphology of the magnetic field measurements. They studied HPS/HCS-ICME interaction using Messenger (ANDREWS et al. (2007)) and Stereo A observations and found a turbulent region within the STEREO A MC flux rope observations; however, no change in Messenger data was observed. They attributed this turbulence to the ICME- HPS/HCS interaction during the ICME propagation through interplanetary space.

This study investigates the properties and characteristics of three large-scale interacting structures (a CIR, associated with a HPS, and an ICME), and seeks to measure the extent to which this interaction affects their magnetic field and plasma properties. In section 3.2, we present the remote sensing and in situ instruments; in section 3.3, we examine the coronal observations of the September 06 CME observation, and its L1 *in situ* interplanetary magnetic field and plasma observations on September 09, also examine the HPS, HCS, SBC and the CIR *in situ* measurements. In addition, the section included a comparison with a CIR recorded in September 04, 2011 by STEREO B in the absence of an ICME. Conclusions are given in section 3.4.

3.2 Instruments

Remote sensing observations used in this study are made by the C2 instrument of the Large Angle Spectroscopic Coronagraph (LASCO)(Brueckner et al., 1995) on board The Solar and Heliospheric Observatory (SOHO)(Domingo et al., 1995) and the COR 2 coronagraph of STEREO A, Extreme Ultraviolet (EUV) images of the low corona are from the Atmospheric Imaging Assembly (AIA)(Lemen et al., 2011) instrument aboard the Solar Dynamics Observatory (SDO)(Pesnell, 2015). Photospheric magnetic map observations are made by the Helioseismic and Magnetic Imager (HMI/SDO(Scherrer et al., 2011)). These remote observations are used to provide context and to interpret the *in-situ* measurements made by spacecraft near Earth.

The *in-situ* data are from the Advanced Composition Explorer (ACE)(Stone et al., 1998) and Wind spacecrafts near L1. The *in-situ* instruments are listed in Table 3.1. The proton density is missing or contain data gaps in the ACE 64s cadence data. The ACE 5 minutes browse is available but not suitable for the scientific studies, so it has used the SOHO/CELIAS 5-minute.

There are large gaps also in the corresponding Wind 1 min magnetic field and plasma measurements. Wind observations, when available, are used for comparison with ACE. The suprathermal electron pitch angle distributions measured by SWEPAM-E/ACE are provided at 10 energy channels ranging from 73eV to 1.37 KeV. Here we use the. 272 eV channel because data at that energy are typically representative of the suprathermal population, although lower energies can still be part of the thermal core distribution, depending on conditions. Higher energies are more prone to contamination by energetic particles or other effects, and the count rates are typically lower. The low counts can also mean that the high energies are more sensitive to errors arising from combining data from detectors with very different gains. This study also used in-situ measurements which mentioned in Table 3.1.

Spacecraft	Magnetic field Instrument	Solar wind Plasma Instrument
ACE	Magnetic Field Experiment, MAG (Smith et al., 1998a)	Solar Wind Electron Proton Alpha Monitor, SWEPAM (McComas et al., 1998)
Wind	Magnetic Field Investigation, MFI (Lepping et al., 1995)	Solar Wind Experiment, SWE (Ogilvie et al., 1995)
STEREO B	In situ Measurements of Particles and CME Transients, IMPACT (Luhmann et al., 2008)	PLASMA AND SUPRATHERMAL ION COMPOSITION (PLASTIC)(Sauvaud et al., 2008)
SOHO	-	Charge, Element, and Isotope Analysis System/Mass Time-of- Light (CELIAS/MTOF) (Ipavich et al., 1998)

Table 3.1 The in situ Magnetic field and Solar wind plasma instruments of ACE, Wind, STB and SOHO

Since the ACE magnetometer and SOHO proton measurements are available throughout the event, they are shown together for the purpose of comparison in many figures. From the relatively close locations of the three L1 spacecraft as shown in Figure 3.1, similar measurements would be expected. However, as will be shown, significant differences are seen during some periods. Large differences over small spatial scales have also been reported for Helios measurements for two spacecraft separated by only 1˚ latitude in the same coronal hole (Schwenn, 1990). Based on STEREO and ACE measurements, Rouillard et al. (2009) found different CIR speed profiles over small latitudinal ranges.

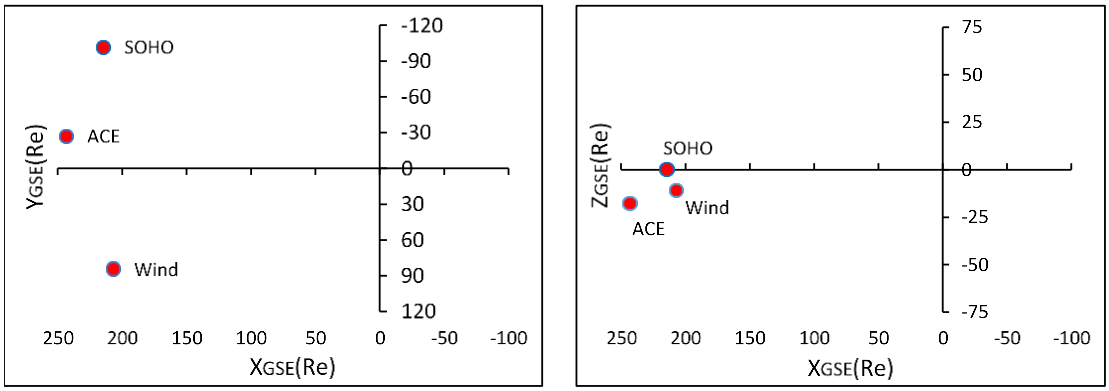

Figure 3.1 The L1 spacecraft positions ACE, Wind and SOHO on September 09, 2011 (1Re= 6371.2 km)

3.3 Results

3.3.1 Eruption and low-coronal propagation

Figure 3.2 shows the solar disk as observed in EUV during September 06, 2011. A large active region (NOAA AR11283), the source of the ICME under study, is situated at N14 W18, with a complex beta-gamma-delta configuration. Also of relevance to this study is the equatorial coronal hole to the east of the meridian (CH475). The coronal hole extends from latitude -25˚ to 30° and is 15° wide in longitude. The coronal hole is a persistent feature for several rotations, and is the source of a CIR. During September 06, there is two halo CME erupted at 02:24 UT from the location N14 W07 and 23:05 UT from the location N14 W18 (the first one mentioned in SOHO/LASCO catalogue as poor event). Also, on September 07, there are two partial halo CMEs erupted at 18:48 UT from the location N23 E54 and at 23:05 UT from the location N14 W28. It has tested the estimated transit times of these CMEs based on the onset times and speed, and the space speed. The September 06, 23:05 UT CME is the optimise to matching with the September 09 ICME. Its estimated transit time is about 61 hours (with space speed about 680 km/s). This value is close to Wu et al. (2016) who have tested these four CME candidates sources of the ICME September 09, 2011 forward shock that emitted during September 06 and 07, 2011, erupted from N17 W07, N14 W18, N23 E54 and N14 W28.They concluded that the September 06 (N14 W18) is the most likely driver of the September 09 ICME forward shock.

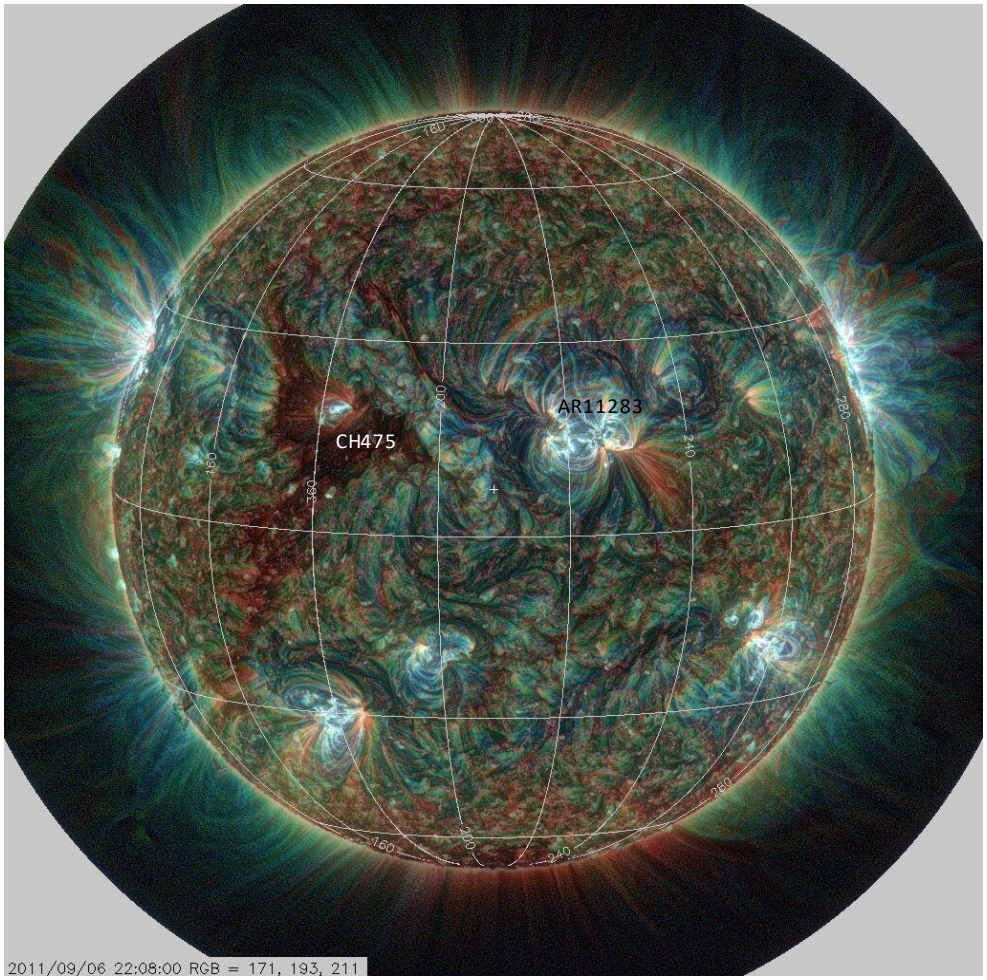

Figure 3.2 Composite EUV image of the solar disk and low corona made using AIA/SDO observations during 2011/09/06 12:00. The three-color red-green-blue image channels are composed of observations made in three AIA channels: 171Å, 193Å and 211Å respectively, corresponding to their most dominant emission lines of Fe IX, Fe XII and Fe XIV with formation temperatures ~ 0.7, 1.2 and 2.0 MK. The images have been processed using Multiscale Gaussian Normalization (MGN, (Morgan and Druckmüller, 2014)).

As shown in the AIA/SDO sequence of Figure 3.3, there is a sigmoid magnetic structure (indicative of a twisted flux tube/toroid instability) embedded within the heart of the west footpoint of the active region. The sigmoid is clearly seen at 22:03 UT. Immediately following there is a very rapid (impulsive) eruption, and a post-flare arcade appears by 22:51 UT. Associated with the eruption is a massive X2.1 flare on September 06, 22:20 UT, accompanied by Type II and IV radio bursts. The pre-eruption configuration and initial stages of the eruption have been simulated in detail using a non-linear force-free model by Jiang et al. (2013). They suggest that reconnection at the null-point cuts overlying tethers and probably triggers the torus instability of the flux rope, which results in the eruption.

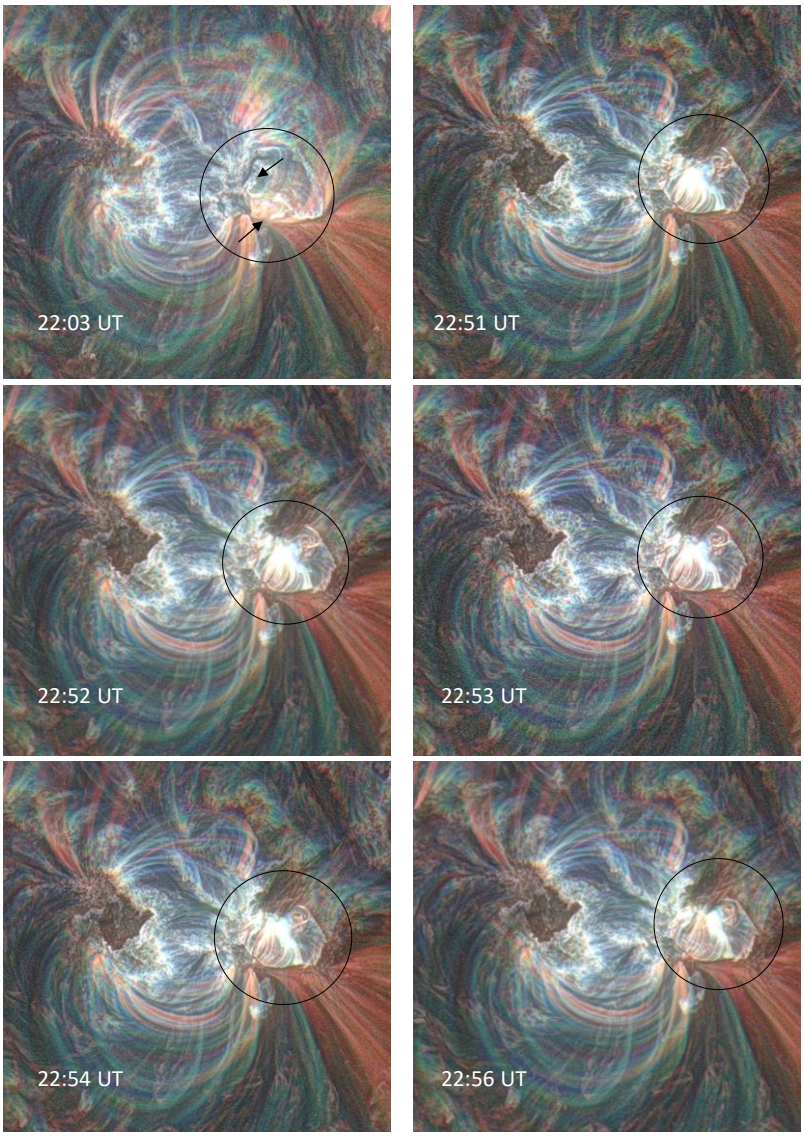

Figure 3.3 The September 6,2011 AR11283 flux rope. The upper left panel displays the S sigmoid at 22:03 UT whereas the other panels show the magnetic flux rope sequence for a few minuites. These images have been processed using MGN. The two arrows on the upper left panel determine the two ends of the S sigmoid and the the black circules on all panels display the flux rope progress position during the panels times.

At around 23:00 UT, the CME of interest from AR11283 appears as a fast halo CME in the LASCO C2 field of view, shown in the top row of Figure 3.4. This is a halo CME skewed towards the north-west corona. In the LASCO C2 image, part of the halo CME shares the field of view with the previous 3-part CME in the north-west, making it difficult to interpret its structure. The bottom row of Figure 3.4 shows the same CME as viewed by STEREO COR2 A.
From this viewpoint, the bulk of the CME of interest is seen just northward of the equator. The other 3-part CME is at apparent high latitude, with only a small overlap between the two. The large CME from AR11283 has an extremely complicated structure, seemingly composed of a main frontal system of distinct loops. These propagate outwards at high speed. Behind, or within, these loops are myriad dense clouds of material that may be interpreted as the CME core. This is not a compact core sitting tidily near the CME centre - it is distributed as several spread-out blobs across a wide portion of the CME. Hours after the main front of the CME has passed from the COR2A field of view, sizeable, fast and dense material continues to

propagate outwards. The last sizeable blob passes out of the field of view at around 05:00 UT on 2011/09/07. The central latitude of the CME is around 20° north, and although the bulk of the CME lies north of the equator, there is considerable material propagating along the equator. The southern extremity of the CME is approximately 30° south.

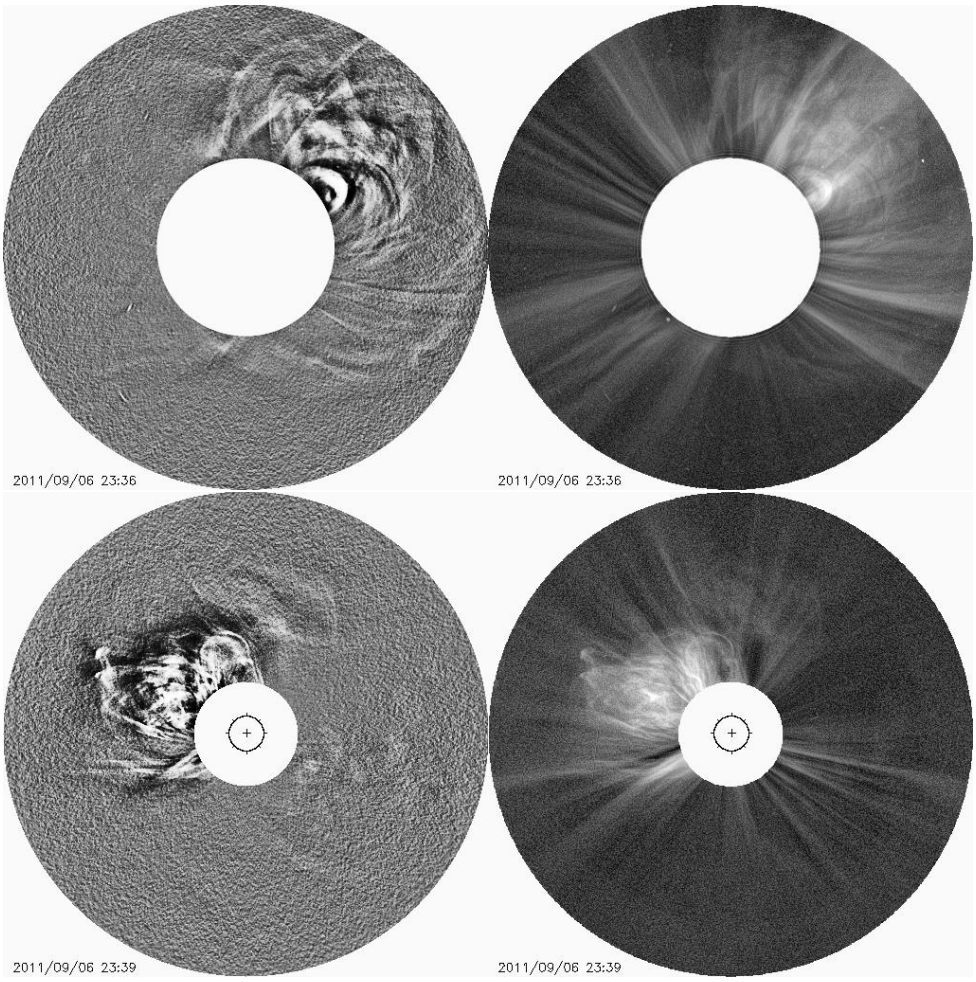

Figure 3.4 Top row shows a LASCO C2 image of 2011/09/06, 23:36 UT, showing a halo CME skewed towards the north-west and a previous 3-part CME in the north-west. Bottom row shows a STEREO COR2 A image of 2011/09/06, 23:39 UT. The CME of interest is distributed from around -30 to +60 from the equator. The previous 3-part CME is at high latitude, although there is some overlap between the two CMEs. The left images have been processed using a Dynamic Separation Technique to remove quiescent radial structure (Morgan and Habbal, 2010), and the right images have been processed using the Normalizing Radial Graded Filter of Morgan et al. (2006).

3.3.2 ICME measurements

ACE *in situ* plasma and magnetic field measurements are displayed in Figure 3.5 for September 09, 00:00 UT to September 11, 12:00 UT, spanning the occurrence of the ICME arising from the 2011/09/06 eruption (the proton density data is from SOHO/CELIAS). The ICME is interacting with the SIR arising from the equatorial coronal hole 475 seen in Figure 3.2. This interaction region is clear given the values of the solar wind flow speeds immediately following the disruption of the ICME, which reaches a maximum of >600 $km\ s^{-1}$. During September 09, both the ACE and Wind spacecrafts recorded multiple inversions of the

azimuthal magnetic field and a frontal large increase in density (SOHO and Wind), plasma beta(Wind)(see Wind magnetic and plasma morphology for September 09 in Figure 3.10) and

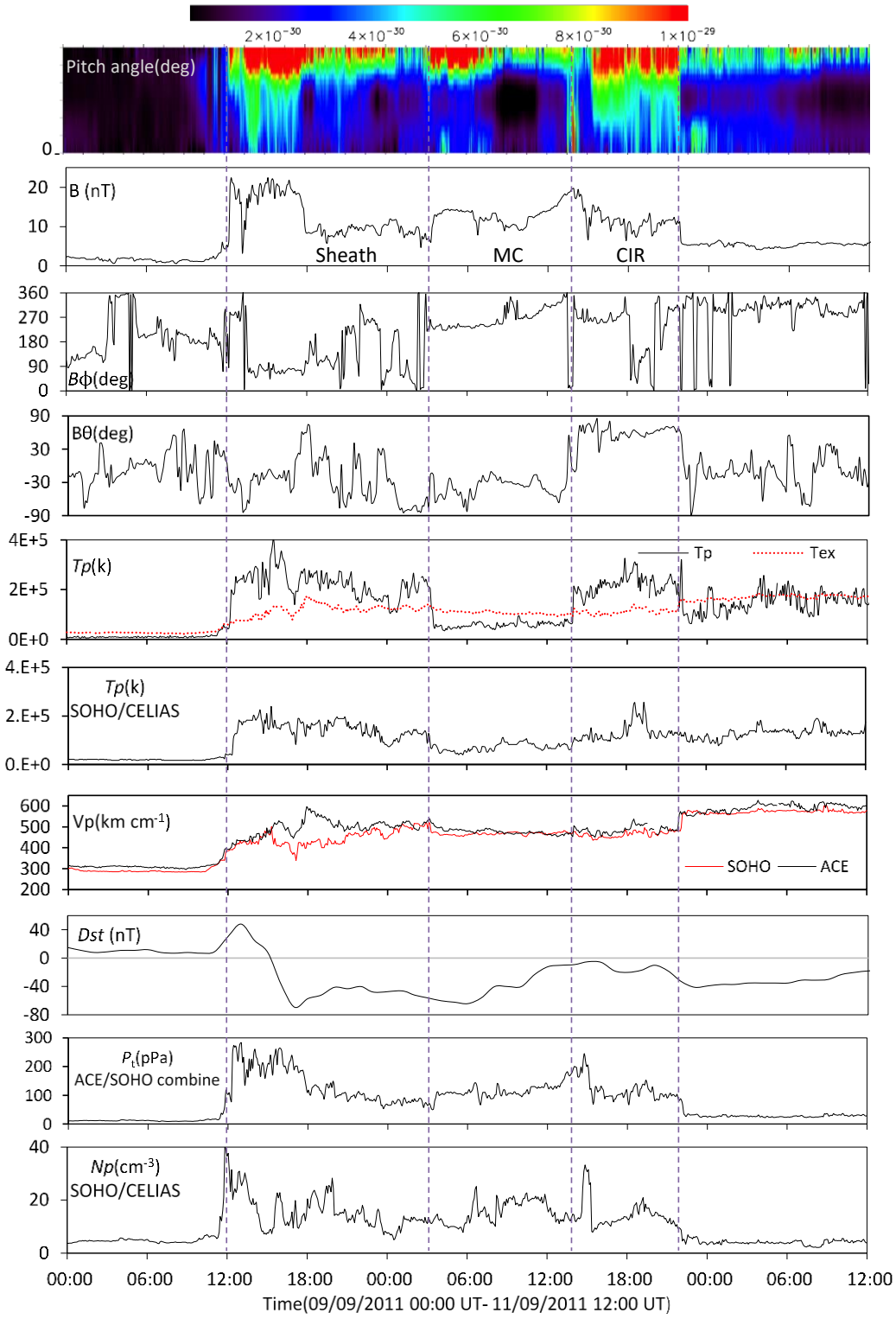

Figure 3.5 displays the event Magnetic field and plasma parameters. From the upper panel: the ACE color-coded electrons pitch angle distributions f(v) (cm^{-6} s^3) at 272 eV energy (Color-coding for f(v) is logarithmic and ranges from $5\times10^{-31}s^3cm^{-6}$(dark blue) to $2\times10^{-29}s^3cm^{-6}$(dark red)), Magnetic field strength B(nT), Bφ(deg), Bϑ(deg), proton temperature Tp(k), SOHO proton temperature Tp(k), ACE(black) and SOHO(red) proton speed Vp(km s^{-1}), Dst index(nT), ACE/SOHO combine total pressure Pt(pPa) and proton density Np(cm^{-3}) from SOHO.

solar wind speed elevation, consistent with an interplanetary forward shock (first vertical dashed line). The increase in the magnetic field magnitude during the shock and the sheath region exceeded 20 nT at times. This shock seems extremely strong, inconsistent with ideal MHD. Later in this chapter we attribute the strength of the shock to the interaction between the ICME and the CIR (section 3.3.6 and 3.3.8). The ICME was geoeffective (*Dst* ~ -69nT). The ICME is driving a forward shock as the cloud front boundary speed relative to the upstream solar wind exceeded the magnetosonic speed (50-70 Km/s).The shock passes over ACE at 2011/09/09, 12:14 UT and is followed by a sheath. The solar wind proton temperature jumps from 4.63×10^4 to 1.98×10^5 k and is accompanied by increases in: magnetic field strength (from ~ 5 to 20 nT); proton density to values of about 40 cm^{-3}(from SOHO); and proton flow speed. The sheath duration is very long (over 15 hrs) suggesting that ACE is traversing the ICME flank. This is largely consistent with the configuration of the CME as viewed by coronagraphs in the low corona.

A distinct region of the ICME follows the sheath, bounded by the 2nd and 3rd vertical dashed lines at 2011/09/10, 03:30 UT and 14:00 UT, and is characterised by an abrupt reduction of proton temperature to values lower than the ambient solar wind e.g. (Richardson and Cane, 2010) , a magnetic field strength increase from 6.2 to 14.4 nT and an azimuthal magnetic field *B*ϕ rotation. The T_p/T_{ex} ratio (Richardson and Cane, 1995) was used to identify the Magnetic cloud MC boundaries. The magnetic field component during this period, shown in more detail in Figure 3.6, reveals a coherent rotation in the *Bx* and *By* components and a less clear rotation in *B*z. These characteristics suggest that ACE is traversing the main flux rope (magnetic cloud) region of the ICME. The magnetic field vectors rotate for 10.5 hrs through an angle >30˚. The sudden variation of *B*z in the mid-point of the MC is maybe due to the ICME-SIR interaction, which can distort the flux rope whilst maintaining the general helical field topology (Zhang et al., 2013).

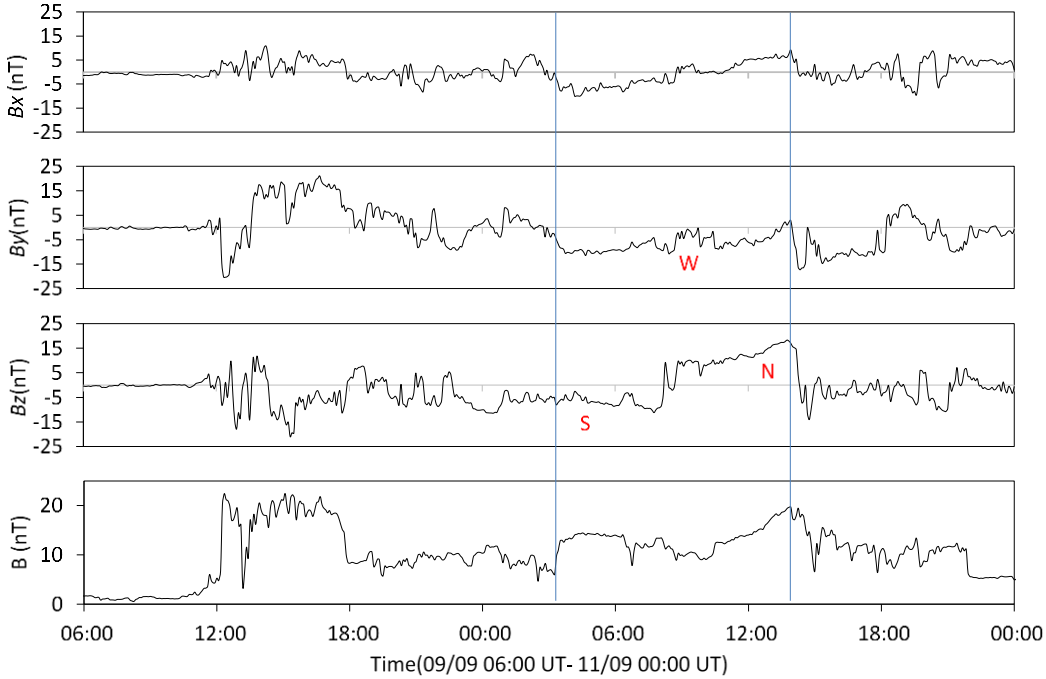

Figure 3.6 The interplanetary magnetic field vectors (Bx,By and Bz) and their directions through the MC. Blue vertical lines are the MC boundaries. The symbols W, S and N refer to the flux rope directions: West, South and North respectively.

Within the magnetic cloud, the *By* component has a unipolar negative polarity as the *Bx* and *Bz* components rotate from negative to positive (south to north). From this, the MC has a South-West-North (SWN) signature and has a Right hand (RH) helicity as viewed by an observer looking towards the Sun (Bothmer and Rust, 1997;Mulligan et al., 1998), and the *Bz* bipolar signature exhibits an elliptically aligned magnetic flux rope (Mulligan et al., 1998). The short duration of the flux rope, preceded by a long sheath duration, may supports the scenario of the spacecraft passing through the ICME flank (qualitatively matching track 4 of Gopalswamy (2006) where the spacecraft traverse through the Shock, Sheath and finally the MC from the flank). The ACE/SOHO combine total perpendicular pressure profile (P_t) can give an indication of the distance of the spacecraft path from the ICME centre. P_t increases at the leading edge of the ICME (Figure 3.5) followed by a long plateau and then another increase at the rear part of the ICME. This Pt morphology matches the Group 2 morphology of (Russell et al. (2005);Jian et al., 2006a) and confirms that the spacecraft traverses the ICME flank.

3.3.3 CIR measurements

The transequatorial coronal hole CH475 (Figure 3.2) persists for several rotations and is the source of the CIR that follows the ICME, readily identified by an overall increase in the solar wind velocity, an enhancement of proton density, temperature and compression of the magnetic field magnitude (Siscoe and Intriligator, 1993;Neugebauer et al., 2004;Jian et al., 2006b). The MC rear speed is slower than the following fast wind, and there is an interaction region at the rear boundary of the MC, including what seems like a slow shock (Figure 3.5, 3rd vertical line), seen at 2011/09/10 13:59 UT and characterised by an increase in proton temperature, an abrupt increase in density and a drop in the magnetic field magnitude. The CIR ends with a distinct fast reverse shock at 21:54 UT, identified by a clear increase in proton speed and a decrease in the magnetic field magnitude and temperature. The formation of the reverse shock and the apparent front slow shock within 1AU is due to the existence of the ICME (see, for example Gosling et al., 1976;Smith and Wolfe, 1976)(more details in section 3.3.7). The high-speed stream (HSS) follows the CIR reverse shock. The proton speed increases abruptly from 480 to 559 Km/s and exceeds 615 Km/s after about 5 hours, and the HSS of CH475 continues for a few days.

The presence of the CIR and HSS may have affected the ICME bulk speed morphology. The decrease of the ICME speed (from almost 600 km/s) within the sheath to ∼450 km/s at the trailing edge of the MC indicates an overall deceleration of the ICME from the low coronal speed, and an expansion of the structure. The size of the sheath is estimated as ∼0.18 AU and that of the MC as ∼ 0.12 AU are less than the typical sizes at 1 AU, despite the continual expansion. This expansion suggests that, besides the possibility of the spacecraft's trajectory passing through the flank, the ICME may have witnessed a deflection due to the neighbouring coronal hole (CH475 high stream) and the SIR overtaking the rarefied region of the MC (e.g. (Gopalswamy et al., 2009).

3.3.4 Geomagnetic response

During the ICME-CIR arrival at Earth, the magnetosphere was under the influence of both structures. Panel 8 of Figure 3.5 shows the *Dst* index, which increases with the arrival of the ICME in response to the shock compression (B magnitude peaked to 20-22 nT). At 2011/09/09 15:00 UT, the main phase (which represents the ring current injection) started with a substantial decrease of *Dst* values to < -69 nT - a moderate storm. The main phase occurs in response to the southward interplanetary magnetic field, when *Bz* dipped to 21 nT south, and followed by a recovery phase where the *Dst* increased gradually until 2011/09/10 16:00 UT. In response to the CIR, the *Dst* varied and dropped again to -41 nT at 2011/09/10 23:00 UT, followed by the CIR recovery phase.

3.3.5 Heating flux distribution and interchange reconnection

Panel 1 of Figure 3.5 shows the suprathermal electron pitch angle distribution at 272 eV energy in the solar wind frame. In general, the suprathermal electrons are unidirectional with a 180° pitch angle, except at a few times at the CIR boundaries. The unidirectional strahl displays a temporal variation with a sporadic broad intense strahl (between 40°- 50°) at the front region of the sheath, MC and during the CIR duration. The strahl became narrower during the rarefied region of the MC and after the CIR reverse shock. We notice that 90° electron depletions are observed on all three days. The appearance of the 180° unidirectional pitch angle during the ICME-CIR passage suggests that the ICME magnetic field lines are predominantly open, which is probably due to interchange reconnection between ICME and the neighbouring coronal hole.

Figure 3.7 highlights the solar photospheric magnetic field map and a schematic of the MC flux rope structure and its footpoints. The flux rope has an SWN signature rotation with a right hand (RH) helicity. The map displays the negative (inward) rooted polarity of the MC left leg and the positive (outward) leg polarity of the right.

During its interval, the MC local magnetic field longitude $B\phi$ was steady (hovering between inward and orthogonal with an inward domination of $\sim 315°$ (in accordance with the Parker spiral distribution of the interplanetary magnetic field). Since the suprathermal electron distribution remained unidirectional at 180° (opposite to the magnetic field direction), and the strahl always travels away from the sun, it can determine the overall magnetic direction as an inward and the left MC inward leg as the immersed side of the flux rope in the photosphere. Figure 3.7 suggests an interchange reconnection scenario: In conjunction with the growth and expansion of the closed flux loop, the negative and inward CH475 open field lines might swerved or diffused toward the photospheric area where the closed magnetic field lines domination and intercepted the propagation of the ICME neighbour outward leg field lines, making the MC completely open during the passage of the spacecraft at 1 AU. This view is supported by the suprathermal electrons streaming distribution within the MC which stayed antiparallel to the magnetic field.

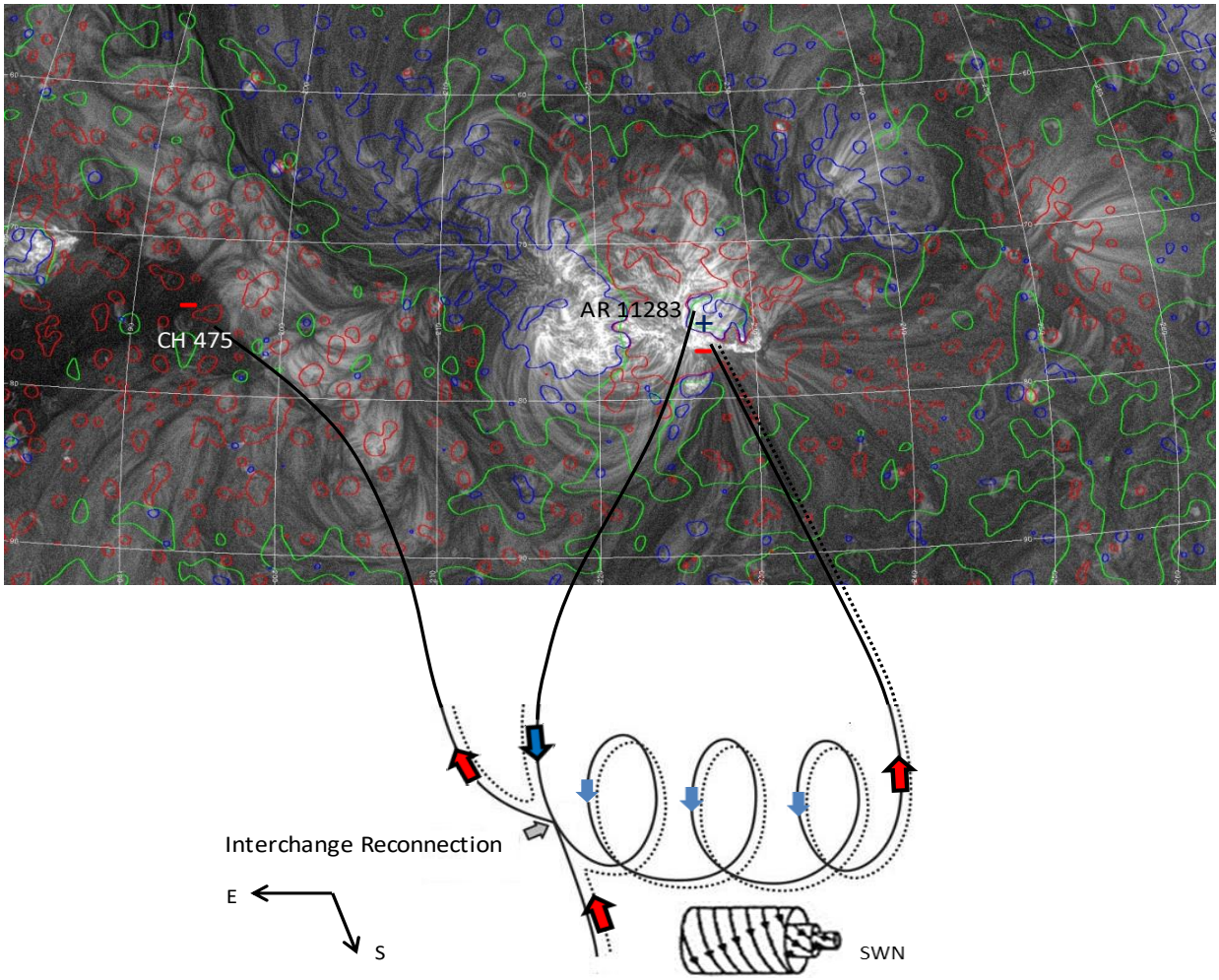

Figure 3.7 displays the photospheric magnetic field map of September 6, 2011 and a schematic of the magnetic flux rope structure. The EUV image is by AIA/SDO, and the photospheric field measurement is gained through Gaussian smoothing of HMI/SDO. It also illustrates interchange reconnection (IR) between the September 6 CME from AR11283 and coronal hole CH475. coronal hole inward field lines diverge towards the flux rope leg outward field line and an IR has occurred. Red arrows refer to the inward field line, blue arrows refer to the outward field lines and grey arrow refer to the site of IR (Modified from Harra et al. (2007)).

The sporadic, short periods of counterstreaming electrons are likely due to: 1) energized electrons leaking from the enhanced flux CIR shock boundaries into the upstream solar wind, producing a ''field-aligned'' beam of electrons which take the outward direction from both CIR shocks (see, for example, Gosling et al., 1993;Steinberg et al., 2005); 2) depletions around a 90˚ pitch angle as a result of magnetic focusing and mirroring (Gosling et al., 2001b), particularly after the CIR reverse shock e.g. (Skoug et al., 2006). Before the CIR reverse shock there is a unidirectional antiparallel stream (at a 180˚ pitch angle) (Figure 3.5 panel 1). Immediately after the CIR reverse shock, the suprathermal electrons pitch angle distribution displays a 90˚ depletion (Figure 3.8), associated with a strahl enhancement at a 180˚ pitch angle. This is likely due to energizing at the CIR reverse shock and a leak in the sunward direction into the upstream solar wind (Steinberg et al., 2005).

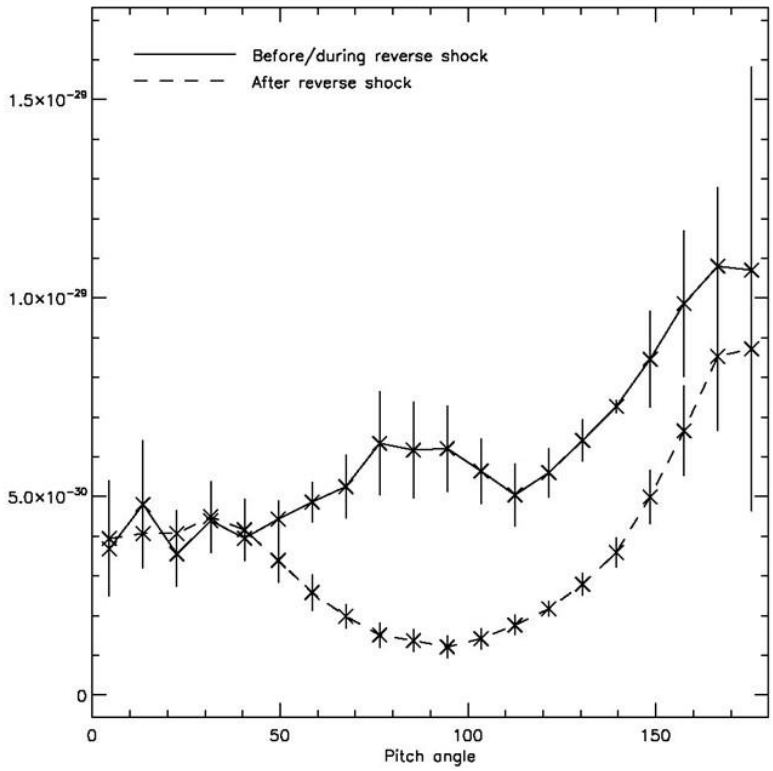

Figure 3.8 Displays the pitch angle distributions of the suprathermal electrons before/during (solid line) and after (dashed line) the CIR reverse shock. The depletion around 90˚ is clear after the shock arrival. Each profile is the median of distributions measured over a period of around 9 hours before and after the shock. The error bars show the standard deviation of values during this 9-hour period.

It is likely that interchange reconnection led to multiple field reversals within both the HCS and the sheath (Figure 3.5, panel 3) whilst the suprathermal electrons remained at a 180° pitch angle (panel 1). Since the strahl usually travels away from the Sun, the overall magnetic field direction of the event remained inward, even with the presence of the local magnetic reversals. This result implies that the pitch angle distributions of the suprathermal electrons are independent of any local magnetic field line torsion, not just in the HCS area, but also in the ICME sheath. In addition, the duration of reversals in the sheath were longer than those in the HCS, despite the high sheath compression by both the HCS at the front and the MC, CIR and HSS at the rear.

3.3.6 HPS/HCS-ICME Interaction region

On September 08, 2011, the suprathermal electron pitch angle distribution was parallel to the magnetic field. During September 09 02:00 UT- 09:00 UT (Figure 3.9, panel 1), there are a series of heat flux dropouts (HFDs), a signature of magnetic reconnection or electron pitch scattering. From approximately (09:00 UT-11:30 UT), the upstream suprathermal electrons showed a distribution peaking at 90 degrees followed by a discontinuity of electron heat flux, likely a shock, coinciding with a clear rising of plasma density and beta (Figure 3.9, panel 3 and Figure 3.10 panel 3 & 6). This is the appearance of the initial boundary of the heliospheric plasma sheet (the first blue vertical line in Figure 3.9).

The heat flux discontinuity seems to be indicative of the arrival of a high speed solar wind stream (HSS). After about 30 minutes (12:14 UT), ACE showed spikes in magnetic field, proton

temperature and total pressure referring to an ICME forward shock (the grey vertical line). During this time (at 11:44 UT), the 180˚ pitch angle distribution of the suprathermal electrons first appeared (the red dashed vertical line in Figure 3.9 and Figure 3.10), indicating a sector boundary crossing (SBC) and associated with *B*ϕ flipping from outward to inward, which means that the heliospheric current sheet (HCS) had the same SBC position (SBC- HCS matching).

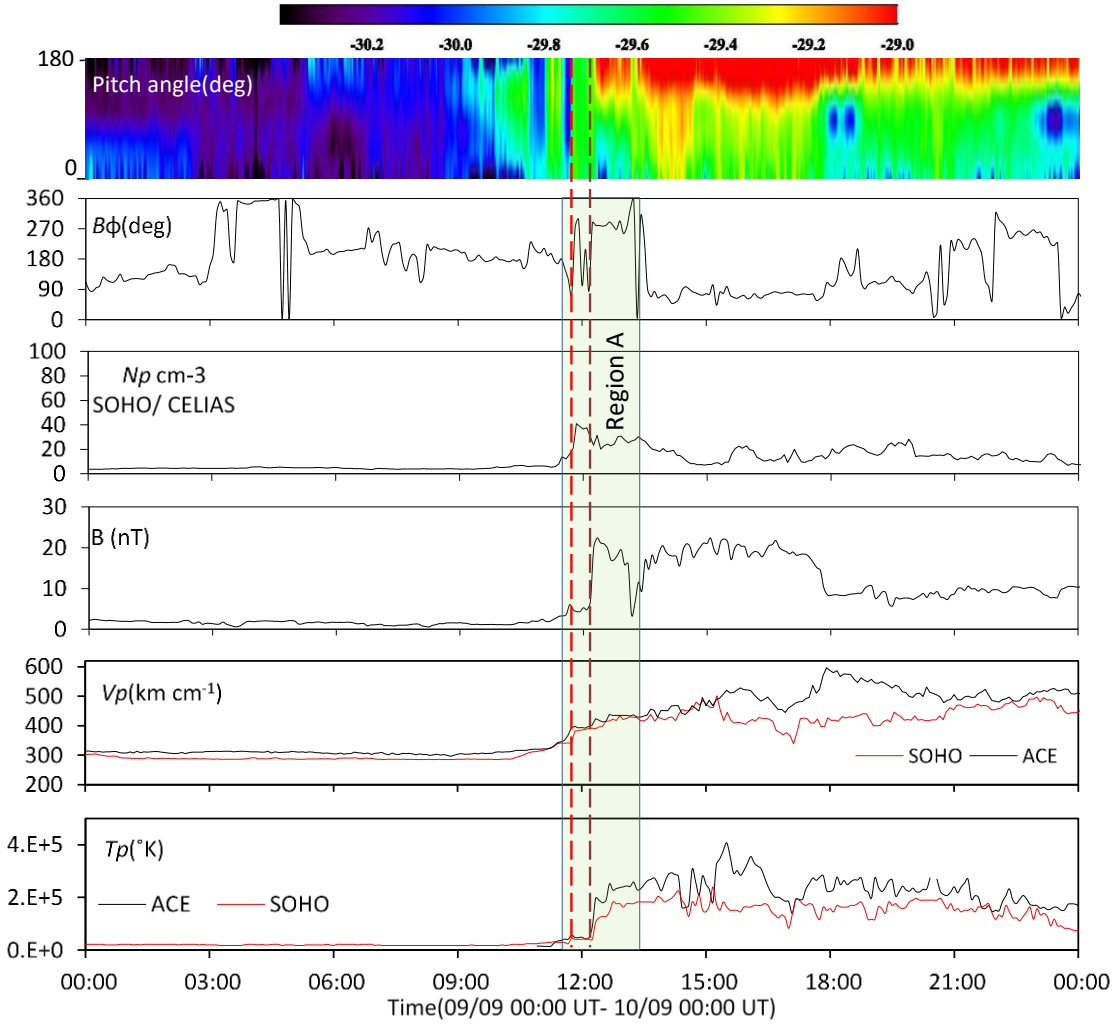

Figure 3.9 This figure highlights the Ace and SOHO region A where the HPS, HCS, SBC and the ICME forward shock occurs (the SOHO proton density profile is to cover the ACE missing data). From top to bottom, the panels show heat flux distribution, Bφ, Np, B, ACE(black) and SOHO(red) proton speed Vp(km s^{-1}), and ACE(black) and SOHO(red) proton temperature Tp(K). The two blue vertical lines refer to the HPS boundaries, the dotted red vertical line refers to the SBC-HCS region and the brown dashed vertical line refers to the ICME forward shock. Note that the heat flux distribution (top panel) shows the electron flux on a log scale to visualise variations of low signals.

For further clarification, we designate the green-shaded region as region A in Figure 3.9. This is the HPS, which has two boundaries (two vertical blue lines) identified by three main criteria: an enhancement in proton density, plasma beta enhancement and the inversion of the interplanetary magnetic field sector (see, for example, Winterhalter et al., 1994;Crooker et al., 2004a;Suess et al., 2009;Simunac et al., 2012;Liu et al., 2014). For the purposes of comparison and to compensate for missing ACE data, Wind data is shown in Figure 3.10**.** At

the HPS boundaries, two spikes in plasma beta can be seen: the first peaking at approximately β=11 and the second at β=28 in Wind (ACE data is missing). These are associated with a high reduction of the magnetic field magnitude and short discontinuities of the heating flux.

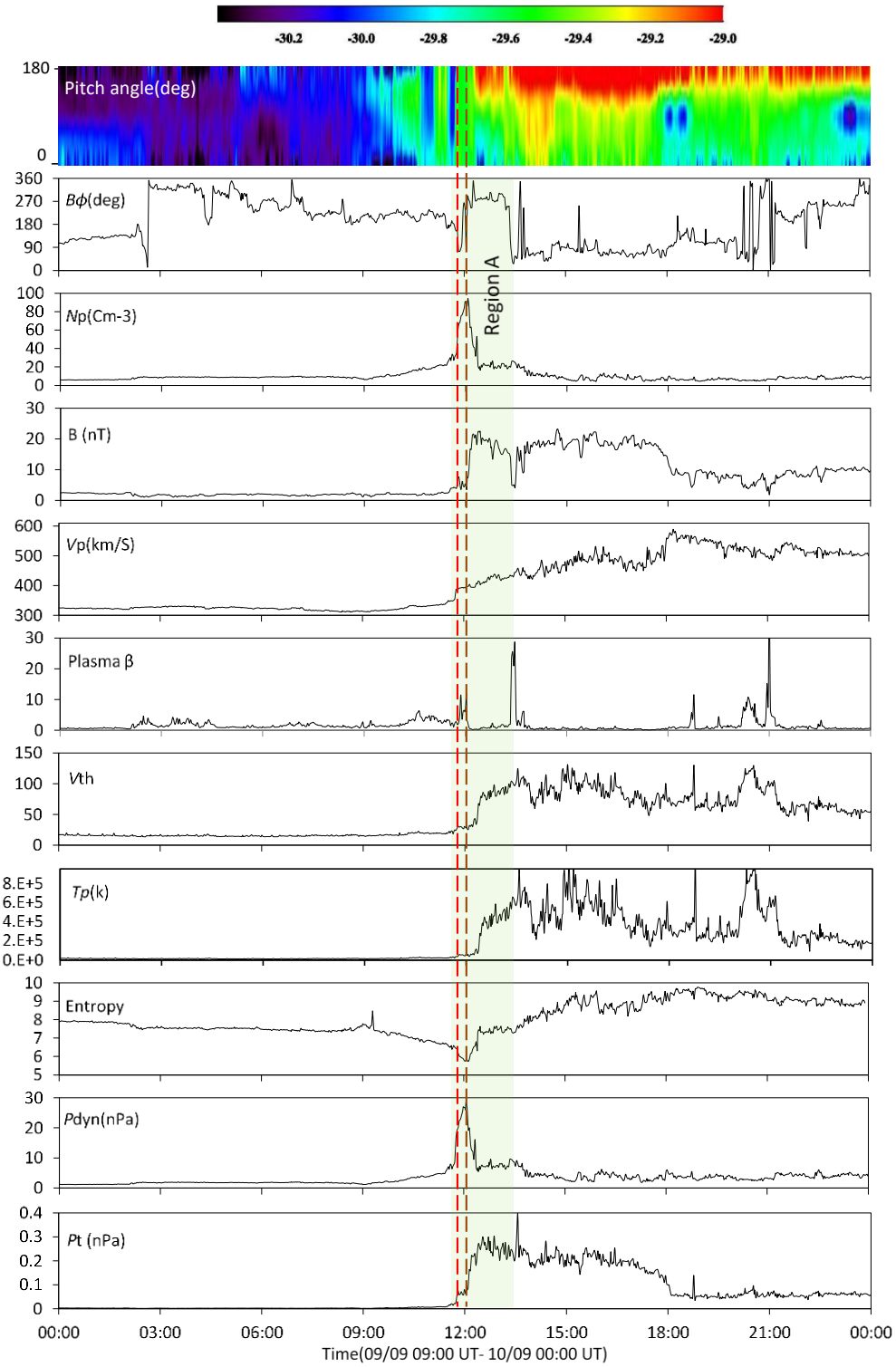

Figure 3.10 Properties of region A as measured by Wind. From top to bottom: heat flux distribution (measured by ACE), Bφ, Np, B, Vp, Plasma beta, Vth, Tp(k), Entropy, Dynamc pressure (nPa) and Pt (nPa). The ACE suprathermal electron distribution is included (1st panel) for comparison. The green shaded region(Region A) is the HPS.The dotted red line refers to the SBC-HCS region and thedotted brown vertical line refers to the ICME forward shock.

The sector boundary lies at the point at which the suprathermal pitch angle distributions changes (Liu et al., 2014). In ideal conditions, the SBC appear to synchronize with the HCS, but in many previous instances this has not been the case (see, for example, Kahler et al., 1996;Crooker et al., 1996). This mismatch has been attributed to many processes associated with magnetic reconnection such as heat flux dropout (McComas et al., 1989) or interchange reconnection (Crooker et al., 2002). The SBC start time was at the same time for all SWEPAM energy channels. The HCS location bordered the first HPS's boundary (the HPS did not straddle the HCS), supporting our finding that interchange reconnection is a dominant process. Guerrero et al. (2011) reference an SBC location at about 13:19 UT without referring to the HCS or HPS. We rule out the possibility of the SBC being located at this position because the first appearance of the 180˚ pitch angle of the suprathermal electrons precede it by more than 1.5 hours. On the other hand, it is possible that the HCS was located at this position (SBC-HCS mismatching) because of the azimuthal magnetic field reversal, the plasma beta spike of the second boundary of the heliospheric plasma sheet, and the dynamic and total pressure balance which were clear in Wind observations (Figure 3.10).

The important features of the plasma and magnetic field measurements made by all three spacecrafts within this interaction region are summarized as:

1. The region begins with a small increase of proton speed (from 321 to 394 kms^{-1}), magnetic field magnitude (from 2.5 to 7 nT), thermal velocity (from 18.3 to 29.3) and total pressure (from 0.02 to 0.05 nPa) associated with a high increase of proton density, reaching 40/cm^3 at SOHO and exceeding 90/cm^3 at Wind. Despite resampling the higher-time-resolution proton data of Wind to match the 5-min sampling of SOHO, this considerable difference in density remains. The SOHO density decreases at the brown dashed line, where the Wind density peaks and decreases later, roughly coincident with the temperature change. There is a delay of about 13 minutes between the temperature increase at ACE/SOHO and the temperature increase at Wind. However, the increase in the magnetic field magnitude occurs at the same time at both ACE and Wind. The differences between ACE/SOHO and Wind are likely due to the small separation between spacecraft (and thus high local variations in the event's properties) and/or to variations in the IMF(Weimer et al., 2002;Weimer et al., 2003;Weimer and King, 2008).

   We attribute the high proton density at the first HPS boundary to interchange reconnection between the ICME and the neighbouring coronal hole open field, which releases a stream of discontinuous plasma parcels into the HPS-ICME interaction region, at the front of the ICME shock, similar to (Wang et al., 2000;Song et al., 2009;Rouillard et al., 2010). The second significant increase of magnetic strength, proton temperature (at ACE and SOHO) and total pressure occurs around 30 minutes after the initial increase, and this is the forward shock. Because of its low speed, it is not possible for the ICME to drive this forward shock. The most likely source of the shock is the ICME-CIR interaction. The impact of the interaction is the suprathermal discontinuity at the front boundary of the HPS, the first small increase in proton speed, magnetic field magnitude, thermal velocity and total pressure, and the noticeable increase of speed within the ICME sheath (see section 3.3.8).
2. The ICME forward shock speed is low due to its position within the HPS, which decelerates and delays the shock inside the HPS (see, for example, Hu and Jia, 2001;Smith

et al., 1998b;Mitsakou and Moussas, 2014). This low speed is perhaps due to energy dissipation during the passage of the forward shock through the HPS (Watanabe, 1989), which reflected on the narrow electron heating flux at the shock position.

3. The density decrease after the shock is due to either a bulk movement of material to the front boundary of the HPS through interchange reconnection or the dissipation that we mentioned in point 2 above. In addition, the high-level density at the HPS front boundary, when compared to the shock density, exaggerates the decrease. The presence of the magnetic strength, total pressure and proton temperature increase supports the existence of this shock at this position.
4. At the onset of the HPS, Wind experience a decline in entropy (Figure 3.10, panel 8), followed by a sharp rise during the ICME forward shock passage, before stabilizing between the shock and the second HPS boundary, due to stable density and temperature. This entropy behaviour, where the increase occurs within the HPS, is rather different from the cases documented by Simunac et al. (2012), in which an increase is reported at the second HPS boundary. We attribute this difference to the existence of the ICME forward shock within the HPS.
5. The total pressure increased at the onset of the first HPS boundary until the ICME shock. This is unprecedented in previous studies of HPS (Winterhalter et al., 1994;Crooker et al., 2004a), which consistently observe total pressure stability within the HPS. This contrast is due to HPS penetration to the ICME front, and subsequent influence of the forward shock. This varying total pressure stabilises after the shock passage because the change in magnetic pressure is balanced by a corresponding change in plasma thermal pressure (Winterhalter et al., 1994).
6. Both the forward shock and the HPS have their imprint on each other. The existence of the forward shock within the HPS change some of its behaviours and vice versa. Their physical parameters are different than when both are individual.

3.3.7 CIR compression due to the ICME

The yellow shaded region in Figure 3.11 supposed to be a transformation area between the ICME rear and the September 10 CIR. lasting for about 80 minutes and distinguished by a steep drop in magnetic field magnitude and a significant rise in plasma density and temperature. The first impression refer to a magnetic reconnection exhaust regions (Gosling et al., 2005), where magnetic field energy is converted into a plasma flow energy (Gosling et al., 2006;Xu et al., 2011).

There is a limited bidirectional pitch angle distribution of suprathermal electrons around the front boundary. We attribute this to the high heating at this first boundary although the general state of this event was unidirectional; however, the second boundary maintained a unidirectional field. In addition, the strahl witnessed a reduction in 180˚ heating flux distribution during this region; by contrast it was higher before the first boundary (during the MC duration) and more intense with broader beam high energies after the second boundary. The different characteristics of this region compared with the two-bounded large interplanetary structures has to do with it being a transition region with its own individual properties. The appearance of the shock-like structure may be attributed to two causes: 1)

the high ICME-CIR compression; and 2) the interplanetary shock, which was recorded by STB on September 04 at 12:38 UT with Mach no. 1.34.

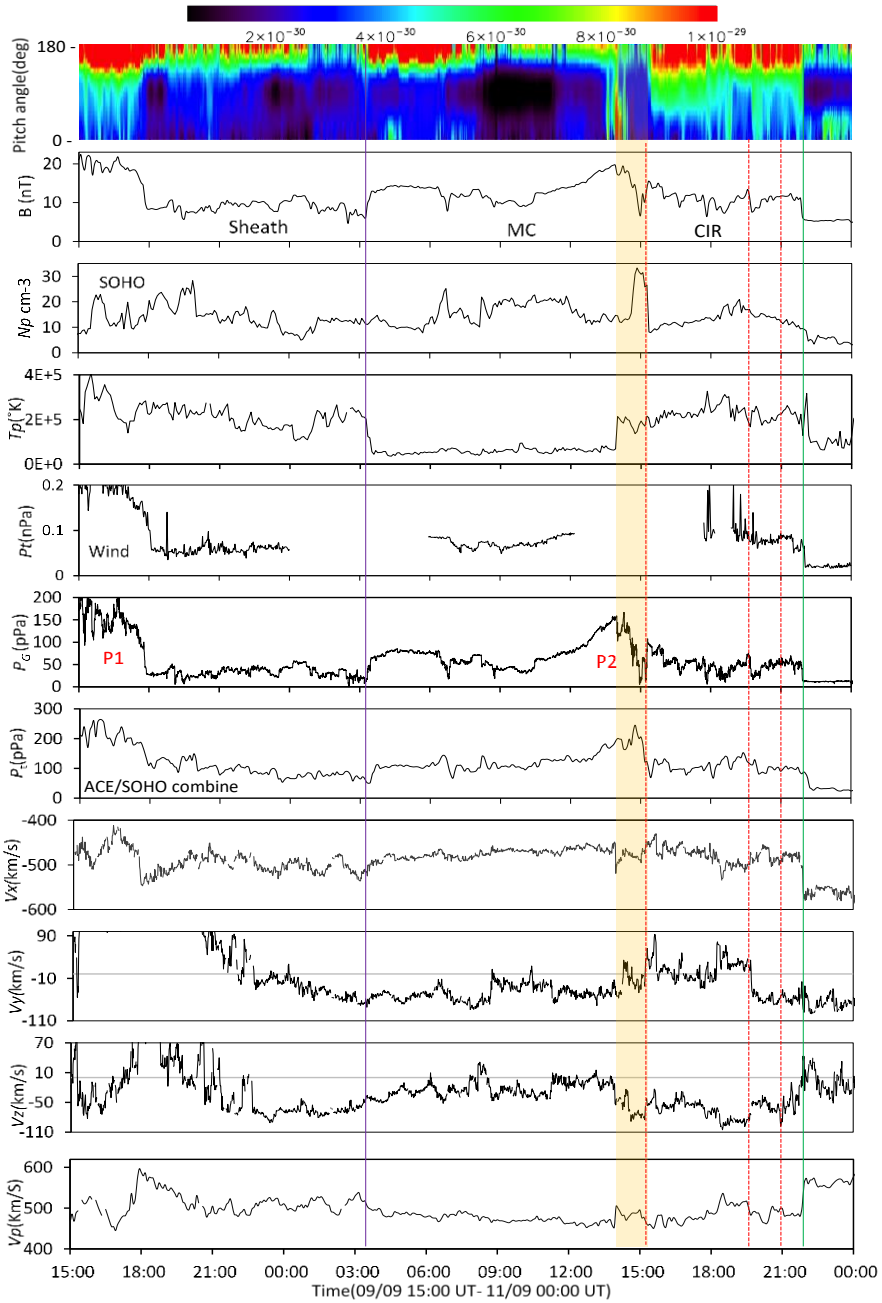

Figure 3.11 Highlights the ICME-CIR interaction region (yellow area). From the upper panel: ACE suprathermal electrons pitch angle distributions(deg), Magnetic field magnitue B(nT), Proton density Np(cm^{-3}) from SOHO, Proron temperature Tp(k), Total pressure Pt(pPa) from Wind, Magnetic pressure PG(pPa), ACE/SOHO combine data of total pressure Pt(pPa) , Solar wind velocity three components in GSE coordination (km/s): Vx, Vy, Vz, and Proton speed Vp(km/s). Purple vertical line refer to the MC onset, the green vertical line is the CIR reverse shock and the three dotted red vertical line are the nominated SIs. P1 & P2 in panel six are the two magnetic pressure peaks at the front and rear boundary of the ICME.

To evaluate the interpretation of the CIR and the transformation region observations, a comparison was made with the same CIR measured in the absence of an ICME by STEREO B on September 04, 2011 19:00 UT. STEREO B had a ~95° separation angle east to the Earth, and measured a total CIR duration of approximately 34 hours. A comparison of the behaviours

of the CIR by STEREO B and then L1 spacecraft reveals many similarities in their properties, despite the interaction described above. The left and right sides of Figure 3.12 show the available measurements of the CIR by the L1 and STEREO B spacecraft respectively. We identify similar features between the two sets of measurements by the blue oval shapes, with the 'P' labels showing peaks or plateaus. The most significant patterns are:

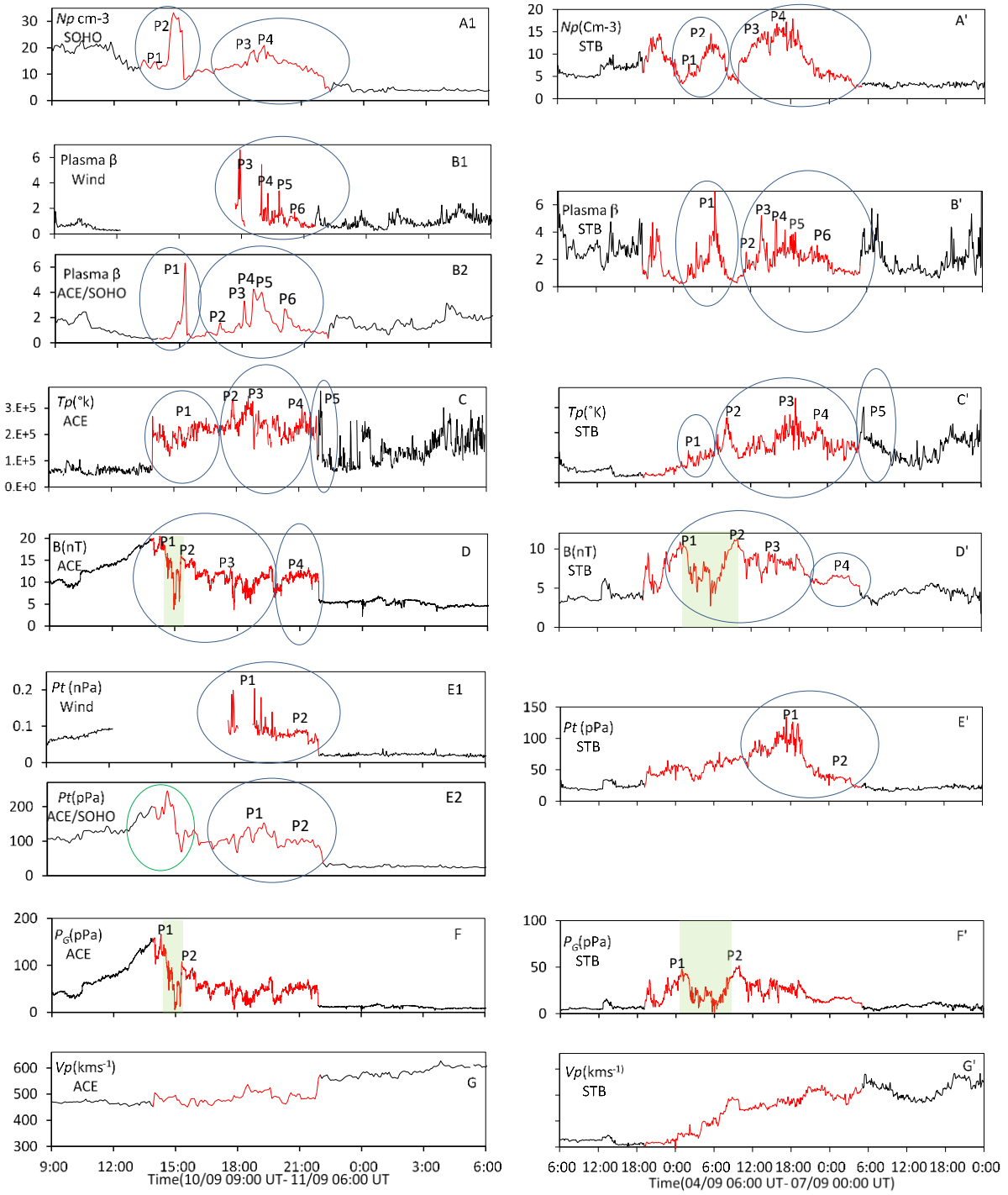

Figure 3.12 Left panels: CIR L1 spacecraft data of Np(cm^{-3}) from SOHO, Plasma beta from Wind, Plasma beta from ACE/SOHO combine,Tp(k) from ACE, B(nT) from ACE, total pressure Pt(nPa) from Wind, total pressure Pt(pPa) from ACE/SOHO combine, magnetic pressure P_G (pPa), ane Proton speed(kms^{-1}) from ACE for the period (10/09 09:00 UT- 11/09 06:00 UT). Right panels: CIR STB data with the same magnetic field and solar wind parameters for the period (04/09 06:00 UT- 07/09 00:00 UT).

1. In panel A1, we label 4 distinct peaks in SOHO proton density by P1-4, and their counterparts in STEREO B in panel A' and note that the STEREO B CIR duration was approximately 34 hrs in comparison to an SOHO CIR duration of approximately 8 hrs (all L1 spacecrafts have the same duration). A comparison of panels B1(Wind plasma beta) and B' similarly shows four pairs of matching peaks of plasma beta. Because of Wind missing data, P1 and P2 do not appear in B1 panel. For just comparison, it has used the ACE/SOHO combine data (panel B2). It displays a noticeable P1 that missing on panel B1. C/C' show the comparison of proton temperature.

2. Similarly, panels D and D' reveal four pairs of magnetic field matches between ACE and CIR STB. The two green-shaded areas in D and D' reveal a magnetic reduction region within the STB CIR and indicates that the magnetic exhaust region in the ICME-CIR compression region is already present before the interaction. From this, it may be concluded that the role of ICME-CIR interaction is merely to compress and reduce the duration of this exhaust region. This runs counter to our previous conclusion that the ICME-CIR interaction is responsible for the creation of the exhausted region. Furthermore, this result suggests that care must be taken in the interpretation of many other similar cases. Accurate interpretation of many complex in situ interaction events is difficult without a comparison of events in the absence of interaction.

3. Panel E1 shows the total pressure morphology from Wind (albeit with a few hour data gap). There is a match between E1 and E' at both P1 and P2. For verification, the ACE/SOHO combined data profile E2 displays the same P1 and P2 and a significant large peak of the total pressure at the CIR frontal edge when it overtakes the MC tail (the area within the green oval). The large value of Pt at the frontal boundary of the CIR implies a high compression because of the interaction with the preceded ICME. Furthermore, the valid magnetic pressure profile F, compared to the STB magnetic pressure F', confirms that the STB CIR witnessed a large compression in magnetic pressure at the frontal region during its travel from the STB to L1 position, in particular at the magnetic exhausted region (green shade). This raises the overall STB CIR magnetic pressure, especially the values of P1 and P2, and reduced the duration between them.

Panels F and E2 provide details of the rise in Max magnetic pressure and the total pressure of the CIR frontal edge when it overtook the MC tail. It has changed hugely due to the interaction from the rear when the CIR is isolated (panels F' and E') to the leading edge after the interaction with the ICME, despite the existence of the magnetic exhausted region between the two structures.

The similarities between magnetic field and plasma profiles emphasise that both spacecrafts traverse the same CIR pattern, and that the different duration is caused by the high compression of the ICME-CIR interaction at the Earth's in situ region. The high compression characteristic of the CIR duration observed by the L1 spacecraft is shorter by about a factor of 4 and produces a fast reverse shock at the rear boundary of the CIR. The first six hours of the unperturbed STEREO B CIR was absenting in ACE measurements, which means that this region was out of the interaction zone.

4. Panels G and G' show very different CIR velocity profiles, with a large contrast between the front and rear boundary in G'(ACE proton speed is less decline, perhaps due to the expansion

with the ICME) which reflects the high impact of this interaction on the CIR speed morphology more than the other solar wind parameters.

5. The values of the magnetic field and plasma at L1 Region have increased coincided with the high compression.

It is reasonable to expect some structural change in the CIR magnetic and particles profiles between the six days' separation of STEREO B and L1, even without the disruption of large ICMEs. A future study will quantify such changes through a long-term study of this CIR, which recurs over several solar rotations during 2011. During the period 4-10 September, the CIR may have been disrupted by a small number of weak CMEs accompanied by class-C flares and one CME with an M5.3 flare in addition to our main ICME event. Also, the September 06 CME was the only halo during this period. The fact that some signatures/parameters are clearly preserved whilst others are completely disrupted suggests a useful method for interpreting ICME-CIR interaction.

3.3.8 ICME-CIR/HSS interaction impacts

The remote sensing observations give a possibility of CME-CME interaction, but the in-situ observations support the September 09- 10, 2011 event as an ICME-CIR embedded. The MC has a clear azimuthal magnetic field rotation (magnetic flux rope) and a weak southward *Bz (Dst≤ -69)* which is incompatible with the ICME-ICME criteria who is often have a non-smooth magnetic rotation(Burlaga et al., 2001;Burlaga et al., 2002) and associated at Earth extended periods of strong southward *Bz* with intense geomagnetic storms(*Dst*≤-100 nT)(Farrugia et al., 2006a;Farrugia et al., 2006b) or (*Dst*≤ -200)(Wang et al., 2003). In addition, the ICME- ICME ICME can have a long duration and may drive the magnetosphere for an extended period (≥ 3 days) (Lugaz and Farrugia, 2014), while a typical CME passes over Earth in ∼ 24 h e.g.(Klein and Burlaga, 1982), some events last well in excess of 30 hrs (Marubashi and Lepping, 2007). The September 09-10 event (ICME- CIR) interval is about 1.5 days with a magnetic cloud duration of about 10 hours. Moreover, the ICME-ICME have a higher proton temperature than the MC on average because of the compression and interaction e.g.(Lugaz et al., 2012;Lugaz et al., 2016).

The effect of the ICME-CIR/HSS interaction was clear from the magnetic strength of the rear tail of the MC. An elevation of the magnetic field magnitude formed a second magnetic pressure peak P2(Figure 3.11). The first magnetic pressure peak P1 was at the front of the ICME (during the shock and the beginning of the sheath). This is also obvious at the ACE/SOHO combine total pressure profile. The role of the embedded CIR/HSS was noticeable by the very high increase of speed within the sheath at ACE between 16:39 UT, September 09 (467.7 kms^{-1}) and 17:54 UT, September 09 (596.6 kms^{-1}) (see Figure 3.9), followed by a gradual deceleration and expansion that continues until the rear of the MC (Figure 3.5, panel 7), reflecting the high compression between the two interplanetary structures. This expansion and deceleration may be due to the coronal hole CH475 which caused the sheath and the MC deflect away to the west. This may also be the reason that the ICME impacted the Earth from the flank. The prominent speed increase is also obvious at Wind (Figure 3.10). Conversely, the SOHO speed is significantly lower than the other two. This suggests that there is some difference after 15 UT, either caused by the different spacecraft locations or by some other

factor (Figure 3.5and Figure 3.9). The differences in velocity between spacecraft remains even after the resampling of data to matching time steps.

It was difficult to identify the stream interface (SI) because of the total pressure missing data (a main criterion) in the CIR interval, and also because approximately 20% of stream interaction regions have a sharp boundary between fast and slow flows (Jian et al., 2008b). We nominated three points to act as an SI based on the criteria: a decrease in proton density; a rise in proton temperature; a flow shear and an increase in proton speed(Burlaga, 1974;Gosling et al., 1978;Jian et al., 2006b;Jian et al., 2008a). The effect of the ICME-CIR interaction was clear insofar as none of the nominated SIs met all the major criteria in an unambiguous and obvious way, and this was probably due to the complexity of ICME-CIR interaction. One of the SIs likely occurred at 19:34 UT, 2011/09/10 (second vertical red line). In this location, the proton density starts to decline accompanied by unclear behaviour of the proton temperature. The most significant phenomena is the change in the azimuthal proton flow speed direction (*Vy*) from west to east (flow shear). Another potential apparent SI was noticed at 20:49 UT, 2011/09/10(third vertical red line) in the form of a reduction in the proton density accompanied by a rise in temperature and a *Vz* shear. The third nominated location was at 15:29 UT, 2011/09/10(first vertical red line): here a steep decrease in proton density, an increase in proton temperature, and a *Vy* flow shear. Within the CIR, there must be at least one SI(Crooker et al., 1999). We think that, because of the complicated interaction, the probability of more than one SI appearing is large in this turbulent CIR region.

3.4 Summary and Conclusions

Over the course of the September 09-10 event, the effect of the HPS-ICME-CIR/HSS interaction was noticeable on the ICME magnetic and particles parameters morphology. Both HPS and CIR/HSS added more complexity to the ICME morphology at the in-situ region and the whole event was ICME-CIR embedded. High elevations in magnetic field magnitude and total pressure at the front of the ICME and high magnetic field magnitude rising at the and the rear, formed the two significant magnetic peaks P1 and P2 respectively. The appearance of the HPS at the front of the ICME and its penetration through the ICME forward shock perhaps assisted in increasing the strength of compression regions. The general features of the magnetic field and total pressure morphology reflect the effect of the ICME interaction with the HPS at the front and the ICME interaction with the CIR at the rear. It is also reflected in the ICME deceleration and expansion from the middle of the sheath until the MC rear boundary. These may be due to the coronal hole CH475 which made the sheath and the MC deflect away to the west and the ICME impact the Earth from the flank even though the CME was a halo. The overall interplanetary magnetic field feature was unidirectional during the event, which led us to propose an interchange reconnection scenario depending on the remote and in situ data.

A significant shift between the high density and the magnetic field magnitude peaks at the front of the ICME. It is attributed to the HPS penetration of the ICME frontal. The ICME forward shock speed was not high, and this was because of its intra-HPS existence which delayed the shock a little. Based on the strahl distributions and *B*ϕ morphology, there was a

match between the SBC and HCS, and the HPS bordered the HCS because of the interchange reconnection. The high proton density within the HPS has attributed to the open magnetic field loop which released the material blob in the HPS. The multiple *B*ϕ reversals during the sheath did not affect the general direction of the interplanetary magnetic field, although it lasted for several hours. The same held true for the local *B*ϕ reversals during the HPS. The multiple magnetic field reversals during the HPS interval, the high elevation of the HPS proton density, and the HPS location where it bordered rather than straddled the HCS, supported the interchange reconnection. Based on the magnetic cloud and the sheath duration, the spacecraft predominantly traversed the ICME from the flank. The forward shock was strong and the ICME speed is not enough to drive it. We attributed the most likely source of the shock is the ICME-CIR interaction. The ICME-CIR/HSS interaction impact was distributed along the September 09-10 event in different locations with different features represented by 1) The HSS imprint on the 272 eV suprathermal electron discontinuity at the ICME frontal forward shock upstream 2) the noticeable high speed elevation in the middle of the sheath 3) the magnetic cloud flux rope *B*z rotation distortion 4) ICME unidirectional suprathermal electrons distribution due to the interchange reconnection 5) Difficulty determining the stream interaction(SI). A three potential SIs were nominated.

This event is very unusual. There are considerable differences in the timing of proton density and temperature features between spacecraft. The SOHO proton speed before ~ 18 UT, September 09, is significantly lower than the other L1 spacecraft, and the Wind forward shock density is much larger than at SOHO, which is likely to be due to the difference in the spacecraft locations or the fluctuations in the interplanetary magnetic field.

On September 04, 2011, STB recorded a CIR passage. The HSS resource was the same coronal hole. A significant matching was noted in the CIR's physical parameter morphologies of both September 04 and 10, and this means that both STB and ACE traverse the same CIR spiral pattern with different durations because of the L1 ICME-CIR interaction. The compression made the ACE CIR duration shorter by about a factor of 4 and some of the CIR physical parameters value has changed. The survival of a magnetic exhausted region at the front of the CIR before and with the interaction, suggests that care must be taken in the interpretation of many other similar cases. Accurate interpretation of many complex *in situ* interaction events is difficult without a comparison of events in the absence of interaction.

The main finding of the study is that the interaction has its impact on all the three interplanetary structures with varying proportions. The major features are: the unusual density of the HPS, the ability to drive a strong forward shock, the unidirectional heat flux along the event, the *B*z distortion of the MC, the reverse shock, and the high compression of factor 4 of the CIR.

Chapter 4

The compound stream event of March 20-25, 2011 as measured by the STEREO B spacecraft

Abstract

The interaction of interplanetary coronal mass ejections (ICMEs) with each other and with co-rotating interaction regions (CIR) changes their configuration, dynamics, magnetic field and plasma characteristics and can make space weather forecasting difficult. During the period of March 20–25, 2011, the Solar Terrestrial Relation Observatory (*STEREO* B) encountered a compound stream containing several interacting structures. Our analysis suggests that the stream consists of two interplanetary coronal mass ejections (ICMEs) followed by an embedded ICME/co-rotating interaction region (CIR). A significant stream interface (SI) has penetrated the magnetic flux rope of ICME3 and has effected its physical properties, particularly the temperature. The sudden appearance of ICME3 within the fast wind side of the CIR causes the temperature to drop suddenly to its lowest level in about 1.2 hours, from 3.89×10^5 K to 1.07×10^4 K. The fast wind which follows the CIR influences not only ICME3's temperature but also its plasma β. In addition, third ICME impacts the CIR through expansion and deceleration. Penetration of a forward pressure wave driven by this combined ICME-CIR causes the second ICME and part of the first one to increase in temperature and plasma beta. Despite the presence of signatures from four large-scale interacting structures within the compound stream, it is difficult to reconcile the *in-situ* sequence with other, remote sensing observations of CMEs and ejecta close to the Sun. Compound streams therefore remain difficult to interpret, and further understanding of the subject will depend on the future study of similar events.

4.1 Introduction

During their propagation through interplanetary space, ICMEs can interact either with each other or with CIRs, making space weather forecasting more difficult. This interaction can alter their configurations, dynamics, and their magnetic field and plasma morphologies (Winslow *et al*., 2016). Examples of alterations include flux rope deformations, reverse shock formations (Lugaz *et al*., 2005), radio emission enhancements, proton temperature increases, and ICME deflections (Lugaz et al., 2012;Liu et al., 2012;Oliveros et al., 2012;Farrugia et al., 2012;Lugaz et al., 2016;Shen et al., 2012).

At 1 AU, interplanetary streams are classified as either ''simple'', ''irregular'', or ''compound'' (Burlaga and Ogilvie, 1972;Burlaga, 1975). Burlaga *et al*. (1986) defined the compound stream as the interaction between a fast and slow stream. Between 0.85 and 6.2 AU, they found that a compound stream formed as a consequence of the interaction between and the coalescence of two exceptionally fast transient streams overtaking two co-rotating streams and a slow transient stream. They defined a stream as an interplanetary flow with speed greater than 475 km/s. Furthermore, Burlaga et al. (1987) suggest that compound streams are formed by the interaction of two or more fast interplanetary ejecta flows, with fast being defined as greater than 450 km/s. They also state there should be at least two interaction regions (two magnetic field magnitude peaks) present. Their study includes many examples of interactions between different transient ejecta, or between transient ejecta and co-rotating streams, and described the results of these interactions in terms of compound streams. During the period of 1972–1983, nine out of 17 intense magnetic storms (*Ap* > 90) occurred as a consequence of amplified magnetic magnitudes as a result of structures interacting within compound streams. Both magnetic field strengths and densities were higher here than for isolated flows. Jian et al. (2008c) identified many hybrid CIR-ICME events and found that their structures sometimes possessed an irregular profile or some complexity in addition to their original morphology. Cane and Richardson (2003) found that only about 8% of ICMEs were identified within the High-Speed Stream (HSS) passage at 1 AU. Perhaps due to the ICME sources always being located far away from the weak field regions, the ICMEs are infrequently embedded within HSS (Forsyth *et al.*, 2006). Over more, ICMEs were found more frequently at the leading front of the HSS or within the slow interstream solar wind. The CIR which follows the ICME is able to overtake the trailing region of the ICME, compressing the rear region and deforming the magnetic cloud (MC) flux rope.

Burlaga *et al.* (2001) classified the faster ejecta into magnetic clouds and complex ejecta. They defined complex ejecta as fast non-co-rotating interplanetary flows (> 600 km/s) with a disturbed magnetic field (not flux ropes) and an average plasma beta β of 0.25 ± 0.09, which is greater than that found in MCs. The features of the individual CMEs disappear as the interaction progresses towards 1 AU (Burlaga *et al*., 2002). On the other hand, Wang et al. (2003) considered multiple magnetic clouds overtaking each other due to successive CMEs as a sort of complex structure. They concluded that each sub cloud is always consistent with isolated MC criteria except for proton temperature, due to the sub cloud compression and a rising plasma beta in the interaction regions.

The formation of ICME-ICME and ICME-CIR interactions within compound streams takes many forms. Sometimes ICME-driven shocks interact with each other without ejecta interacting, or the two ejecta interact with each other and an associated magnetic reconnection exhausted region appears between them as a result of these different interacting structures. Sometimes the ICME-driven shock which follows, blows through the preceding ICME and interacts with its ejecta (Lugaz et al., 2015;Mishra et al., 2015;Liu et al., 2012). The consequence of these interactions lead to an enhancement of the southward geomagnetic field, which occurs in intense magnetic storms (Farrugia and Berdichevsky, 2004;Farrugia et al., 2006a;Liu et al., 2015) .

Throughout the solar cycle duration, the rate of large CMEs increases from 2–3 per week at solar minimum to 5-6 per day at solar maximum. Therefore, ICME-ICME interactions occur more frequently (but not exclusively) at solar maximum, making space weather forecasting difficult. Interacting ICMEs may originate from different source regions near the Sun, or from the same region: remote and *in situ* observations reveal that many ICME-ICME interactions occur due to recurrent CMEs which are launched from the same solar active region.

Tracking the propagation of CMEs from their launch at the Sun and through interplanetary space leads to a better understanding of the interaction of ICMEs with each other, the solar wind, and other structures, and also allows improved predictions of their arrival time at Earth (Mishra *et al.*, 2015). The launch of STEREO (Kaiser, 2005) enabled this tracking by providing continuous imaging from the Heliospheric Imagers (HI) on board The Sun Earth Connection Coronal and Heliospheric Investigation (SECCHI, Howard et al. (2002)). Recently, many ICMEs interaction events have been studied by combining *in situ* measurements with wide angle point of view observations from HIs onboard STEREO; examples of this include the May 23-24, 2010 event (Lugaz *et al*., 2012), the August 1, 2010 event (Temmer et al., 2012;Harrison et al., 2012), and the February 13-15, 2011 event (Maričić et al., 2014;Temmer et al., 2014). Numerical modeling is an important factor in understanding ICME propagation and interaction (Prise et al., 2015;Winslow et al., 2016).

This chapter is a study of an *in-situ* compound stream encountered by STEREO B (STB) over the period March 20 – 26, 2011. Sections 4.2 and 4.3 present remote sensing and *in situ* observations. Sections 4.4, 4.5 and 4.6 presents an analysis and interpretation of the results. The impact of the merged ICME/CIR is discussed in the last section.

4.2 Remote sensing observations

In this section, remote sensing observations from the March 17 active region are presented, which is the likely source of the March 20-25 *in situ* event. Figure 4.1 a and b show the Extreme Ultraviolet Imager (EUVI/STB) 195 A images of the low corona. The images show two flares at 12:15 UT (left) and 14:15 UT (right) originating from the same active region.

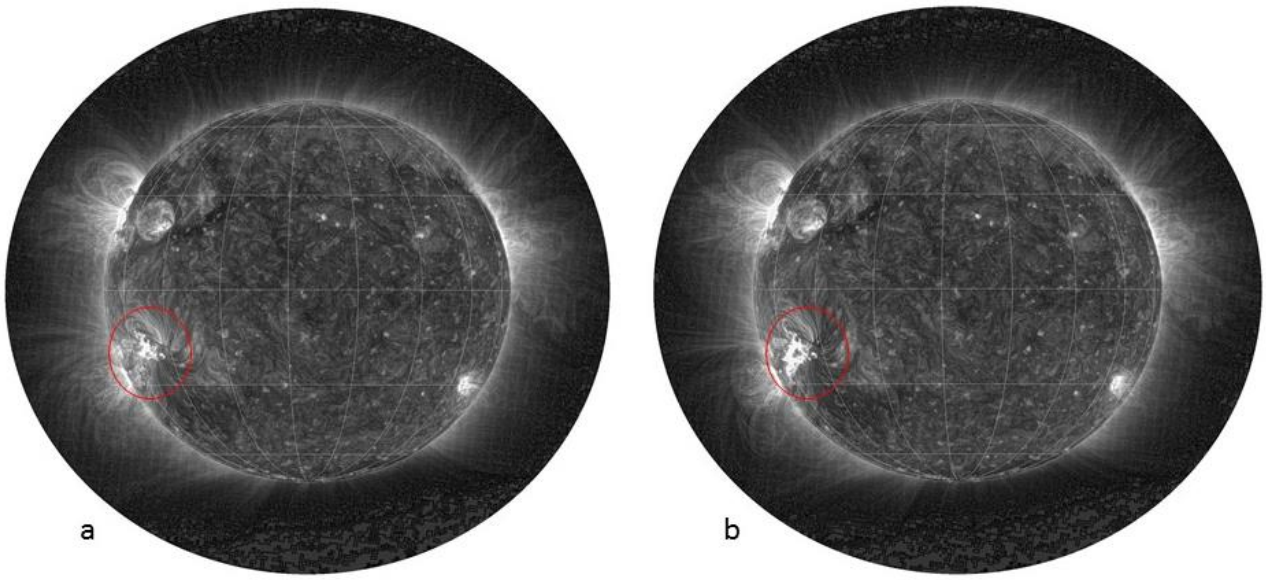

Figure 4.1 STEREO B EUVI 195 A images, with an active region circled in red. The time of the images is 12:15 UT (left) and 14:15 UT (right), coinciding with the occurrence of two flares in the active region. These images have been processed using Multiscale Gaussian Normalization Morgan and Druckmüller (2014).

Figure 4.2 shows a sequence of events as observed by the LASCO C2 (Brueckner et al., 1995)coronagraph. Before the launch of the large CME, there is a large system of expanding loops above an active region (indicated by the black ellipse). These loop systems are similar to those described by Morgan *et al.* (2013). This system of expanding loops is a precursor for a large CME originating from the same active region. This CME can first be seen in the top right panel of Figure 4.2, as indicated by the green ellipse. Over the next few panels, the CME is seen to be a wide, complicated CME containing several sub-structures. Some of the more prominent of these sub-structures are indicated by red and purple ellipses in the second and third row of Figure 4.2. In the wake of the CME, several complicated ejecta can be seen, as indicated by the green, blue, yellow and other ellipses. The flare at 12:15UT from the active region is clearly associated with the large CME (inside the dark blue ellipse). The large CME is mentioned in the STEREO A/B List of ICMEs (Jian *et al*., 2013) as a possible source of the *in situ* ICME which is described in the next section, but no reference is made to multiple ICMEs. Unfortunately, the STEREO B HI images do not show this large CME due to the viewing direction.

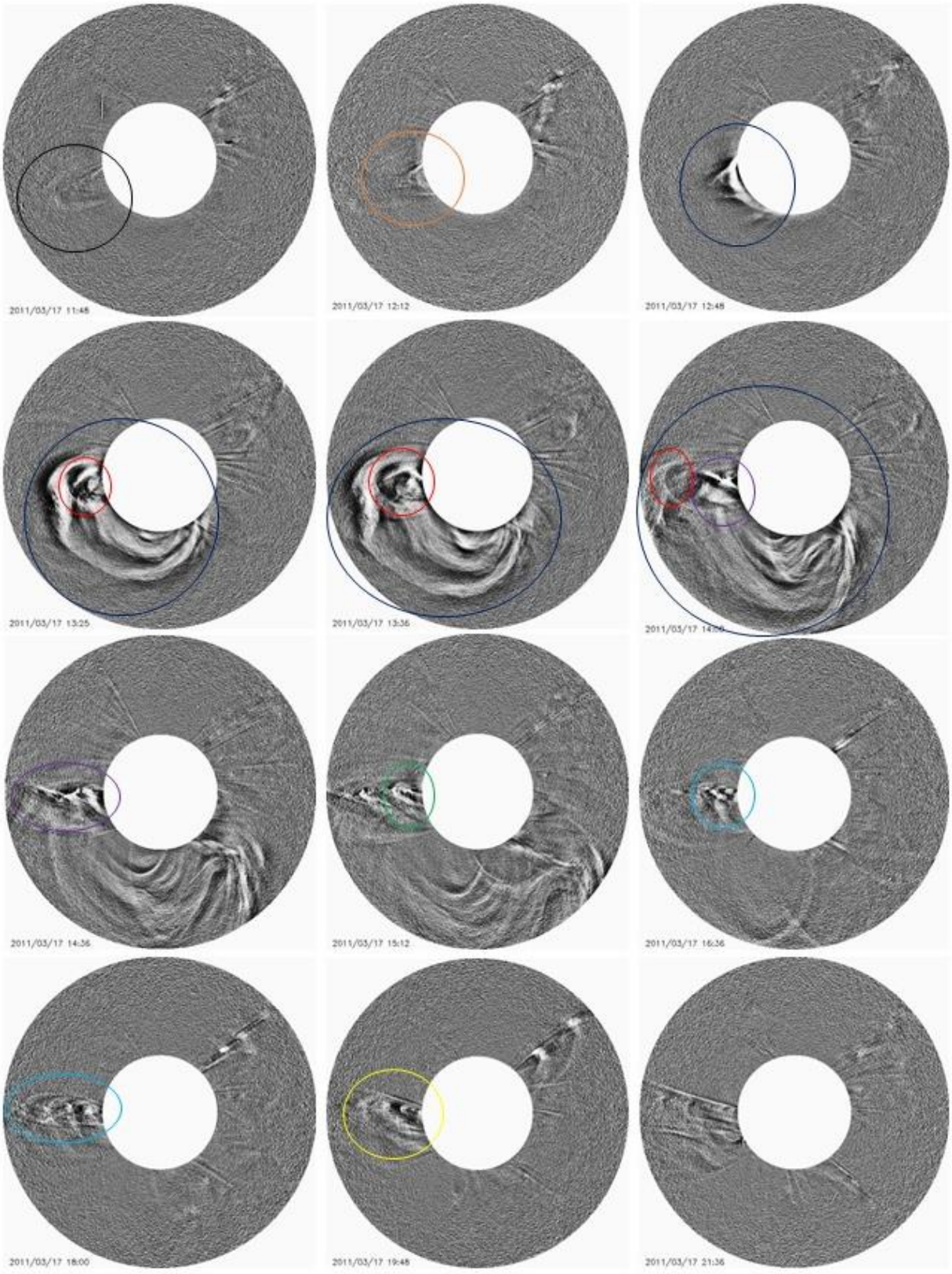

Figure 4.2 SOHO/LASCO C2 images for 17-03-2011 (11:48 UT- 21:36 UT) display multiple dynamic features. Different coloured elliptic outlines indicate different events as described in the main text. These images have been processed to remove large-scale quiescent structures (i.e. streamers) using the Dynamic Separation Technique (Morgan et al. (2012);Morgan, 2015).

Figure 4.3 shows more detail of the active region that is the source of much of the activity seen in the coronagraph data, as observed by EUVI/STB in the 195A channel. Following the 12:15UT flare, the active region has two large separated loop systems (1 and 2). After the second flare at 14:15UT, the outline of these loops becomes clearer, and then they gradually seem to merge into one arcade. The second flare is not associated with a large CME, but it is probably linked to smaller ejecta seen by LASCO C2 in the wake of the first large CME.
The presence of only one large CME in the remote sensing results seems to be inconsistent with the *in-situ* data that will be presented in the next section, which suggests the presence of two or more ICMEs. However, the remote sensing results do clearly show the complexity of the active source region, the system of expanding loops in front of the CME, the complexity of the CME itself and the presence of ejecta following the CME.

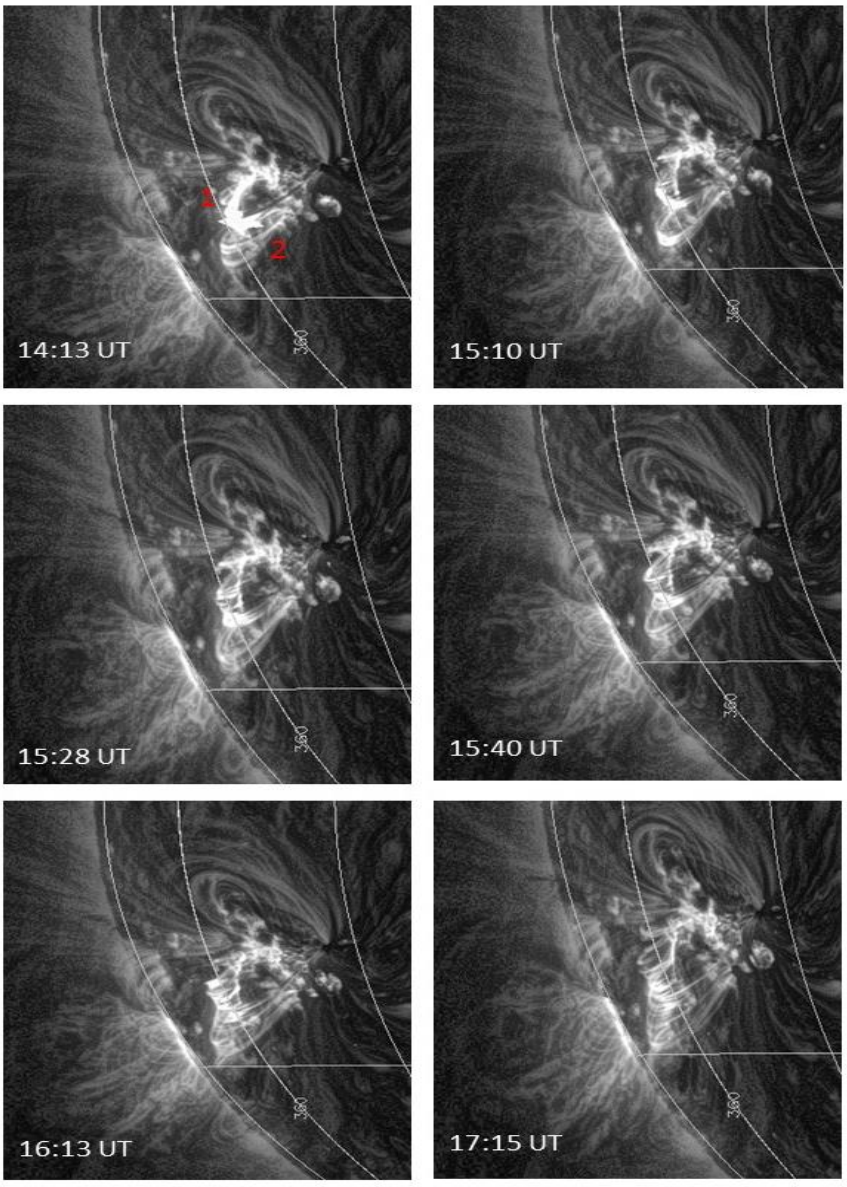

Figure 4.3 Further detail of the active region circled in red in figure 4.1 as observed by EUVI/STB in the 195 A channel. Two separated systems of coronal loops are labelled 1 and 2 and detailed in the main text.

Figure 4.4 shows a large CME observed on March 21, 2011, 15:36 UT by SOHO/ LASCO C2 with a linear speed of 963 km/s. The estimated transit time imply that it is the reference of the last in situ ICME (details in next sections).

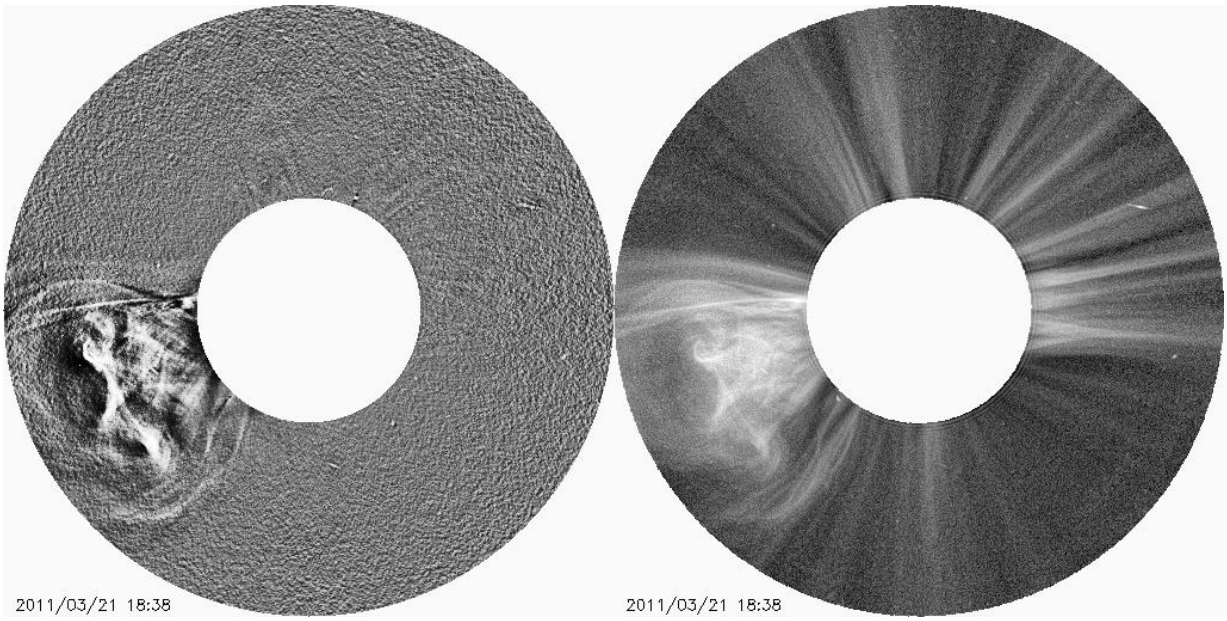

Figure 4.4 SOHO/LASCO C2 image of the March 21, 2011, 15:36 UT large CME.The left image has been processed using a Dynamic Separation Technique(Morgan and Habbal, 2010) , and the right image has been processed using Normalizing Radial Graded Filter of Morgan et al. (2006).

4.3 *In situ* observations

Figure 4.5 displays the 1 min magnetic field and plasma measurements taken from the magnetometer (MAG) (Acuña *et al*., 2008) and the *In Situ* Measurements of Particles and CME Transient (IMPACT) instrument (Luhmann *et al.*, 2008) onboard STEREO B over the period March 20, 00:00 UT to March 26, 00:00 UT. The suprathermal electron data was obtained by the Solar Wind Electron Analyser (SWEA) (Sauvaud et al., 2008). The event begins with a forward shock (S1) on March 20 at 17:20 UT(1st vertical line), manifesting an enhancement of the magnetic field magnitude, proton temperature, and a gradual elevation in proton density and speed. The duration between the 1st and 3rd vertical lines is highly variable and complex, which implies the passage of a sheath region. Within the sheath, there is a large reduction in magnetic field strength (shaded yellow) for about three hours (March 21 00:30 – 04:10 UT) associated with high density and increasing plasma beta. The heating flux distribution angle changed from 0° to 180°, and a magnetic clock angle reversal (2nd vertical line) indicates the presence of a heliospheric plasma sheet. The magnetic field strength then underwent a second reduction (March 21, 07:35 – 10:15 UT), with a large increase in density and plasma beta (higher than that of the surrounding), which is associated with a change in the magnetic field orientation.

The 18hr duration between the 3rd and 4th vertical lines can be identified as a MC flux rope based on several criteria Zurbuchen and Richardson (2006): a drop in the proton temperature and plasma beta accompanied by a smooth coherent rotation of the magnetic field. Between the 4th and 5th vertical lines, the coherent magnetic rotation becomes less smooth for about 12 hours, but it appears to be a continuation of the MC flux rope (panel 5). The magnetic strength maintains its value in the range of 7.2 – 10.8 nT and the suprathermal electrons maintain their bidirectional distribution, implying a closed magnetic field region. The broad flat profile of the magnetic clock angle suggests that the MC has somehow broken out of a larger MC structure. This may be due to the long duration of the complex series of ejecta emerging from the active region in the wake of the initial large CME following the March 17 CME. This ICME will be referred to as ICME1.

Within the ICME1 flux rope, there is a noticeable shock structure (S2) which first appears on March 21, 18:40 UT, accompanied by a small but sharp increase in magnetic field magnitude (from 9.3 to 12.7 nT), an increase in proton speed V_p from 445 to 487 km/s, a rise in total pressure P_t, and a short, transient elevation of the proton temperature. Unfortunately, there is a short data gap of around between 19:30UT to 22:05UT. Between March 22, 14:05- 15:10 UT following ICME 1 the magnetic field magnitude decreases, associated with a heat flux discontinuity and an increase in plasma beta, proton temperature, speed and total pressure in comparison to the ambient solar wind. The duration between the 5th and 6th vertical lines is a magnetic reconnection exhaust region. During the interval between the 6th and 7th vertical lines, the magnetic field strength varies between 6.1 and 9.3 nT, associated with low plasma beta (average value 0.15) and very low density. The 194 – 314 eV suprathermal electron pitch angle distributions also display counter-streaming, associated with closed magnetic field lines. This leads us to consider this interval as another ICME (labelled ICME2, discussed in section 4.4 & 4.5). The dominant heat flux direction for both magnetic clouds (panel 1) rotates with the magnetic field (panel 5), maintaining an inward direction, consistent with the passage of the spacecraft close to the flank of both MCs (with both MC sides connected to the Sun).

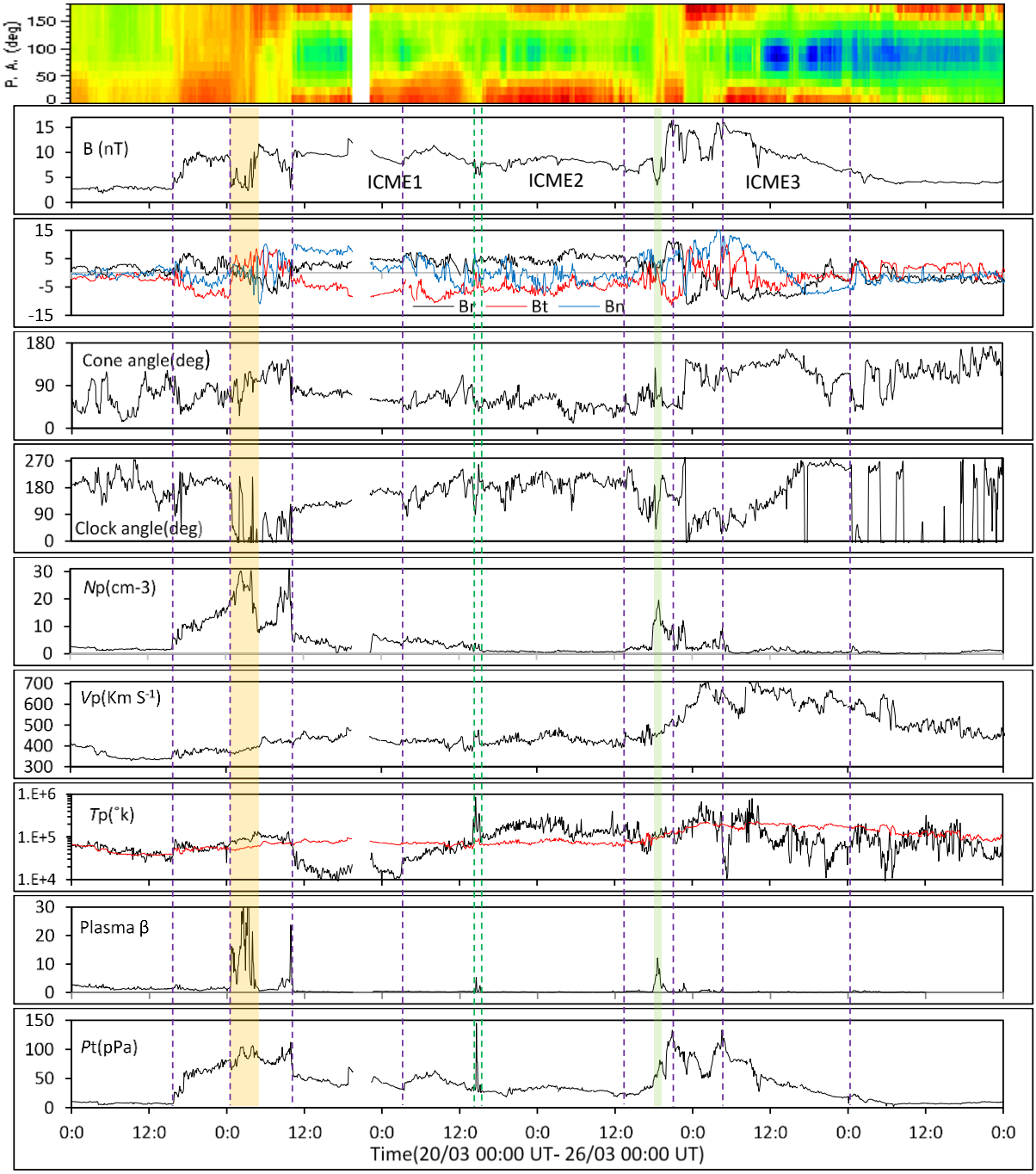

Figure 4.5 The magnetic field and plasma parameters of the event. From the top the panels display the suprathermal electron pitch angle distribution (194–314 eV), the magnetic field strength B(nT), Br, Bt, Bn(nT), cone angle (deg), clock angle (deg), proton density Np(cm^{-3}), proton speed Vp(kms^{-1}), proton temperature Tp(K)(black) and experimental temperature Tex (K)(red), solar wind plasma beta , dynamic pressure (nPa), and total perpendicular pressure (pPa).

After ICME2, there is a heat flux dropout, followed by a merged ICME-CIR (labelled ICME3). The CIR appears on March 23, 13:10 UT (7th vertical line), accompanied by an increase in solar wind speed from 390 to 466 km/s, and a small rise in density and plasma beta. A sudden magnetic field magnitude drops (shaded green) represents the impact of the interaction region between ICME2 and CIR/ICME3. The magnetic field reduction reaches its lowest value

at 3.7 nT, which is associated with a sharp rise in proton density N_p and plasma beta β, suggesting a magnetic reconnection exhaust region (Gosling *et al.*, 2007). After this, the solar wind speed experiences a substantial yet gradual increase (March 23, 19:50 UT) with a significant jump in magnetic field strength, total pressure, and enhanced heat flux at 0°, all suggesting the presence of a CIR. A SI feature appears at the 8th vertical line - the total pressure peaks with a gradual decline to both sides, there is a drop-in density, and temperature starts to increase.

The signature of ICME3 begins around March 24, 05:10 UT (9th vertical line), identified by an initial non-smooth rotation in the *Bn* component for about 4.5 hours, followed by a smooth and coherent magnetic field rotation until March 24, 17:30 UT- a duration of about 14 hours. This period has variable temperature, beginning with a considerable decrease followed by a large increase (for about three hours) and then a decrease that is less than the experimental temperature T_{ex} throughout the remainder of ICME3. The period also exhibits low plasma beta and bidirectional suprathermal electron pitch angle distribution. After March 24, 17:30 UT, following an initial variation, *Bn* maintains its rotation until the 10th vertical dotted line (March 25, 00:50 UT). The estimated transit time of 21 March, 2011 CME (based on the onset time and speed, and the space speed) imply that it is the most likely source of the ICME3. The CIR has mentioned in the Jian et al. (2013) list as a hybrid stream interaction region.The CIR/ICME3 interaction with the other preceding structures is discussed in Section 4.4 & 4.5.

4.4 Pressure wave analysis

The STB March 20 event is composed of several interplanetary structures (three ICMEs and a CIR). Their magnetic and plasma profiles can be distinguished, and they satisfy the definition of a compound stream (Burlaga *et al.*, 1987), from which it can be deduced that they are not complex ejecta (Burlaga *et al.*, 2001). The ICME boundaries are identified based on discontinuities in the magnetic field, heat flux, temperature, plasma beta, and density (Figure 4.5). The structural interactions may have a considerable effect on the proton temperature profile. Plasma beta will therefore be used here as the main parameter for identifying the ICME boundaries (Liu *et al.*, 2012). The appearance of the heliospheric current sheet (2nd vertical line) within the sheath is a temporary change of the interplanetary magnetic field sector boundary during the passage of ICME1, the ICME therefore disrupts the coronal streamer belt locally(Zhao and Hoeksema, 1996).

Figure 4.6 displays the magnetic and solar wind profiles for the duration of March 20, 12:00 UT– March 24, 00:00 UT. The figure illustrates two different interplanetary structures, ICME1 and ICME2, which are separated by a magnetic reconnection exhausted region(between 4th and 5th vertical blue lines), which suggests that ICME1 and ICME2 did not merge even after their collision. Their similarity in size and energy may be the main reason why this event was a multiple ICME event (Lugaz *et al.*, 2016). Within ICME1(between 2nd and 4th vertical blue lines), S2(3rd vertical blue line) looks like a pressure wave because the Alfven speed is about 185 km/s and the proton speed increase is less than 50 kms^{-1} with Mach number M_A =2.3.

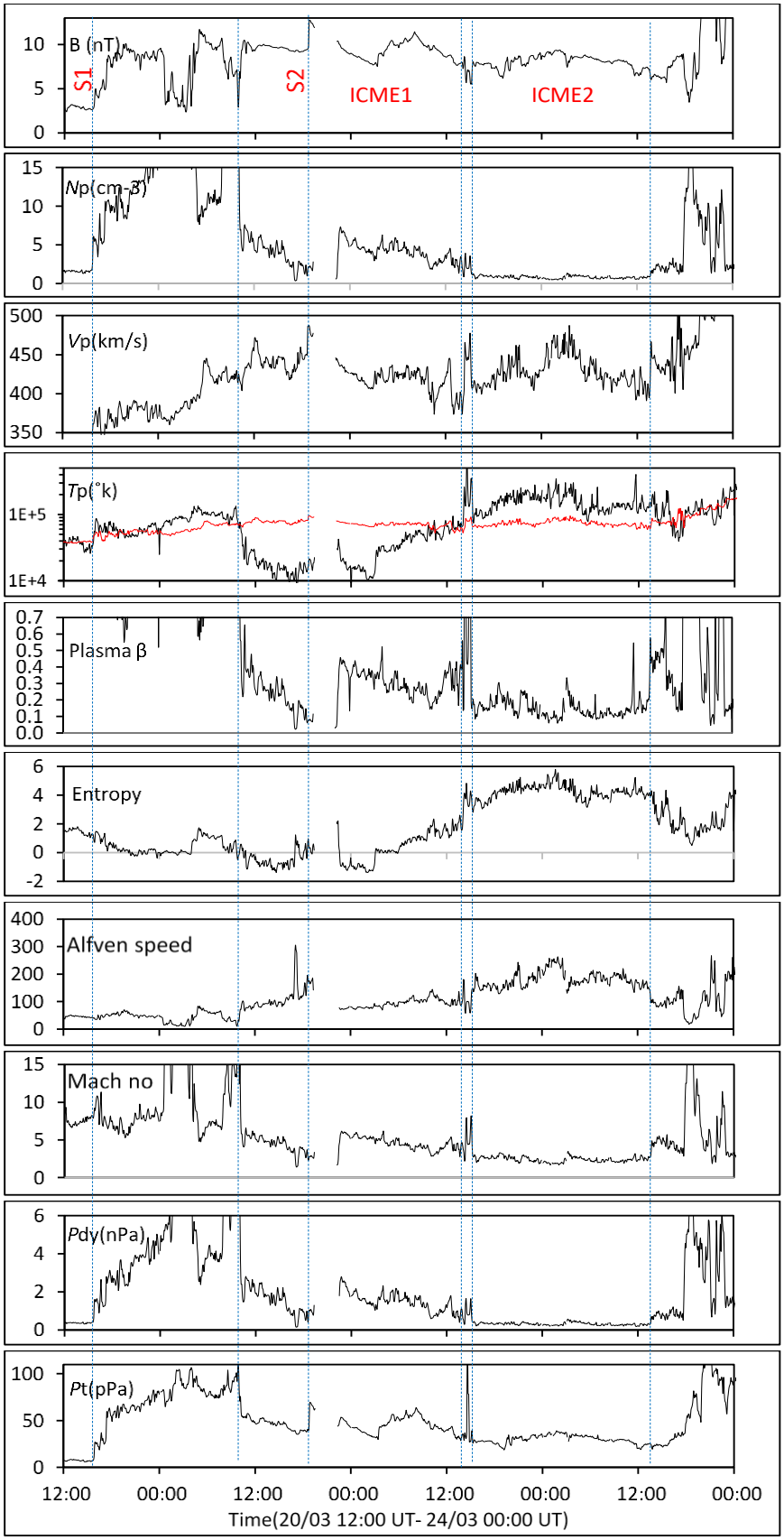

Figure 4.6 The Magnetic field and plasma parameters for the duration of March 20, 12:00 UT – March 24, 00:00 UT. From the upper panel: Magnetic field strength B(nT), proton density Np(cm^{-3}), proton speed Vp(kms^{-1}), proton temperature Tp(K)(black) and experimental temperature Tex(K)(red), solar wind plasma β, Entropy, Alfven speed Av, Mach number M_A, Dynamic pressure Pdy(nPa), and total perendicular pressure Pt(pPa).

The solar wind profiles suggest two possible sources for the S2 feature. The first possibility is due to the following ICME (ICME2). Both the density and plasma beta morphology perhaps support this scenario because of the noticeable gradual increase in both values going from the rear boundary of ICME1 to the S2 location.
A second possibility is due to the combination of both CIR and ICME3, passing through ICME2 and then ICME1 causing heating, compression and acceleration in many locations. The high temperature of ICME2 support the penetration of S2 through ICME2. furthermore, the location of the maximum Alfven speed which is close to the middle of ICME2, is likely to dissipate the coming shock from the fastest region(CIR/ICME3). In addition, the heat flux profile throughout ICME1 and ICME2 supports this posibility(discussed in the next section). The penetrating S2 is likely to decay because of the enhanced Alfvenic speed in the middle of ICME2. Efficiency in particle acceleration is expected to change due to modifications in the shock strength and structure by the ICME2, and particles accelerated at S2 may be trapped by the closed magnetic fields within the preceding ejecta or guided along the helical field lines.
The shock weakens due to the large upstream Alfvenic speed (250 km/s), an increase from about 150 km/s from the trailing boundary to the center of ICME2. The proton speed also increases by about 80 km/s, which is sufficient to ensure that the shock does not continue as a fast mode shock while it propagates itself. We interpret the speed profile of S2 as a magnetosonic pressure wave decaying from a magnetosonic shock due to the reduction of the local plasma beta, and dissipating while advancing into ICME2.

4.5 ICMEs analysis

The suprathermal electron pitch angle distribution displays a similar heat flux distribution along the three ICMEs (Figure 4.5): a bidirectional behavior with a significant enhancement at 0°. The dominant suprathermal electron pitch angle direction for both ICME1 and ICME2 rotate with the magnetic field clock angle, maintaining an inward direction along the magnetic field consistent with the STB path close to the flank of both MCs (with both MC sides rooted on the solar surface). The total pressure morphology supports the possibility of spacecraft passage through the flanks (Russell *et al.*, 2005). The non-smooth profile of the longitudinal magnetic field may be due to the legs of the ICME. As suggested by Owens (2016), the flux rope may be confined to the MC and not to its legs, even though the legs are magnetically connected with the Sun. Throughout the event, the only disappearance of the 0° heat flux enhancement is during the short period before the ICME1 pressure wave, which implying that the pressure wave S2 (which started as a forward shock driven by CIR/ICME3 and travels through ICME2 and ICME1) plays a role in energizing the 0° heat flux in every region that it penetrates, and that it rotates with the magnetic field. Due to this, the S2 upstream region maintains its suprathermal electron distribution at both sides without any enhancement.
The pressure wave S2 has an effect on the temperature profile. Despite the high temperature along ICME2 (the highest of all the ICMEs), this is mostly due to the collision with ICME1 and ICME3, thereby resulting in its compression. It is also possible that the passage of the forward shock driven by ICME3 increases compression. We believe that the effect of S2 on ICME2 was greater than on ICME1. The shock reaches the pressure wave level with access to the rear

ICME1 boundary, and this reduces the compression and is followed by plasma heating. The temperature of ICME2 is greater than ICME1 due to ICME1 being an MC and ICME2 being an ejecta. Naturally the ejecta temperature is greater than the MC temperature. Within ICME1 and after the pressure wave passes, β is between 0.5 and 0.15, with an average value of 0.31, whereas its average value is 0.15 throughout ICME2. The β profile supports the scenario of the shock path propagating through both ICMEs, causing a rapid and immediate effect on the plasma β profile. This is apparent from the high value in the middle of ICME1 where S2 is located; with the move towards the rear of ICME1, β declined gradually. The plasma β values during both ICME1 and ICME2 are higher than the typical isolated ICME β values.

4.6 CIR/ICME3 embedded

Figure 4.7 focuses on the merged CIR/ICME3 region. The first signature of this region is seen on March 23, 13:10 UT (see the 1st vertical dotted line) accompanied by an increase in the solar wind speed, density, and plasma β, followed on March 23, 17:50 UT by a sudden magnetic field magnitude drop (shaded green) associated with a sharp rise in N_p (1.6 to 19.6 cm^{-3}) and plasma β (0.1 to 8.2), suggesting a magnetic reconnection exhausted region caused by a transferring of magnetic energy into particle energy (Gosling *et al.*, 2007). Following this region, the solar wind speed increases gradually, with a significant jump in the magnetic field strength and total pressure occurring on March 23, 17:45 UT (from 7.2 to 15.7 nT). There is also an enhancement in heat flux at 0° associated with the CIR and indicating an SI at 20:55 UT. P_t peaks and N_p decreases, but there is no change in T_p (see the 2nd vertical dotted line).

The heat flux direction rotates with the magnetic field, maintaining an inward direction along the magnetic field. A second magnetic field decrease occurs on March 23, 22:30 UT, and is associated with decreasing density, increasing plasma β, and magnetic field cone and clock angle reversals. This suggests the existence of a Heliospheric current sheet HCS (see the 3rd vertical line) which matches a sector boundary crossing (a 180° suprathermal pitch angle distribution as a consequence of the magnetic field's outward direction). A third magnetic field reduction can be seen on March 24, between 1:00 and 03:55 UT. Here the heat flux remains enhanced, with no significant rise in either density or plasma β, meaning that any magnetic reconnection exhaust is either weak or absent. This may be due to the symmetrical nature of the particles at the boundaries of this region because of the embedded state. The ICME3 start time is close to 03:00 UT on May 24 (see the 4th vertical line), with a high elevation in the magnetic strength and total pressure. The plasma profile properties before and during this time are complicated, especially during the preceding drop in the magnetic field. As mentioned before, this supports the probable symmetric nature of the boundary plasma as a result of the merger of the CIR and ICME3.

A second P_t peak (see Figure 4.7) is accompanied by a gradual proton speed reduction (see the 5th vertical dotted line). The solar wind parameters at this peak show a second potential SI location (maximum P_t, temperature about to increase, shear velocity location). However, a sudden drop in proton temperature to its lowest value (see the 6th vertical dotted line) occurs for a short time (about three hours), followed by a high rise for about five hours, associated with a large jump in V_p. The large temperature drops at the 6th vertical dotted line is an

indicator of the MC start time. This is associated with a decrease in plasma β, a counter-streaming heat flux, and a decline in proton speed due to the high expansion and deceleration

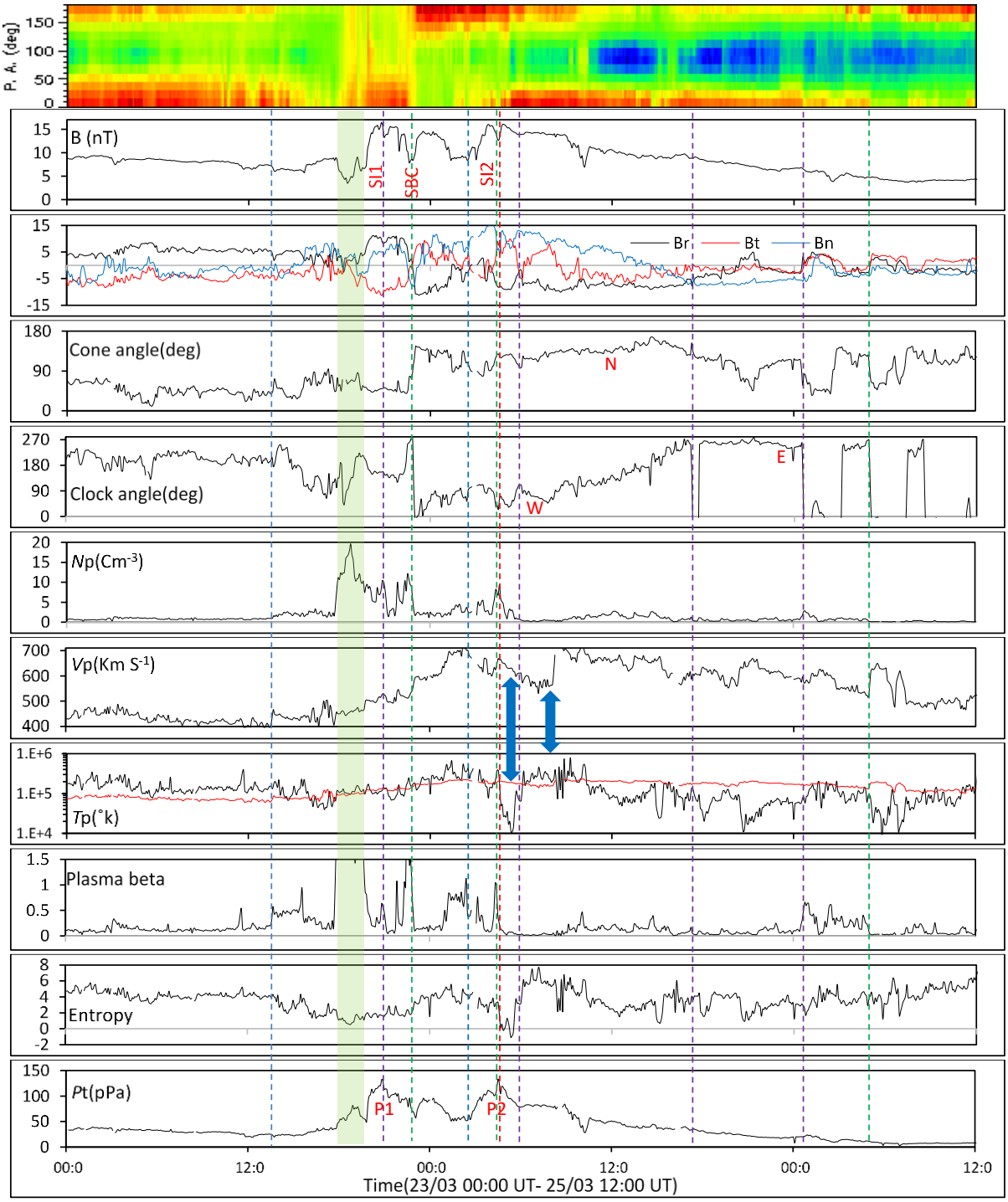

Figure 4.7 The magnetic field and plasma parameters for the duration March 23, 00:00 UT – March 25, 12:00 UT. From the upper panel: the suprathermal electron pitch angle distribution (194–314 eV), magnetic field strength B(nT), Br, Bt, Bn(nT), cone angle (deg), Clock angle(deg), proton density Np(cm^{-3}), proton speed Vp(kms^{-1}), proton temperature Tp(K) and experimental temperature Tex (K)(red line), solar wind plasma β, entropy, dynamic pressure (nPa), and total perpendicular pressure (pPa).

of the MC in the fast wind side of the CIR as the structures interact. The MC clock angle (5th panel) starts with a small crank rotation for about 4.5 hours and becomes smooth until March 25, 00:45 UT, reaching an angle >30˚ for a duration of about 20 hours and confirming the existence of a MC flux rope within the CIR. The *Bn* profile displays a smooth magnetic field with coherent rotation lasting from March 24, 06:05 (see the 7th vertical dotted line) to March 24, 17:30 UT (see the 8th vertical dotted line) and lasts about 11.5 hours in total. The *Bn* appears bent or flexed, and maintains its rotation until the 9th vertical dotted line on March 25, 00:50 UT. The clock angle rotation continues with a very short reversal at the 8th vertical dotted line. However, this is a local reversal, because the dominant heat flux is sunward within the counter-streaming; this may be attributed to the large-scale helicity (Crooker *et al.*, 1996).

4.7 The impact of the ICME3/CIR merger

ICME3 has an impact on both the CIR speed and temperature profile. The sudden appearance of ICME3 within the fast wind side of the CIR causes the temperature (which would usually be expected to increase after SI2 in the absence of interaction with the MC) to drop suddenly to its lowest level in about 1.2 hours, from 3.89 x 10^5 K to 1.07 x 10^4 K. Furthermore, the fast-solar wind speed is reduced during its expansion and deceleration within this area (see the 1st blue heavy straight line in Figure 4.7). The impacts of the CIR/ICME3 interaction include the high temperature elevation following the initial large reduction (Figure 4.7, the 2nd blue heavy straight line) and the large increase in solar wind speed. The ICME3 temperature is higher than expected due to the high-speed acceleration and its position within this hot, high-speed stream. Another relevant factor is the location of a second SI(SI2) within the MC. The presence of an SI is supported by a clear increase in entropy, accompanied by a decrease in proton density and an increase in proton temperature and a p_t peak, which are typical SI criteria. After about five hours the MC temperature decreases as a result of its deceleration and expansion towards the final boundary, but remains higher than typical MC temperatures in most regions (T_p < 0.5 T_{ex}). The fast wind which follows the CIR influences not only the ICME3 temperature but also its plasma β. The average β value of ICME3 is 0.16 with a peak of 0.4, which is a little higher than typical values for the MC (0.06 ± 0.04) (Farrugia et al., 1993;Burlaga et al., 2001). The entropy is also unstable compared to that of the two previous ICMEs. The weakness of the magnetic reconnection exhausted region within the CIR/ICME shows that the two structures are embedded. It also suggests that the interaction between the two wide, coherent total pressure peaks (P1 and P2) is greater and more complicated than the ICME1-ICME2 interaction within the same compound stream.

4.8 Discussion & Conclusions

The *in-situ* measurements taken by STEREO B reveal three ICMEs or interplanetary ejecta. These findings are difficult to reconcile with remote sensing observations. The results suggest either that ICME2 is a compressed interplanetary ejecta region between ICME1 and CIR/ICME3, or that there were originally three CMEs, but due to the complexity and the position of the active region, the remote sensing images were unable to display the sequences of events clearly. The *in-situ* data at 1 AU shows a penetration of a forward pressure wave

driven by the ICME3/CIR, associated with a rise in temperature throughout the second ICME and in part of the first one. The third ICME is merged with and embedded in a CIR. The lack of magnetic energy conversion into particle energy at the magnetic reconnection exhausted region between the CIR and ICME3 supports the interpretation that these are an embedded structure.

The magnetic reconnection exhausted region between ICME1 and ICME2 shows that they are separate structures with distinct region boundaries, and that they are two different interplanetary ejecta. This exhausted region is weaker than its counterpart between ICME2rear boundary and ICME3/CIR, possibly due to the asymmetric distribution of plasma between the ICME2 rear boundary and the CIR front boundary.

The appearance of the first heliospheric plasma sheet within the sheath is a temporary change of the interplanetary magnetic field sector boundary during the passage of ICME1, the ICME therefore disrupts the coronal streamer belt locally. Whilst a reverse shock is expected to follow ICME2 as its speed is decreased due to ICME1, none is present in this case. This may be due to the dissipation and decay of the second shock (S2). A significant appearance of a SI within the ICME3 magnetic flux rope suggests that the SI has penetrated the flux rope and has changed its characteristics. The sudden appearance of ICME3 within the fast wind side of the CIR causes the temperature to drop suddenly to its lowest level in about 1.2 hours. ICME3 impacts the CIR through expansion and deceleration. Later, the ICME3 temperature is higher than expected due to the high-speed acceleration and its position within this hot, high-speed stream.

The suprathermal electron pitch angle distribution throughout the event displays an absence of interchange reconnection, although there is an interaction between open and closed magnetic field structures (CIR and ICMEs). This result implies that the CIR magnetic field direction is inwards during the interaction with the ICME inward flank which is not conducive to reconnection.

The main finding of the study is is the significant impact of the MC on the CIR temperature and speed. The MC has reduced the temperature by about factor of 36 during about 1 hour.

Chapter 5

Evolution of a Co-rotating Interaction Region and its interaction with other structures over 180 degrees of longitude

Abstract

In situ measurements by multiple spacecraft of a Corotating Interaction Region (CIR) from 20 April 2011 to 8 May 2011 reveals interaction with two magnetic clouds (MC) embedded within the CIR at both near Earth and STEREO A (STA) positions. The impact of these interplanetary magnetic flux ropes on the CIR changes its reverse shock(RS) and stream interaction (SI) behaviour, with the SI signature appearing within the MC flux rope which is itself embedded within the CIR. The presence of a reverse shock at STEREO B (STB), subsequent absence at L1 region, and then an appearance at STEREO A, implies that the CIR reverse shock behaviour is sensitive to interaction with interplanetary coronal mass ejections (ICME). It also reveals the CIR's ability to recover its magnetic field and plasma characteristics after disruption by ICMEs. The L1 ICME changes the CIR speed and dynamic pressure profiles. consequently, the acting forces at both reverse shock sides have changed, leading to the disappearance of the reverse shock at L1. At STA, the ICME deceleration has moved the position of the CIR's maximum speed (*V*max) back to the rear CIR boundary, similar to position at STB. The SIs location has approached the Vmax location. These two changes made the profile of the dynamic pressure near the rear of the CIR to return to a state similar to that seen at STB, and thus, the reverse shock reappears, which means that the RS behaviour is subject to the local interplanetary conditions.

The ICME-CIR interaction at L1 and STA effects the HCS through the growth of the heliospheric plasma sheet (HPS) at the front of the events, and coincided with the existence of the magnetic clouds within the CIR.

The flux ropes complicate the CIR solar wind morphology and affects the location of the SI, or to cause the appearance of more than one SI. There is also an obvious signature of a SI penetration through the magnetic cloud flux rope at STA, which is itself embedded within the CIR.

5.1 Introduction

Stream interaction regions (SIRs) are the consequence of the interaction between the fast solar wind originating from solar coronal holes and the preceding low speed interplanetary solar wind (Pizzo, 1978). When the fast plasma catches up with the slow plasma, a compression region will start to appear at the front boundary and a rarefaction region will appear at the rear of the fast-solar wind, as shown in Figure 5.1. The fast-slow SI starts in the inner stream (Richter and Luttrell, 1986). The coronal holes are long-lived structures that rotate with the sun, which means that the SIRs may recur over several solar rotations, and are called co-rotating interaction regions (CIRs) (Smith and Wolfe, 1976;Gosling and Pizzo, 1999). At 1AU, CIRs are not always bounded by forward and reverse shocks (RSs) - they are commonly formed by around 2AU (Gosling et al., 1976;Hundhausen and Gosling, 1976). During solar rotation, the flow patterns defined by SIRs/CIRs form a spiral in the equatorial solar plane(Crooker et al., 1999). Somewhere within the SIR, the plasma density drops, the temperature rises, and a flow shear appears. This is the stream interface (SI): a distinct boundary between fast and slow flow (Burlaga, 1975), accompanied by a significant total perpendicular pressure P_t enhancement (Jian et al., 2006b) and a gradual decline at both peak sides. The coronal sources of fast and slow streams sometimes witness dramatic changes within one solar rotation, which can make the interplanetary interaction regions disappear within one solar rotation (Balogh et al., 1999). During their propagation through the heliosphere, interplanetary coronal mass ejections (ICMEs) and SIRs have time to interact and merge (Du et al., 2007;Whang et al., 2001). They are occasionally deformed from the interplanetary Parker spiral (Jian et al., 2008c), which adds complexity to the SIR morphology. Most of the fast streams emerging from high- or mid-latitude coronal holes can extend to lower latitudes and form SIRs, and sometimes they emerge directly from equatorial or low-latitude coronal holes, particularly at solar maximum (Jian et al., 2008b).

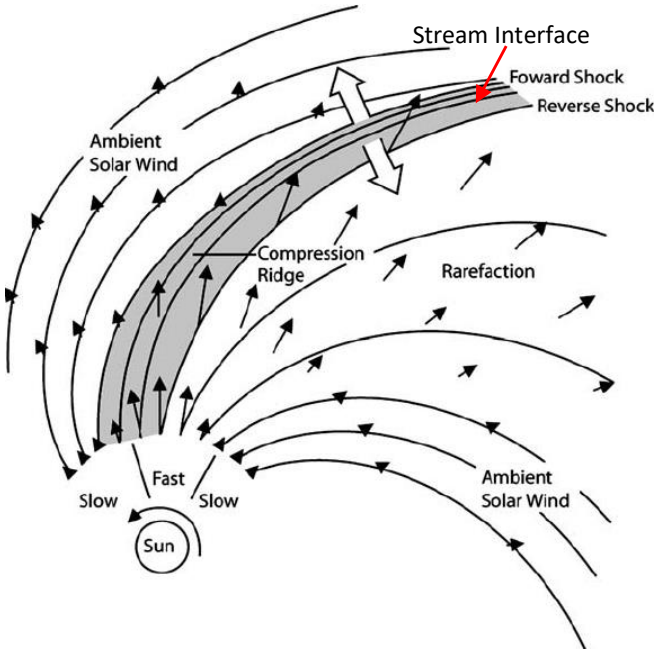

Figure 5.1 A schematic of the 2D solar equatorial plane of a SIR structure in the inner heliosphere. The grey shaded area is the compression region include the stream interface. Solid lines show the magnetic field lines and the length of the arrows is a measure of the flow speed (Pizzo, 1978).

The launch of the Solar Terrestrial Relations Observatory (STEREO)(Kaiser et al., 2008), which includes STEREO A (STA) and STEREO B (STB), offered a new opportunity for multiple viewpoint studies of CIRs and ICMEs. Many studies of CIRs and their interactions with the ambient solar wind during their propagation through the heliosphere have depended on STA and STB remote sensing and in situ measurements (Rouillard et al., 2009;Rouillard et al., 2010;Jian et al., 2009;Mason et al., 2009).

Jian et al. (2009) studied the differences in SIR properties by using multi spacecraft measurements (ACE, WIND, STA and STB, and Ulysses) for the period May to November 2007 near solar minimum. They discussed the effect of the temporal and spatial variations of the SIR's characteristics at these spacecraft positions. During this duration, Ulysses passed through the latitudinal region near the solar South Pole on March 2007 and it then moved northward, passing the ecliptic plane on 19 August 2007. In the August case (for example), the SI that is seen in STA has disappeared two days later at ULYSSES, whereas in the November case the SI that appeared in STB cannot be seen in the westward spacecraft STA. Jian et al. (2009) found that density and temperature variations do not clearly trend to "steepen" or "widen" in a particular way near the stream interface of the SIRs. However, the competitiveness of the compression and expansion effects on the entire SIR is noticeable.

Provornikova et al. (2012) studied the effect of merging CIRs (at solar minimum) on their driven shocks during their propagation into the heliosheath by using Voyager 2 observations and a three-dimensional MHD model. They found that reverse shocks disappear, and forward shocks weaken due to the CIRs interaction with their rarefaction regions. They proposed that the interaction of the CIRs shocks and the rarefaction regions could be the reason for these RSs disappearing in the heliosheath. Broussard et al. (1978) found that the evolution of coronal holes leads to long-term variations in the high speed stream (HSS) and to changes in the CIR morphology at 1 AU.

Schwenn (1990) used Helios mission (1974–1985) data to study the impact of latitudinal separation on multiple-spacecraft measurements of high speed streams and CIR. The separation between two different spacecrafts' heliographic latitudes can lead to considerably different CIR measurements despite having the same coronal hole source. Gosling et al. (1993) used ULYSSES measurements at a heliocentric distance of about 5 AU to show that the transit to high heliographic latitudes leads to systematic flow deflection for both CIRs' forward and reverse shocks. With the beginning of the STEREO era, many authors have pointed to the importance of latitudinal separation on the energetic particles emitted from CIRs shocks (Mason et al., 2009;Leske et al., 2010). During 2007 and 2008 (solar minimum period) and depending on multi spacecraft measurements (ACE, WIND, and STEREO), Mason et al. (2009) described spatial and temporal effects on the CIRs' *He* and heavy ions spectra emissions. These authors found that the changes in CIRs energetic particles over periods of up to 5 days are due to the small and irregular changes in the coronal hole's size, in addition to the different latitudinal separations. Gómez-Herrero et al. (2011) added another contribution to the evolution of CIR particle energy, which is the presence of transient structures such as ICMEs in the vicinity of, or embedded in, the CIR. They presented a comparison of multi spacecraft observations of the same CIR event for the period from 21 February 2008 to 5 April

2009 (Carrington rotations 2067–2082). Several ICMEs were in the vicinity or embedded within the CIRs and they accelerated the ions from hundreds of Kev to a few MeV.

In this chapter, we try to understand more about changes in a CIR's magnetic and plasma properties at 1 AU when it interacts with a magnetic flux rope (MFR) and ICME, in comparison to the undisturbed CIR. This is achieved through multiple spacecraft measurements of the CIR through 180 degrees' longitudinal rotation during solar maximum. We also highlight the impact of this interaction on the ICME and HCS behaviour. In Section 5.2, we present the *in situ* magnetic and plasma observations of four spacecraft (WIND, ACE, STA and STB). The same CIR is recorded by the four spacecraft with a MFR and ICME/CIR interaction at L1 and STA respectively. Section 5.3 highlights the properties and characteristics of the large-scale structures during their interaction and the effects on their characteristics during 180 degrees of rotation. Conclusions are given in section 5.4.

5.2 *In Situ* observations

For both STA and STB, we use the 1 min magnetic field measurements from the magnetometer (MAG Acuña et al. (2008)), the suprathermal electron distributions from the solar wind electron analyser (SWEA Sauvaud et al. (2008)) and the plasma and suprathermal ion composition (PLASTIC) (Galvin et al., 2008). The period of the study was from 20 April 2011 to 8 May 2011. During this period, the angular longitude separation between STB and STA grew from about 185.2° to 186.1° while the separation angle with Earth grew from about 94.7° to 94.1° for STB and from about 90.5° to 92° for STA.

At STB, a CIR signature was measured on 23 April 12:06 UT (Figure 5.2a, fourth vertical dotted line). It is preceded by a sector boundary crossing (SBC) of about 56 hrs (first vertical dotted line), which is recorded on 20 April 10:03 UT. When the SBC stars, the suprathermal electrons pitch angle distribution (1st panel) flips from 0 to 180 degrees. To distinguish the true position of the SBC from a local magnetic field inversion, we depend on both the heat flux distributions and the magnetic field measurements. The SBC is matched with the HCS location, which is displayed as the first vertical dotted line. When the CIR starts, there is a 180 degrees heat flux enhancement. An initial identification of the SI (pile up of total pressure with gradual declines at both sides) is at the fifth vertical dotted line (about 23 April, 19:30 UT), and an obvious fast RS appears at the sixth vertical dotted line. An interplanetary shock (third vertical dotted line) appears before the CIR by about 11 hours, associated with a brief enhancement in magnetic strength and a small increase in proton speed V_p, temperature T_p and density N_p. It preceded by a magnetic plateau region of about 55 hrs (between the second and third vertical dotted lines).

At the L1 position, the WIND spacecraft 1 min data of the magnetic field investigation (MFI Lepping et al. (1995)) and solar wind experiment (SWE Ogilvie et al. (1995)) are used, shown in Figure 5.2b. For comparison, and also due to missing data in some instruments, we also show in Figure 5.3 the Advanced Composition Explorer (ACE) 16 sec magnetic field measurements from the magnetic field investigation (MAG) Smith et al. (1998a) and (SWEPAM/SWICS merged data, see:

http://www.srl.caltech.edu/ACE/ASC/level2/sweswi_l3desc.html). Since WIND and ACE are closely separated, we have also included in Figure 5.2b the 273 eV ACE suprathermal electrons pitch angle distributions. The first sign of the CIR passage started on 29 April, at about 13:50 UT (Figure 5.2b, 2nd vertical dotted line) with an increase in magnetic strength, V_p, N_p and total pressure P_t. The CIR start is accompanied with a magnetic cone angle rotation and a plasma beta reduction, which is the signature of a magnetic flux rope MFR (blue shade) embedded within the CIR, with a magnetic field rotation duration of about 6.5 hrs (April 29, 14:30 UT-20:55 UT) and a 180 degrees' heat flux enhancement. The existence of the MFR in this location may mean that some of other CIR criteria are absent (further details are given in the next section).

The high-speed stream (HSS) source is coronal hole CH446, which is the same source as that measured by STB. *Vp* ranges between 477–770 km/s under the influence of the HSS. A SI is identified from a maximum peak in total pressure P_t (3rd vertical dotted line).The SDO Fe XII 193 A and STEREO EUVI 195 A solar images shown in Figure 5.4 confirm the correct coronal hole source. The SBC at WIND is associated with a heliospheric plasma sheet (HPS) (i.e. increase in proton density, low proton entropy), and the plasma beta elevation at ACE is very clear (Figure 5.3). In addition, the V_p profile in both is flat throughout the HPS. The fast RS has disappeared at the L1 position. The magnetic plateau region has compressed to about 19 hrs and is followed by the appearance of a magnetic exhausted region (orange shade). In addition, the magnetic plateau front boundary has approached and reached the SBC position(1st vertical dotted line).

As indicated by the second vertical dotted line in Figure 5.2c, the CIR is measured by STA on 6 May 22:00 UT, followed by the HSS from the same coronal hole source. There is an ICME signature at the front boundary of the CIR (second vertical dotted line) with a clear magnetic flux rope apparent from the coherent magnetic field rotation for about 6 hours (blue shade), from 7 May 00:36 UT to 06:19 UT, a bidirectional suprathermal electrons distribution, a magnetic strength between 10.5–17.1 nT, and a low plasma beta with an average 0.53. A SI is identified from a maximum peak in total pressure Pt on 7 May, at 07:10 UT, shown by the third vertical dotted line. The HPS maintains its position at the front boundary of the magnetic plateau whereas the HCS location within the HPS has shifted closer to the HPS front boundary (first vertical dotted line). The magnetic plateau region experienced an extension in the duration, which looks is probably a recovery phase, and it is now close to its duration as was at STB but with an increase in the magnetic magnitude and an enhancement of the heat flux at 180 degrees. The magnetic exhausted region at the rear of plateau (orange shade) became very prominent (larger decrease in magnetic field and increase in plasma beta). The fast RS reappeared with a magnetic strength, T_p, V_p and P_t properties as were at STB' fast RS (fourth vertical dotted line).

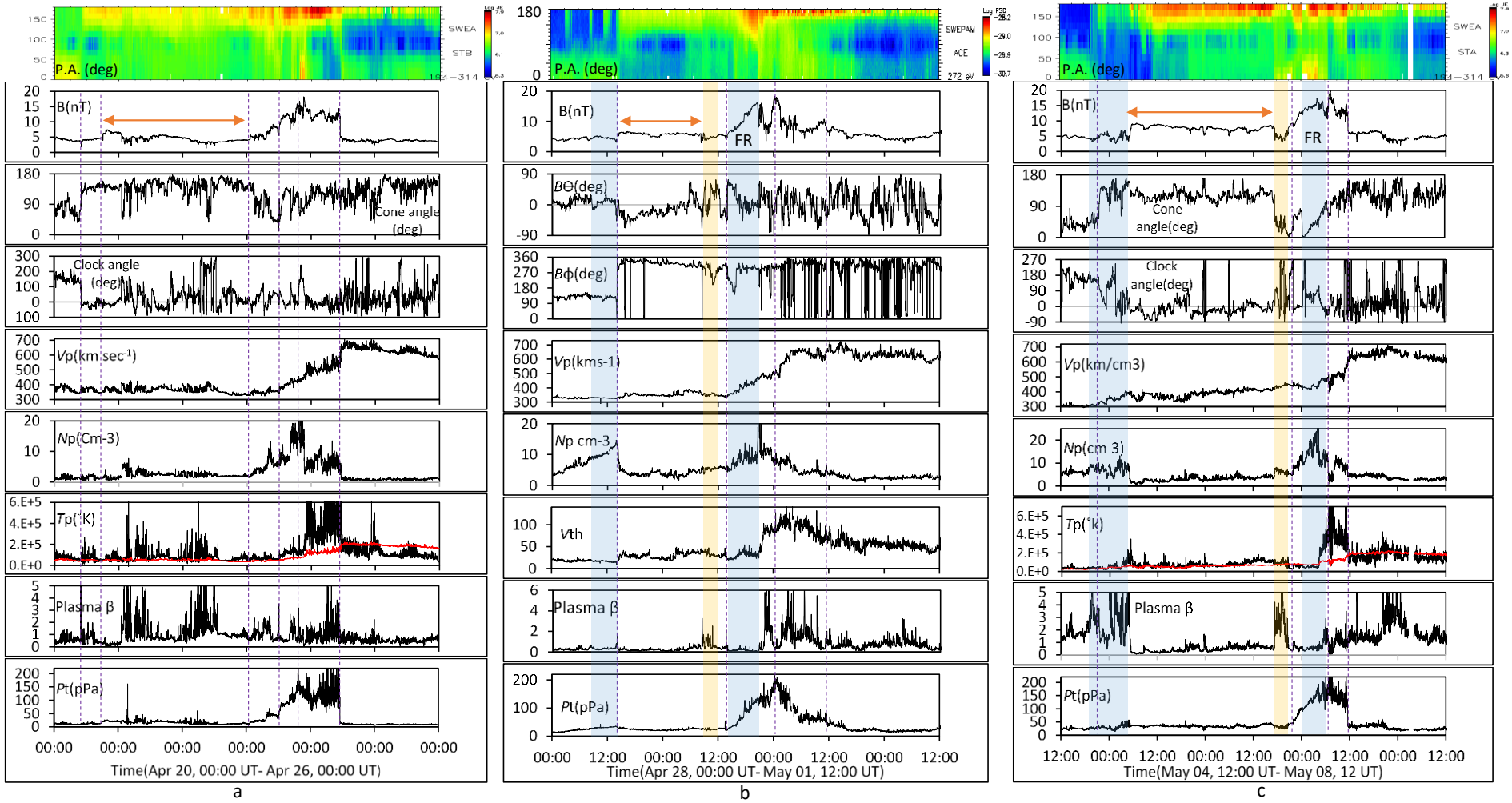

Figure 5.2 In situ measurements of STB, WIND and STA. For both STA and STB (a and c panels): Suprathermal electrons pitch angle distributions (194-314 eV), Magnetic field magnitude B(nT), Cone angle(deg), Clock angle(deg), Proton speed Vp(kmsec^{-1}), Proton density Np(Cm^{-3}), Proton temperature Tp(˚K) and and experimental temperature Tex (K)(red line), Plasma beta and total perpendicular pressure Pt(pPa). For Wind (b panel): ACE Suprathermal electrons pitch angle distributions (272 eV), Magnetic field magnitude B(nT), Cone angle(deg), Clock angle(deg), Proton speed Vp(km sec^{-1}), Proton density Np(Cm^{-3}), thermal velocity, Plasma beta and Total perpendicular pressure Pt(pPa).

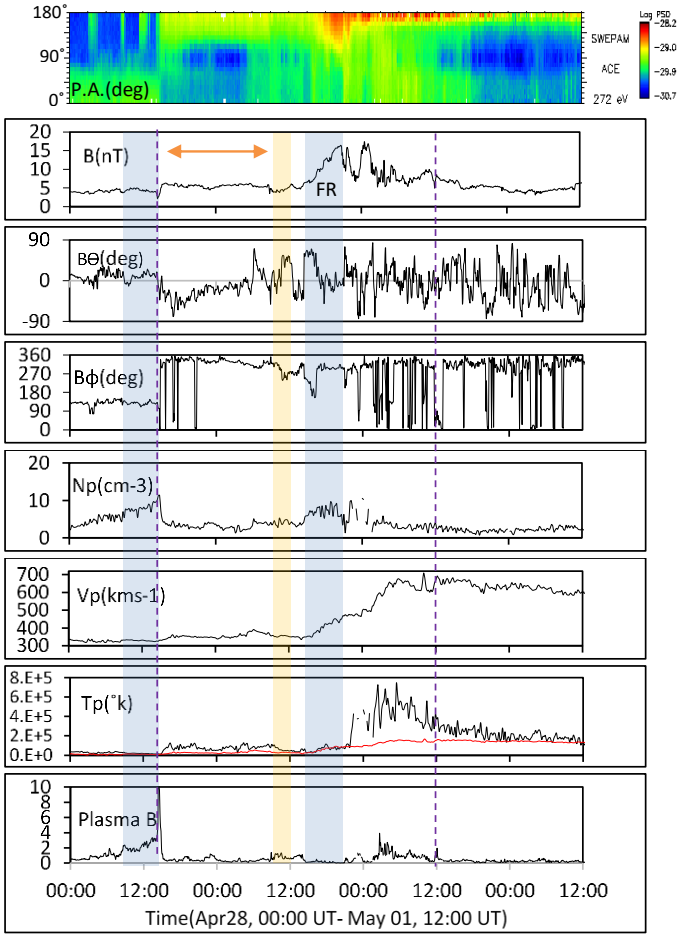

Figure 5.3 Ace measurements: Suprathermal electrons pitch angle distributions (272 eV), Magnetic field magnitude B(nT), BΘ(deg), Bφ(deg), Proton density Np(cm^{-3}), Proton speed Vp($kmsec^{-1}$), Proton temperature Tp(°K) and experimental temperature Tex (K)(red line), and Plasma beta. The first blue shaded is the HPS region, whereas the second is the magnetic flux rope.

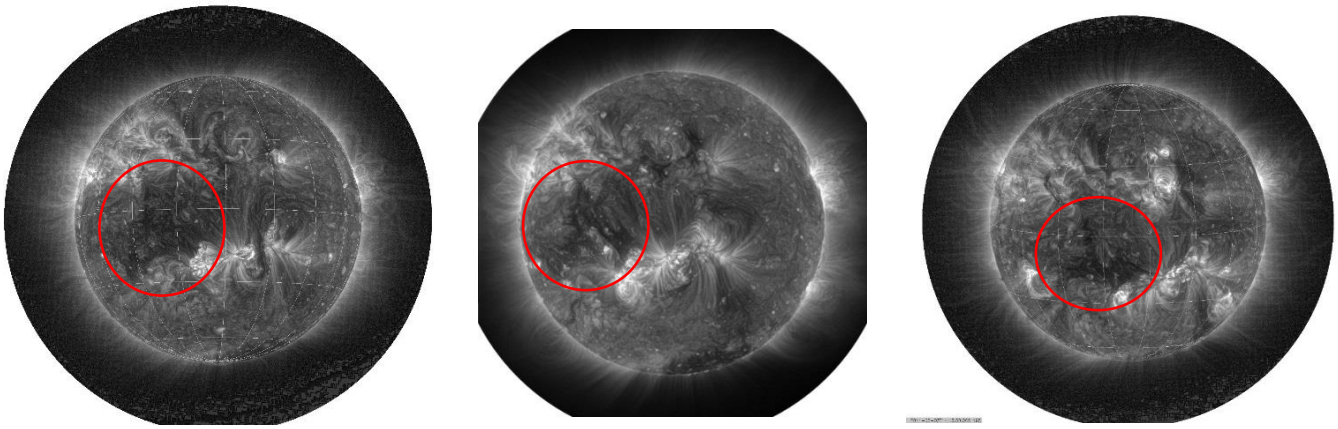

Figure 5.4 Images of the coronal hole (circled red) by STB EUVI 195A (April 19, 2011, left), SDO/AIA 193A (April 25, 2011, middle) and STA EUVI 195A (May 03, 2011, right) (available at http://eagle.imaps.aber.ac.uk/)

5.3 Analyses and Discussion

In this section, we discuss the main changes to the CIR characteristics as measured by STB, at L1 and by STA. We also discuss the properties and characteristics of the ICMEs and HCS that interact with the CIR through this period.

STB measures magnetic and plasma profiles typical of a CIR with a strong RS. The unusual thing in this event is the large separation between the HCS/SBC and the CIR position, but this is not unprecedented. Neugebauer et al. (2004) reported on several SIRs without sector boundaries. The last vertical dotted line in Figure 5.2a shows the end of the CIR. A 90 degrees' heat flux depletion is clear at the end of the CIR (Figure 5.2a, 1st panel). About 20% of SIRs have a slow/fast sharp boundary (Jian et al., 2009) and not all SIs display clear signatures of discontinuities (Crooker et al., 1999); therefore, we identify an initial SI location at the second vertical dotted line of Figure 5.5a (To clarify more, it has added this figure with shorter duration) through a peak in total pressure with gradual declines at both sides. Indeed, the P_t morphology in STB looks like a plateau with multiple peaks. We believe that the fast-slow stream interaction (SI) is in the growth stage, so it is difficult to place too much confidence in the exact location of the SI. Criteria other than P_t (e.g. the proton density drop, temperature and entropy jump) suggests another possible locations for the SI as the third and fourth vertical dotted line (Figure 5.5a).

At the L1 Position (Figure 5.2b), the significant appearance of the HPS (which is absent in STB) is perhaps due to the MFR/CIR interaction. The interaction may cause a temporary increase in interchange reconnection and subsequent propagating transient blobs between the coronal hole open field and the adjacent closed field of the MFR near the cusp of the streamer belt near the Sun. The magnetic plateau duration is shorter than at STB because of compression and, therefore, it reduced the duration time between the CIR front boundary and the SBC. It shortened to about 24 hours, and the slight increase in the magnetic field at its front boundary resembles a pressure wave. In addition, the front boundary of the magnetic plateau became close to the HCS location and adjacent to the rear boundary of the HPS. However, the HCS position at the HPS boundary supports the idea that an interchange reconnection assisted to release the parcels through the HPS. The orange shaded region is a magnetic exhausted region at an early stage of its formation (a small drop in magnetic strength, plasma beta increase and a low-density elevation). The formation of a magnetic exhausted region may be due to the asymmetric nature of the plasma at the region boundaries. The magnetic reduction is clearer in the magnetic magnitude measured by ACE (Figure 5.3, the orange shaded region).

The flux rope duration is about 6.5 hours (Figure 5.5b, blue shaded). It looks like a small-scale flux rope (i.e. a short duration with magnetic field shear angles at the two boundaries across the two magnetic exhausted boundaries) (Cartwright and Moldwin, 2008;Tian et al., 2010;Zheng and Hu, 2016). The temporary magnetic field reversal at the flux rope front boundary is due to the MFR being replaced locally by the HCS and connecting with solar winds of different magnetic field polarities.

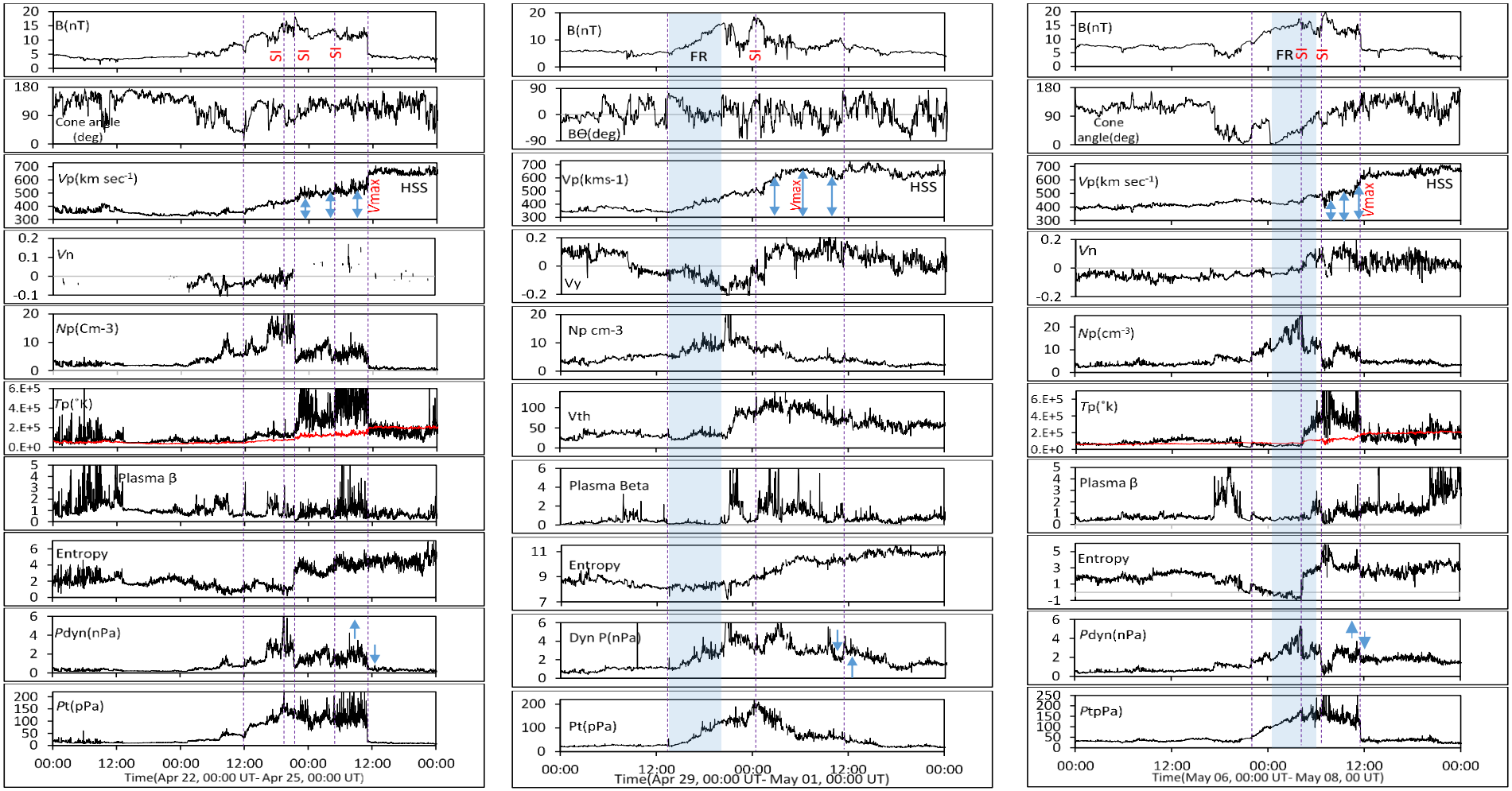

Figure 5.5 In situ measurements of STB(a), WIND(b) and STA(c). For both STA and STB, the panels display: Magnetic field magnitude B(nT), Cone angle(deg), Proton speed Vp(km sec^{-1}), Azimuthal velocity Vn, Proton density Np(Cm-3), Proton temperature Tp(°K), Plasma beta, Entropy, Dynamic pressure(nPa) and Total perpendicular pressure Pt(pPa). For Wind panels: Magnetic field magnitude B(nT), Cone angle(deg), Proton speed Vp(kms^{-1}), Azimuthal velocity Vy, Proton density Np(Cm-3), Thermal velocity Vth, Plasma beta, Entropy, Dynamic pressure(nPa), Total perpendicular pressure Pt(pPa). The blue shaded are the flux ropes regions at Wind and STA.

The MFR has been listed in the WIND ICME Catalogue with start time 29 April, 09:07 UT, as a magnetic obstacle from 13:55–20:52 UT and ICME end time at 29 April, 22:04 UT. The Richardson & Cane ICME Catalogue does not refer to this ICME, which confirms the diversity of ICME definitions and criteria. In addition, we have checked the Wind magnetic cloud list Lepping et al. (2015) and there are no events listed in this period. It is quite difficult to identify the L1 MFR source because remote sensing of the low corona only reveals a few small CMEs between 24 May and 25 May, but we believe it was from one of two potential sources: 1) the narrow 24 April CME (about 07:24 UT), which is a faint, narrow and small-scale eruption (Figure 5.6) or 2) a local magnetic reconnection in the extended corona or solar wind.

Within the flux rope, T_p is higher than the typical MC ($T_p < 0.5T_{ex}$)(see Figure 5.3), which means that it is either truly not an ICME (just a flux rope), and not necessarily be associated with a decreased temperature (Rouillard, 2011), or the temperature profile reflects the impact of MFR/CIR interaction on the T_p characteristics. The unidirectional 180 degrees pitch angle distributions along the MFR (Figure 5.2b) suggest that the magnetic field lines forming it are open with one end rooted at the solar surface, which is likely due to interchange reconnection with the transequatorial coronal hole CH446. In addition, the enhancement of the 180 degrees heating flux through the FR duration compared to what it is at the follower CIR implies that the spacecraft traverse through a different plasma nature.

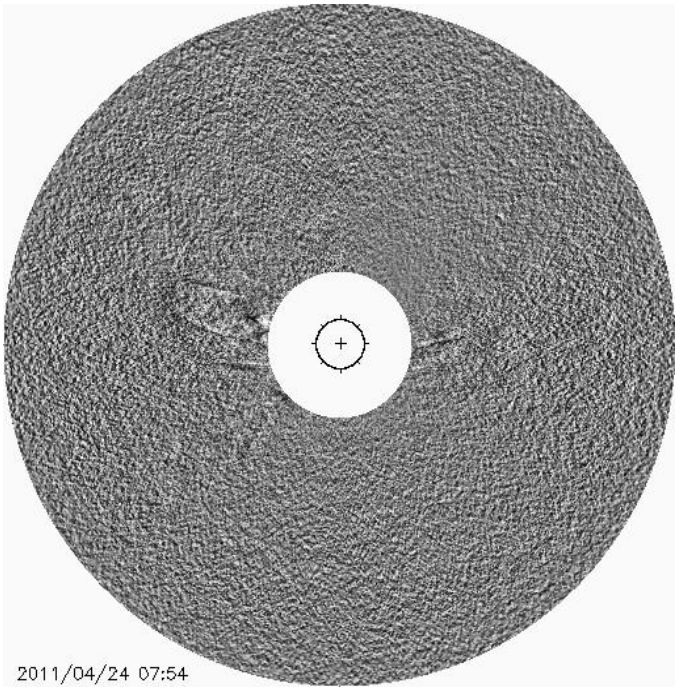

Figure 5.6 The faint signature of a CME observed on April 24 07:54 UT from the STA Cor2 coronagraph. The image has been processed to remove static radial structures (i.e. streamers).

The CIR start time is difficult to identify due to the embedded MFR/CIR. The first vertical dotted line in Figure 5.5b tended to fit the CIR criteria. The magnetic field strength and proton speed start to increase present a CIR and MFR matching location in their onset time. There is a considerable decrease in magnetic strength following the flux rope, indicative of a magnetic exhausted region between regions of quite different natures. The second vertical dotted line in Figure 5.5b displays a SI with a peak in magnetic strength and total pressure, gradual decline in density, and temperature elevation. It is more obvious than at STB.

The impact of the MFR/CIR interaction is considerable on the entropy profile. The large entropy increases at STB (Figure 5.5a, 3rd vertical dotted line) is absent at WIND (Figure 5.5b) and becomes flat, which may be interpreted as overlap between the MFR and CIR.
The most notable change in the L1 CIR morphology is the disappearance of the RS. The interaction with the flux rope at the CIR front boundary and the clear appearance of the SI makes the speed increase steeper at the front region, which predominantly reduces the speed shear strength at the RS. In other words, the flux rope and the SI have changed the position of the CIR' maximum speed (V_{max}) to move forward away from its rear location after what it was at the rear boundary of the CIR on STB, as shown in Figure 5.5 a&b, 3rd panels. Subsequently, the acting forces at both RS' sides have changed, with a domination of the rarefaction leading boundary region (CIR up stream), which led to weakening the RS. This interpretation is supported by the dynamic pressure P_{dyn} panels (Figure 5.5 a& b). At STB, P_{dyn} was very low at the rarefaction region (CIR upstream) compared with that at the CIR rear boundary (CIR downstream). This situation is reversed completely at WIND (see blue arrows in the two dynamic pressure panels), referring to a new feature.

At the STA position (Figure 5.2c), the HPS maintains its position within the front boundary of the magnetic plateau but the HCS location (first vertical dotted line) is closer to the HPS front boundary. This may be due to the magnetic plateau region that has expanded since the L1 position and has returned to the longer duration measured at the position of STB. This expansion is associated with a magnetic strength elevation and a 180 degrees suprathermal electron distribution enhancement, referring to energizing by inward electrons. As the plateau, magnetic magnitude increases, the magnetic exhausted region (orange shade) became clearer (with more magnetic magnitude drop and plasma beta rising). This may due to the different distributions of the particles at the magnetic exhausted boundaries or because of the multiple local magnetic fields reversals appeared in this region as a result of its location at the front of a MC flux rope.
The ICME and CIR appear at the first vertical dotted line (Figure 5.5c) - this agree with the STEREO A/B Lists of SIRs and ICMEs (Jian *et al*., 2013) (Dr Lan K. Jian, University of Maryland College Park, e mail correspondence March 27, 2017). Figure 5.7 shows a large CME observed on 3 May by STA COR1 and EUVI 195 and SOHO LASCO C2. The huge 3 May CME (which is mentioned in the list of interplanetary coronal mass ejections observed by STA and STB(Jian *et al*., 2013)) and the associated filament eruption is the likely source of the ICME measured by STA.

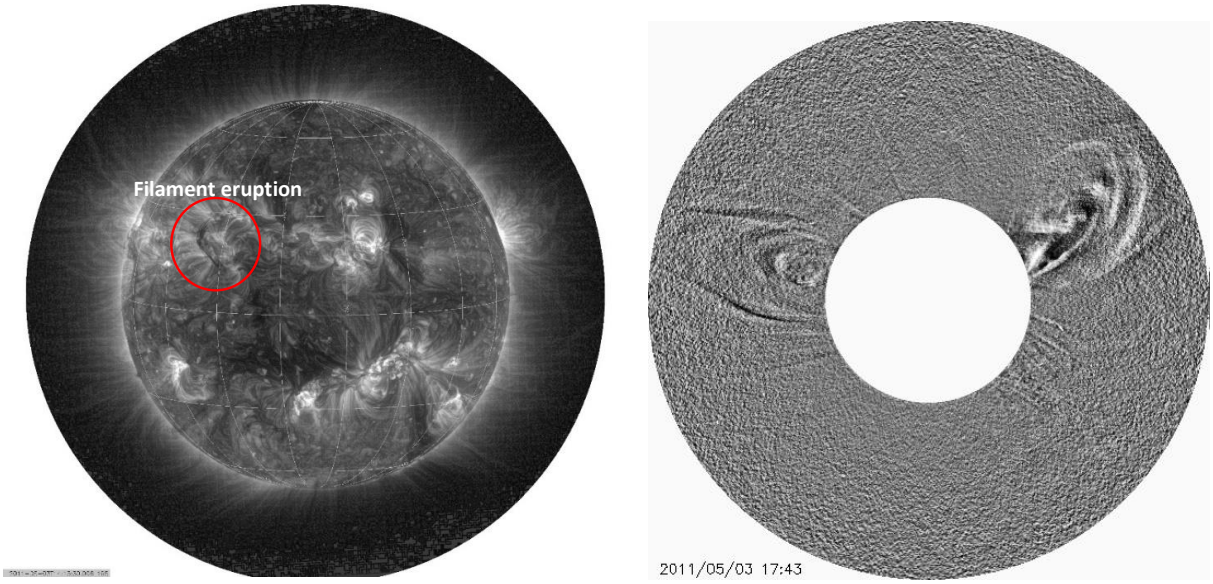

Figure 5.7 May 03, 17:43 UT CME. The left panel displays the active region with a filament eruption circled in red (observed by STA EUVI 195). The right panel shows the CME which observed by SOHO LASCO C2 (available at http://eagle.imaps.aber.ac.uk/).

Within the magnetic cloud (shaded blue in Figure 5.5c), the plasma beta values are higher than the values when the MC may be isolated(example (Wang et al. (2003)). This reveals the CIR role in increasing this value when the MC is within it. For the first 4 hours of the MC duration, the T_p is less than T_{ex} . A sudden temperature and entropy high jump (2nd vertical dotted line) on May 7, at 04:15 UT associated with a sudden high drop in density and a V_n shear. These signatures refer to a stream interface location within the magnetic cloud FR. The third vertical dotted line refers to the SI location that we determined in Figure 5.2c, depending on the maximum total pressure. We believe that this SI is the same SI at WIND. The appearance of more than one SI supports the idea in the previous chapters about the possibility of more than one SI appearing during the ICME/CIR embedded. It also reflects the role of CIR in building a SI within the MC. The CIR and ICME front region witnessed a deceleration and expansion, which make the CIR' Vmax position move back towards the rear boundary, as it was in STB (Figure 5.5c, 3rd panel). This process may have stimulated the appearance of the SI within the MC.

The flow shear changes on the SIs at WIND and STA perhaps due to the spatial changing and temporal coronal hole variations (Figure 5.4), which is the source of the fast flow. The noticeable feature at the STA is the return of the RS to appears again. The ICME deceleration has moved the position of the CIR's maximum speed (*V*max) back to the rear CIR' boundary, similar to position at STB. The SIs location has approached the *V*max location. These two changes made the profile of the dynamic pressure near the rear of the CIR to return to a state similar to that seen at STB (see *Figure 5.5*c, 3rd and 9th panels), and thus, the reverse shock reappears.*The* P_{dyn} become lower at the rarefaction region (CIR upstream) compared with

that at the CIR rear boundary (CIR downstream). As in STB, the last vertical dotted line refers to the end of the CIR. The 90 degrees' heat flux depletion was clear at the end of the CIR (see Figure 5.2, Panel 1).
The proton speed profiles at all the spacecraft reveal the role of this parameter in controlling the RS behaviour. The blue arrows in Figure 5.5, third panels, show the CIR *V*max position displacement during the three spacecraft positions.

5.4 Conclusions

Our conclusions are summarized as follows:
In all spacecraft positions, although the global HCS was far away ahead of the events, the HCS has affected by the FRs/CIR interaction. The obvious appearance and growth of the HPS at wind and STA is due to the interchange reconnection which assists to release the parcels through the HPS.
The impacts of the CIR- FR interactions have distributed along the events. The presence of a reverse shock at STB, subsequent absence at L1 region, and then an appearance at STA, implies that the CIR reverse shock behaviour is sensitive to the interaction with transient interplanetary structures. It also reveals the CIR's ability to recover its magnetic field and plasma characteristics after disruption by ICMEs.

The L1 ICME changes the CIR speed and dynamic pressure profiles. consequently, the acting forces at both reverse shock sides have changed, leading to the disappearance of the reverse shock at L1. At STA, the ICME deceleration has moved the position of the CIR's maximum speed (*V*max) back to the rear CIR boundary, similar to position at STB. The SIs location has approached the Vmax location. These two changes made the profile of the dynamic pressure near the rear of the CIR to return to a state similar to that seen at STB, and thus, the reverse shock reappears, which means that the RS behaviour is subject to the local interplanetary conditions.
The flux ropes complicate the CIR solar wind morphology and affects the location of the SI, or to cause the appearance of more than one SI. There is also an obvious signature of a SI penetration through the magnetic cloud flux rope at STA, which is itself embedded within the CIR.
The main finding of the study is: 1- the CIR reverse shock behaviour. It is subject to the local interplanetary circumstance. 2- the SI ability to change the magnetic flux rope plasma profiles but no magnetic rotation deformation. 3- the long traviling separation(about 185 degree of longitude) reveal that the CIR can recover its magnetic field and plasma characteristics after disruption by ICME.

Chapter 6

Conclusions

6.1 Overall conclusions

The September 09-10, 2011 event of the HPS-ICME-CIR/HSS interaction affected the properties and characteristics of the three interplanetary structures. The impact is significant along the whole event, including a driven strong forward shock, a heating flux discontinuity upstream of the ICME front shock, the very high proton density at the frontal boundary of the HPS and forward shock, the significant speed elevation within the sheath, the distortion of *Bz* in the magnetic cloud, the indistinct location of the stream interface, and the reverse shock at the rear boundary of the CIR. Interchange reconnection is invoked to interpret the dominant unidirectional component of the suprathermal electron distribution throughout the event. Despite the disruption caused by the ICME, some general features of the CIR are preserved, as seen by a comparison with the CIR seen in the absence of an ICME a few days earlier by STEREO B. This allows an estimate of the compression of the CIR by the ICME as a factor of ~ 4, and further enables some qualitative comparison and further insight into the interaction.

A compound stream of three ICMEs and a CIR which displays another type of interaction between the interplanetary large-scale structures. The third ICME has merged with, and is embedded within the CIR. These findings are difficult to reconcile with remote sensing observations. The results suggest either that ICME2 is a compressed interplanetary ejecta region between ICME1 and CIR/ICME3, or that there were originally three CMEs, but due to the complexity and the position of the active region, the remote sensing images were unable to display the sequences of events clearly. The *in-situ* data at 1 AU shows a penetration of a forward pressure wave driven by the ICME3/CIR, associated with a rise in temperature throughout the second ICME and in part of the first one. The magnetic reconnection exhausted region between ICME1 and ICME2 shows that they are separate structures with distinct region boundaries, and that they are two different interplanetary ejecta. This exhausted region is weaker than its counterpart between the ICME2 rear boundary and ICME3/CIR, possibly due to the asymmetric distribution of plasma between the ICME2 rear boundary and the CIR front boundary. The presence of a SI within the ICME3 magnetic flux rope suggests that the SI has penetrated the flux rope and has changed its characteristics. The sudden appearance of ICME3 within the fast wind side of the CIR causes the temperature to drop suddenly to its lowest level in about 1.2 hours, from 3.89×10^5 K to 1.07×10^4 K. ICME3 impacts the CIR through expansion and deceleration. Penetration of a forward pressure wave driven by this combined ICME-CIR causes the second ICME and part of the first one to increase in temperature and plasma beta.

Based on multi-spacecraft in situ measurements (STB, Wind, Ace, and STA), we tracked the evolution of a CIR through 180 degrees of longitude, including interaction with two-magnetic cloud flux ropes embedded within the CIR at the L1 and STA positions. In all spacecraft positions, although the global HCS is situated ahead of the events, the HCS is affected by the interaction. The obvious appearance of the HPS at Wind and STA is due to the interchange reconnection which assists to release plasma parcels along the HPS.
The effects of the CIR- FR interaction is distributed throughout the events. The presence of a reverse shock at STB, subsequent absence at L1 region, and then an appearance at STA, implies that the CIR reverse shock behaviour is sensitive to the interaction with transient interplanetary structures. It also reveals the CIR's ability to recover its magnetic field and plasma characteristics after disruption by ICMEs. The L1 ICME changes the CIR speed and dynamic pressure profiles, consequently, the acting forces at both reverse shock sides have changed, leading to the disappearance of the reverse shock at this location. The ICME deceleration at STA enabled the CIR to recover its maximum speed (*V*max) position and back to the rear boundary as was at STB. Also, the SIs location has approached the Vmax location. These two changes made the CIR rear force which encounters the follower rarefaction to have the same strength that it had before (at STB) and thus, a reverse shock got back to appear again. The flux ropes complicate the CIR solar wind morphology and affects the location of the SI, or even cause the appearance of more than one SI. There is also an obvious signature of SI penetration through the magnetic cloud flux rope at STA, which is itself embedded within the CIR.

6.2 Future work

Multi-point observations of ICMEs-SIRs interaction shows that each event has its individual evolution and configuration, and the relationship of MCs to ICMEs-drive shocks is still an open issue in space research. Following the results of chapter 3, a future study will investigate more complex HPS-ICME-CIR *in situ* cases, possibly establishing common interaction features and quantifying the degree of variation between interacting events. This will aid the understanding of the impact of these interactions on the propagation of large-scale structures through interplanetary space. The survival of a magnetic exhausted region at the front boundary of the CIR before and with the interaction, suggests that more studies of many other similar cases should be conducted. Accurate interpretation of many complex *in situ* interaction events is difficult without a comparison of events in the absence of interaction. Through the result of chapter 4, the presence of the stream interface SI within the flux rope is noteable, and more similar cases should be investigated to establish their probability of occurrence. Additional studies of similar compound stream cases which show poor matching with solar remote-sensing observations may tell us to what extent *in situ* measurements can be interpreted without the additional constraint of remote observations.

Following the results of chapter 5, a study is planned to track the evolution of the CIR during its propagation through the interplanetary spiral patterns between 90 to 180 degrees of longitude based on L1, STEREO A and B measurements over several solar rotations. This will give us information on the ability of CIRs to maintain their magnetic field and plasma profiles over long periods.

Bibliography

ACUÑA, M., CURTIS, D., SCHEIFELE, J., RUSSELL, C., SCHROEDER, P., SZABO, A. & LUHMANN, J. 2008. The STEREO/IMPACT magnetic field experiment. *Space Science Reviews,* 136**,** 203-226.

AKASOFU, S.-I. & CHAPMAN, S. 1972. Solar-terrestrial physics.

AL-HADDAD, N., NIEVES-CHINCHILLA, T., SAVANI, N. P., MÖSTL, C., MARUBASHI, K., HIDALGO, M. A., ROUSSEV, I., POEDTS, S. & FARRUGIA, C. J. 2013. Magnetic field configuration models and reconstruction methods for interplanetary coronal mass ejections. *Solar Physics,* 284**,** 129-149.

ANDERSON, B., SKOUG, R., STEINBERG, J. & MCCOMAS, D. 2012. Variability of the solar wind suprathermal electron strahl. *Journal of Geophysical Research: Space Physics,* 117.

ANDREWS, G. B., ZURBUCHEN, T. H., MAUK, B. H., MALCOM, H., FISK, L. A., GLOECKLER, G., HO, G. C., KELLEY, J. S., KOEHN, P. L. & LEFEVERE, T. W. 2007. The Energetic Particle and Plasma Spectrometer Instrument on the MESSENGER Spacecraft. *Space science reviews,* 131**,** 523-556.

ASCHWANDEN, M. J., BOERNER, P., SCHRIJVER, C. J. & MALANUSHENKO, A. 2013. Automated temperature and emission measure analysis of coronal loops and active regions observed with the Atmospheric Imaging Assembly on the Solar Dynamics Observatory (SDO/AIA). *Solar Physics***,** 1-26.

BALOGH, A., BOTHMER, V., CROOKER, N., FORSYTH, R., GLOECKLER, G., HEWISH, A., HILCHENBACH, M., KALLENBACH, R., KLECKER, B. & LINKER, J. 1999. The solar origin of corotating interaction regions and their formation in the inner heliosphere. *Space Science Reviews,* 89**,** 141-178.

BAME, S., ASBRIDGE, J., FELDMAN, W., FENIMORE, E. & GOSLING, J. 1979. Solar wind heavy ions from flare-heated coronal plasma. *Solar Physics,* 62**,** 179-201.

BELCHER, J. & DAVIS, L. 1971. Large-amplitude Alfvén waves in the interplanetary medium, 2. *Journal of Geophysical Research,* 76**,** 3534-3563.

BLANCO, J., RODRÍGUEZ-PACHECO, J., HIDALGO, M. & SEQUEIROS, J. 2006. Analysis of the heliospheric current sheet fine structure: Single or multiple current sheets. *Journal of atmospheric and solar-terrestrial physics,* 68**,** 2173-2181.

BORRINI, G., GOSLING, J., BAME, S. & FELDMAN, W. 1982. Helium abundance enhancements in the solar wind. *Journal of Geophysical Research: Space Physics,* 87**,** 7370-7378.

BORRINI, G., GOSLING, J., BAME, S., FELDMAN, W. & WILCOX, J. 1981. Solar wind helium and hydrogen structure near the heliospheric current sheet: A signal of coronal streamers at 1 AU. *Journal of Geophysical Research: Space Physics,* 86**,** 4565-4573.

BOTHMER, V. & RUST, D. 1997. The field configuration of magnetic clouds and the solar cycle. *Coronal mass ejections***,** 139-146.

BOTHMER, V. & SCHWENN, R. 1994. Eruptive prominences as sources of magnetic clouds in the solar wind. *Space Science Reviews,* 70**,** 215-220.

BOTHMER, V. & SCHWENN, R. The structure and origin of magnetic clouds in the solar wind. Annales Geophysicae, 1997. Springer, 1-24.

BOTHMER, V. & SCHWENN, R. 1998. The structure and origin of magnetic clouds in the solar wind. *Ann. Geophys.,* 16**,** 1-24.

BRANDT, J. C. 1970. Introduction to the solar wind.

BROOKS, D. H., WARREN, H. P. & YOUNG, P. R. 2011. EUV spectral line formation and the temperature structure of active region fan loops: observations with Hinode/EIS and SDO/AIA. *The Astrophysical Journal,* 730**,** 85.

BROUSSARD, R., SHEELEY, N., TOUSEY, R. & UNDERWOOD, J. 1978. A survey of coronal holes and their solar wind associations throughout sunspot cycle 20. *Solar Physics,* 56**,** 161-183.

BRUECKNER, G., HOWARD, R., KOOMEN, M., KORENDYKE, C., MICHELS, D., MOSES, J., SOCKER, D., DERE, K., LAMY, P. & LLEBARIA, A. 1995. The large angle spectroscopic coronagraph (LASCO). *Solar Physics,* 162**,** 357-402.

BURLAGA, L. 1974. Interplanetary stream interfaces. *Journal of Geophysical Research,* 79**,** 3717-3725.
BURLAGA, L. 1975. Interplanetary streams and their interaction with the earth. *Space Science Reviews,* 17**,** 327-352.
BURLAGA, L. 1988. Magnetic clouds and force-free fields with constant alpha. *Journal of Geophysical Research: Space Physics,* 93**,** 7217-7224.
BURLAGA, L., BEHANNON, K. & KLEIN, L. 1987. Compound streams, magnetic clouds, and major geomagnetic storms. *Journal of Geophysical Research: Space Physics,* 92**,** 5725-5734.
BURLAGA, L., FITZENREITER, R., LEPPING, R., OGILVIE, K., SZABO, A., LAZARUS, A., STEINBERG, J., GLOECKLER, G., HOWARD, R. & MICHELS, D. 1998. A magnetic cloud containing prominence material: January 1997. *Journal of Geophysical Research: Space Physics,* 103**,** 277-285.
BURLAGA, L., LEPPING, R. & JONES, J. 1990. Global configuration of a magnetic cloud. *Physics of magnetic flux ropes***,** 373-377.
BURLAGA, L., MCDONALD, F. & SCHWENN, R. 1986. Formation of a compound stream between 0.85 AU and 6.2 AU and its effects on solar energetic particles and galactic cosmic rays. *Journal of Geophysical Research: Space Physics,* 91**,** 13331-13340.
BURLAGA, L. & OGILVIE, K. 1972. Solar wind temperature and speed.
BURLAGA, L., PLUNKETT, S. & ST CYR, O. 2002. Successive CMEs and complex ejecta. *Journal of Geophysical Research: Space Physics,* 107.
BURLAGA, L., SITTLER, E., MARIANI, F. & SCHWENN, R. 1981. Magnetic loop behind an interplanetary shock: Voyager, Helios, and IMP 8 observations. *Journal of Geophysical Research: Space Physics,* 86**,** 6673-6684.
BURLAGA, L., SKOUG, R., SMITH, C., WEBB, D., ZURBUCHEN, T. & REINARD, A. 2001. Fast ejecta during the ascending phase of solar cycle 23: ACE observations, 1998–1999. *Journal of Geophysical Research: Space Physics,* 106**,** 20957-20977.
CANE, H. & RICHARDSON, I. 2003. Interplanetary coronal mass ejections in the near-Earth solar wind during 1996–2002. *Journal of Geophysical Research: Space Physics,* 108.
CANE, H. V. 2000. Coronal mass ejections and Forbush decreases. *Cosmic Rays and Earth.* Springer.
CANNON, P., ANGLING, M., BARCLAY, L., CURRY, C., DYER, C., EDWARDS, R., GREENE, G., HAPGOOD, M., HORNE, R. B. & JACKSON, D. 2013. *Extreme space weather: impacts on engineered systems and infrastructure*, Royal Academy of Engineering.
CARTWRIGHT, M. & MOLDWIN, M. 2008. Comparison of small-scale flux rope magnetic properties to large-scale magnetic clouds: Evidence for reconnection across the HCS? *Journal of Geophysical Research: Space Physics,* 113.
CHEN, P. 2009. The relation between EIT waves and coronal mass ejections. *The Astrophysical Journal Letters,* 698**,** L112.
CHEN, P. 2011. Coronal mass ejections: models and their observational basis. *Living Reviews in Solar Physics,* 8**,** 1-92.
CHOLLET, E., SKOUG, R., STEINBERG, J., CROOKER, N., GIACALONE, J., MAKSIMOVIC, M., ISSAUTIER, K., MEYER-VERNET, N., MONCUQUET, M. & PANTELLINI, F. Reconnection and Disconnection: Observations of Suprathermal Electron Heat Flux Dropouts. AIP Conference Proceedings, 2010. AIP, 600-603.
CID, C., CREMADES, H., ARAN, A., MANDRINI, C., SANAHUJA, B., SCHMIEDER, B., MENVIELLE, M., RODRIGUEZ, L., SAIZ, E. & CERRATO, Y. 2012. Can a halo CME from the limb be geoeffective? *Journal of Geophysical Research: Space Physics,* 117.
CREMADES, H. & BOTHMER, V. 2004. On the three-dimensional configuration of coronal mass ejections. *Astronomy & Astrophysics,* 422**,** 307-322.
CREMADES, H., BOTHMER, V. & TRIPATHI, D. 2006. Properties of structured coronal mass ejections in solar cycle 23. *Advances in Space Research,* 38**,** 461-465.
CROOKER, N. Heliospheric current sheet structure. AIP Conference Proceedings, 1999. AIP, 93-98.
CROOKER, N. Heliospheric plasma and current sheet structure. AIP Conference Proceedings, 2003. IOP INSTITUTE OF PHYSICS PUBLISHING LTD, 93-97.

CROOKER, N., BURTON, M., SISCOE, G., KAHLER, S., GOSLING, J. & SMITH, E. 1996. Solar wind streamer belt structure. *Journal of Geophysical Research: Space Physics,* 101**,** 24331-24341.

CROOKER, N., GOSLING, J., BOTHMER, V., FORSYTH, R., GAZIS, P., HEWISH, A., HORBURY, T., INTRILIGATOR, D., JOKIPII, J. R. & KÓTA, J. 1999. CIR morphology, turbulence, discontinuities, and energetic particles. *Space Science Reviews,* 89**,** 179-220.

CROOKER, N., GOSLING, J. & KAHLER, S. 1998. Magnetic clouds at sector boundaries. *Journal of Geophysical Research: Space Physics,* 103**,** 301-306.

CROOKER, N., GOSLING, J. & KAHLER, S. 2002. Reducing heliospheric magnetic flux from coronal mass ejections without disconnection. *Journal of Geophysical Research: Space Physics,* 107.

CROOKER, N. & HORBURY, T. 2006. Solar imprint on ICMEs, their magnetic connectivity, and heliospheric evolution. *Space science reviews,* 123**,** 93-109.

CROOKER, N., HUANG, C. L., LAMASSA, S., LARSON, D., KAHLER, S. & SPENCE, H. E. 2004a. Heliospheric plasma sheets. *Journal of Geophysical Research: Space Physics,* 109.

CROOKER, N. & INTRILIGATOR, D. 1996. A magnetic cloud as a distended flux rope occlusion in the heliospheric current sheet. *Journal of Geophysical Research: Space Physics,* 101**,** 24343-24348.

CROOKER, N., KAHLER, S., GOSLING, J. & LEPPING, R. 2008. Evidence in magnetic clouds for systematic open flux transport on the Sun. *Journal of Geophysical Research: Space Physics,* 113.

CROOKER, N., KAHLER, S., LARSON, D. & LIN, R. 2004b. Large-scale magnetic field inversions at sector boundaries. *Journal of Geophysical Research: Space Physics,* 109.

CROOKER, N., SISCOE, G., SHODHAN, S., WEBB, D., GOSLING, J. & SMITH, E. J. 1993. Multiple heliospheric current sheets and coronal streamer belt dynamics. *Journal of Geophysical Research: Space Physics,* 98**,** 9371-9381.

CROOKER, N. & WEBB, D. 2006. Remote sensing of the solar site of interchange reconnection associated with the May 1997 magnetic cloud. *Journal of Geophysical Research: Space Physics,* 111.

DAVIES, J., HARRISON, R., ROUILLARD, A., SHEELEY, N., PERRY, C., BEWSHER, D., DAVIS, C., EYLES, C., CROTHERS, S. & BROWN, D. 2009. A synoptic view of solar transient evolution in the inner heliosphere using the Heliospheric Imagers on STEREO. *Geophysical Research Letters,* 36.

DEL ZANNA, G. & MASON, H. 2003. Solar active regions: SOHO/CDS and TRACE observations of quiescent coronal loops. *Astronomy & Astrophysics,* 406**,** 1089-1103.

DÉMOULIN, P. 2013. Evolution of interplanetary coronal mass ejections and magnetic clouds in the heliosphere. *Proceedings of the International Astronomical Union,* 8**,** 245-254.

DÉMOULIN, P. & DASSO, S. 2009. Causes and consequences of magnetic cloud expansion. *Astronomy & Astrophysics,* 498**,** 551-566.

DOMINGO, V., FLECK, B. & POLAND, A. I. 1995. The SOHO mission: an overview. *Solar Physics,* 162**,** 1-37.

DU, D., WANG, C. & HU, Q. 2007. Propagation and evolution of a magnetic cloud from ACE to Ulysses. *Journal of Geophysical Research: Space Physics,* 112.

DU, D., ZUO, P. & ZHANG, X. 2010. Interplanetary coronal mass ejections observed by Ulysses through its three solar orbits. *Solar Physics,* 262**,** 171-190.

EMSLIE, A., KUCHAREK, H., DENNIS, B., GOPALSWAMY, N., HOLMAN, G., SHARE, G., VOURLIDAS, A., FORBES, T., GALLAGHER, P. & MASON, G. 2004. Energy partition in two solar flare/CME events. *Journal of Geophysical Research: Space Physics,* 109.

FAINBERG, J., OSHEROVICH, V., STONE, R., MACDOWALL, R., BALOGH, A., WINTERHALTER, D., GOSLING, J. T., HABBAL, S. R., KURTH, W. S. & NEUGEBAUER, M. Ulysses observations of electron and proton components in a magnetic cloud and related wave activity. AIP Conference Proceedings, 1996. AIP, 554-557.

FARRUGIA, C. & BERDICHEVSKY, D. Evolutionary signatures in complex ejecta and their driven shocks. Annales Geophysicae, 2004. 3679-3698.

FARRUGIA, C., BERDICHEVSKY, D., MÖSTL, C., GALVIN, A., LEITNER, M., POPECKI, M., SIMUNAC, K., OPITZ, A., LAVRAUD, B. & OGILVIE, K. 2011. Multiple, distant (40) in situ observations of a

magnetic cloud and a corotating interaction region complex. *Journal of Atmospheric and Solar-Terrestrial Physics,* 73**,** 1254-1269.

FARRUGIA, C., BURLAGA, L., OSHEROVICH, V., RICHARDSON, I., FREEMAN, M., LEPPING, R. & LAZARUS, A. 1993. A study of an expanding interplanetary magnetic cloud and its interaction with the Earth's magnetosphere: The interplanetary aspect. *Journal of Geophysical Research: Space Physics,* 98**,** 7621-7632.

FARRUGIA, C., JORDANOVA, V., THOMSEN, M., LU, G., COWLEY, S. & OGILVIE, K. 2006a. A two-ejecta event associated with a two-step geomagnetic storm. *Journal of Geophysical Research: Space Physics,* 111.

FARRUGIA, C., KILPUA, E., JIAN, L., LIU, Y., EASTWOOD, J., HARRISON, R., WEBB, D., TEMMER, M., ODSTRCIL, D. & DAVIES, J. 2012. Multi-point shock and flux rope analysis of multiple interplanetary coronal mass ejections around 2010 August 1 in the inner heliosphere. *The Astrophysical Journal,* 758**,** 10.

FARRUGIA, C., MATSUI, H., KUCHAREK, H., JORDANOVA, V., TORBERT, R., OGILVIE, K., BERDICHEVSKY, D., SMITH, C. & SKOUG, R. 2006b. Survey of intense Sun–Earth connection events (1995–2003). *Advances in Space Research,* 38**,** 498-502.

FELDMAN, U. & LANDI, E. 2008. The temperature structure of solar coronal plasmas a. *Physics of Plasmas,* 15**,** 056501.

FELDMAN, W., ANDERSON, R., ASBRIDGE, J., BAME, S., GOSLING, J. & ZWICKL, R. 1982. Plasma electron signature of magnetic connection to the Earth's bow shock: ISEE 3. *Journal of Geophysical Research: Space Physics,* 87**,** 632-642.

FISK, L. 1996. Motion of the footpoints of heliospheric magnetic field lines at the Sun: Implications for recurrent energetic particle events at high heliographic latitudes. *Journal of Geophysical Research: Space Physics,* 101**,** 15547-15553.

FISK, L. 2005. The open magnetic flux of the Sun. I. Transport by reconnections with coronal loops. *The Astrophysical Journal,* 626**,** 563.

FISK, L., ZURBUCHEN, T. & SCHWADRON, N. 1999. On the coronal magnetic field: Consequences of large-scale motions. *The Astrophysical Journal,* 521**,** 868.

FITZENREITER, R. & OGILVIE, K. 1992. Heat flux dropouts in the solar wind and Coulomb scattering effects. *Journal of Geophysical Research: Space Physics,* 97**,** 19213-19219.

FORBES, T. 2000. A review on the genesis of coronal mass ejections. *Journal of Geophysical Research: Space Physics,* 105**,** 23153-23165.

FORBUSH, S. E. 1937. On the effects in cosmic-ray intensity observed during the recent magnetic storm. *Physical Review,* 51**,** 1108.

FORBUSH, S. E. 1946. Three unusual cosmic-ray increases possibly due to charged particles from the Sun. *Physical Review,* 70**,** 771.

FORSYTH, R., BALOGH, A., SMITH, E. & GOSLING, J. 1997. Ulysses observations of the northward extension of the heliospheric current sheet. *Geophysical research letters,* 24**,** 3101-3104.

FORSYTH, R., BOTHMER, V., CID, C., CROOKER, N., HORBURY, T., KECSKEMETY, K., KLECKER, B., LINKER, J., ODSTRCIL, D. & REINER, M. 2006. ICMEs in the inner heliosphere: Origin, evolution and propagation effects. *Coronal Mass Ejections.* Springer.

GABRIEL, A. 1971. Measurements on the Lyman alpha corona. *Solar Physics,* 21**,** 392-400.

GABRIEL, A. H. & MASON, H. E. Solar physics. Applied Atomic Collision Physics, Volume 1: Atmospheric Physics and Chemistry, 1982. 345-397.

GALVIN, A., KISTLER, L., POPECKI, M., FARRUGIA, C., SIMUNAC, K., ELLIS, L., MÖBIUS, E., LEE, M., BOEHM, M. & CARROLL, J. 2008. The Plasma and Suprathermal Ion Composition (PLASTIC) investigation on the STEREO observatories. *The STEREO Mission.* Springer.

GARY, G. A. 2001. Plasma beta above a solar active region: rethinking the paradigm. *Solar Physics,* 203**,** 71-86.

GASLING, J., ASBRIDGE, J., BAME, S., FELDMAN, W. & ZWICKL, R. 1980. Observations of large fluxes of He+ in the solar wind following an interplanetary shock. *J. Geophys. Res,* 85**,** 3431.

GLOECKLER, G., FISK, L. A., HEFTI, S., SCHWADRON, N. A., ZURBUCHEN, T. H., IPAVICH, F. M., GEISS, J., BOCHSLER, P. & WIMMER-SCHWEINGRUBER, R. F. 1999. Unusual composition of the solar wind in the 2–3 May 1998 CME observed with SWICS on ACE. *Geophysical Research Letters,* 26**,** 157-160.

GOLDSTEIN, H. 1983. On the field configuration in magnetic clouds.

GÓMEZ-HERRERO, R., MALANDRAKI, O., DRESING, N., KILPUA, E., HEBER, B., KLASSEN, A., MÜLLER-MELLIN, R. & WIMMER-SCHWEINGRUBER, R. 2011. Spatial and temporal variations of CIRs: Multi-point observations by STEREO. *Journal of Atmospheric and Solar-Terrestrial Physics,* 73**,** 551-565.

GONZALEZ, W., TSURUTANI, B., LEPPING, R. & SCHWENN, R. 2002. Interplanetary phenomena associated with very intense geomagnetic storms. *Journal of Atmospheric and Solar-Terrestrial Physics,* 64**,** 173-181.

GONZALEZ, W. D., TSURUTANI, B. T. & DE GONZALEZ, A. L. C. 1999. Interplanetary origin of geomagnetic storms. *Space Science Reviews,* 88**,** 529-562.

GOPALSWAMY, N. 2006. Properties of interplanetary coronal mass ejections. *Space Science Reviews,* 124**,** 145-168.

GOPALSWAMY, N. Coronal mass ejections and space weather. Climate and Weather of the Sun-Earth System (CAWSES): selected papers from the 2007 Kyoto symposium, 2009a. Terrapub, 77-120.

GOPALSWAMY, N. 2009b. Halo coronal mass ejections and geomagnetic storms. *Earth, planets and space,* 61**,** 595-597.

GOPALSWAMY, N., AKIYAMA, S., YASHIRO, S., MICHALEK, G. & LEPPING, R. 2008. Solar sources and geospace consequences of interplanetary magnetic clouds observed during solar cycle 23. *Journal of Atmospheric and Solar-Terrestrial Physics,* 70**,** 245-253.

GOPALSWAMY, N. & KUNDU, M. 1992. Estimation of the mass of a coronal mass ejection from radio observations. *The Astrophysical Journal,* 390**,** L37-L39.

GOPALSWAMY, N., KUNDU, M., MANOHARAN, P., RAOULT, A., NITTA, N. & ZARKA, P. 1997. X-ray and radio studies of a coronal eruption: shock wave, plasmoid, and coronal mass ejection. *The Astrophysical Journal,* 486**,** 1036.

GOPALSWAMY, N., LARA, A., YASHIRO, S., NUNES, S. & HOWARD, R. A. Coronal mass ejection activity during solar cycle 23. Solar Variability as an Input to the Earth's Environment, 2003a. 403-414.

GOPALSWAMY, N., MÄKELÄ, P., XIE, H., AKIYAMA, S. & YASHIRO, S. 2009. CME interactions with coronal holes and their interplanetary consequences. *Journal of Geophysical Research: Space Physics,* 114.

GOPALSWAMY, N., SHIMOJO, M., LU, W., YASHIRO, S., SHIBASAKI, K. & HOWARD, R. 2003b. Prominence eruptions and coronal mass ejection: a statistical study using microwave observations. *The Astrophysical Journal,* 586**,** 562.

GOPALSWAMY, N., YASHIRO, S. & AKIYAMA, S. 2007. Geoeffectiveness of halo coronal mass ejections. *Journal of Geophysical Research: Space Physics,* 112.

GOSLING, J. 1975. Large-scale inhomogeneities in the solar wind of solar origin. *Reviews of Geophysics,* 13**,** 1053-1058.

GOSLING, J., ASBRIDGE, J., BAME, S. & FELDMAN, W. 1978. Solar wind stream interfaces. *Journal of Geophysical Research: Space Physics,* 83**,** 1401-1412.

GOSLING, J., BAME, S., MCCOMAS, D., PHILLIPS, J., PIZZO, V., GOLDSTEIN, B. & NEUGEBAUER, M. 1993. Latitudinal variation of solar wind corotating stream interaction regions: Ulysses. *Geophysical research letters,* 20**,** 2789-2792.

GOSLING, J., BIRN, J. & HESSE, M. 1995. Three-dimensional magnetic reconnection and the magnetic topology of coronal mass ejection events. *Geophysical research letters,* 22**,** 869-872.

GOSLING, J., ERIKSSON, S., MCCOMAS, D., PHAN, T. & SKOUG, R. 2007. Multiple magnetic reconnection sites associated with a coronal mass ejection in the solar wind. *Journal of Geophysical Research: Space Physics,* 112.

GOSLING, J., ERIKSSON, S. & SCHWENN, R. 2006. Petschek-type magnetic reconnection exhausts in the solar wind well inside 1 AU: Helios. *Journal of Geophysical Research: Space Physics,* 111.

GOSLING, J., HUNDHAUSEN, A. & BAME, S. 1976. SOLAR-WIND STREAM EVOLUTION AT LARGE HELIOCENTRIC DISTANCES-EXPERIMENTAL DEMONSTRATION AND TEST OF A MODEL. *JOURNAL OF GEOPHYSICAL RESEARCH-SPACE PHYSICS,* 81**,** 2111-2122.

GOSLING, J. & MCCOMAS, D. 1987. Field line draping about fast coronal mass ejecta: A source of strong out-of-the-ecliptic interplanetary magnetic fields. *Geophysical Research Letters,* 14**,** 355-358.

GOSLING, J., MCCOMAS, D., PHILLIPS, J., WEISS, L., PIZZO, V., GOLDSTEIN, B. & FORSYTH, R. 1994. A new class of forward-reverse shock pairs in the solar wind. *Geophysical research letters,* 21**,** 2271-2274.

GOSLING, J., MCCOMAS, D., SKOUG, R. & FORSYTH, R. 2001a. Stream interaction regions at high heliographic latitudes during Ulysses' second polar orbit. *The 3-D Heliosphere at Solar Maximum.* Springer.

GOSLING, J. & PIZZO, V. 1999. Formation and evolution of corotating interaction regions and their three dimensional structure. *Corotating Interaction Regions.* Springer.

GOSLING, J., SKOUG, R. & FELDMAN, W. 2001b. Solar wind electron halo depletions at 90 pitch angle. *Geophysical research letters,* 28**,** 4155-4158.

GOSLING, J., SKOUG, R., FELDMAN, W. & MCCOMAS, D. 2002. Symmetric suprathermal electron depletions on closed field lines in the solar wind. *Geophysical research letters,* 29.

GOSLING, J., SKOUG, R., MCCOMAS, D. & SMITH, C. 2005. Direct evidence for magnetic reconnection in the solar wind near 1 AU. *Journal of Geophysical Research: Space Physics,* 110.

GOSLING, J. T. 1990. Coronal mass ejections and magnetic flux ropes in interplanetary space. *Physics of Magnetic Flux Ropes***,** 343-364.

GOSLING, J. T., BAKER, D. N., BAME, S. J., FELDMAN, W. C., ZWICKL, R. D. & SMITH, E. J. 1987. Bidirectional solar wind electron heat flux events. *Journal of Geophysical Research: Space Physics,* 92**,** 8519-8535.

GOSLING, J. T., BORRINI, G., ASBRIDGE, J. R., BAME, S. J., FELDMAN, W. C. & HANSEN, R. T. 1981. Coronal streamers in the solar wind at 1 AU. *Journal of Geophysical Research: Space Physics,* 86**,** 5438-5448.

GOSLING, J. T., PIZZO, V. & BAME, S. J. 1973. Anomalously low proton temperatures in the solar wind following interplanetary shock waves—evidence for magnetic bottles? *Journal of Geophysical Research,* 78**,** 2001-2009.

GUARNIERI, F. L., TSURUTANI, B. T., GONZALEZ, W. D., ECHER, E., GONZALEZ, A. L., GRANDE, M. & SORAAS, F. ICME and CIR storms with particular emphasis on HILDCAA events. ILWS Workshop, 2006. 19-20.

GUERRERO, A., CID, C., CERRATO, Y., SAIZ, E., PALACIOS, J. & SEATON, D. Geoeffectiveness of two CMEs interacting with the same CH. *Geophysical Research Abstracts, Vol. 14, EGU2012-9720, 2012, EGU General Assembly 2012*.

GUI, B., SHEN, C., WANG, Y., YE, P., LIU, J., WANG, S. & ZHAO, X. 2011. Quantitative analysis of CME deflections in the corona. *Solar Physics,* 271**,** 111-139.

HABBAL, S. R., MORGAN, H., DRUCKMÜLLER, M., DING, A., COOPER, J., DAW, A. & SITTLER, E. 2013. Probing the Fundamental Physics of the Solar Corona with Lunar Solar Occultation Observations. *Solar Physics***,** 1-16.

HAGGERTY, D., ROELOF, E., SMITH, C., NESS, N., TOKAR, R. & SKOUG, R. 2000. Interplanetary magnetic field connection to the L1 Lagrangian orbit during upstream energetic ion events. *Journal of Geophysical Research: Space Physics,* 105**,** 25123-25131.

HARRA, L. K., CROOKER, N. U., MANDRINI, C. H., VAN DRIEL-GESZTELYI, L., DASSO, S., WANG, J., ELLIOTT, H., ATTRILL, G., JACKSON, B. V. & BISI, M. M. 2007. How does large flaring activity from the same active region produce oppositely directed magnetic clouds? *Solar Physics,* 244**,** 95-114.

HARRISON, R., DAVIES, J., MÖSTL, C., LIU, Y., TEMMER, M., BISI, M., EASTWOOD, J., DE KONING, C., NITTA, N. & ROLLETT, T. 2012. An analysis of the origin and propagation of the multiple coronal mass ejections of 2010 August 1. *The Astrophysical Journal,* 750**,** 45.

HARTEN, R. & CLARK, K. 1995. The design features of the GGS Wind and Polar spacecraft. *Space Science Reviews,* 71**,** 23-40.

HENKE, T., WOCH, J., SCHWENN, R., MALL, U., GLOECKLER, G., STEIGER, R. V., FORSYTH, R. & BALOGH, A. 2001. Ionization state and magnetic topology of coronal mass ejections. *Journal of Geophysical Research: Space Physics,* 106**,** 10597-10613.

HIDALGO, M., NIEVES-CHINCHILLA, T. & CID, C. 2002. Elliptical cross-section model for the magnetic topology of magnetic clouds. *Geophysical research letters,* 29.

HIRSHBERG, J., BAME, S. & ROBBINS, D. 1972. Solar flares and solar wind helium enrichments: July 1965–July 1967. *Solar Physics,* 23**,** 467-486.

HIRSHBERG, J. & COLBURN, D. 1969. Interplanetary field and geomagnetic variations—a unifield view. *Planetary and Space Science,* 17**,** 1183-1206.

HO, G. C., HAMILTON, D. C., GLOECKLER, G. & BOCHSLER, P. 2000. Enhanced solar wind ^{3}He2+ associated with coronal mass ejections. *Geophysical research letters,* 27**,** 309-312.

HOWARD, R., MOSES, J., SOCKER, D., DERE, K., COOK, J. & CONSORTIUM, S. 2002. Sun earth connection coronal and heliospheric investigation (SECCHI). *Advances in Space Research,* 29**,** 2017-2026.

HOWARD, R., MOSES, J., VOURLIDAS, A., NEWMARK, J., SOCKER, D., PLUNKETT, S., KORENDYKE, C., COOK, J., HURLEY, A. & DAVILA, J. 2008. Sun Earth connection coronal and heliospheric investigation (SECCHI). *Space Science Reviews,* 136**,** 67.

HOWARD, R., SHEELEY, N., KOOMEN, M. & MICHELS, D. 1985. Coronal mass ejections: 1979–1981. *Journal of Geophysical Research: Space Physics,* 90**,** 8173-8191.

HOWARD, T. 2011. *Coronal mass ejections: An introduction*, Springer Science & Business Media.

HU, Y. & JIA, X. 2001. Interplanetary shock interaction with the heliospheric current sheet and its associated structures. *Journal of Geophysical Research: Space Physics,* 106**,** 29299-29304.

HUDSON, H., ACTON, L. & FREELAND, S. 1996. A long-duration solar flare with mass ejection and global consequences. *The Astrophysical Journal,* 470**,** 629.

HUNDHAUSEN, A. 1972. Composition and dynamics of the solar wind plasma. *Solar-Terrestrial Physics/1970.* Springer.

HUNDHAUSEN, A. An interplanetary view of coronal holes. Coronal holes and high speed wind streams, 1977. 225-329.

HUNDHAUSEN, A. 1993. Sizes and locations of coronal mass ejections: SMM observations from 1980 and 1984-1989. *Journal of Geophysical Research: Space Physics,* 98**,** 13177-13200.

HUNDHAUSEN, A. 1995. The solar wind. *Introduction to space physics***,** 91-128.

HUNDHAUSEN, A. & GOSLING, J. 1976. Solar wind structure at large heliocentric distances: An interpretation of Pioneer 10 observations. *Journal of Geophysical Research,* 81**,** 1436-1440.

ILLING, R. & HUNDHAUSEN, A. 1985. Observation of a coronal transient from 1.2 to 6 solar radii. *Journal of Geophysical Research: Space Physics,* 90**,** 275-282.

INTRILIGATOR, D. S. & SISCOE, G. L. 1994. Stream interfaces and energetic ions closer than expected: Analyses of Pioneers 10 and 11 observations. *Geophysical research letters,* 21**,** 1117-1120.

IPAVICH, F., GALVIN, A., GLOECKLER, G., HOVESTADT, D., BAME, S., KLECKER, B., SCHOLER, M., FISK, L. & FAN, C. 1986. Solar wind Fe and CNO measurements in high-speed flows. *Journal of Geophysical Research: Space Physics,* 91**,** 4133-4141.

IPAVICH, F. M., GALVIN, A. B., LASLEY, S. E., PAQUETTE, J. A., HEFTI, S., REICHE, K. U., COPLAN, M. A., GLOECKLER, G., BOCHSLER, P., HOVESTADT, D., GRÜNWALDT, H., HILCHENBACH, M., GLIEM, F., AXFORD, W. I., BALSIGER, H., BÜRGI, A., GEISS, J., HSIEH, K. C., KALLENBACH, R., KLECKER, B., LEE, M. A., MANAGADZE, G. G., MARSCH, E., MÖBIUS, E., NEUGEBAUER, M., SCHOLER, M., VERIGIN, M. I., WILKEN, B. & WURZ, P. 1998. Solar wind measurements with SOHO: The CELIAS/MTOF proton monitor. *Journal of Geophysical Research: Space Physics,* 103**,** 17205-17213.

ISAVNIN, A., VOURLIDAS, A. & KILPUA, E. 2013. Three-dimensional evolution of erupted flux ropes from the Sun (2–20 r⊙) to 1 AU. *Solar Physics,* 284**,** 203-215.

JANOO, L., FARRUGIA, C., TORBERT, R., QUINN, J., SZABO, A., LEPPING, R., OGILVIE, K., LIN, R., LARSON, D. & SCUDDER, J. 1998. Field and flow perturbations in the October 18–19, 1995, magnetic cloud. *Journal of Geophysical Research: Space Physics,* 103**,** 17249-17259.

JIAN, L., RUSSELL, C., GOSLING, J. & LUHMANN, J. Identifying and Characterizing ICMEs Using Total Perpendicular Pressure. AGU Spring Meeting Abstracts, 2005a.

JIAN, L., RUSSELL, C., GOSLING, J. & LUHMANN, J. Total pressure signature as a qualitative indicator of the impact parameter during ICME encounters. Solar Wind 11/SOHO 16, Connecting Sun and Heliosphere, 2005b. 731.

JIAN, L., RUSSELL, C., LUHMANN, J., GALVIN, A. & MACNEICE, P. 2009. Multi-spacecraft observations: Stream interactions and associated structures. *Solar Physics,* 259**,** 345-360.

JIAN, L., RUSSELL, C., LUHMANN, J., GALVIN, A., SIMUNAC, K., ZANK, G. P., BOROVSKY, J., BRUNO, R., CIRTAIN, J. & CRANMER, S. Solar wind observations at STEREO: 2007-2011. AIP Conference Proceedings, 2013. AIP, 191-194.

JIAN, L., RUSSELL, C., LUHMANN, J. & SKOUG, R. 2006a. Properties of interplanetary coronal mass ejections at one AU during 1995–2004. *Solar Physics,* 239**,** 393-436.

JIAN, L., RUSSELL, C., LUHMANN, J. & SKOUG, R. 2006b. Properties of stream interactions at one AU during 1995–2004. *Solar Physics,* 239**,** 337-392.

JIAN, L., RUSSELL, C., LUHMANN, J. & SKOUG, R. 2008a. Evolution of solar wind structures from 0.72 to 1AU. *Advances in Space Research,* 41**,** 259-266.

JIAN, L., RUSSELL, C., LUHMANN, J., SKOUG, R. & STEINBERG, J. 2008b. Stream interactions and interplanetary coronal mass ejections at 0.72 AU. *Solar Physics,* 249**,** 85-101.

JIAN, L., RUSSELL, C., LUHMANN, J., SKOUG, R. & STEINBERG, J. 2008c. Stream interactions and interplanetary coronal mass ejections at 5.3 AU near the solar ecliptic plane. *Solar Physics,* 250**,** 375-402.

JIANG, C., FENG, X., WU, S. & HU, Q. 2013. Magnetohydrodynamic simulation of a sigmoid eruption of active region 11283. *The Astrophysical Journal Letters,* 771**,** L30.

JOKIPII, J. & KOTA, J. 1989. The polar heliospheric magnetic field. *Geophysical Research Letters,* 16**,** 1-4.

JOKIPII, J. & THOMAS, B. 1981. Effects of drift on the transport of cosmic rays. IV-Modulation by a wavy interplanetary current sheet. *The Astrophysical Journal,* 243**,** 1115-1122.

KAHLER, S., CROCKER, N. & GOSLING, J. 1996. The topology of intrasector reversals of the interplanetary magnetic field. *Journal of Geophysical Research: Space Physics,* 101**,** 24373-24382.

KAHLER, S., CROOKER, N. & GOSLING, J. 1998. Properties of interplanetary magnetic sector boundaries based on electron heat-flux flow directions. *Journal of Geophysical Research: Space Physics,* 103**,** 20603-20612.

KAHLER, S., CROOKER, N. & GOSLING, J. 1999. The polarities and locations of interplanetary coronal mass ejections in large interplanetary magnetic sectors. *Journal of Geophysical Research: Space Physics,* 104**,** 9919-9924.

KAHLER, S., CROOKER, N. & LARSON, D. 2003. Probing the magnetic polarity structure of the heliospheric current sheet. *Journal of Geophysical Research: Space Physics,* 108.

KAHLER, S., HILDNER, E. & VAN HOLLEBEKE, M. 1978. Prompt solar proton events and coronal mass ejections. *Solar Physics,* 57**,** 429-443.

KAHLER, S. & LIN, R. 1994. The determination of interplanetary magnetic field polarities around sector boundaries using E> 2 keV electrons. *Geophysical research letters,* 21**,** 1575-1578.

KAHLER, S. & LIN, R. 1995. An examination of directional discontinuities and magnetic polarity changes around interplanetary sector boundaries usingE> 2 keV electrons. *Solar Physics,* 161**,** 183-195.

KAISER, M. 2005. The STEREO mission: an overview. *advances in Space Research,* 36**,** 1483-1488.

KAISER, M. L. & ADAMS, W. J. Stereo mission overview. Aerospace Conference, 2007 IEEE, 2007. IEEE, 1-8.

KAISER, M. L., KUCERA, T. A., DAVILA, J. M., ST. CYR, O. C., GUHATHAKURTA, M. & CHRISTIAN, E. 2008. The STEREO Mission: An Introduction. *Space Science Reviews,* 136**,** 5-16.

KAJDIßC, P., BLANCO-CANO, X., OPITZ, A., SAUVAUD, J., AGUILAR-RODRIGUEZ, E., RUSSELL, C., LUHMANN, J., JIAN, L., ROUILLARD, A. & LAVRAUD, B. Electron distributions upstream and downstream of ICME driven IP shocks. AIP Conf. Proc, 2013. 203-206.

KASPER, J. C. 2002. *Solar wind plasma: kinetic properties and micro-instabilities.* Massachusetts Institute of Technology.

KATAOKA, R. & MIYOSHI, Y. 2006. Flux enhancement of radiation belt electrons during geomagnetic storms driven by coronal mass ejections and corotating interaction regions. *Space Weather,* 4.

KHABAROVA, O. & ZASTENKER, G. 2011. Sharp changes of solar wind ion flux and density within and outside current sheets. *Solar Physics,* 270**,** 311-329.

KILPUA, E., ISAVNIN, A., VOURLIDAS, A., KOSKINEN, H. & RODRIGUEZ, L. On the relationship between interplanetary coronal mass ejections and magnetic clouds. Annales Geophysicae, 2013. COPERNICUS GESELLSCHAFT MBH.

KILPUA, E., JIAN, L., LI, Y., LUHMANN, J. & RUSSELL, C. 2011. Multipoint ICME encounters: Pre-STEREO and STEREO observations. *Journal of Atmospheric and Solar-Terrestrial Physics,* 73**,** 1228-1241.

KILPUA, E., JIAN, L., LI, Y., LUHMANN, J. & RUSSELL, C. 2012. Observations of ICMEs and ICME-like solar wind structures from 2007–2010 using near-Earth and STEREO observations. *Solar Physics,* 281**,** 391-409.

KILPUA, E., LIEWER, P., FARRUGIA, C., LUHMANN, J., MÖSTL, C., LI, Y., LIU, Y., LYNCH, B., RUSSELL, C. & VOURLIDAS, A. 2009. Multispacecraft observations of magnetic clouds and their solar origins between 19 and 23 May 2007. *Solar Physics,* 254**,** 325-344.

KIM, R.-S., CHO, K.-S., KIM, K.-H., PARK, Y.-D., MOON, Y.-J., YI, Y., LEE, J., WANG, H., SONG, H. & DRYER, M. 2008. CME earthward direction as an important geoeffectiveness indicator. *The Astrophysical Journal,* 677**,** 1378.

KIM, R.-S., GOPALSWAMY, N., CHO, K.-S., MOON, Y.-J. & YASHIRO, S. 2013. Propagation characteristics of CMEs associated with magnetic clouds and ejecta. *Solar Physics,* 284**,** 77-88.

KLEIN, L. W. & BURLAGA, L. F. 1982. Interplanetary magnetic clouds At 1 AU. *Journal of Geophysical Research: Space Physics,* 87**,** 613-624.

KOSKINEN, H. 2011. *Physics of Space Storms: From the Solar Surface to the Earth*, Springer Science & Business Media.

KRIEGER, A., TIMOTHY, A. & ROELOF, E. 1973. A coronal hole and its identification as the source of a high velocity solar wind stream. *Solar Physics,* 29**,** 505-525.

KRUGER, A. & SCHMAHL, E. 1981. Introduction to Solar Radio Astronomy and Radio Physics. *Sky and Telescope,* 61**,** 147.

LABROSSE, N., HEINZEL, P., VIAL, J.-C., KUCERA, T., PARENTI, S., GUNÁR, S., SCHMIEDER, B. & KILPER, G. 2010. Physics of solar prominences: I—Spectral diagnostics and non-LTE modelling. *Space Science Reviews,* 151**,** 243-332.

LANG, K. R. 2013. The Extended Solar Atmosphere. *Essential Astrophysics.* Springer.

LARSON, D., LIN, R., MCTIERNAN, J., MCFADDEN, J., ERGUN, R., MCCARTHY, M., REME, H., SANDERSON, T., KAISER, M. & LEPPING, R. 1997. Tracing the topology of the October 18–20, 1995, magnetic cloud with$\sim$ 0.1–10^2 keV electrons. *Geophysical research letters,* 24**,** 1911-1914.

LAZARUS, A., KASPER, J., SZABO, A. & OGILVIE, K. Solar wind streams and their interactions. AIP Conference Proceedings, 2003. IOP INSTITUTE OF PHYSICS PUBLISHING LTD, 187-189.

LEMEN, J. R., AKIN, D. J., BOERNER, P. F., CHOU, C., DRAKE, J. F., DUNCAN, D. W., EDWARDS, C. G., FRIEDLAENDER, F. M., HEYMAN, G. F. & HURLBURT, N. E. 2011. The atmospheric imaging

assembly (AIA) on the solar dynamics observatory (SDO). *The Solar Dynamics Observatory.* Springer.

LEMEN, J. R., TITLE, A. M., AKIN, D. J., BOERNER, P. F., CHOU, C., DRAKE, J. F., DUNCAN, D. W., EDWARDS, C. G., FRIEDLAENDER, F. M. & HEYMAN, G. F. 2012. The atmospheric imaging assembly (AIA) on the solar dynamics observatory (SDO). *Solar Physics,* 275**,** 17-40.

LEONARD, A. & MORGAN, H. 2014. Temperature diagnostics of the solar atmosphere using SunPy. *arXiv preprint arXiv:1412.6483*.

LEPPING, R. 2004. MAGNETIC CLOUD FIT PARAMETERS AS DETERMINED BY MFI DATA.

LEPPING, R., ACŨNA, M., BURLAGA, L., FARRELL, W., SLAVIN, J., SCHATTEN, K., MARIANI, F., NESS, N., NEUBAUER, F. & WHANG, Y. 1995. The WIND magnetic field investigation. *Space Science Reviews,* 71**,** 207-229.

LEPPING, R., BERDICHEVSKY, D., WU, C.-C., SZABO, A., NAROCK, T., MARIANI, F., LAZARUS, A. & QUIVERS, A. A summary of WIND magnetic clouds for years 1995-2003: model-fitted parameters, associated errors and classifications. Annales Geophysicae, 2006. 215-245.

LEPPING, R., BURLAGA, L., SZABO, A., OGILVIE, K., MISH, W., VASSILIADIS, D., LAZARUS, A., STEINBERG, J., FARRUGIA, C. & JANOO, L. 1997. The Wind magnetic cloud and events of October 18–20, 1995: Interplanetary properties and as triggers for geomagnetic activity. *Journal of Geophysical Research: Space Physics,* 102**,** 14049-14063.

LEPPING, R., WU, C.-C., BERDICHEVSKY, D. & SZABO, A. 2015. Wind magnetic clouds for 2010–2012: Model parameter fittings, associated shock waves, and comparisons to earlier periods. *Solar Physics,* 290**,** 2265-2290.

LEPPING, R. P., JONES, J. A. & BURLAGA, L. F. 1990. Magnetic field structure of interplanetary magnetic clouds at 1 AU. *Journal of Geophysical Research: Space Physics,* 95**,** 11957-11965.

LEPRI, S. & ZURBUCHEN, T. 2004. Iron charge state distributions as an indicator of hot ICMEs: Possible sources and temporal and spatial variations during solar maximum. *Journal of Geophysical Research: Space Physics,* 109.

LEPRI, S., ZURBUCHEN, T., FISK, L., RICHARDSON, I., CANE, H. A. & GLOECKLER, G. 2001. Iron charge distribution as an identifier of interplanetary coronal mass ejections. *Journal of Geophysical Research: Space Physics,* 106**,** 29231-29238.

LESKE, R., MEWALDT, R., MASON, G., COHEN, C., CUMMINGS, A., LABRADOR, A., STONE, E., WIEDENBECK, M., VON ROSENVINGE, T. & MAKSIMOVIC, M. STEREO and ACE observations of energetic particles from corotating interaction regions. AIP Conference Proceedings, 2010. AIP, 379-382.

LI, Y., LUHMANN, J., LYNCH, B. & KILPUA, E. 2011. Cyclic reversal of magnetic cloud poloidal field. *Solar Physics,* 270**,** 331-346.

LIN, J., RAYMOND, J. & VAN BALLEGOOIJEN, A. 2004. The role of magnetic reconnection in the observable features of solar eruptions. *The Astrophysical Journal,* 602**,** 422.

LIN, N., KELLOGG, P., GOETZ, K., MONSON, S., MACDOWALL, R., HABBAL, S. R. & HALAS, C. D. Plasma waves in coronal mass ejections: Ulysses observations. AIP Conference Proceedings, 1999. AIP, 673-676.

LIN, R. & KAHLER, S. 1992. Interplanetary magnetic field connection to the Sun during electron heat flux dropouts in the solar wind. *Journal of Geophysical Research: Space Physics,* 97**,** 8203-8209.

LIU, Y., RICHARDSON, J., BELCHER, J., KASPER, J. & SKOUG, R. 2006. Plasma depletion and mirror waves ahead of interplanetary coronal mass ejections. *Journal of Geophysical Research: Space Physics,* 111.

LIU, Y. D., HU, H., WANG, R., YANG, Z., ZHU, B., LIU, Y. A., LUHMANN, J. G. & RICHARDSON, J. D. 2015. Plasma and magnetic field characteristics of solar coronal mass ejections in relation to geomagnetic storm intensity and variability. *The Astrophysical Journal Letters,* 809**,** L34.

LIU, Y. D., LUHMANN, J. G., MÖSTL, C., MARTINEZ-OLIVEROS, J. C., BALE, S. D., LIN, R. P., HARRISON, R. A., TEMMER, M., WEBB, D. F. & ODSTRCIL, D. 2012. Interactions between coronal mass

ejections viewed in coordinated imaging and in situ observations. *The Astrophysical Journal Letters,* 746**,** L15.

LIU, Y. M., HUANG, J., WANG, C., KLECKER, B., GALVIN, A., SIMUNAC, K., POPECKI, M., KISTLER, L., FARRUGIA, C. & LEE, M. 2014. A statistical analysis of heliospheric plasma sheets, heliospheric current sheets, and sector boundaries observed in situ by STEREO. *Journal of Geophysical Research: Space Physics,* 119**,** 8721-8732.

LOEWE, C. & PRÖLSS, G. 1997. Classification and mean behavior of magnetic storms. *Journal of Geophysical Research: Space Physics,* 102**,** 14209-14213.

LOPEZ, R. 1987. Solar cycle invariance in solar wind proton temperature relationships. *Journal of Geophysical Research: Space Physics,* 92**,** 11189-11194.

LUGAZ, N. & FARRUGIA, C. 2014. A new class of complex ejecta resulting from the interaction of two CMEs and its expected geoeffectiveness. *Geophysical Research Letters,* 41**,** 769-776.

LUGAZ, N., FARRUGIA, C., DAVIES, J., MÖSTL, C., DAVIS, C., ROUSSEV, I. & TEMMER, M. 2012. The deflection of the two interacting coronal mass ejections of 2010 May 23-24 as revealed by combined in situ measurements and heliospheric imaging. *The Astrophysical Journal,* 759**,** 68.

LUGAZ, N., FARRUGIA, C., SMITH, C. & PAULSON, K. 2015. Shocks inside CMEs: A survey of properties from 1997 to 2006. *Journal of Geophysical Research: Space Physics,* 120**,** 2409-2427.

LUGAZ, N., HERNANDEZ-CHARPAK, J., ROUSSEV, I., DAVIS, C., VOURLIDAS, A. & DAVIES, J. 2010. Determining the azimuthal properties of coronal mass ejections from multi-spacecraft remote-sensing observations with STEREO SECCHI. *The Astrophysical Journal,* 715**,** 493.

LUGAZ, N., MANCHESTER IV, W. & GOMBOSI, T. 2005. Numerical simulation of the interaction of two coronal mass ejections from Sun to Earth. *The Astrophysical Journal,* 634**,** 651.

LUGAZ, N., TEMMER, M., WANG, Y. & FARRUGIA, C. J. 2016. The Interaction of Successive Coronal Mass Ejections: A Review. *arXiv preprint arXiv:1612.02398*.

LUHMANN, J., CURTIS, D., SCHROEDER, P., MCCAULEY, J., LIN, R., LARSON, D., BALE, S., SAUVAUD, J.-A., AOUSTIN, C. & MEWALDT, R. 2008. STEREO IMPACT investigation goals, measurements, and data products overview. *Space Science Reviews,* 136**,** 117-184.

LUNDQUIST, S. 1950. Magneto-hydrostatic fields. *Arkiv for fysik,* 2**,** 361-365.

LUNDQUIST, S. 1951. On the stability of magneto-hydrostatic fields. *Physical Review,* 83**,** 307.

LYNCH, B., ANTIOCHOS, S., LI, Y., LUHMANN, J. & DEVORE, C. 2009. Rotation of coronal mass ejections during eruption. *The Astrophysical Journal,* 697**,** 1918.

MAIA, D., VOURLIDAS, A., PICK, M., HOWARD, R., SCHWENN, R. & MAGALHAES, A. 1999. Radio signatures of a fast coronal mass ejection development on November 6, 1997. *Journal of Geophysical Research: Space Physics,* 104**,** 12507-12513.

MÄKELÄ, P., GOPALSWAMY, N., XIE, H., MOHAMED, A. A., AKIYAMA, S. & YASHIRO, S. 2013. Coronal hole influence on the observed structure of interplanetary CMEs. *Solar Physics,* 284**,** 59-75.

MARIČIĆ, D., VRŠNAK, B., DUMBOVIĆ, M., ŽIC, T., ROŠA, D., HRŽINA, D., LULIĆ, S., ROMŠTAJN, I., BUŠIĆ, I. & SALAMON, K. 2014. Kinematics of interacting ICMEs and related Forbush decrease: case study. *Solar physics,* 289**,** 351-368.

MARSDEN, R., SANDERSON, T., TRANQUILLE, C., WENZEL, K. P. & SMITH, E. 1987. ISEE 3 observations of low-energy proton bidirectional events and their relation to isolated interplanetary magnetic structures. *Journal of Geophysical Research: Space Physics,* 92**,** 11009-11019.

MARTENS, P. & KUIN, N. 1989. A circuit model for filament eruptions and two-ribbon flares. *Solar physics,* 122**,** 263-302.

MARUBASHI, K. 1986. Structure of the interplanetary magnetic clouds and their solar origins. *Advances in Space Research,* 6**,** 335-338.

MARUBASHI, K. 2000. Physics of interplanetary magnetic flux ropes: Toward prediction of geomagnetic storms. *Advances in Space Research,* 26**,** 55-66.

MARUBASHI, K. & LEPPING, R. Long-duration magnetic clouds: a comparison of analyses using torus- and cylinder-shaped flux rope models. Annales Geophysicae, 2007. 2453-2477.

MASON, G., DESAI, M., MALL, U., KORTH, A., BUCIK, R., VON ROSENVINGE, T. & SIMUNAC, K. 2009. In situ observations of CIRs on STEREO, Wind, and ACE during 2007–2008. *Solar Physics,* 256**,** 393-408.

MCCOMAS, D., BAME, S., BARKER, P., FELDMAN, W., PHILLIPS, J., RILEY, P. & GRIFFEE, J. 1998. Solar wind electron proton alpha monitor (SWEPAM) for the Advanced Composition Explorer. *The Advanced Composition Explorer Mission.* Springer.

MCCOMAS, D., EBERT, R., ELLIOTT, H., GOLDSTEIN, B., GOSLING, J., SCHWADRON, N. & SKOUG, R. 2008. Weaker solar wind from the polar coronal holes and the whole Sun. *Geophysical Research Letters,* 35.

MCCOMAS, D. J. 1995. Tongues, bottles, and disconnected loops: The opening and closing of the interplanetary magnetic field. *Reviews of Geophysics,* 33**,** 603-608.

MCCOMAS, D. J., GOSLING, J. T., PHILLIPS, J. L., BAME, S. J., LUHMANN, J. G. & SMITH, E. J. 1989. Electron heat flux dropouts in the solar wind: Evidence for interplanetary magnetic field reconnection? *Journal of Geophysical Research: Space Physics,* 94**,** 6907-6916.

MEUNIER, N. 2003. Statistical properties of magnetic structures: Their dependence on scale and solar activity. *Astronomy & Astrophysics,* 405**,** 1107-1120.

MISHRA, W., SRIVASTAVA, N. & CHAKRABARTY, D. 2015. Evolution and consequences of interacting CMEs of 9–10 November 2012 using STEREO/SECCHI and in situ observations. *Solar Physics,* 290**,** 527-552.

MITSAKOU, E. & MOUSSAS, X. 2014. Statistical study of ICMES and their sheaths during solar cycle 23 (1996–2008). *Solar Physics,* 289**,** 3137-3157.

MONTGOMERY, M. D., ASBRIDGE, J. R., BAME, S. J. & FELDMAN, W. C. 1974. Solar wind electron temperature depressions following some interplanetary shock waves: Evidence for magnetic merging? *Journal of Geophysical Research,* 79**,** 3103-3110.

MOON, Y.-J., CHO, K.-S., DRYER, M., KIM, Y.-H., BONG, S.-C., CHAE, J. & PARK, Y. 2005. New geoeffective parameters of very fast halo coronal mass ejections. *The Astrophysical Journal,* 624**,** 414.

MORGAN, H. 2011. The Rotation of the White Light Solar Corona at Height 4 R⊙ from 1996 to 2010: A Tomographical Study of Large Angle and Spectrometric Coronagraph C2 Observations. *The Astrophysical Journal,* 738**,** 189.

MORGAN, H. 2015. AN ATLAS OF CORONAL ELECTRON DENSITY AT 5R⊙. I. DATA PROCESSING AND CALIBRATION. *The Astrophysical Journal Supplement Series,* 219**,** 23.

MORGAN, H., BYRNE, J. P. & HABBAL, S. R. 2012. Automatically detecting and tracking coronal mass ejections. I. Separation of dynamic and quiescent components in coronagraph images. *The Astrophysical Journal,* 752**,** 144.

MORGAN, H. & DRUCKMÜLLER, M. 2014. Multi-scale Gaussian normalization for solar image processing. *Solar physics,* 289**,** 2945-2955.

MORGAN, H. & HABBAL, S. R. 2010. Observational aspects of the three-dimensional coronal structure over a solar activity cycle. *The Astrophysical Journal,* 710**,** 1.

MORGAN, H., HABBAL, S. R. & WOO, R. 2006. The depiction of coronal structure in white-light images. *Solar Physics,* 236**,** 263-272.

MORGAN, H., JESKA, L. & LEONARD, D. 2013. The expansion of active regions into the extended solar corona. *The Astrophysical Journal Supplement Series,* 206**,** 19.

MORGAN, H. & TAROYAN, Y. 2017. Global conditions in the solar corona from 2010 to 2017. *Science Advances,* 3**,** e1602056.

MORRISON, P. Solar-connected variations of the cosmic rays. Physical Review, 1954. AMERICAN PHYSICAL SOC ONE PHYSICS ELLIPSE, COLLEGE PK, MD 20740-3844 USA, 646-646.

MÖSTL, C., FARRUGIA, C. J., TEMMER, M., MIKLENIC, C., VERONIG, A. M., GALVIN, A. B., LEITNER, M. & BIERNAT, H. K. 2009. Linking remote imagery of a coronal mass ejection to its in situ signatures at 1 AU. *The Astrophysical Journal Letters,* 705**,** L180.

MÖSTL, C., TEMMER, M., ROLLETT, T., FARRUGIA, C. J., LIU, Y., VERONIG, A. M., LEITNER, M., GALVIN, A. B. & BIERNAT, H. K. 2010. STEREO and Wind observations of a fast ICME flank triggering a prolonged geomagnetic storm on 5–7 April 2010. *Geophysical Research Letters,* 37.

MULLIGAN, T. & RUSSELL, C. 2001. Multispacecraft modeling of the flux rope structure of interplanetary coronal mass ejections: Cylindrically symmetric versus nonsymmetric topologies. *Journal of Geophysical Research: Space Physics,* 106**,** 10581-10596.

MULLIGAN, T., RUSSELL, C., ANDERSON, B., LOHR, D., RUST, D., TOTH, B., ZANETTI, L., ACUNA, M., LEPPING, R. & GOSLING, J. 1999. Intercomparison of NEAR and Wind interplanetary coronal mass ejection observations. *Journal of Geophysical Research: Space Physics,* 104**,** 28217-28223.

MULLIGAN, T., RUSSELL, C. & LUHMANN, J. 1998. Solar cycle evolution of the structure of magnetic clouds in the inner heliosphere. *Geophysical Research Letters,* 25**,** 2959-2962.

NELSON, G. & MELROSE, D. 1985. Type II bursts. *Solar Radiophysics: Studies of Emission from the Sun at Metre Wavelengths,* 1**,** 333-359.

NEUGEBAUER, M., LIEWER, P., GOLDSTEIN, B., ZHOU, X. & STEINBERG, J. 2004. Solar wind stream interaction regions without sector boundaries. *Journal of Geophysical Research: Space Physics,* 109.

OGILVIE, K., CHORNAY, D., FRITZENREITER, R., HUNSAKER, F., KELLER, J., LOBELL, J., MILLER, G., SCUDDER, J., SITTLER, E. & TORBERT, R. 1995. SWE, a comprehensive plasma instrument for the Wind spacecraft. *Space Science Reviews,* 71**,** 55-77.

OLIVEROS, J. C. M., RAFTERY, C. L., BAIN, H. M., LIU, Y., KRUPAR, V., BALE, S. & KRUCKER, S. 2012. The 2010 August 1 type II burst: A CME-CME interaction and its radio and white-light manifestations. *The Astrophysical Journal,* 748**,** 66.

OWENS, M. 2016. Do the legs of magnetic clouds contain twisted flux-rope magnetic fields? *The Astrophysical Journal,* 818**,** 197.

OWENS, M., CROOKER, N. & LOCKWOOD, M. 2013. Solar origin of heliospheric magnetic field inversions: Evidence for coronal loop opening within pseudostreamers. *Journal of Geophysical Research: Space Physics,* 118**,** 1868-1879.

OWENS, M. J., CROOKER, N. & LOCKWOOD, M. 2011. How is open solar magnetic flux lost over the solar cycle? *Journal of Geophysical Research: Space Physics,* 116.

OWENS, M. J. & FORSYTH, R. J. 2013. The heliospheric magnetic field. *Living Reviews in Solar Physics,* 10**,** 1-52.

PAGEL, C., CROOKER, N. & LARSON, D. 2005. Assessing electron heat flux dropouts as signatures of magnetic field line disconnection from the Sun. *Geophysical research letters,* 32.

PALMER, I., ALLUM, F. & SINGER, S. 1978. Bidirectional anisotropies in solar cosmic ray events: Evidence for magnetic bottles. *Journal of Geophysical Research: Space Physics,* 83**,** 75-90.

PARKER, E. 1961. Sudden Expansion of the Corona Following a Large Solar Flare and the Attendant Magnetic Field and Cosmic-Ray Effects. *The Astrophysical Journal,* 133**,** 1014.

PARKER, E. N. 1958. Dynamics of the interplanetary gas and magnetic fields. *The Astrophysical Journal,* 128**,** 664.

PARKER, E. N. 1963. Interplanetary dynamical processes. *New York, Interscience Publishers, 1963.,* 1.

PESNELL, W. D. 2015. *Solar dynamics observatory (SDO)*, Springer.

PIZZO, V. 1978. A three-dimensional model of corotating streams in the solar wind, 1. Theoretical foundations. *Journal of Geophysical Research: Space Physics,* 83**,** 5563-5572.

PIZZO, V. 1991. The evolution of corotating stream fronts near the ecliptic plane in the inner solar system: 2. Three-dimensional tilted-dipole fronts. *Journal of Geophysical Research: Space Physics,* 96**,** 5405-5420.

PRISE, A., HARRA, L., MATTHEWS, S., ARRIDGE, C. S. & ACHILLEOS, N. 2015. Analysis of a coronal mass ejection and corotating interaction region as they travel from the Sun passing Venus, Earth, Mars, and Saturn. *Journal of Geophysical Research: Space Physics,* 120**,** 1566-1588.

PROVORNIKOVA, E., OPHER, M., IZMODENOV, V. & TOTH, G. 2012. Do Corotating Interaction Region Associated Shocks Survive When They Propagate into the Heliosheath? *The Astrophysical Journal Letters,* 756**,** L37.

PUDOVKIN, M., ZAITSEVA, S. & BENEVOLENSKA, E. 1979. The structure and parameters of flare streams. *Journal of Geophysical Research: Space Physics,* 84**,** 6649-6652.

RATCLIFFE, J. A. 1972. Introduction to the ionosphere and magnetosphere.

RICHARDSON, I., BERDICHEVSKY, D., DESCH, M. & FARRUGIA, C. 2000. Solar-cycle variation of low density solar wind during more than three solar cycles. *Geophys. Res. Lett,* 27**,** 3761.

RICHARDSON, I. & CANE, H. 1993. Signatures of shock drivers in the solar wind and their dependence on the solar source location. *Journal of Geophysical Research: Space Physics,* 98**,** 15295-15304.

RICHARDSON, I. & CANE, H. 1995. Regions of abnormally low proton temperature in the solar wind (1965–1991) and their association with ejecta. *Journal of Geophysical Research: Space Physics,* 100**,** 23397-23412.

RICHARDSON, I. & CANE, H. 2010. Near-Earth interplanetary coronal mass ejections during solar cycle 23 (1996–2009): Catalog and summary of properties. *Solar Physics,* 264**,** 189-237.

RICHARDSON, I., FARRUGIA, C. & CANE, H. 1997. A statistical study of the behavior of the electron temperature in ejecta. *Journal of Geophysical Research: Space Physics,* 102**,** 4691-4699.

RICHARDSON, I., WIBBERENZ, G. & CANE, H. 1996. The relationship between recurring cosmic ray depressions and corotating solar wind streams at≤ 1 AU: IMP 8 and Helios 1 and 2 anticoincidence guard rate observations. *Journal of Geophysical Research: Space Physics,* 101**,** 13483-13496.

RICHTER, A. & LUTTRELL, A. 1986. Superposed epoch analysis of corotating interaction regions at 0.3 and 1.0 AU: A comparative study. *Journal of Geophysical Research: Space Physics,* 91**,** 5873-5878.

RILEY, P., LIONELLO, R., MIKIĆ, Z. & LINKER, J. 2008. Using global simulations to relate the three-part structure of coronal mass ejections to in situ signatures. *The Astrophysical Journal,* 672**,** 1221.

RILEY, P. & RICHARDSON, I. 2013. Using statistical multivariable models to understand the relationship between interplanetary coronal mass ejecta and magnetic flux ropes. *Solar Physics,* 284**,** 217-233.

RODRIGUEZ, L., MIERLA, M., ZHUKOV, A., WEST, M. & KILPUA, E. 2011. Linking remote-sensing and in situ observations of coronal mass ejections using STEREO. *Solar Physics,* 270**,** 561-573.

RODRIGUEZ, L., WOCH, J., KRUPP, N., FRÄNZ, M., VON STEIGER, R., FORSYTH, R., REISENFELD, D. & GLAßMEIER, K. H. 2004. A statistical study of oxygen freezing-in temperature and energetic particles inside magnetic clouds observed by Ulysses. *Journal of Geophysical Research: Space Physics,* 109.

ROMERO-HERNANDEZ, E. & GONZALEZ-ESPARZA, J. Multi-spacecraft study of five ICMEs and their shock waves: Helios, IMP-8 and Voyagers observations. AIP Conference Proceedings, 2013. AIP, 267-270.

ROUILLARD, A. 2011. Relating white light and in situ observations of coronal mass ejections: A review. *Journal of Atmospheric and Solar-Terrestrial Physics,* 73**,** 1201-1213.

ROUILLARD, A., SAVANI, N., DAVIES, J., LAVRAUD, B., FORSYTH, R., MORLEY, S., OPITZ, A., SHEELEY, N., BURLAGA, L. & SAUVAUD, J.-A. 2009. A multispacecraft analysis of a small-scale transient entrained by solar wind streams. *Solar Physics,* 256**,** 307-326.

ROUILLARD, A. P., LAVRAUD, B., DAVIES, J. A., SAVANI, N. P., BURLAGA, L. F., FORSYTH, R. J., SAUVAUD, J. A., OPITZ, A., LOCKWOOD, M., LUHMANN, J. G., SIMUNAC, K. D. C., GALVIN, A. B., DAVIS, C. J. & HARRISON, R. A. 2010. Intermittent release of transients in the slow solar wind: 2. In situ evidence. *Journal of Geophysical Research: Space Physics,* 115**,** n/a-n/a.

RUSSELL, C. 2001. Solar wind and interplanetary magnetic field: A tutorial. *Space Weather***,** 73-89.

RUSSELL, C. & SHINDE, A. 2003. ICME identification from solar wind ion measurements. *Solar Physics,* 216**,** 285-294.

RUSSELL, C. & SHINDE, A. 2005. On defining interplanetary coronal mass ejections from fluid parameters. *Solar Physics,* 229**,** 323-344.

RUSSELL, C., SHINDE, A. & JIAN, L. 2005. A new parameter to define interplanetary coronal mass ejections. *Advances in Space Research,* 35**,** 2178-2184.

SAUVAUD, J.-A., LARSON, D., AOUSTIN, C., CURTIS, D., MÉDALE, J.-L., FEDOROV, A., ROUZAUD, J., LUHMANN, J., MOREAU, T. & SCHRÖDER, P. 2008. The IMPACT solar wind electron analyzer (SWEA). *The STEREO Mission.* Springer.

SCHERRER, P. H., SCHOU, J., BUSH, R., KOSOVICHEV, A., BOGART, R., HOEKSEMA, J., LIU, Y., DUVALL JR, T., ZHAO, J. & SCHRIJVER, C. 2011. The helioseismic and magnetic imager (HMI) investigation for the solar dynamics observatory (SDO). *The Solar Dynamics Observatory.* Springer.

SCHOU, J., SCHERRER, P., BUSH, R., WACHTER, R., COUVIDAT, S., RABELLO-SOARES, M., BOGART, R., HOEKSEMA, J., LIU, Y. & DUVALL JR, T. 2011. Design and ground calibration of the Helioseismic and Magnetic Imager (HMI) instrument on the Solar Dynamics Observatory (SDO). *The Solar Dynamics Observatory.* Springer.

SCHWENN, R. 1990. Large-scale structure of the interplanetary medium. *Physics of the inner Heliosphere I.* Springer.

SCHWENN, R. 2006. Space weather: The solar perspective. *Living Reviews in Solar Physics,* 3**,** 1-72.

SCHWENN, R., ROSENBAUER, H. & MÜHLHÄUSER, K. H. 1980. Singly-ionized helium in the driver gas of an interplanetary shock wave. *Geophysical Research Letters,* 7**,** 201-204.

SHEN, C., WANG, Y., GUI, B., YE, P. & WANG, S. 2011. Kinematic evolution of a slow CME in corona viewed by STEREO-B on 8 October 2007. *Solar Physics,* 269**,** 389-400.

SHEN, C., WANG, Y., WANG, S., LIU, Y., LIU, R., VOURLIDAS, A., MIAO, B., YE, P., LIU, J. & ZHOU, Z. 2012. Super-elastic collision of large-scale magnetized plasmoids in the heliosphere. *Nature Physics,* 8**,** 923-928.

SHODHAN, S., CROOKER, N., KAHLER, S., FITZENREITER, R., LARSON, D., LEPPING, R., SISCOE, G. & GOSLING, J. 2000. Counterstreaming electrons in magnetic clouds. *Journal of Geophysical Research: Space Physics,* 105**,** 27261-27268.

SIMUNAC, K., GALVIN, A., FARRUGIA, C., KISTLER, L., KUCHAREK, H., LAVRAUD, B., LIU, Y.-M., LUHMANN, J., OGILVIE, K. & OPITZ, A. 2012. The heliospheric plasma sheet observed in situ by three spacecraft over four solar rotations. *Solar Physics,* 281**,** 423-447.

SISCOE, G. & INTRILIGATOR, D. 1993. Three views of two giant streams: Aligned observations at 1 AU, 4.6 AU, and 5.9 AU. *Geophysical research letters,* 20**,** 2267-2270.

SISCOE, G. L., GOLDSTEIN, B. & LAZARUS, A. 1969. An east-west asymmetry in the solar wind velocity. *Journal of Geophysical Research,* 74**,** 1759-1762.

SITTLER, E. & BURLAGA, L. 1998. Electron temperatures within magnetic clouds between 2 and 4 AU: Voyager 2 observations. *Journal of Geophysical Research: Space Physics,* 103**,** 17447-17454.

SKOUG, R., GOSLING, J., MCCOMAS, D., SMITH, C. & HU, Q. 2006. Suprathermal electron 90 pitch angle depletions at reverse shocks in the solar wind. *Journal of Geophysical Research: Space Physics,* 111.

SMITH, C. W., L'HEUREUX, J., NESS, N. F., ACUÑA, M. H., BURLAGA, L. F. & SCHEIFELE, J. 1998a. The ACE magnetic fields experiment. *The Advanced Composition Explorer Mission.* Springer.

SMITH, E. J. 2001. The heliospheric current sheet. *Journal of Geophysical Research: Space Physics,* 106**,** 15819-15831.

SMITH, E. J., TSURUTANI, B. T. & ROSENBERG, R. L. 1978. Observations of the interplanetary sector structure up to heliographic latitudes of 16: Pioneer 11. *Journal of Geophysical Research: Space Physics,* 83**,** 717-724.

SMITH, E. J. & WOLFE, J. H. 1976. Observations of interaction regions and corotating shocks between one and five AU: Pioneers 10 and 11. *Geophysical Research Letters,* 3**,** 137-140.

SMITH, Z., ODSTRCIL, D. & DRYER, M. 1998b. A 2.5-dimensional MHD parametric study of interplanetary shock interactions with the heliospheric current sheet/heliospheric plasma sheet. *Journal of Geophysical Research: Space Physics,* 103**,** 20581-20589.

SONG, H., CHEN, Y., LIU, K., FENG, S. & XIA, L. 2009. Quasi-periodic releases of streamer blobs and velocity variability of the slow solar wind near the Sun. *Solar Physics,* 258**,** 129-140.

SPREITER, J. R., SUMMERS, A. L. & ALKSNE, A. Y. 1966. Hydromagnetic flow around the magnetosphere. *Planetary and Space Science,* 14**,** 223IN1251-250IN2253.

STEINBERG, J., GOSLING, J., SKOUG, R. & WIENS, R. 2005. Suprathermal electrons in high-speed streams from coronal holes: Counterstreaming on open field lines at 1 AU. *Journal of Geophysical Research: Space Physics,* 110.

STEINBERG, J., LAZARUS, A., OGILVIE, K., LEPPING, R. & BYRNES, J. 1996. Differential flow between solar wind protons and alpha particles: First WIND observations. *Geophysical research letters,* 23**,** 1183-1186.

STONE, E., FRANDSEN, A., MEWALDT, R., CHRISTIAN, E., MARGOLIES, D., ORMES, J. & SNOW, F. 1998. The advanced composition explorer. *The Advanced Composition Explorer Mission.* Springer.

SUBRAMANIAN, P., ARUNBABU, K., VOURLIDAS, A. & MAURIYA, A. 2014. Self-similar expansion of solar coronal mass ejections: Implications for Lorentz self-force driving. *The Astrophysical Journal,* 790**,** 125.

SUESS, S., KO, Y. K., VON STEIGER, R. & MOORE, R. 2009. Quiescent current sheets in the solar wind and origins of slow wind. *Journal of Geophysical Research: Space Physics,* 114.

SUESS, S., MCCOMAS, D., BAME, S. & GOLDSTEIN, B. 1995. Solar wind eddies and the heliospheric current sheet. *Journal of Geophysical Research: Space Physics,* 100**,** 12261-12273.

SVALGAARD, L. & WILCOX, J. M. 1975. Long term evolution of solar sector structure. *Solar Physics,* 41**,** 461-475.

SVALGAARD, L., WILCOX, J. M., SCHERRER, P. H. & HOWARD, R. 1975. The sun's magnetic sector structure. *Solar Physics,* 45**,** 83-91.

TEMMER, M., VERONIG, A., PEINHART, V. & VRŠNAK, B. 2014. Asymmetry in the CME-CME interaction process for the events from 2011 February 14-15. *The Astrophysical Journal,* 785**,** 85.

TEMMER, M., VRŠNAK, B., ROLLETT, T., BEIN, B., DE KONING, C. A., LIU, Y., BOSMAN, E., DAVIES, J. A., MÖSTL, C. & ŽIC, T. 2012. Characteristics of kinematics of a coronal mass ejection during the 2010 August 1 CME–CME interaction event. *The Astrophysical Journal,* 749**,** 57.

THOMPSON, W., WEI, K., BURKEPILE, J., DAVILA, J. & CYR, O. S. 2010. Background subtraction for the SECCHI/COR1 telescope aboard STEREO. *Solar Physics,* 262**,** 213-231.

TIAN, H., YAO, S., ZONG, Q., HE, J. & QI, Y. 2010. Signatures of magnetic reconnection at boundaries of interplanetary small-scale magnetic flux ropes. *The Astrophysical Journal,* 720**,** 454.

TOUSEY, R. The solar corona. Space Research Conference, 1973. 713-730.

TSURUTANI, B. T. & GONZALEZ, W. D. 1997. *The interplanetary causes of magnetic storms: A review*, Wiley Online Library.

TSURUTANI, B. T., GONZALEZ, W. D., GONZALEZ, A. L., TANG, F., ARBALLO, J. K. & OKADA, M. 1995. Interplanetary origin of geomagnetic activity in the declining phase of the solar cycle. *Journal of Geophysical Research: Space Physics,* 100**,** 21717-21733.

TSURUTANI, B. T., MCPHERRON, R. L., GONZALEZ, W. D., LU, G., GOPALSWAMY, N. & GUARNIERI, F. L. 2006. Magnetic storms caused by corotating solar wind streams. *Recurrent Magnetic Storms: Corotating Solar Wind Streams***,** 1-17.

TURNER, R. E. 2006. Space weather challenges intrinsic to the human exploration of space. *Solar Eruptions and Energetic Particles***,** 367-374.

VAIANA, G., KRIEGER, A. & TIMOTHY, A. 1973. Identification and analysis of structures in the corona from X-ray photography. *Solar Physics,* 32**,** 81-116.

VANDAS, M., ODSTRČIL, D. & WATARI, S. 2002. Three-dimensional MHD simulation of a loop-like magnetic cloud in the solar wind. *Journal of Geophysical Research: Space Physics,* 107.

VON STEIGER, R. & RICHARDSON, J. 2006. ICMEs in the outer heliosphere and at high latitudes: An introduction. *Coronal Mass Ejections.* Springer.

VOURLIDAS, A., LYNCH, B. J., HOWARD, R. A. & LI, Y. 2013. How many CMEs have flux ropes? Deciphering the signatures of shocks, flux ropes, and prominences in coronagraph observations of CMEs. *Solar Physics,* 284**,** 179-201.

WANG, Y.-M. & SHEELEY JR, N. 1993. Understanding the rotation of coronal holes. *The Astrophysical Journal,* 414**,** 916-927.

WANG, Y.-M. & SHEELEY JR, N. 2003. On the topological evolution of the coronal magnetic field during the solar cycle. *The Astrophysical Journal,* 599**,** 1404.

WANG, Y.-M., SHEELEY JR, N., SOCKER, D., HOWARD, R., BRUECKNER, G., MICHELS, D., MOSES, D., CYR, O. S., LLEBARIA, A. & DELABOUDINIERE, J.-P. 1998a. Observations of correlated white-light and extreme-ultraviolet jets from polar coronal holes. *The Astrophysical Journal,* 508**,** 899.

WANG, Y.-M., SHEELEY JR, N., WALTERS, J., BRUECKNER, G., HOWARD, R., MICHELS, D., LAMY, P., SCHWENN, R. & SIMNETT, G. 1998b. Origin of streamer material in the outer corona. *The Astrophysical Journal Letters,* 498**,** L165.

WANG, Y., SHEN, C., WANG, S. & YE, P. 2004. Deflection of coronal mass ejection in the interplanetary medium. *Solar Physics,* 222**,** 329-343.

WANG, Y., WANG, B., SHEN, C., SHEN, F. & LUGAZ, N. 2014. Deflected propagation of a coronal mass ejection from the corona to interplanetary space. *Journal of Geophysical Research: Space Physics,* 119**,** 5117-5132.

WANG, Y., YE, P., WANG, S., ZHOU, G. & WANG, J. 2002. A statistical study on the geoeffectiveness of Earth-directed coronal mass ejections from March 1997 to December 2000. *Journal of Geophysical Research: Space Physics,* 107.

WANG, Y. & ZHANG, J. 2007. A comparative study between eruptive X-class flares associated with coronal mass ejections and confined X-class flares. *The Astrophysical Journal,* 665**,** 1428.

WANG, Y. M., SHEELEY, N., SOCKER, D., HOWARD, R. & RICH, N. 2000. The dynamical nature of coronal streamers. *Journal of Geophysical Research: Space Physics,* 105**,** 25133-25142.

WANG, Y. M., YE, P. Z. & WANG, S. 2003. Multiple magnetic clouds: Several examples during March–April 2001. *Journal of Geophysical Research: Space Physics,* 108.

WATANABE, T. 1989. Solar wind latitude/longitude variations derived from interplanetary scintillations. *Advances in Space Research,* 9**,** 99-110.

WEBB, D. & HUNDHAUSEN, A. 1987. Activity associated with the solar origin of coronal mass ejections. *Solar physics,* 108**,** 383-401.

WEI, F., LIU, R., FAN, Q. & FENG, X. 2003. Identification of the magnetic cloud boundary layers. *Journal of Geophysical Research: Space Physics,* 108.

WEIMER, D., OBER, D., MAYNARD, N., BURKE, W., COLLIER, M., MCCOMAS, D., NESS, N. & SMITH, C. 2002. Variable time delays in the propagation of the interplanetary magnetic field. *Journal of Geophysical Research: Space Physics,* 107.

WEIMER, D., OBER, D., MAYNARD, N., COLLIER, M., MCCOMAS, D., NESS, N., SMITH, C. & WATERMANN, J. 2003. Predicting interplanetary magnetic field (IMF) propagation delay times using the minimum variance technique. *Journal of Geophysical Research: Space Physics,* 108.

WEIMER, D. R. & KING, J. H. 2008. Improved calculations of interplanetary magnetic field phase front angles and propagation time delays. *Journal of Geophysical Research: Space Physics,* 113.

WHANG, Y., BURLAGA, L., NESS, N. & SMITH, C. 2001. The Bastille Day shocks and merged interaction region. *Solar Physics,* 204**,** 253-263.

WIEGELMANN, T., THALMANN, J. K. & SOLANKI, S. K. 2014. The magnetic field in the solar atmosphere. *The Astronomy and Astrophysics Review,* 22**,** 1-106.

WILCOX, J. M. & NESS, N. F. 1965. Quasi-stationary corotating structure in the interplanetary medium. *Journal of Geophysical Research,* 70**,** 5793-5805.

WILD, J. & SMERD, S. 1972. Radio bursts from the solar corona. *Annual Review of Astronomy and Astrophysics,* 10**,** 159-196.

WIMMER-SCHWEINGRUBER, R., CROOKER, N., BALOGH, A., BOTHMER, V., FORSYTH, R., GAZIS, P., GOSLING, J., HORBURY, T., KILCHENMANN, A. & RICHARDSON, I. 2006. Understanding interplanetary coronal mass ejection signatures. *Space Science Reviews,* 123**,** 177-216.

WIMMER-SCHWEINGRUBER, R. F., STEIGER, R. & PAERLI, R. 1999. Solar wind stream interfaces in corotating interaction regions: New SWICS/Ulysses results. *Journal of Geophysical Research: Space Physics,* 104**,** 9933-9945.

WINSLOW, R. M., LUGAZ, N., SCHWADRON, N. A., FARRUGIA, C. J., YU, W., RAINES, J. M., MAYS, M. L., GALVIN, A. B. & ZURBUCHEN, T. H. 2016. Longitudinal conjunction between MESSENGER and STEREO A: development of ICME complexity through stream interactions. *Journal of Geophysical Research: Space Physics*.

WINTERHALTER, D., SMITH, E., BURTON, M., MURPHY, N. & MCCOMAS, D. 1994. The heliospheric plasma sheet. *Journal of Geophysical Research: Space Physics,* 99**,** 6667-6680.

WU, C.-C. & LEPPING, R. 2011. Statistical comparison of magnetic clouds with interplanetary coronal mass ejections for solar cycle 23. *Solar Physics,* 269**,** 141-153.

WU, C.-C., LIOU, K., VOURLIDAS, A., PLUNKETT, S., DRYER, M., WU, S. T., SOCKER, D., WOOD, B. E., HUTTING, L. & HOWARD, R. A. 2016. Numerical simulation of multiple CME-driven shocks in the month of 2011 September. *Journal of Geophysical Research: Space Physics,* 121**,** 1839-1856.

XIE, H., GOPALSWAMY, N. & CYR, O. S. 2013. Near-sun flux-rope structure of CMEs. *Solar Physics,* 284**,** 47-58.

XU, X., WEI, F. & FENG, X. 2011. Observations of reconnection exhausts associated with large-scale current sheets within a complex ICME at 1 AU. *Journal of Geophysical Research: Space Physics,* 116.

YASHIRO, S., GOPALSWAMY, N., MICHALEK, G., ST CYR, O., PLUNKETT, S., RICH, N. & HOWARD, R. 2004. A catalog of white light coronal mass ejections observed by the SOHO spacecraft. *Journal of Geophysical Research: Space Physics,* 109.

ZHANG, G. & BURLAGA, L. 1988. Magnetic clouds, geomagnetic disturbances, and cosmic ray decreases. *Journal of Geophysical Research: Space Physics,* 93**,** 2511-2518.

ZHANG, J., DERE, K., HOWARD, R. & BOTHMER, V. 2003. Identification of solar sources of major geomagnetic storms between 1996 and 2000. *The Astrophysical Journal,* 582**,** 520.

ZHANG, J., HESS, P. & POOMVISES, W. 2013. A Comparative Study of Coronal Mass Ejections with and Without Magnetic Cloud Structure near the Earth: Are All Interplanetary CMEs Flux Ropes? *Solar Physics,* 284**,** 89-104.

ZHANG, J., RICHARDSON, I., WEBB, D., GOPALSWAMY, N., HUTTUNEN, E., KASPER, J., NITTA, N., POOMVISES, W., THOMPSON, B. & WU, C. C. 2007. Solar and interplanetary sources of major geomagnetic storms (Dst≤− 100 nT) during 1996–2005. *Journal of Geophysical Research: Space Physics,* 112.

ZHAO, X. & HOEKSEMA, J. T. 1996. Effect of coronal mass ejections on the structure of the heliospheric current sheet. *Journal of Geophysical Research: Space Physics,* 101**,** 4825-4834.

ZHAO, X. & WEBB, D. 2003. Source regions and storm effectiveness of frontside full halo coronal mass ejections. *Journal of Geophysical Research: Space Physics,* 108.

ZHENG, J. & HU, Q. Observations and analysis of small-scale magnetic flux ropes in the solar wind. Journal of Physics: Conference Series, 2016. IOP Publishing, 012028.

ZURBUCHEN, T., HEFTI, S., FISK, L., GLOECKLER, G., SCHWADRON, N., SMITH, C., NESS, N., SKOUG, R., MCCOMAS, D. & BURLAGA, L. 2001. On the origin of microscale magnetic holes in the solar wind. *Journal of Geophysical Research: Space Physics,* 106**,** 16001-16010.

ZURBUCHEN, T., SCHWADRON, N. & FISK, L. 1997. Direct observational evidence for a heliospheric magnetic field with large excursions in latitude. *Journal of Geophysical Research: Space Physics,* 102**,** 24175-24181.

ZURBUCHEN, T. H. 2007. A new view of the coupling of the Sun and the heliosphere. *Annu. Rev. Astron. Astrophys.,* 45**,** 297-338.

ZURBUCHEN, T. H., FISK, L., LEPRI, S., VON STEIGER, R., VELLI, M., BRUNO, R. & MALARA, F. The composition of interplanetary coronal mass ejections. AIP Conference Proceedings, 2003. AIP, 604-607.

ZURBUCHEN, T. H. & RICHARDSON, I. G. 2006. In-situ solar wind and magnetic field signatures of interplanetary coronal mass ejections. *Space Science Reviews,* 123**,** 31-43.